Gamma- and beta-decay spectroscopy of ^{190}W, ^{205}Au and ^{203}Au.

Gregory Francis Farrelly

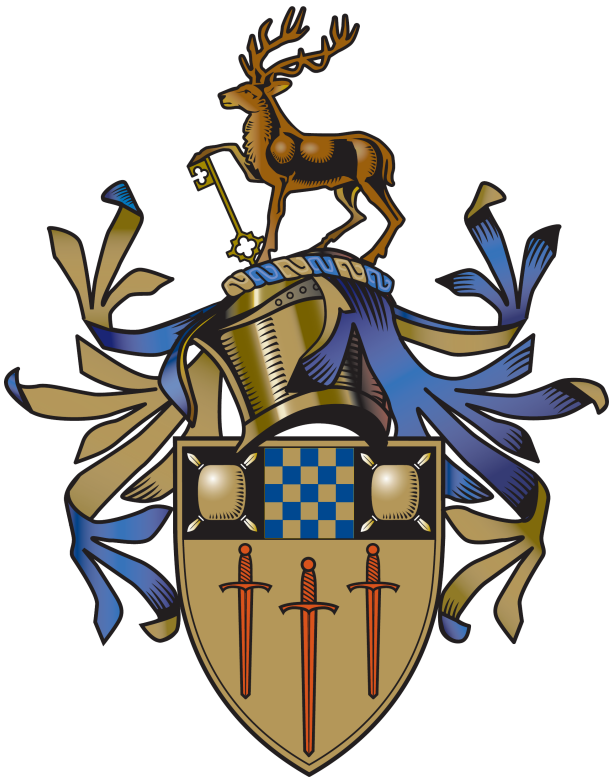

Department of Physics,
University of Surrey

A thesis submitted for the degree of Doctor of Philosophy

June 14, 2010

Contents

List of Figures

List of Tables

Abstract

Three exotic, neutron-rich nuclides with isomeric states have been analysed and the results discussed in this thesis: ^{190}W, ^{205}Au and ^{203}Au. The nuclides were produced using relativistic projectile fragmentation of a 1 GeV per nucleon ^{208}Pb beam on a thick (2.5 g/cm^2) Be target. Fragments were separated and identified in-flight using the GSI Fragment Separator before implantation in a stopper. The RISING gamma spectrometer was used to observe the decay of isomeric states.

^{190}W is a deformed nuclide displaying behaviour consistent with K-isomerism. Gamma transitions observed in a previous experiment indicated decay from a 10^- isomer via a rotational band to the ground state, although one of the transitions within this band is absent in the present analysis. Gamma coincidence and time-difference measurements have been made, resulting in a modified decay scheme. Reduced hindrance factors, potential energy surface and blocked BCS calculations have also been used to enable possible values of spin-parity for the isomer to be assigned. In contrast, ^{205}Au and ^{203}Au are on, or close to, the N=126 closed shell and their isomeric states are due to spin isomerism. Both nuclides were produced in the first "active stopper" experiment at GSI, allowing the detection of both internal conversion electrons and beta-delayed gamma rays. An isomer whose decay has high multipolarity (M4) was detected in ^{205}Au, and some evidence found that the isomeric state decays in two ways: by gamma decay to the ground state and by beta-decay to excited states in ^{205}Hg. The absence of such an isomer in ^{203}Au is discussed in the light of shell model calculations.

Acknowledgements

I would like to thank my wife, Claire, for agreeing to let me undertake this extraordinary adventure. She has coped brilliantly with the challenges of our considerably reduced income during my studies, my frequent trips away from home, and her anxiety at the distance and faster speeds involved in my commuting to Guildford by motorbike. I also thank Lucy, my daughter, for dealing with a student father who was often absent and even more eccentric than usual.

I must put on record my thanks to my supervisor Dr. Zsolt Podolyák, who had the unenviable task of taking on an aged schoolteacher as his first full-term Ph.D. student. He has always shown patience with my inane questions and the tardiness of my analysis. To the ever enthusiastic and incorrigible Prof. Paddy Regan, my co-supervisor, I offer my gratitude for all his help and encouragement, as well as for the pleasure of his company - Saol fada chugat!

I would like to acknowledge the help and advice given by Emeritus Distinguished Prof. Bill Gelletly, Emeritus Prof. Ron Johnson, Professors Phil 'isomer' Walker and Wilton 'if it's Thursday I must be in Vancouver' Catford, Drs. Stéphane Pietri, Paul Stevenson, Zhong Liu, Adam Garnsworthy, Jeff "No.1 Postdoc" Thomas and Ajay Deo. I also wish to thank my fellow research students: Ian Cullen, Elizabeth Cunningham, Emma Suckling, Nicky Patterson, Dr. Nasser Alkhomashi, Nawras Al-Dahan, Simon Brown, Gemma Wilson (who proof-read this thesis), Dr. Ed Simpson (who assisted with the shell model calculations for the Au nuclides), and especially Dr. Steven Steer, for help above and beyond the call of duty.

I owe a huge debt to Prof. Alison Bruce for agreeing to take me on as a potential Ph.D. student at the University of Brighton and for her constant encouragement. I am aware that without her support and the willingness of Prof. Bill Gelletly to give me a chance, despite my age, this adventure would not have been possible. I also owe Dr. Peter Phillips, with whom I taught Physics at Coloma school, my thanks for first suggesting that a Ph.D. at my age might not be such a mad idea and for being my academic referee. I am grateful to the late Prof. W.E. Burcham, F.R.S., and Prof. George C. Morrison, under both of whom I studied at the University of Birmingham, for encouraging my interest in experimental nuclear structure physics and to Father Roger Nesbitt, who enabled me to see that science itself is a sign of God's existence.

I would also like to acknowledge the financial support of the Engineering and Physical Sciences Research Council (EPSRC) who funded my Ph.D.

"Non est ad astra mollis e terris via."
(from 'Hercules Furens' - Lucius Annaeus Seneca)

To Claire, with love

Chapter 1

Introduction

Around 6000 different nuclides are predicted to exist between the proton and neutron drip lines [1]; around 3600 nuclides have been experimentally discovered to date, of which 198 are considered 'stable' [2], i.e. having half-lives commensurate with the age of the Earth. The majority of known nuclides are therefore unstable and thus radioactive. Analysis of the radiation spectra from such nuclides has enabled a considerable amount of detail concerning the structure of atomic nuclei to be gained.

The nuclear 'landscape' is shown in Fig. 1.1. The nuclides investigated in this thesis lie on the neutron-rich side of the 'valley of stability' and are 'exotic', i.e. they have an extraordinary ratio of protons and neutrons compared to stable nuclides. The primary purpose of experimental investigations on exotic nuclides is to gain insight into nuclear structure as one departs from stability, particularly as regards the systematics of energy levels, shells (and possible shell quenching), changes in nuclear shape, and new or competing modes of excitation. In addition, a specific motivation for studying exotic, neutron-rich nuclei is related to astrophysics, in particular the *r-process*. This process is believed to occur in core-collapse supernovae and accounts for the creation of about half of the neutron-rich nuclei heavier than iron. There is a succession of rapid (hence the name *r-process*) neutron captures on iron 'seed' nuclei. The analogous rapid capture of protons is called the *rp-process*. The other principal mechanism for the production of heavy elements is the *s-process* ('slow' neutron capture process), primarily occurring in AGB stars [3].

The advent of radioactive beams for experiments at facilities such as GSI (Gesellschaft für Schwerionenforschung), in Germany, has enabled the production of previously inaccessible heavy, neutron-rich, exotic nuclides. Projectile fragmentation, combined with high sensitivity gamma and electron detection arrays, has enabled these ions to be investigated. The resulting experimental data allows nucleosynthesis models to be tested and refined.

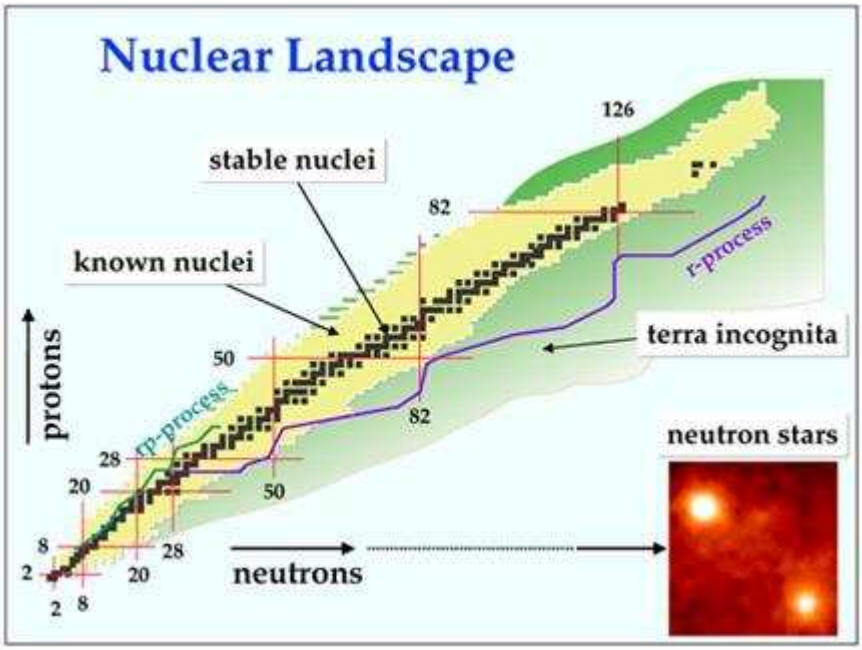

Figure 1.1: The nuclear landscape: black squares represent stable nuclei, yellow squares indicate unstable nuclei produced and studied in the laboratory, and the thousands of unstable, unexplored nuclei are indicated in green (Terra Incognita). The red vertical and horizontal lines show the magic numbers, where there are closed nucleonic shells, thus longer half-lives. Two paths of astrophysical processes for nucleosynthesis (r-process - purple line; rp-process - turquoise line) are also shown [4].

The nuclides investigated in this thesis are exotic and neutron-rich (relative to stable isotopes), but are situated in contrasting regions of the Segrè chart: ^{190}W is in a region between proton and neutron closed shells, exhibiting collective structure, shape deformation, proton-neutron and multi-nucleon interactions, whereas ^{205}Au and ^{203}Au are on, or near, the N=126 closed shell, hence they are dominated by proton-hole shell structure.

Isomers are 'metastable' or long-lived nuclear states. They may occur for a variety of reasons (see Section 2.1.4), all of them related to differences in nuclear shape or spin within the same nuclide. Their large range of lifetimes, ranging from nanoseconds to years, enables the study of unusual and extreme states of nuclei, and an understanding

of their occurrence and degree of stability affords further nuclear structure insights [5]. Heavy, neutron-rich nuclei, such as those investigated in this thesis, are of considerable interest since they offer favourable conditions for the formation of isomeric states. This is primarily due to the presence of high-j orbitals such as $\nu\, i_{13/2}, \nu\, g_{9/2}, \nu\, j_{15/2}$ and $\pi\, h_{11/2}$ which are close to both the proton and neutron Fermi surfaces. The residual interaction between specific high-j orbitals can be analysed by considering the energies of the isomeric states. Also, the neutron separation energy is predicted to fall to a few MeV for heavy nuclei with N>126, allowing the possibility of weakly bound isomeric states, thus showing features similar to those of the ground-state properties of nuclides near the neutron drip line. The great difficulty in reaching the neutron drip line for heavy nuclei experimentally means that the study of these isomeric states may be the best way to study drip line phenomena such as changes in the pairing interaction or the coupling between bound and continuum states [6].

1.1 Motivation for the investigation of ^{190}W

Experimental results have confirmed theoretical calculations that show that most deformed nuclei are prolate in shape, so those nuclides with oblate or triaxial shapes are of particular interest. $^{190}_{74}W_{116}$ is located in a particularly interesting region of the nuclear chart. Lying between closed shells (several proton and neutron holes outside a doubly magic nucleus), it shows characteristic shape deformation. The experimental E_{4^+}/E_{2^+} ratio departs from the tendency of the lighter isotones (N=108, 110, 112 and 114) to change smoothly from a rigid rotor (ratio $\sim$ 3.33) to a triaxial rotor (ratio $\sim$ 2.5) as atomic number increases [7, 8], indicating that ^{190}W is gamma-soft (see Section 2.1.3). Several different types of calculation have been carried out, some of which suggest that the phenomenon of shape coexistence may occur in this nuclide since just below the magic numbers the energetics of low-Ω orbitals leads to small regions where oblate states may dominate at low spins, in contrast to the usual prolate deformation for most of the nuclear chart [9]. This implies that prolate-oblate shape transitions, as well as K-isomerism (see Section 2.1.4) may be possible in this nuclide [10]. The isomeric state investigated here is

assumed to be a K-isomer, arising from the competition of quasiparticle states with the collective rotation of the core.

Robledo *et al.* have performed calculations using the Hartree-Fock-Bogoliubov (HFB) method, combined with suitable effective interactions (Gogny D1S, Gogny D1N and Skyrme SLy4) to carry out constrained calculations in the collective β and γ deformation variables (see Section 2.1.2) for neutron-rich Yb, Hf, W, Os and Pt isotopes [11]. Instead of the $\beta - \gamma$ potential energy surface (PES) plots, the $Q_0 - \gamma$ plane has been used, where $Q_0 = \sqrt{Q_{20}^2 + Q_{22}^2}$, cf. Equations (2.9) and (2.10), with $\gamma = 0°$ indicating prolate deformation and $\gamma = 60°$ indicating oblate deformation.

Plotting energy against the quadrupole deformation parameter Q_{20}, using a Gogny DIS force, for isotones of even-even nuclides from Yb to Pt shows two minima, one prolate and one oblate, separated by a barrier whose energy decreases with increasing Z and increasing N, cf. Fig. 1.2. Shape coexistence is indicated by the minima lying close in energy in several cases. The fact that their quadrupole deformations are approximately the same in size but opposite in sign suggests that these nuclides may be gamma soft. Prolate to oblate shape transition is indicated for N=116, ^{190}W having the closest energies for the minima across the N=116 isotones considered.

Q_0-γ potential energy contours, cf. Fig. 1.3, show clearly that, for fixed N, an increase in Z increases triaxiality; indeed the Pt isotopes (the ones with the highest Z) are almost all triaxial. For fixed Z, increasing N leads to a transition from prolate to oblate deformation. The prolate to oblate transition appears to occur at N=116. In terms of the deformation parameters, the ground state β value decreases and γ increases as N increases in this region (as N approaches 126). As Z increases towards 82, β again decreases but there is no specific trend in γ. For the tungsten isotopes, this transition from prolate to oblate shape is such that there is considerable triaxiality as one moves up the isotopic chain: ^{184}W and ^{186}W are prolate, ^{190}W, ^{192}W and ^{194}W are triaxial, and ^{196}W is oblate, according to these calculations. Furthermore, the triaxial minimum is very shallow, less than 0.5 MeV below the axially symmetric saddle points [11]. This could indicate a transition from the SU(3) dynamic symmetry of the interacting boson model (IBM), for deformed rotors, via

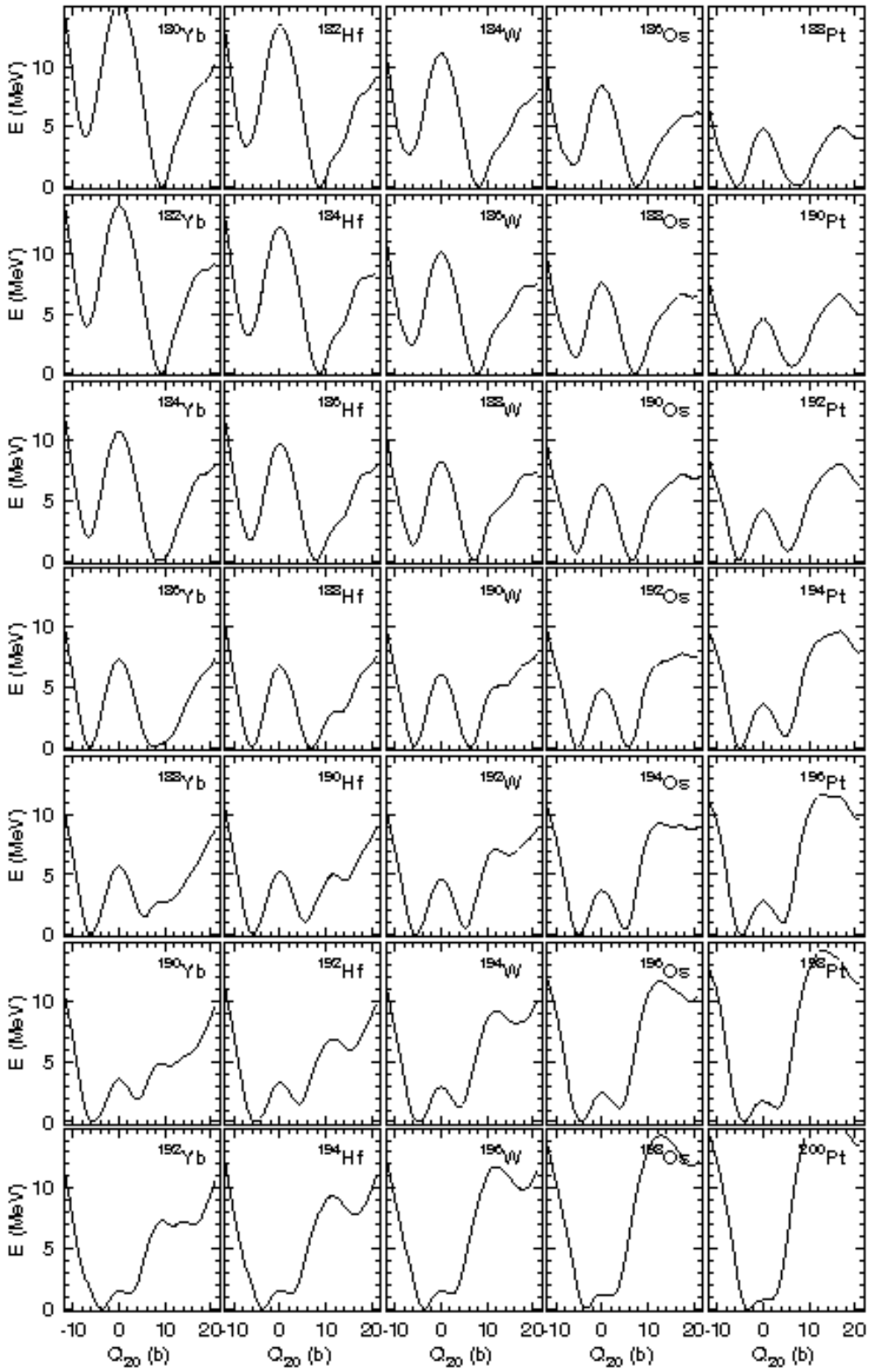

Figure 1.2: Potential energy curves for Yb, Hf, W, Os and Pt isotopes as a function of the axial quadrupole moment Q_{20} calculated with the Gogny D1S interaction for all the nuclei considered. Each row corresponds to a fixed neutron number ranging from N = 110 for the top row up to N = 122 for the bottom row [11].

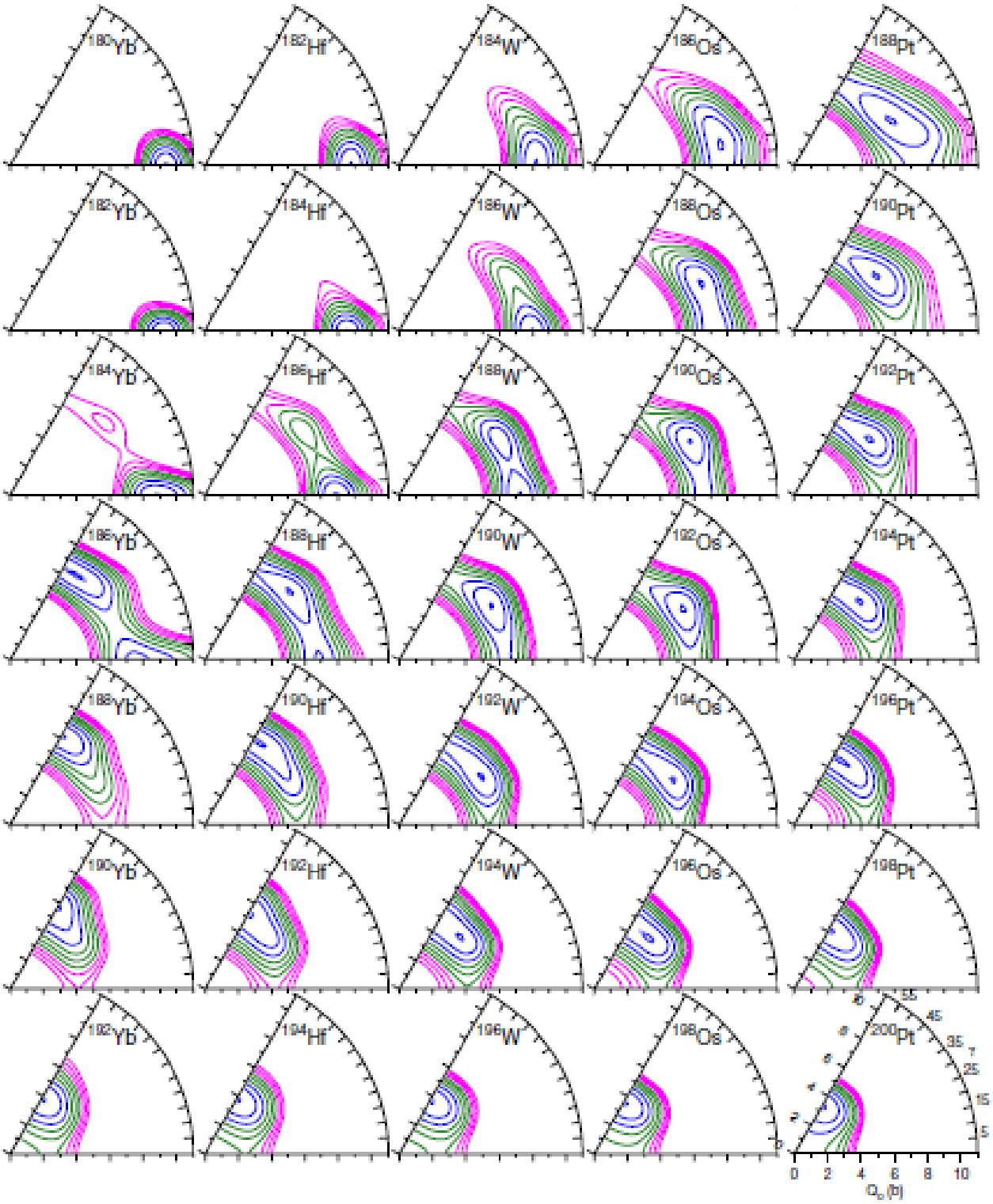

Figure 1.3: $Q_0-\gamma$ planes for Yb, Hf, W, Os and Pt isotopes computed with the Gogny D1S force for all the isotopes considered. The range of Q_0 considered has been reduced so as to focus on the interval around the minima. The contour lines go from the minimum energy up to 2 MeV higher in steps of 0.25 MeV. Blue contours are the three lowest energies, green ones the next three, and magenta contours correspond to the three with higher energies [11].

the O(6) dynamic symmetry, for γ-soft systems, back to the SU(3) symmetry [12].

The calculations of Robledo *et al.* [11] and Sarriguren *et al.* [8] indicate that ^{190}W is the nuclide which is of key importance for prolate-oblate shape transitions and triaxiality in this region of the nuclear chart.

1.2 Motivation for the investigation of ^{205}Au and ^{203}Au

Both ^{205}Au and ^{203}Au lie close to the doubly magic ^{208}Pb, with Z=82 and N=126 closed shells, thus there is effectively no shape deformation. The doubly magic ^{208}Pb nucleus provides the heaviest classic shell model core. Isomeric states here, then, will not derive from K-isomerism or shape isomerism but from transitions hindered due to the high multipolarity or low energy of the electromagnetic decays necessary to depopulate them, as described in Section 2.1.4. Experimental information on the neutron-rich N = 126 nuclei has been scarce to date, information on the excited states of proton-hole, N = 126, isotones being restricted to $^{207}_{81}$Tl, $^{206}_{80}$Hg and $^{204}_{78}$Pt (for more information and references see the published paper [13] in Appendix B). The scarcity of such information arises from the experimental challenges of producing these nuclides, but such information (concerning probable energies, spins and parities) can be used to help calculate more complex configurations.

Only a tentative spin-parity of the ground state of $^{205}_{79}$Au$_{126}$ is known, based on beta-decay and gamma-decay to the ground state of ^{205}Hg [14]. ^{205}Au has 79 protons and 126 neutrons, thus is singly-magic with three proton holes, two of which are paired in the $3s_{1/2}$ orbital, leaving a hole in the $2d_{3/2}$ orbital in the ground state, cf. Fig. 2.8. The isomeric state investigated arises, it is suggested, from a proton-hole excitation to the $1h_{11/2}$ state; this requires a hindered M4 transition for decay to the ground state. Such a transition would be highly converted, implying that it would be detectable in an experimental set-up sensitive to conversion electrons.

$^{203}_{79}$Au$_{124}$ has two neutron holes in addition to its three proton holes in the ^{208}Pb closed core, so one might expect the neutron holes to pair, yielding a very similar level structure to ^{205}Au at low-lying energies. However, unlike ^{205}Au, there may also be proton-neutron

interactions among the valence holes, thus changing the level structure and affecting the existence of particular isomeric states.

Chapter 2

Theory

2.1 Nuclear models

Of the four fundamental forces of nature, two are specifically related to nuclear physics: the strong and the weak forces. The strong force is responsible for the fact that nuclei exist at all since otherwise the repulsion of the positively charged protons, due to the electromagnetic force, would prohibit the coexistence in a small space of any atomic nuclei with more than one proton. Neutrons are composed of two down quarks and an up quark (udd); protons consist of two up quarks and a down quark (uud). These quarks are confined, i.e. bound together so strongly that they do not exist (under the conditions here considered) as individual particles. The nuclear strong force is itself a sort of vestige of the inter-quark force. It is repulsive for an inter-nucleon range $\lesssim 0.5\,\mathrm{fm}$, otherwise being attractive, though decreasing with distance rapidly, giving an effective range of about 1 fm.

Since there are many nucleons interacting in the nucleus, there is no complete theory of nuclear structure (the "many-body problem" in physics is such that the interaction of more than two bodies is not analytically solvable), despite our understanding of the strong nuclear force (cf. Lilley p.35 [15], [16]). Among the different models used to describe basic nuclear structure the two principal ones are the liquid-drop model and the shell model. The former is a macroscopic model, treating the nucleus semi-classically as a drop of liquid. In a liquid drop there is a surface tension and a short range repulsive force

preventing collapse of the drop. The nuclear density, ρ, is found to be roughly constant, i.e. independent of size, as in a liquid drop. Since $\rho = \frac{Am}{V}$, where m is the average nucleon mass, A the atomic mass and V the nuclear volume, and $V \propto R^3$, this implies $R \propto A^{1/3}$. The radius, R, of a nucleus can thus be modelled as:

$$R = R_0 A^{1/3} \tag{2.1}$$

with $R_0 = 1.25\,\text{fm}$ [17, p.54].

As shown in Fig. 2.1, the nuclear binding energy per nucleon is roughly constant at about 8 MeV for $A \geq 12$ due to the saturation of the short-range nuclear strong force. The binding energy per nucleon increases as atomic mass increases up to a maximum around the Fe-Ni region ($A \approx 56 - 60$), then decreases above this primarily because of Coulomb repulsion. This model is particularly useful in describing 'bulk' properties of the nucleus such as deformation, vibration and rotation.

2.1.1 The Shell Model

This is a microscopic model in which the nucleons behave somewhat like electrons in the atom, being described by quantum numbers confining them to shells. The evidence for shell structure comes from many sources (cf. Krane pp.117-121 [17]). A clear example is the way in which the nuclear binding energy per nucleon reaches a maximum at the so-called 'magic numbers'. These magic numbers represent the closure of quantum shells, implying that the next nucleon has to occupy the next highest, and thus less tightly bound, shell. Near these closed shells, nucleons can be described as 'valence' nucleons outside an 'inert' core. The protons and neutrons fill their shells independently and, since nucleons are fermions, the Pauli Exclusion Principle dictates that no two identical nucleons may occupy an identical state.

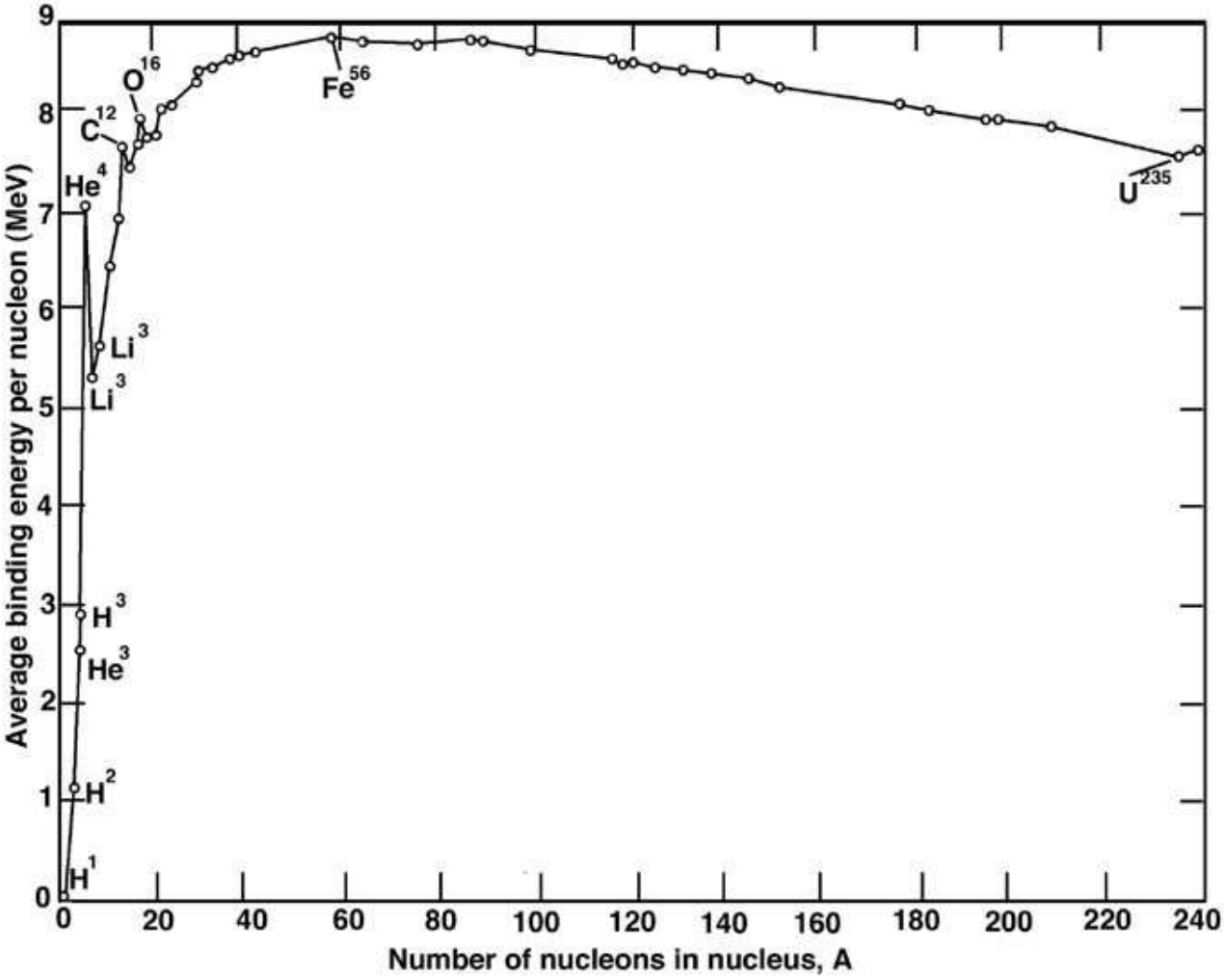

Figure 2.1: Nuclear binding energy per nucleon (taken from [18]).

The Independent Particle Model

The principle of the conservation of energy in quantum mechanics leads to the Schrödinger wave equation. The time-independent version is:

$$-\frac{\hbar^2}{2m}\nabla^2\psi + V\psi = E\psi \tag{2.2}$$

where ψ is the wavefunction that describes the particle (nucleon) under consideration, V is the potential (formed by the the strong interaction between the nucleons), m the nucleon mass and E the energy. In this model the nucleon moves inside a certain potential well (which keeps it bound to the nucleus) *independently of the other nucleons.* In reality, this nuclear potential is the result of the field due to the strong force from the other nucleons;

mean field models take the latter as their starting point. By analogy with atomic energy levels, one can characterise each level by quantum numbers, including orbital angular momentum, l, and intrinsic spin, s, the parity of each state being $(-1)^l$.

A generalised form of the left-hand side of Equation 2.2 is the Hamiltonian, $\hat{H}$, the total energy operator. Modelling the nuclear potential as that of a simple harmonic oscillator (S.H.O.) gives:

$$\hat{H} = -\frac{\hbar^2}{2m}\nabla^2 + \tfrac{1}{2}m\omega^2 r^2 \tag{2.3}$$

where ω corresponds to the classical angular frequency. The solution of the Schrödinger wave equation for this potential in three dimensions gives energy levels quantised as $E_N = (N + \frac{3}{2})\hbar\omega_0$ where ω_0 is the angular frequency at the minimum energy. However, in this model the nuclear potential tends to infinity as $r \to \infty$. Furthermore, it does not reproduce many of the so-called 'magic numbers' for the closed shells in nuclides. A more realistic potential is the Woods-Saxon potential:

$$V(r) = \frac{V_0}{1 + \exp\left(\frac{r-R}{a}\right)} \tag{2.4}$$

where r is the distance from the centre of the potential, R is the mean radius (at which $V = \frac{V_0}{2}$, i.e. the half-maximum), a is the 'surface/skin thickness', a measure of how rapidly the potential decreases to zero from the flat, core region, such that the 1st to 9th deciles of the potential occur over a distance $4a \ln 3$, around 0.5 fm, and V_0 is the depth of the potential well, around 50 MeV [17]; this is shown in Fig. 2.2. For large atomic mass, A, this has the following desired properties:

- It is attractive and increases monotonically with distance.
- For large A, it is approximately flat in the centre.
- Nucleons near the surface of the nucleus (i.e. having $r \approx R$ within a distance of order a) experience a large force towards the centre.
- It rapidly approaches zero as r becomes very large ($r - R >> a$), reflecting the short-distance nature of the strong nuclear force.

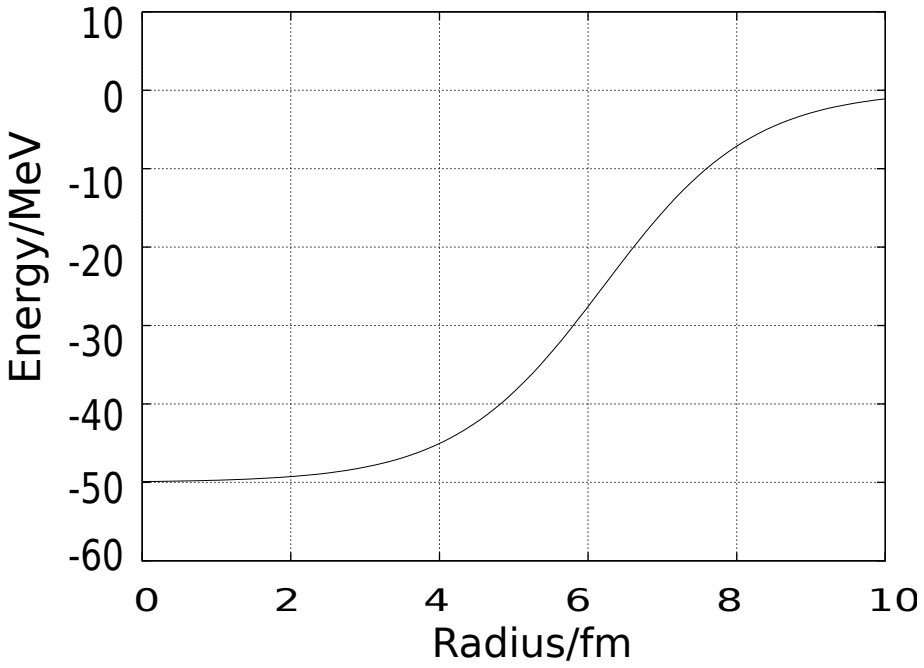

Figure 2.2: Woods-Saxon potential for A $\sim$ 200.

This potential is similar to adding a $\boldsymbol{l} \cdot \boldsymbol{l}$ term to the S.H.O. potential, causing the potential to be deeper for orbits with higher values of l. The result is to break the degeneracy of the S.H.O. energy levels, the orbits with larger l being lower in energy.

A negative spin-orbit term, V_{SO}, added to this potential produces the required magic numbers and spins of the ground states of spherically symmetric nuclei [19, 20]. This term is of the form $V_{SO}(r)\ \boldsymbol{l} \cdot \boldsymbol{s}$ where $\boldsymbol{l}$ and $\boldsymbol{s}$ are the orbital and intrinsic spin angular momenta respectively. This negative term ensures that single particle states with higher $\boldsymbol{j}$, where $\boldsymbol{j} = \boldsymbol{l} + \boldsymbol{s}$, are lower in energy; $\boldsymbol{j}$ then, rather than $\boldsymbol{l}$ or $\boldsymbol{s}$, is a good quantum number. This spin-orbit term splits energy levels with the same l, the amount of splitting increasing with increasing l. Some orbitals are pushed down from the S.H.O. level with quantum number N to the $N-1$ level. These are the so-called 'intruder orbits', of opposite parity to the states they join. This is shown in Fig. 2.3 [21].

The Pairing interaction

Two identical nucleons in equivalent orbits, i.e. with the same quantum numbers: $n_1, l_1, j_1 = n_2, l_2, j_2$, can couple their total angular momenta from a maximum of j_1+j_2-1 (the Pauli Exclusion Principle forbids $j_1 + j_2$) to a minimum of zero ($|\mathbf{J}| = j_1 - j_2 = 0$),

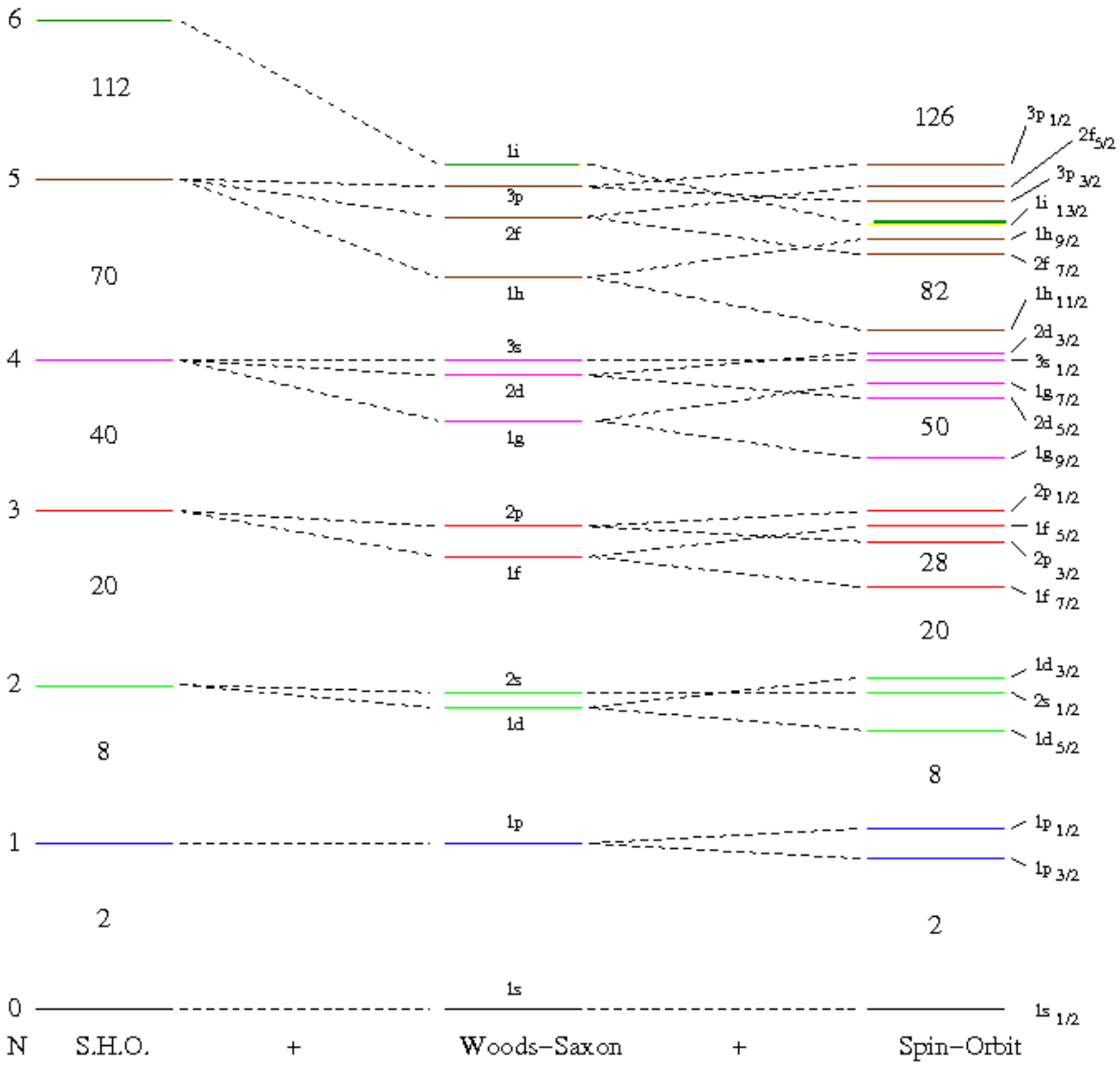

Figure 2.3: Single particle levels (not to scale), adapted from [21].
Left: S.H.O. potential.
Centre: Addition of the Woods-Saxon potential, splitting the degenerate levels.
Right: Addition of the spin-orbit interaction, reproducing the magic numbers.

Figure 2.4: $j = (7/2)^2$ coupled configuration using no residual interaction (left), and with the pairing interaction (right).

in which the spins are anti-parallel. A wealth of experimental observations indicates that the ground state in even-even nuclei is 0^+ [17, p. 71]. This state is lower in energy than the other angular momentum couplings, cf. Fig. 2.4, due to the pairing interaction. This attractive interaction of $\backsim$ 1-2 MeV (cf. Casten p.164 [22]) affects only identical nucleons whose angular momenta are coupled to 0^+ and gives rise to the 'pairing gap' between this 0^+ state and other non-collective intrinsic states. This pairing interaction has non-diagonal matrix elements (allowing mixing of 0^+ states), enabling the *scattering* of pairs of particles from one orbit to another, causing a partial occupancy of orbits near the Fermi level, i.e. the energy defined by the kinetic energy of the highest occupied state for identical particles in their lowest energy configuration [15].

The pairing interaction changes the model of particle-hole excitation from the last filled orbit (the Fermi surface with energy λ) to that of a *quasi-particle*. The probability amplitudes for the k^{th} orbital being occupied and unoccupied by a pair of particles are ν_k and u_k respectively, giving:

$$|\nu_k|^2 + |u_k|^2 = 1 \tag{2.5}$$

The energy of the quasiparticle state, E_i, is:

$$E_i = \sqrt{(\varepsilon_i - \lambda)^2 + \Delta^2)} \tag{2.6}$$

where ε_i is the single particle energy and Δ is the pairing gap parameter:

$$\Delta = G \sum_{i,j} u_i \nu_j \tag{2.7}$$

where G is the strength of the pairing interaction [22].

2.1.2 Deformation

Closed shell nuclei are spherical, but quadrupole moments for nuclei beyond closed shells indicate that the latter have non-spherical shapes. Rainwater [23, 24] suggested that valence nucleons (or holes) can polarise the core into a spheroidal shape, thus the collective motion of nucleons affects individual particle orbits because it changes the effective potential by which the latter are defined [25]. Away from closed shells the independent particle model becomes very difficult to calculate since there are many valence nucleons, increasing the number of possible configurations and residual interactions. Significant proton-neutron (p-n) interactions enable configuration mixing and deformed shapes. A successful approach is to use perturbations to the independent particle model involving a deformed (i.e. non-spherical) potential.

For realistic ellipsoidal (axially symmetric) deformations, the radius of such a nucleus may be described by:

$$R = R_0 \left[1 + \sum_{\mu} \alpha_{2\mu} Y_{2\mu}(\theta, \phi) \right] \tag{2.8}$$

where R_0 is the radius of a spherical nucleus with the same volume, the $\alpha_{2\mu}$ are (quadrupole) expansion coefficients and $Y_{2\mu}$ are the quadrupole spherical harmonics (cf. Casten p.167 [22]).

Corresponding quadrupole operators are:

$$Q_{20} = z^2 - \frac{1}{2}(x^2 + y^2) \qquad \text{and} \qquad Q_{22} = \frac{\sqrt{3}}{2}(x^2 - y^2) \tag{2.9}$$

The five parameters $\alpha_{2\mu}$ that characterise the nuclear shape reduce to two real, independent variables α_{20} and α_{22}=α_{2-2}, which, together with the three Euler angles, give a complete description of the system. Instead of α_{20} and α_{22}, it is convenient to use the

so-called Hill-Wheeler coordinates β and γ, defined as [26]:

$$\alpha_{20} = \beta \cos\gamma \qquad \text{and} \qquad \alpha_{22} = \frac{1}{\sqrt{2}} \cdot \beta \sin\gamma$$

These are related to the quadrupole operators as:

$$\beta = \frac{\sqrt{4\pi}}{5} \frac{Q_{20}}{A\langle r^2 \rangle} \qquad \text{and} \tan\gamma = \frac{Q_{22}}{Q_{20}} \tag{2.10}$$

where β represents the quadrupole deformation (often written as β_2 to distinguish it from higher multipole deformations, particularly the hexadecapole deformation parameter β_4), and γ is a parameter for a degree of freedom perpendicular to the axis of symmetry, cf. Figs. 2.5 and 2.6. Using a commonly accepted convention, $\gamma = 0°$ indicates an axially symmetric prolate shape, $\gamma = 60°$ an axially symmetric oblate shape, and $\gamma = 30°$ is "triaxial", i.e. has the maximum axial asymmetry. Where the γ degree of freedom is not under consideration, a common convention is to take $\beta > 0$ for prolate nuclei and $\beta < 0$ for oblate nuclei.

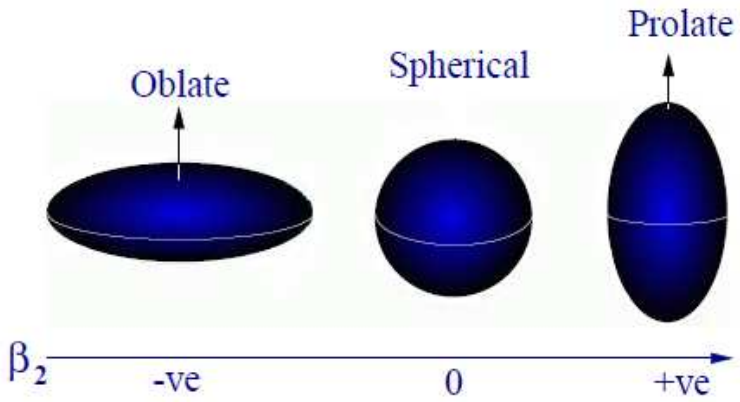

Figure 2.5: β_2 deformation. The arrows indicate the symmetry axis (from T. Vincent, private communication to C.Wheldon [27]).

Potential-energy-surface (P.E.S.) calculations

To calculate the shapes and energies of specific multi-quasiparticle configurations, Xu *et al.* [29] have developed configuration-constrained Potential-Energy-Surface (PES) calcu-

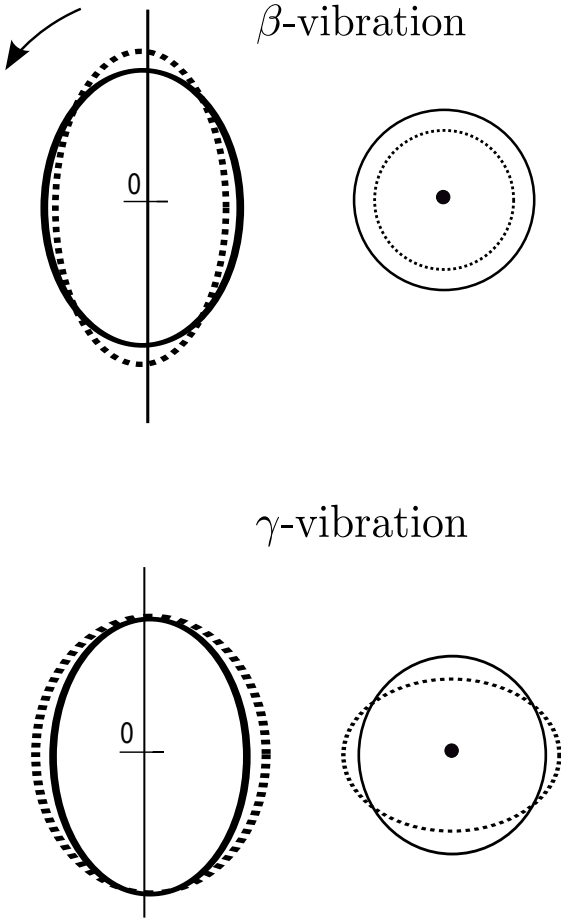

Figure 2.6: β and γ vibrations/rotations. The symmetry axis is shown vertically on the left. The diagrams on the right are equatorial sections with the symmetry axis shown as the central dot. The arrows show simple rotation of the deformed nucleus (from Burcham [28]).

lations that include the γ degree of freedom. The total energy for a given nucleus and configuration is calculated for a range of β_2 and γ using:

$$E_{total}(\beta_2, \gamma, \beta_4) = E_{macroscopic} + E_{shell-correction} + E_{pairing} \tag{2.11}$$

such that at every point on the $\beta_2 - \gamma$ plane the total energy is minimised with respect to β_4. $E_{macroscopic}$ is calculated using the Liquid Drop Model, $E_{shell-correction}$ is found using the Strutinsky shell-correction [30], and the pairing energy, $E_{pairing}$, which is configuration dependent, is obtained using the Lipkin-Nogami treatment [31]. The calculated pairing strengths for protons and neutrons, G^0_π and G^0_ν respectively, are renormalised to reproduce experimental odd-even mass differences in the region of interest [32]; for ^{190}W, the

renormalised values calculated by F.Xu were G_π=1.05 G^0_π and G_ν=1.14 G^0_ν [33].

K quantum number

The K quantum number is defined as: $K = \sum_i \Omega_i$, where Ω is the projection of $\boldsymbol{j}$ on the axis of symmetry, cf. Fig. 2.7. Since $\boldsymbol{j} = \boldsymbol{l} + \boldsymbol{s}$, the projections are such that: $\Omega = \Lambda + \Sigma = \Lambda \pm \frac{1}{2}$. K is a useful quantum number since it is conserved for deformed nuclei of a given deformation.

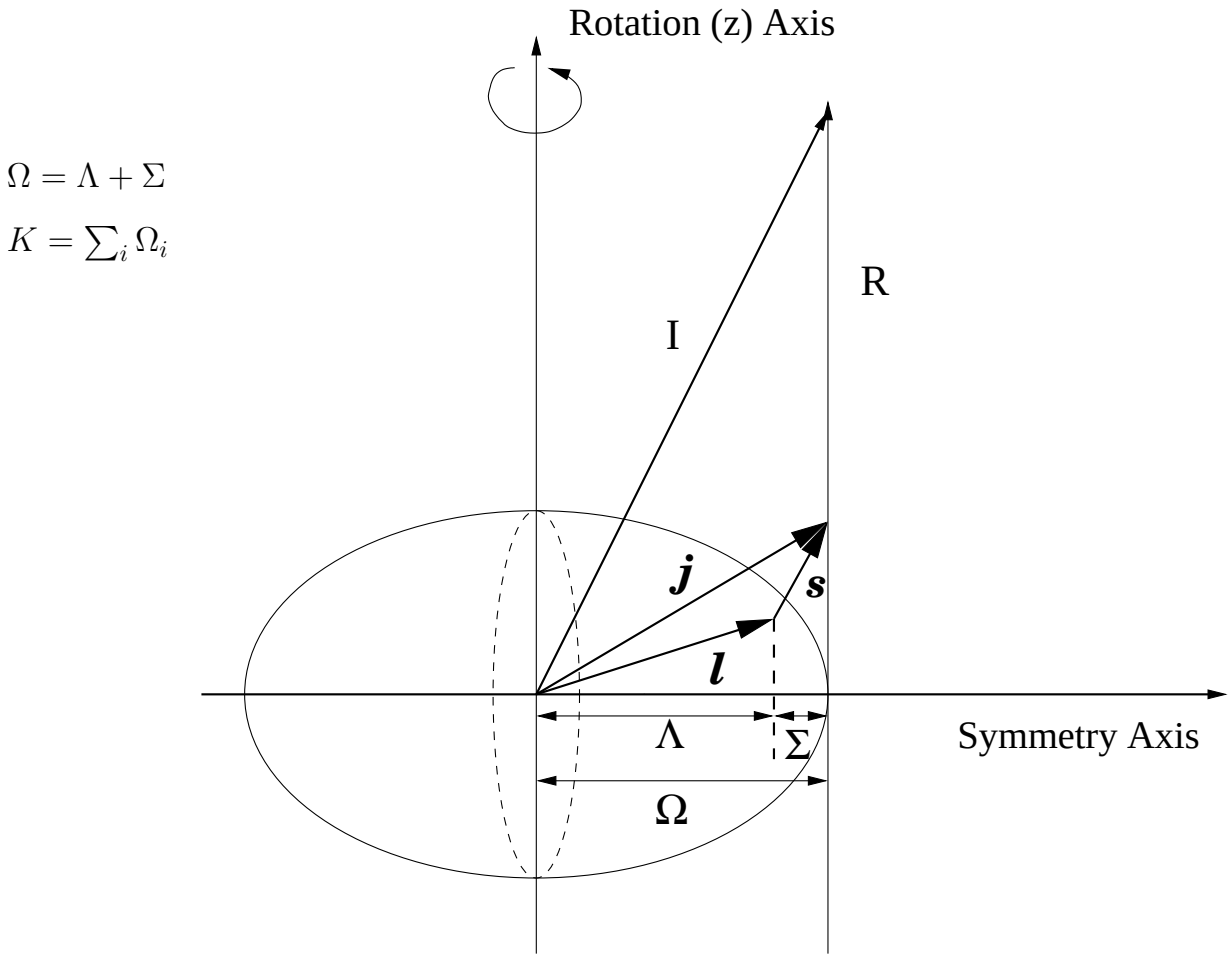

Figure 2.7: Asymptotic quantum numbers for a deformed nucleus [34].

For prolate deformation, low K values correspond to motion which overlaps most with the nuclear surface, thus low K values are lower in energy than high K values, and vice-versa for oblate deformation.

The Nilsson Model

In this model the potential is based on an axially symmetric, deformed oscillator [35]. The z-axis is arbitrarily chosen as the axis of symmetry/deformation, the other axes being equal in length so that $\omega_x = \omega_y \neq \omega_z$, z being longer than x or y for prolate deformation and shorter for oblate deformation. A 'centrifugal' term, $\boldsymbol{l} \cdot \boldsymbol{l}$, is added to the spin-orbit correction to this deformed oscillator potential, giving the following expression for the Hamiltonian:

$$\hat{H} = -\frac{\hbar^2}{2m}\nabla^2 + \frac{m}{2}\left[\omega_x^2(x^2+y^2) + \omega_z^2 z^2\right] + C\ \boldsymbol{l.s} + D\ \boldsymbol{l.l} \tag{2.12}$$

where C and D are experimentally determined constants. For large deformations the last two terms are negligible (cf. Casten p.343 [22]).

Labelling of the orbits uses the following notation:

$$\Omega^{\pi} = [N n_z \Lambda] \tag{2.13}$$

The three quantum numbers inside the square brackets are, in order, the principal quantum number, the number of nodes the wavefunction has along the symmetry axis, and the component of angular momentum along the symmetry axis. Larger n_z values correspond to wavefunctions that are more extended in the z direction, implying lower energy orbitals. Strictly speaking, only Ω (and thus K) and π, given by $(-1)^N$, are good quantum numbers, but with larger deformation N, n_z and Λ become good 'asymptotically'.

Nilsson diagrams relevant for the data analysed here are given in Figs. 2.8 and 2.9. Each Nilsson level can contain two identical nucleons since there is a twofold degeneracy in K, corresponding to the fact that orbitals with a given angle above the symmetry axis have the same value of K as those with the same angle below the axis (cf. Fig. 2.7). In these Nilsson diagrams an alternative quadrupole deformation parameter, ε_2, is used, where $\epsilon_2 \simeq 0.95\,\beta_2$ (cf. Firestone: Appendix [36]), and ε_4, a hexadecapole deformation parameter, is fixed as a fraction of ε_2 [37].

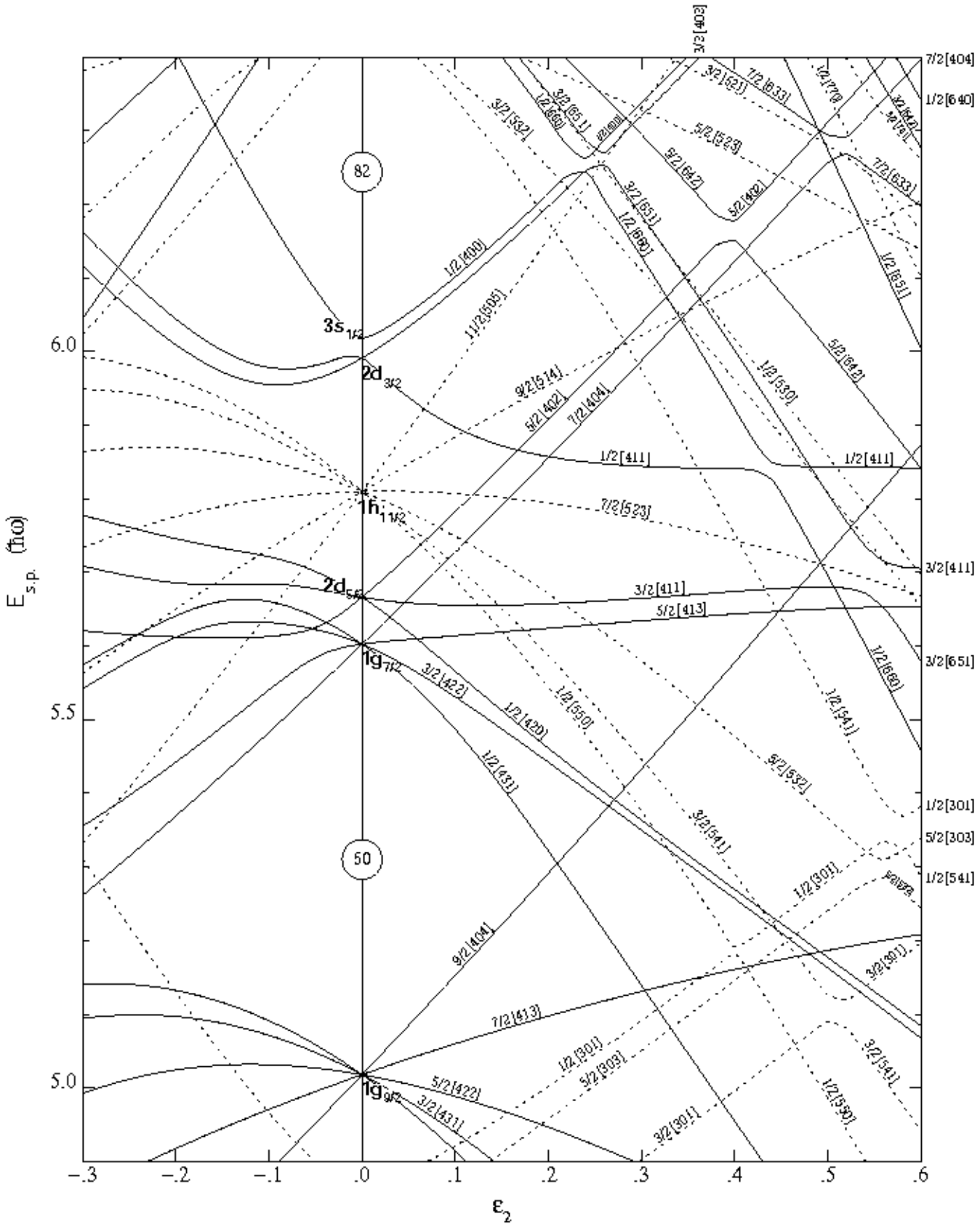

Figure 2.8: Nilsson diagram for protons, $50 \leq Z \leq 82$, taken from ref. [36]. $\epsilon_4 = \epsilon_2^2/6$. The energies are measured in units of the harmonic oscillator frequency, $\hbar\omega_0 = 41A^{-1/3}$ MeV.

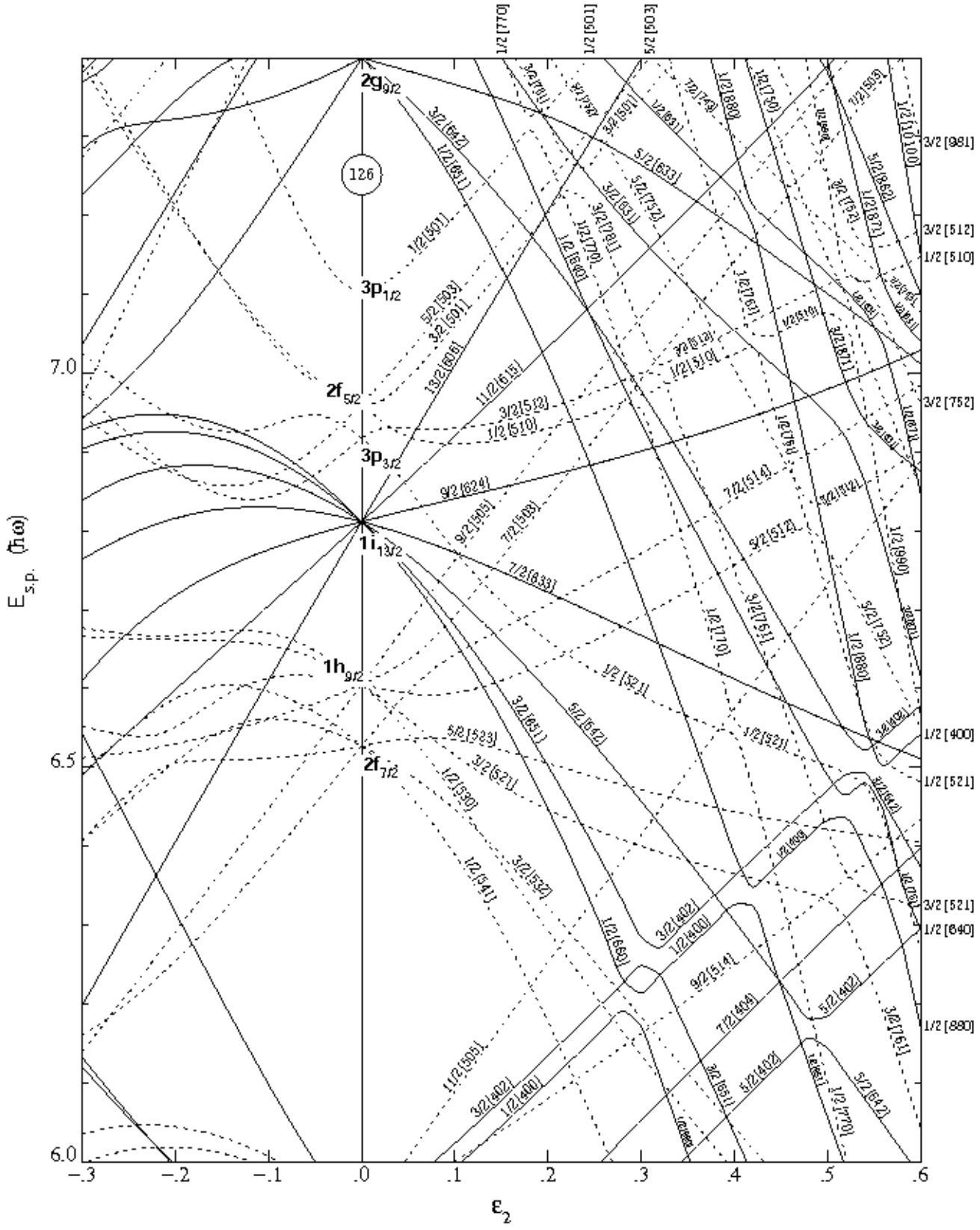

Figure 2.9: Nilsson diagram for neutrons, $82 \leq N \leq 126$, taken from ref. [36]. $\epsilon_4 = -\epsilon_2^2/6$. The energies are measured in units of the harmonic oscillator frequency, $\hbar\omega_0 = 41A^{-1/3}$ MeV.

2.1.3 Collective excitations

Vibrational modes of excitation are described in terms of phonons. The lowest energy excitation of a spherically symmetric shape is a quadrupole vibration, in which the phonon has 2 units of angular momentum (i.e. $2\hbar$). This implies that the first vibrational excited state has spin-parity 2^+. Two quadrupole phonons can couple their momenta to produce nearly degenerate states at twice the energy of the first (vibrational) 2^+ state to produce states at 0^+, 2^+ and 4^+. This means that the E_{4+}/E_{2^+} ratio is exactly 2 for a spherically symmetric vibrator.

For a deformed axially symmetric shape, rotation of the nucleus can occur (possibly in addition to vibrational modes of excitation). This can be modelled semi-classically, thus the rotational energy for a nucleus with moment of inertia $\mathcal{I}$, for a given total angular momentum, **J** is:

$$E(J) = \frac{\hbar^2}{2\mathcal{I}} J(J+1) \tag{2.14}$$

In quantum mechanical terms it is convenient to separate the wave function describing such nuclear states into an intrinsic wave function, describing the core nucleus which rotates, and a rotational wave function describing its laboratory motion.

The creation of such nuclides with different energies and spins leads to different intrinsic states and shapes, thus several different rotational bands can occur, built upon the different intrinsic states [38]. The K quantum number, described above in Section 2.1.2 is a good quantum number here. For $K^\pi = 0^+$, the rotational symmetry of the wavefunction permits even values of J only, whereas for $K^\pi = 0^-$ only odd values are allowed, thus for even-even nuclei such as ^{190}W, only even J are allowed. Equation (2.14) indicates that E_{4+}/E_{2^+} for the rotational band is 10/3 for a perfectly rigid rotor. For $K > 0$, the only restriction is that $J \geq K$, thus we have $J = K, K+1, K+2, K+3$, etc.

Gamma softness

A nucleus is regarded as being gamma-soft when a range of possible shapes with respect to the γ degree of freedom is allowed within a relatively small excitation energy. In this case, the nucleus is sensitive to the shape-polarising effects of specific multi-quasiparticle

configurations and the nuclear shape may easily change between prolate and oblate [26]. The excitation energy of the first 2^+ state can be used to indicate the quadrupole deformation. The ratio of the first 4^+ to the first 2^+ gamma energies, $E_{4_1^+}/E_{2_1^+}$, distinguishes between axially symmetric deformed rotor nuclei (a ratio of 3.33), a spherical, vibrational nucleus (ratio 2.0) and a triaxial rotor (ratio ~ 2.5).

2.1.4 Isomers

As mentioned in Section 2.2.1, isomers are metastable states. The different origins of their long half-lives give rise to their classification as shape isomers (such as fission isomers), K-isomers, spin-trap isomers, etc. Since it is the underlying shape and/or couplings of orbital spin that give rise to isomeric states, the study of such states yields important information about nuclear structure, especially regarding the limits of nuclear stability for exotic nuclides and stellar nucleosynthesis [39]. For example, analysis of the decay of a $K^\pi = 35/2^-$ isomer in ^{179}W revealed the influence of 'tilted'- or t-bands for the first time and levels above the $K^\pi = 25^+$ K-isomer in ^{182}Os have been identified and interpreted as the first evidence for multi-phonon excitations in a well deformed nucleus [40].

Indeed, their long half-lives, typically of the order of microseconds (compared to typical gamma decay half-lives of picoseconds), are long enough to enable the identification of heavy exotic nuclei within the complex 'cocktail' of nuclides produced in projectile fragmentation (see Section 3.1.2) by correlating the isomerically delayed gamma decays with the implanted ions long after the prompt gamma radiation has disappeared.

Most isomers have a single-particle structure involving a number of specific unpaired nucleon orbitals coupled to produce states of higher spin than other couplings at a similar energy. The decay of these isomers involves the removal of a large amount of angular momentum. Other isomers occur because the decay transition is of low energy, thus reducing the transition probability, cf. Equation (2.28). The observed radiation from isomers often violate selection rules, indicating that states with particular spin-parity have a strong dependence on low-amplitude wavefunction admixtures [39].

K isomers

For deformed, axially symmetric nuclei, K may be regarded as a good quantum number (see Section 2.1.2) and we may define the *degree of K-forbiddenness* as:

$$\nu = \Delta K - \lambda \tag{2.15}$$

where λ is the multipolarity of the gamma transition.

For an axially symmetric, deformed nucleus, the collective rotation of the nuclear core occurs about an axis perpendicular to the symmetry axis, resulting in a value of $K = 0$ for the ground state band. K-isomers occur in such nuclei when there is a secondary minimum in the potential energy surface for a certain value of K (cf. Fig. 2.10). K-isomers are expected in regions where high-Ω orbitals of deformed nuclei are near the Fermi surface. In fact, most K-isomers have been found to exist in the mass A$\sim$130 and A$\sim$180 regions of the nuclear chart. Such *K-traps* involve transitions with large changes in the *orientation* of the angular momentum.

At the secondary minimum, the nucleus is hindered from changing its spin orientation relative to the axis of symmetry. The degree of K-forbiddenness (cf. Equation (2.15)) indicates this hindrance. In general, the reduced transition probabilities (cf. 2.2.2) decrease approximately by a factor of 100 per degree of K-forbiddenness [41]. The fact that K-forbidden transitions occur at all is an indication of the mixing of different K states, usually explained in terms of Coriolis mixing (in which the quasiparticle rotations align with the core rotation as the latter increases) or γ-tunnelling [42]. In γ-soft nuclei, γ-vibrations couple states with K quantum numbers differing by two units ($\Delta K = \pm 2$ mixing), whereas Coriolis coupling changes the *orientation* of angular momentum and leads to $\Delta K = \pm 1$ mixing in rotating nuclei [42]. Such effects together with other causes of K-mixing determine K-isomer decay rates.

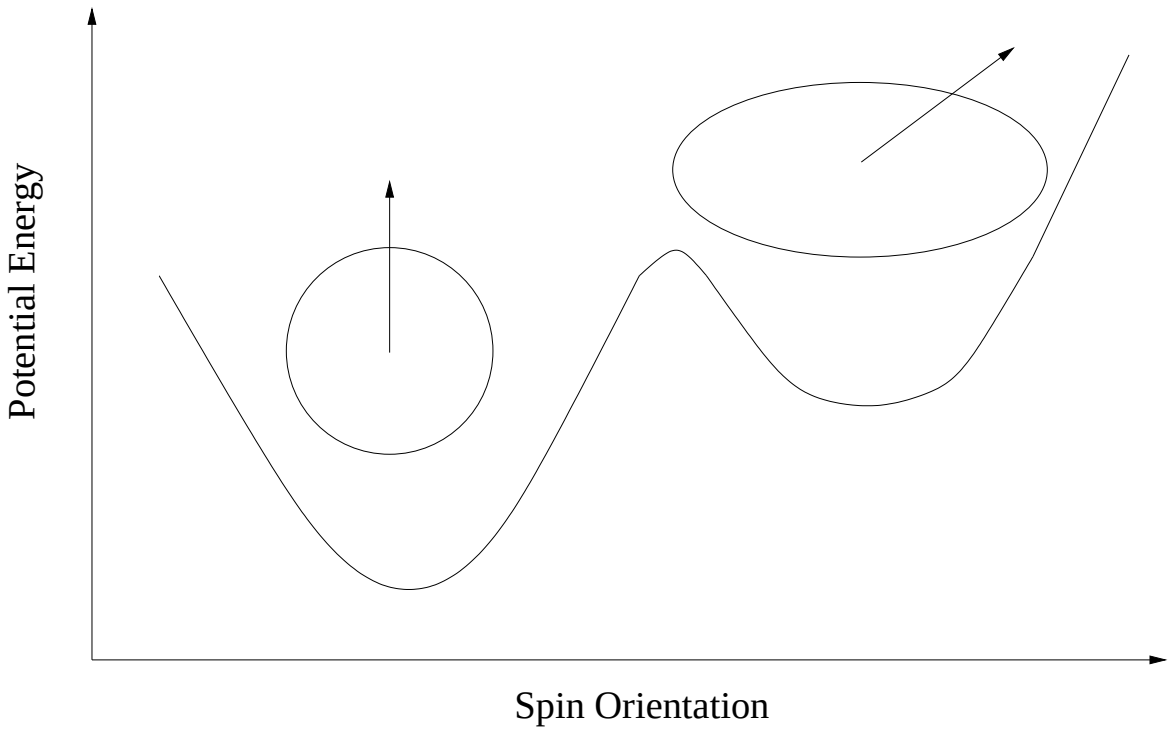

Figure 2.10: K-isomers can occur when the potential energy has a secondary minimum for a certain value of K [43].

BCS theory

Bardeen, Cooper and Schrieffer developed the theory of superconductivity (BCS theory) based on electron pair correlations (Cooper pairs) with equal and opposite angular momenta (time-reversed orbits). This theory can also be applied to the pairing force between like nucleons. Coriolis forces tend to decouple pairing correlations in a rotating nucleus, analogous to the application of a magnetic field to a superconducting metal [34].

As noted above, in Section 2.1.1, pairs of nucleons near the Fermi surface can scatter between single-particle states, thus, in the ground state, orbitals close to the Fermi surface have occupation probabilities of less than 1: $\nu_k < 1$. However, when a single particle is *excited* to such an orbital, nucleon pairs can no longer *scatter* into the orbital (due to the Pauli exclusion principle), so the occupation probability for a nucleon pair in this state becomes zero. This effect is called *blocking*. In this case, the pairing gap parameter, Δ (cf. Equation (2.6)), is given by:

$$\Delta = G \sum_{i \neq j} u_i \nu_j \tag{2.16}$$

The excitation energy of a given multi-quasiparticle configuration is the sum of the proton and neutron quasiparticle energies involved in the configuration [26]. Different values of G should be used for protons (G_π) and neutrons (G_ν) in the A $\sim$ 190 region since protons and neutrons occupy different Nilsson orbitals. From the definition of ν_k in Equation (2.5), the number of particles involved in the calculation, n, is:

$$n = 2\sum_k \nu_k^2 \tag{2.17}$$

and the probability of a state being occupied,

$$\nu_k^2 = \frac{1}{2}\left[1 - \frac{\varepsilon_k - \lambda}{E_k}\right] \tag{2.18}$$

These two equations, then, define the Fermi surface with energy λ. A code developed by Jain *et al.* [44] for blocked BCS calculations was used in the analysis of the data for ^{190}W (see Section 5.1.4). Use of this code requires the deformation parameters ε_2 and ε_4, and the (monopole) pairing strength for neutrons (G_ν) and protons (G_π). This code does not include the residual nucleon-nucleon interaction arising from the coupling of the intrinsic spins of the particles, an interaction that favours the alignment of intrinsic spins for non-identical nucleons and the anti-alignment of like nucleons with $\sim 100\,\text{keV}$ in extra binding energy [45].

2.2 Radioactive decay

Nuclear systems, like other systems in nature, tend to transform to their lowest energy state(s) so that they can exist in stable, or nearly stable, equilibrium. These transformations primarily involve radioactive decay or fission. There are a number of factors that influence the rate of decay but for a simple single decay channel the decay probability is constant, although the precise time of an individual decay cannot be determined. The decay rate or activity, $-\frac{dN}{dt}$, is proportional to the number of radioactive nuclei present

at time t. The decay constant, λ, is defined such that:

$$-\frac{dN}{dt} = \lambda N \tag{2.19}$$

The decay probability, given by λ, and the half-life, $T_{1/2}$, are inversely proportional:

$$T_{\frac{1}{2}} = \frac{\ln 2}{\lambda} \tag{2.20}$$

Similarly, the mean life, or (mean) lifetime $\tau = \frac{1}{\lambda}$, is widely used.

2.2.1 Types of radioactive decay

(a) α **decay and fission**

These are decay processes involving the nuclear strong force, decreasing the overall energy of the system because the sum of the binding energies of the new nuclides formed is greater than the binding energy of the original nuclide (cf. Fig. 2.1). The energy difference is accounted for by the kinetic energy of the α-particles, neutrons and nuclides produced. In α decay the resulting nuclide, Y in Equation (2.21), is often in an excited state, resulting in subsequent de-excitation, usually by γ decay.

$$^{A}_{Z}X \rightarrow {}^{A-4}_{Z-2}Y + {}^{4}_{2}\mathrm{He} \tag{2.21}$$

Unstable, transuranic isotopes move to a state of lower energy primarily by alpha decay, whereas lighter isotopes that lie high up on the sides of the 'valley of stability' move to a state of lower energy most directly by moving 'downhill' via beta decay (β^+ if the isotope is on the proton-rich side of the line of greatest stability, β^- if it is on the neutron-rich side). *"If, however, the isotope is only a little way up from the bottom of the valley, alpha decay may be about as likely as beta decay. In those cases, then, both decays will be observed, in some proportions"* [46].

(b) β **decay**

This involves the nuclear weak force and may be regarded naively as a change of a neutron into a proton or vice-versa. There are three possible processes:

- β^- decay

$$n \rightarrow p + e^- + \bar{\nu} \tag{2.22}$$

- β^+ decay

$$p \rightarrow n + e^+ + \nu \tag{2.23}$$

- Electron capture (EC)

$$p + e^- \rightarrow n + \nu \tag{2.24}$$

These processes enable decay towards the valley of stability: β^- decay for nuclides on the neutron-rich side of the valley, β^+ decay and electron capture for decay from the proton-rich side. The two types of β decay involve the production of the very penetrating, very light mass particle, the neutrino, ν, or its antiparticle, $\bar{\nu}$. It is the sharing of the reaction energy between the electron and the (anti-)neutrino that accounts for the continuous electron energy spectrum in β^- decay (one ignores the relatively small recoil energy of the daughter nuclide), compared to the sharp monoenergetic neutron energy in electron capture, and the monoenergetic electron energies resulting from internal conversion (see below).

(c) γ **decay and internal conversion**

- γ **decay**

This does <u>not</u> involve the nuclear force, primarily, but the far weaker electromagnetic force. There is no change in the nucleus as regards the number of protons and the number of neutrons, but the emission of a γ-ray photon removes energy, enabling the nucleus to undergo a transition to a lower energy, thus (usually) a more stable state. The minimum energy configuration is called the "ground state".

From the principle of conservation of momentum, the emission of a photon entails the recoil of the nucleus, but since the nucleus is much more massive than the photon (with zero rest mass), the recoil energy can generally be ignored in calculating the energy of the emitted γ-photon, E_γ. Thus $E_\gamma = \Delta E = E_i - E_f$, where the subscripts refer to the initial and final nuclear energy levels respectively. The probability of a given gamma transition depends strongly on the energy difference between the states involved, on whether the transition is electric or magnetic in nature, and on the multipolarity. The angular momentum difference between two nuclear states is carried away by the γ photon such that the angular momentum of a gamma transition, $\mathbf{L}$, is given by: $\mathbf{L} = \mathbf{I_i} - \mathbf{I_f}$, leading to the selection rule:

$$|\mathbf{I_i} - \mathbf{I_f}| \leq |\mathbf{L}| \leq |\mathbf{I_i} + \mathbf{I_f}| \tag{2.25}$$

- **Internal conversion**

  Internal conversion competes with γ decay and it is useful to define the internal conversion coefficient in terms of the electron and gamma decay probabilities, λ_e and λ_γ respectively, as: $\alpha = \dfrac{\lambda_e}{\lambda_\gamma}$. More specifically, $\alpha_K = \dfrac{\lambda_{e,K}}{\lambda_\gamma}$ and $\alpha = \alpha_K + \alpha_L + ...$ (where the contribution from all other shells rapidly decreases in magnitude). The conversion coefficient depends on the type, energy and multipolarity of the transition and on the atomic number of the nuclide. Krane [17, pp. 345-6] gives non-relativistic approximations for α which indicate that it:

  - increases as Z^3
  - decreases rapidly with transition energy as $E^{-(L+5/2)}$ for electric transitions and as $E^{-(L+3/2)}$ for magnetic transitions
  - increases rapidly with multipole order
  - is higher (for the same energy, atomic number and atomic shell) for magnetic transitions than electric transitions of the same order, e.g. α_K is

higher for M1 than E1.

– decreases with increasing atomic shell number

2.2.2 Electromagnetic transition probabilities

Partial half-life

A given nuclear level may de-excite by several possible decay branches. The partial half-life for photon emission of the k^{th} branch of n decay branches, $T_{1/2}(k)^{\gamma}$ is given by:

$$T_{1/2}(k)^{\gamma} = t_{1/2} \sum_{i=1}^{n} (I_i) \frac{1+\alpha_i}{I_k} \tag{2.26}$$

where $t_{1/2}$ is the half-life of the level, I_i the intensity of the i^{th} branch, and α_i the corresponding internal conversion coefficient.

Reduced transition probabilities

The probability per unit time of an electromagnetic transition, T_{if} from an initial energy level E_i, spin $\mathbf{I_i}$ and parity π_i to a final state with corresponding parameters E_f, $\mathbf{I_f}$ and π_f is approximately (cf. Burcham p.260 [28]):

$$T_{if} = \frac{2\pi}{\hbar} |\langle \Psi_f | M_{em}(\lambda) | \Psi_i \rangle|^2 \rho(E) \tag{2.27}$$

where $\langle \Psi_f | M_{em}(\lambda) | \Psi_i \rangle$ is the matrix element for the electric or magnetic interaction between initial and final states, and $\rho(E)$ is the density of momentum states, i.e. the number of such states per unit energy[1]. For multipolarity L, this gives [28, pp.262-264]:

$$T_{if} = \frac{1}{\tau} = \left(\frac{\mu_0 c^2}{4\pi} \right) \frac{8\pi(L+1)}{L[(2L+1)!!]^2} \frac{1}{\hbar} \left(\frac{E_\gamma}{\hbar c} \right)^{2L+1} B(L) \tag{2.28}$$

where $B(L)$ is the *reduced transition probability*, the factor containing information that is essentially nuclear. For comparison purposes, the Weisskopf formula uses the single-

[1] T is used here rather than λ, cf. Equation (2.19), to avoid confusion with the electromagnetic multipolarity.

particle (s.p.) shell model for a proton from an initial state to a final state of zero angular momentum. Estimates for the electric and magnetic single particle reduced transition probabilities are given respectively by:

$$B_{sp}(EL) = \frac{e^2}{4\pi}\left(\frac{3}{3+L}\right)^2 R^{2L} \tag{2.29}$$

$$B_{sp}(ML) = \frac{10\hbar}{4\pi}\left(\frac{e}{m_p c}\right)^2\left(\frac{3}{3+L}\right)^2 R^{2L-2} \tag{2.30}$$

where $R = 1.2 \times 10^{-15} A^{1/3}\,\mathrm{m}$.

The experimental reduced transition probabilities may now be conveniently measured in Weisskopf units (W.u.), defined by:

$$B(L)[W.u.] = \frac{B(L)_{exp.}}{B(L)_{s.p.}} = \frac{T^{\gamma}_{1/2}(L)_{s.p.}}{T^{\gamma}_{1/2}(L)_{exp.}} \tag{2.31}$$

where the subscript *exp* refers to the values obtained from experiment. Formulae for the s.p. partial half-lives (cf. Firestone: Appendix [36]) are shown in Table 2.1.

Table 2.1: Formulae for single-particle transition half-lives, corrected for internal conversion. Energies are measured in keV.

Electric	$t^{\gamma}_{1/2}$ **(s)**	**Magnetic**	$t^{\gamma}_{1/2}$ **(s)**
E1	$\frac{6.76\times10^{-6}}{{E_\gamma}^3 A^{2/3}}$	M1	$\frac{2.20\times10^{-5}}{{E_\gamma}^3}$
E2	$\frac{9.52\times10^{6}}{{E_\gamma}^5 A^{4/3}}$	M2	$\frac{3.10\times10^{7}}{{E_\gamma}^5 A^{2/3}}$
E3	$\frac{2.04\times10^{19}}{{E_\gamma}^7 A^{2}}$	M3	$\frac{6.66\times10^{19}}{{E_\gamma}^7 A^{4/3}}$
E4	$\frac{6.50\times10^{31}}{{E_\gamma}^9 A^{8/3}}$	M4	$\frac{2.12\times10^{32}}{{E_\gamma}^9 A^{2}}$
E5	$\frac{2.89\times10^{44}}{{E_\gamma}^{11} A^{10/3}}$	M5	$\frac{9.42\times10^{44}}{{E_\gamma}^{11} A^{8/3}}$

Hindrance factors, F_W, are also often used. They give a measure of the extent to which a transition is hindered relative to the Weisskopf estimate. These are simply the reciprocals of the reduced transition probabilities (in W.u.):

$$F_W = \frac{T^{\gamma}_{1/2}(L)_{exp.}}{T^{\gamma}_{1/2}(L)_{s.p.}} = \frac{1}{B(L)[W.u.]} \tag{2.32}$$

The reduced hindrance per degree of forbiddenness (see Section 2.1.4) is then defined

as:

$$f_\nu = (F_W)^{1/\nu} \tag{2.33}$$

Chapter 3

Experimental setup and techniques

As noted above, projectile fragmentation is an efficient method for producing exotic, neutron-rich nuclides. The FRS spectrometer, described below, enables the clean identification of nuclides implanted in a stopper, correlating the implantation of specific ions with their subsequent gamma and beta decays with high efficiency and sensitivity. The correlation minimises the background radiation associated with the slowing down and implantation of such high-energy ions. The active stopper setup described here was specifically designed for the RISING experimental collaboration and was used for the first time in February 2007, yielding the results given in this thesis for ^{205,203}Au.

3.1 Production

Neutron-rich nuclei can be produced by several reaction methods, such as fusion-evaporation, deep inelastic collisions, fragmentation and fission. However, thin targets ($\sim 1\,\mathrm{mg/cm^2}$) are generally required for fusion-evaporation, deep inelastic or multi-nucleon transfer reactions, thus restricting the rates of production. ISOL (Isotope Separation On Line) is an alternative method, available at CERN-ISOLDE and elsewhere. In this method the exotic nuclei are created by a light ion beam impinging on a thick target, the resulting nuclei being extracted, ionised and accelerated. For those ions that are efficiently released from the target-ion source system, this yields high beam intensities, but it is restricted to nuclides with half-lives of a few seconds or more. In-flight separation used in the setup

described here, unlike the ISOL method, does not have the extraction problems associated with the chemical and material properties of the ion source.

Fragmentation studies at intermediate energies have shown that isomeric states can be populated with relatively large cross sections [6]. Although the cross sections for the production of neutron-rich heavy nuclides in relativistic fragmentation is small, of the order of mb or less (μb in the case of ^{192}W), such nuclides are essentially inaccessible using fusion-evaporation and and are too heavy to be populated in fission. Relativistic projectile fragmentation is therefore an efficient method of populating nuclei such as those investigated here.

3.1.1 Primary Beam

The primary beam, ^{208}Pb in the experiments under consideration here, is obtained by using ion sources to produce ions which are then injected into GSI's 120 m long UNIversal Linear ACcelerator, UNILAC, accelerating them to speeds around 20% of the speed of light, giving energies of around 10 MeV/u. The beam is then injected into the heavy-ion ("SchwerIonen") Synchrotron, SIS-18. This has a circumference of 216 m and a maximum bending power of 18 Tm. The ions increase in energy, increasing in speed during their hundreds of thousands of revolutions in the synchrotron to around 90% of the speed of light. Extraction results in a pulsed 'primary' beam of heavy ions with energies ~ 1 GeV/u at intensities of around 1×10^8 - 1×10^9 pps (the intensities and spill structures are given in Tables A.1, A.2 and A.3). The beam is then directed onto the production target in order to produce the nuclides of interest. The targets used for the FRS are positioned on a water-cooled ladder which holds up to 15 targets of 20 mm diameter [47]. Details of the targets used in the experiments considered here are given in Appendix A. A schematic showing the synchrotron, FRS spectrometer and storage ring (ESR) is shown in Fig. 3.1.

3.1.2 Projectile Fragmentation

Heavy, neutron-rich, rare earth nuclei, such as ^{190}W, are very difficult to produce. However, relativistic projectile fragmentation has been very successful in producing such nu-

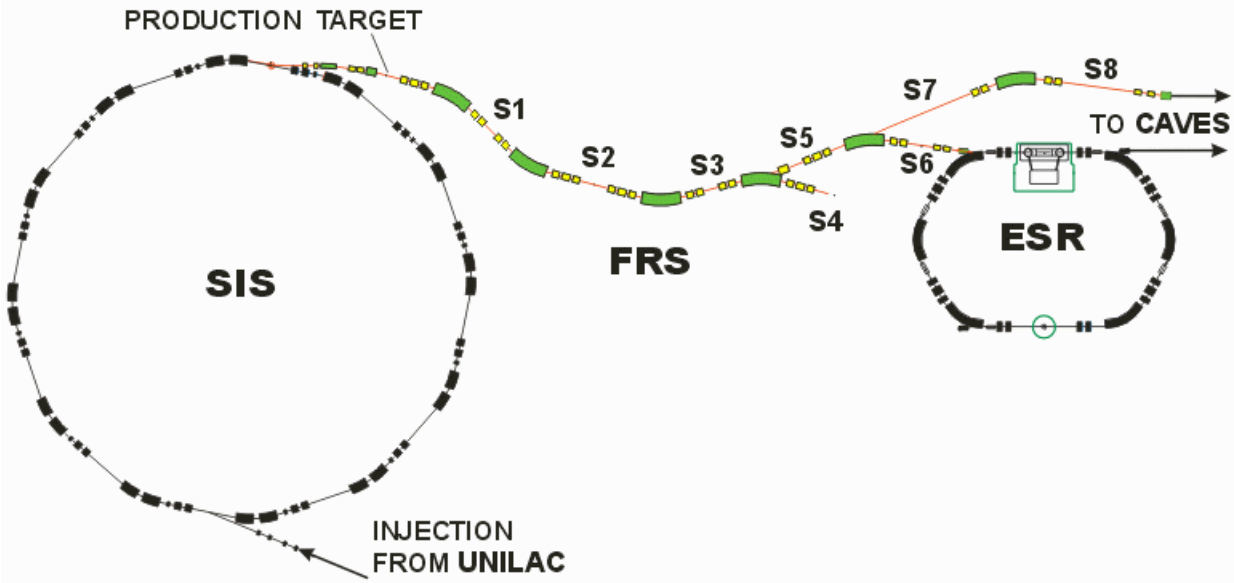

Figure 3.1: Schematic of the setup at GSI, showing SIS synchrotron, FRS spectrometer and ESR storage ring (taken from GSI FRS website [48]).

clei [6]. For example, the most neutron-rich, stable tungsten isotope is ^{186}W, so the production of tungsten isotopes with up to seven more neutrons in the experiment analysed here (tungsten isotopes up to ^{193}W were produced) is itself a clear indication of the effectiveness of relativistic projectile fragmentation reactions in producing exotic, neutron-rich nuclei.

Serber [49] has shown that at high energies the collision time between the incident particle and the target is so small compared to the time between collisions within the nucleus that the target nucleus may be regarded as transparent. The collision of a heavy ion on a light target, ^{208}Pb on Be in the experiments discussed here, involves inverse kinematics and will be central or peripheral, depending on the impact parameter. Central collisions give rise to fusion and multi-fragmentation processes, peripheral ones to projectile fragmentation, the reaction of interest here. One may regard the process as having two stages: abrasion and ablation [50]. In the abrasion stage, the projectile and target collide with a collision time of order 10^{-23} s; the nucleons in the overlapping volume are stripped off, as in classical abrasion. The *participants* produce a *fireball*, the remaining volumes being *spectators*, as shown in Fig. 3.2. This leads to the formation of a *pre-fragment*, close in mass to that of the projectile. In the ablation stage this pre-fragment de-excites by

gamma emission and nucleon (chiefly neutron) evaporation, leading to the production of the fragment required.

Due to the high energy and velocity of the heavy projectile ions impinging on the much lighter, stationary nucleus, the "cocktail" of ion fragments produced is such that the fragments are forward focussed and have approximately the same velocity.

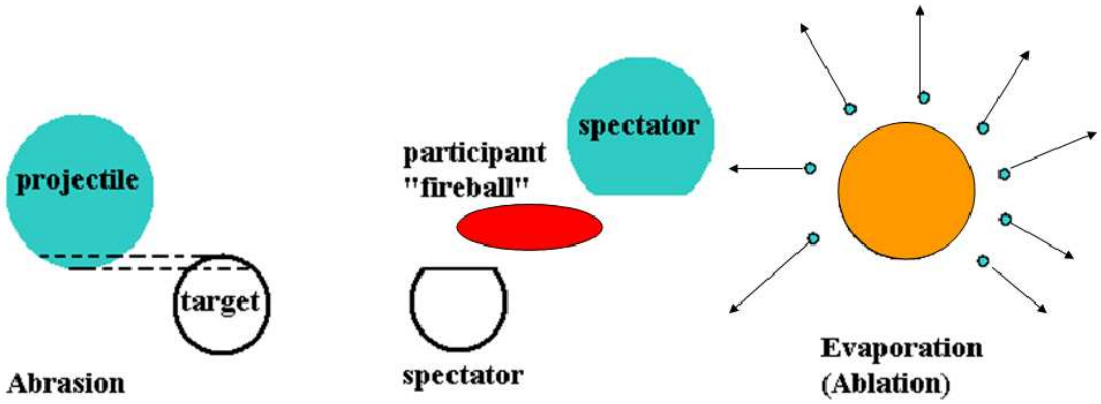

Figure 3.2: Simplified Abrasion-Ablation process adapted from T.Kurtukian [50].

The fragments are separated, identified and transported by the FRS (FRagment Separator) [47] to the final stopper where the Ge detector array is located, thus enabling γ-spectroscopy of isomeric states to be carried out. Only those excited states whose lifetimes are longer than the time taken to transport the ions from target to stopper ($\sim$ 300 ns) can be detected. Similarly, the maximum acquisition time ($\sim 400\,\mu$s) for the DGF modules (see Section 3.4.1) places an upper limit on the lifetimes of detectable isomeric states of ~ 1 ms.

Other Reactions

There are a number of reactions that may occur as the projectile ions impinge on the target, such as spallation, fission, and (partial) fusion, as well as projectile fragmentation. These depend, *inter alia*, on energy and the impact parameter (for more details on reactions and cross sections, see reference [51]). As noted above, projectile fragmenta-

tion reactions will have the highest cross sections for high energy, high impact parameter (peripheral) collisions. As the ions lose energy during their trajectory through the FRS, fission and other reaction mechanisms will have increasing cross sections, necessitating the removal of such events in a 'clean-up' procedure (see Section 4.1.1).

3.2 The Fragment Separator (FRS)

A schematic of the beam, FRS and associated detectors is shown in Fig. 3.3, in which it can be seen that after the FRS the beam can be directed elsewhere, e.g. the storage ring (cf. Fig. 3.1). An FRS "setting" for the production of a particular nuclide is such that the FRS is "tuned", using the magnets and slits, so that the given nuclide is centred at the final focal plane.

A simplified schematic of the setup, emphasizing the relative position of the detectors, is given in Fig. 3.4. The nomenclature is such that the detectors, slits and magnets have an initial number referring to their position relative to the previous dipole magnet, as shown in the diagram, e.g. S2 is the intermediate focus (after the second dipole magnet), so Sci21 refers to a scintillator at this position, MUSIC 42 refers to the second MUSIC (Multi-Sampling Ionisation Chamber, cf. Section 3.3.4) after the fourth dipole magnet, etc.

The relevant distances and materials for the ^{192}W setting are given in Table A.1, those for ^{203}Au in Table A.2 and those for ^{205}Au in Table A.3.

3.2.1 Magnets

The four dipole magnets bend the charged ion beam using the Lorentz magnetic force as the centripetal bending force:

$$\mathbf{F} = q\mathbf{v} \times \mathbf{B} = -\frac{mv^2}{\rho}\hat{\boldsymbol{\rho}} = -\frac{\gamma A u v^2}{\rho}\hat{\boldsymbol{\rho}} \tag{3.1}$$

where γ is the relativistic Lorentz factor, $\frac{1}{\sqrt{1-\beta^2}}$, with $\beta = \frac{v}{c}$, A is the atomic mass, u the atomic mass unit ($\approx 931.5\,\mathrm{MeV}$) and ρ the bending radius. This equation may be

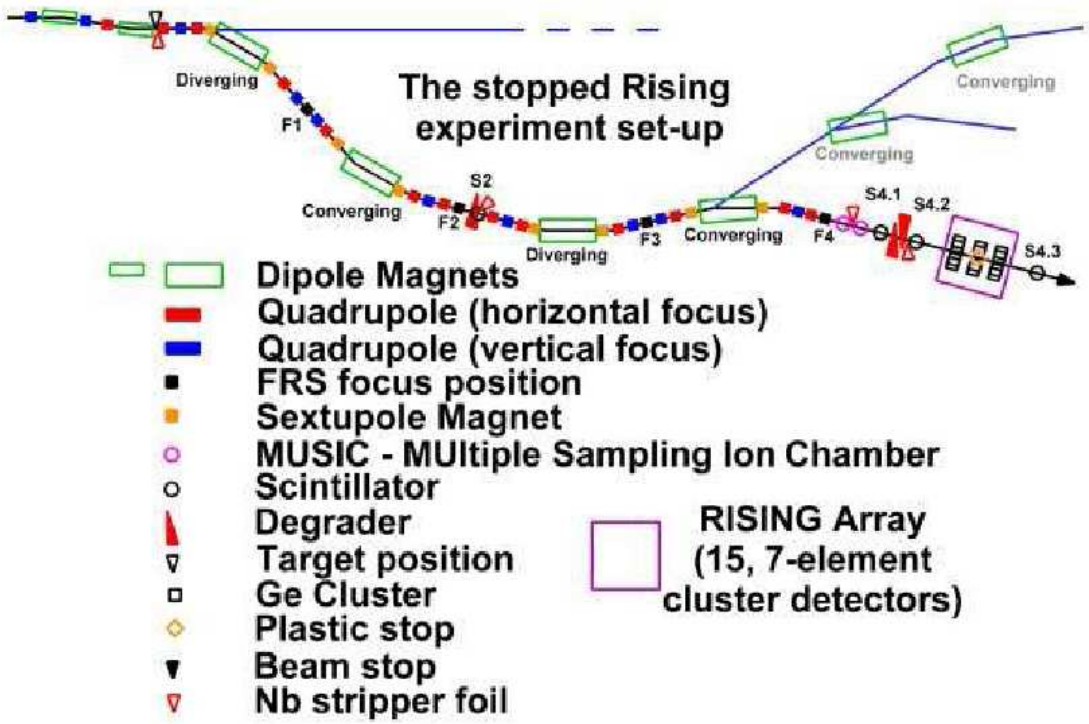

Figure 3.3: Schematic of the FRS setup [52].

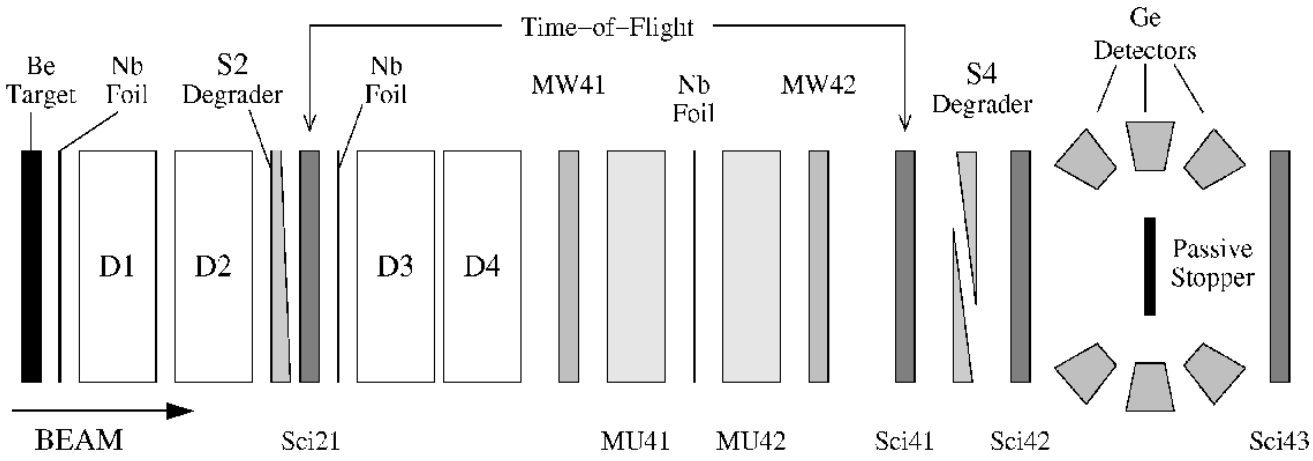

Figure 3.4: Schematic of the relative positions of the detectors [53].

rearranged to give the magnetic rigidity, $B\rho$:

$$B\rho = \frac{p}{q} = \frac{\beta\gamma uc}{e}\frac{A}{Q} \tag{3.2}$$

where $Q = Z$ for fully stripped ions, $Q = Z - 1$ for H-like ions, etc. β and γ can be determined from the time-of-flight since the total distance of the trajectory of the ions is fixed.

The bending radii of the dipole magnets are fixed at around 11 m, giving a curvature angle of 30°, but their magnetic field strengths can be varied up to about 1.6 T [47], yielding typical magnetic rigidities of the order of 10 Tm. The ions are focussed axially by the quadrupole magnets. These focus in one plane but, because of their geometrical configuration, this causes the beam to defocus/diverge in the perpendicular plane cf. Fig. 3.5 [54].

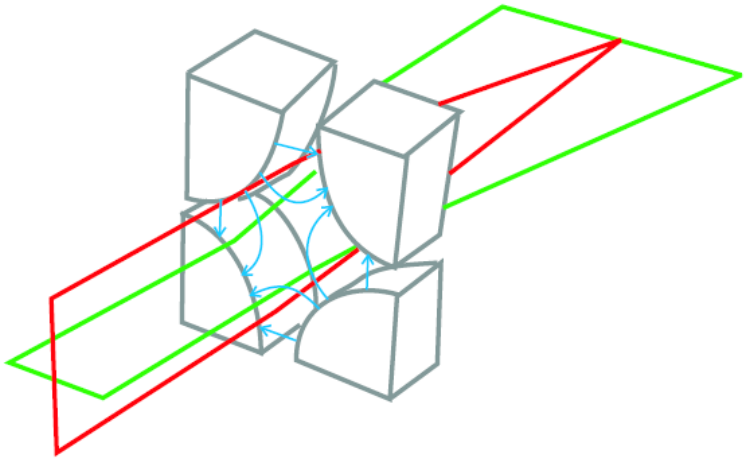

Figure 3.5: Quadrupole magnet focussing in the vertical plane and defocussing in the horizontal plane (taken from [54]).

The focal plane is horizontal (the x-direction), so the quadrupoles occur in triplets for alternate gradient focussing, i.e. focussing first in the x-direction, then the y-direction (to correct for the prior divergence in this plane), then again in the x-direction. Sextupole magnets, located immediately before and after the dipole magnets, apply second-order corrections to the beam focussing. The maximum acceptance in the x-direction is ±100 mm. The dipole magnet settings for the ^{192}W setting are shown in Table A.1 in Appendix A.

3.2.2 Beam Optics and the Intermediate Degrader

The primary purpose of the FRS is to separate the nuclides of interest so that they may be identified and further investigated. Magnetic spectrometers separate by the momentum-to-charge ratio, as indicated by Equation (3.2). However, high-energy projectile fragmentation produces fragments at very similar relativistic velocities, thus the first two dipoles merely effect a mass-to-charge ratio separation, insufficient to identify nuclides from the large range of ions produced. Fragments in the same charge state with the same magnetic rigidity have the same A/Q and are thus focussed at the same horizontal position at the intermediate degrader [47].

The method of ion selection used here is the $B\rho-\Delta E-B\rho$ method: A/Q separation by the first two magnetic dipoles, then separation by energy loss in an intermediate degrader, then another A/Q separation by the last two magnetic dipoles, cf. Fig. 3.4. Thus, after the first half of the FRS (i.e. from target to the S2 focal plane) the fragments pass through a degrader with a thickness corresponding to about 50% of the range of the fragments [55]. Ions passing through this degrader will lose energy in proportion to the square of their charge (equal to their atomic number for fully-stripped ions), as given by the Bethe-Bloch formula [56, p. 31]:

$$-\frac{dE}{dx} = \frac{4\pi z^2}{m_0 v^2} NB \tag{3.3}$$

where

$$B \equiv Z\left[\ln\frac{2m_0v^2}{I} - \ln\left(1-\frac{v^2}{c^2}\right) - \frac{v^2}{c^2}\right] \tag{3.4}$$

where v and ze are the speed and charge of the primary particle (ion), N and Z are the number density (the number of atoms per unit volume) and atomic number, respectively, of the absorber atoms, m_0 the electron rest mass, and I an experimentally determined parameter related to excitation/ionisation of the absorber. The Bethe-Bloch formula is valid provided the speed of the charged particles that are stopping is large compared with the speed of the atomic electrons. The momentum loss in this degrader, therefore, has a very different dependence on Q and v than that due to changes in the magnetic

rigidity, cf. Equation (3.2). In particular, it can be deduced that ions of the same A/Q but different charge (hence different Z) will experience different energy and momentum losses. Separation of the nuclides is thus achieved by making two different 'cuts' across the Segrè chart and introducing a dependence on Z at the intermediate degrader.

The second stage of the FRS (using dipole magnets 3 and 4) then transports the ions according to the magnetic rigidity given by the values of A, Q, v and B in the second half of the FRS. This is shown schematically for the two 'halves' of the FRS in Fig. 3.6 [54], in which the wedge degrader is achromatic (see Section 3.2.2).

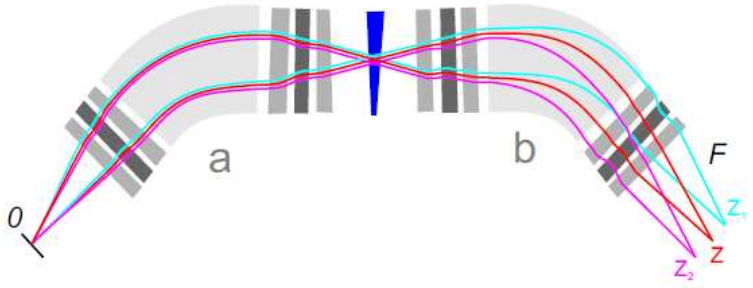

Figure 3.6: Fragment separation for a two-dipole spectrometer using a wedge degrader. Three different isotopes with the same A/Q ratio and the same velocity pass through the first spectrometer stage. The achromatic intermediate degrader slows the ions down depending on their charge. The different isotopes are then separated in the second stage. (Reproduced from reference [54]).

Degrader profiles

As noted above, the wedge shape of the intermediate degrader means that the energy loss is dependent upon position, thus on A/Q. In fact, the energy loss is calculated from the difference in the magnetic rigidities between the first half and second half of the FRS using position and time-of-flight measurements given by the time signals from the PMT tubes of scintillators at S2 and S4. The arbitrary units used for the energy loss in this analysis are scaled from the following expression, where the subscript 2 refers to the second half of the FRS, ρ_2 is the average bending radius, and β and γ have their usual meaning as relativistic factors:

$$\frac{B\rho_2}{\beta_2}\left(-\frac{\Delta\gamma}{\gamma_2}\right) \tag{3.5}$$

The geometric profile of the intermediate degrader is varied by using a variable thickness degrader consisting of two Al wedges, two wedge-shaped discs, and a ladder with several Al Mg_3 plates of different thicknesses. These components are shown in Fig. 3.7.

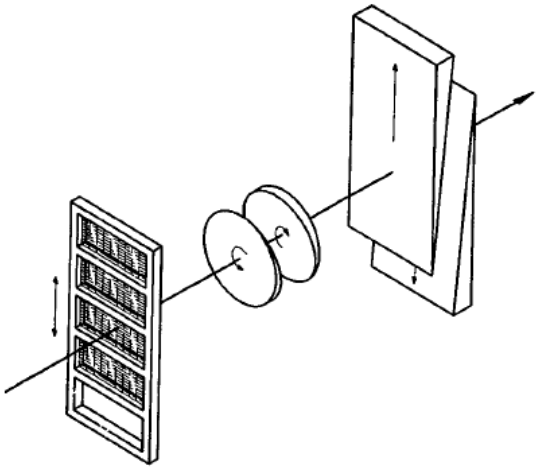

Figure 3.7: The ladder and Al wedges are the homogeneous parts of the degrader, whereas the degrader slope in the x direction can be adjusted with two wedge-shaped discs that rotate simultaneously in opposite directions [47].

Changing the profile of the degrader alters the particular properties of the beam optics after the degrader. Operation of the FRS in achromatic mode is chosen to allow good horizontal separation of isotopes at the final focal plane, used in the 'passive stopper' arrangement (the setup used for the ^{192}W setting), whereas the monochromatic mode is used for good separation of isotopes by depth. The latter is the mode used for the 'active stopper' experiments (the setup used for the ^{203,205}Au settings) in which it is essential that the ions of interest are implanted precisely in a DSSSD detector, allowing tagging of the beta-delayed gamma decay. The different characteristics of the two modes are shown in Figs. 3.8 and 3.9, plotted using the LISE program [57].

Achromatic mode

For any nuclide, the profile of the degrader can be chosen in such a way that the momentum dispersion before the degrader is compensated for by the dipoles after it, thus the system is achromatic for this particular nuclide. In this mode the horizontal position

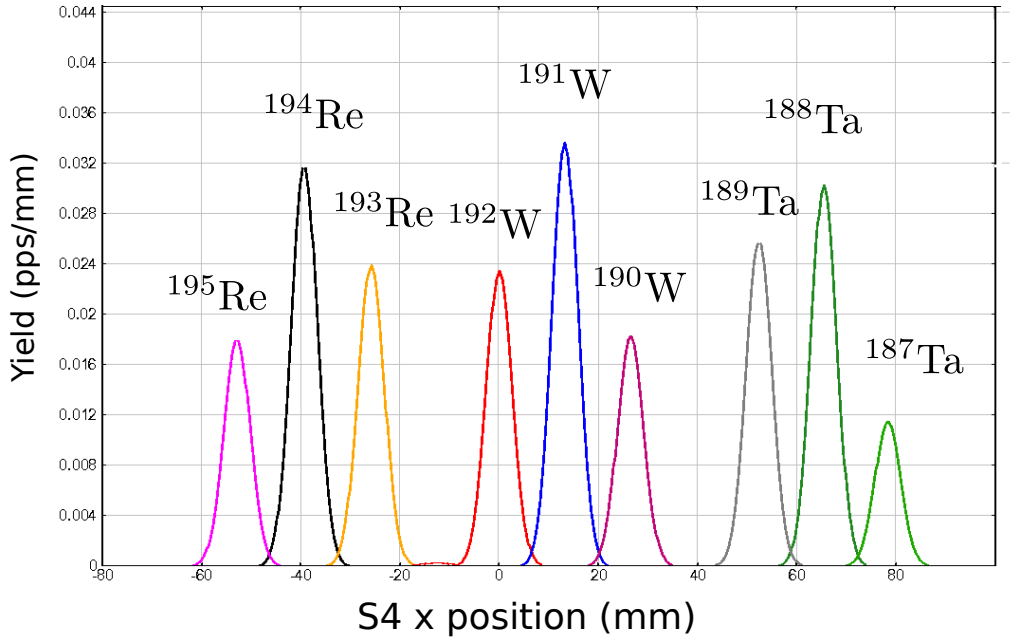

Figure 3.8: Achromatic mode for the ^{192}W setting. This plot, obtained using a LISE simulation [57], shows a selection of fully-stripped ions only. The relative separation in the final focal plane according to Z and A/Q is evident. Note that LISE reverses the direction of x compared to the experimental setup.

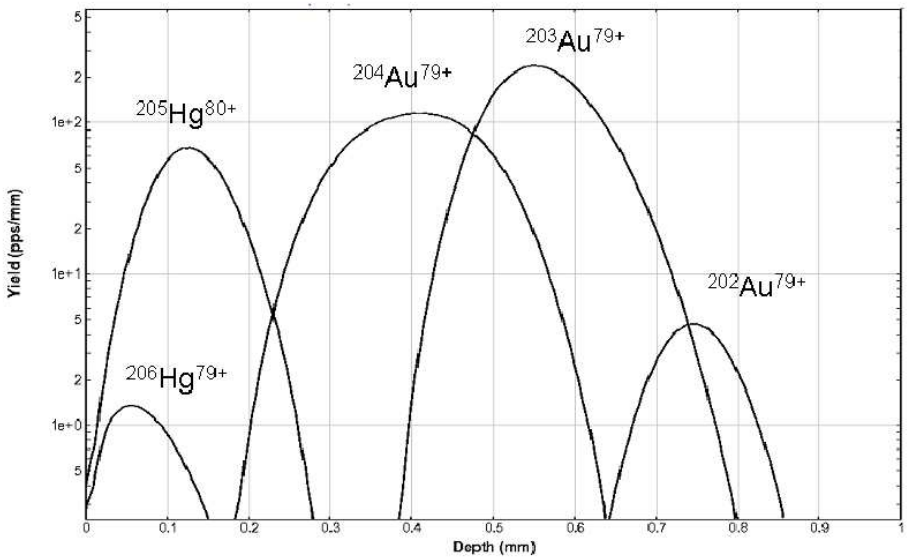

Figure 3.9: Monochromatic mode for the ^{203}Au setting. This plot, obtained using a LISE simulation [57], shows the implantation depths of ions in the active stopper at the final focal plane.

is independent of the momentum and the final beam spot size is relatively small even for large momentum acceptances [58]. For full momentum acceptance (i.e. slits at S2 fully open), the degrader thickness has to be matched to the dispersion, D_1, in the first half of the FRS, in order to obtain achromaticity. This means that the energy ratio, η, of ions incident at a given horizontal distance apart at the degrader must be the same for the ions emergent at the equivalent horizontal separation on exit. If the ratio of momentum dispersions at the exit and entrance of the degrader is 1, then, as shown in Fig. 3.10, for ions 1 cm apart, i.e. x=1 (using the usual convention of x being the direction in which the ions are dispersed, horizontal in this setup), we have [59]:

$$\begin{aligned} E_1 - e\left(\frac{dE}{dx}\right)_{E_1} &= E_2 \\ \eta E_1 - e'\left(\frac{dE}{dx}\right)_{\eta E_1} &= \eta E_2 \end{aligned} \tag{3.6}$$

where $\eta = (1+\frac{1}{D_1})^2$ (with D_1, the dispersion in the first half of the FRS, in cm/%), and E_1 and E_2 are the energies at the positions with degrader thicknesses e and e' respectively, as shown in Fig. 3.10. Given that $\left(\frac{dE}{dx}\right)_E \propto \frac{Az^2}{E}$, cf. Equation (3.3), it follows that $\frac{e'}{e} = \eta^2$. The condition for achromaticity thus depends entirely on the dispersion in the first half of the FRS, thus is the same for different nuclides at different energies.

At the entrance of the degrader, the separation, Δx, of two ions with momenta p_0 and $p_0 + \Delta p$ is:

$$\Delta x = D_1 \frac{\Delta p}{p_0} \tag{3.7}$$

Full achromaticity means that the dispersion in the first half of the FRS is cancelled by a reverse dispersion in the second half, provided that we allow for the magnification in this first half, M_1:

$$D_2 = -D_1 M_1 \tag{3.8}$$

The angle of the degrader, θ, is of course dependent on the thickness profile and determines whether the degrader is achromatic or monochromatic (or neither). In achromatic mode, the angle, θ_a, is such that:

$$\tan\theta_a = \frac{\Delta e}{\Delta x} \approx \lambda \frac{e}{D_1} \tag{3.9}$$

where e is the reference thickness of the degrader, $\frac{\Delta e}{\Delta x}$ measures the increase in thickness per unit distance in the x direction, and λ is a parameter related to the range, R, in the stopping material (cf. [50]) such that:

$$\frac{\delta R}{R} \approx \lambda \frac{\delta p}{p} \tag{3.10}$$

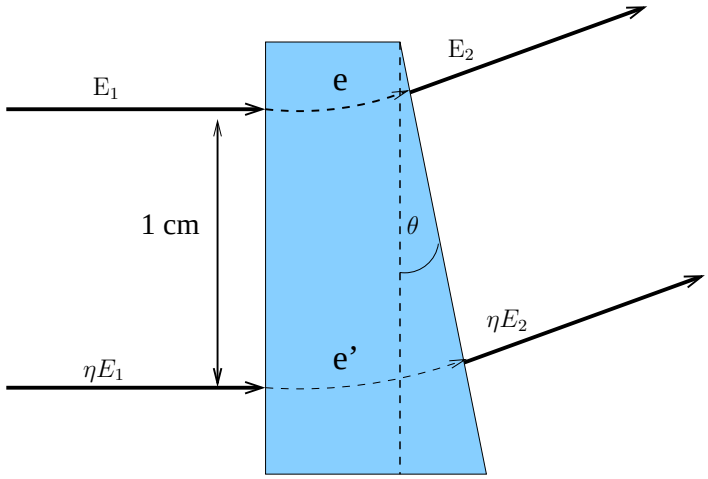

Figure 3.10: The wedge-shaped degrader (thickness exaggerated) at the intermediate focal plane, showing the different thicknesses and energy losses depending on position (adapted from reference [59]).

Monochromatic mode

In this mode, ions of a specific nuclide arrive at the degrader at different x positions with different momenta and energies. The degrader profile is such that the energy and momentum losses through the degrader cause the ions to be equalised to a new, lower energy and momentum. Different nuclides are thus characterised by a specific energy and momentum after this degrader and therefore have a different range in the final stopper. There is no achromatic focussing in this mode of operation.

Now, Equation (3.10) implies that

$$\Delta R \approx \lambda \frac{\Delta p}{p_0} R_0 \tag{3.11}$$

where R_0 and $R_0 + \Delta R$ are the ranges of these ions through the degrader. Substituting for $\frac{\Delta p}{p_0}$ from Equation (3.7) gives:

$$\Delta R \approx \lambda \frac{\Delta x}{D_1} R_0 \tag{3.12}$$

This range difference, ΔR, can be matched by the profile of the degrader such that $\Delta e = \Delta R$. Thus the profile of the monochromatic degrader has angle θ_m such that:

$$\tan \theta_m = \frac{\Delta e}{\Delta x} \approx \lambda \frac{R_0}{D_1} \tag{3.13}$$

Slits

Thick copper blocks are used as slits to reduce the width, and thus the momentum acceptance, of the beam. In this way, unwanted nuclides can be removed and selection improved. These slits are located at the entrance of the FRS and before each focus (S1, S2, S3 and S4).

Foil strippers

Although most of the ions enter the vacuum beamline of the FRS fully stripped of electrons, they subsequently pass through aluminium in the degraders, gas in the MUSIC chambers, and beamline windows. Therefore, the ions may pick up one or more electrons. Niobium foils, placed as backing after the Be target, after the intermediate degrader, and between the two MUSIC chambers, are used to strip electrons from the transmitted ions. Their thicknesses are given in Appendix A.

Charge States

Depending on the slit settings, the masses, and the energies involved, there can be considerable contamination at the final focal plane from nuclides in different charge states. An example of charge state contamination is shown in Fig. 3.11. Therefore, it is desirable that a charge state selection is made before particle identification, as described below in Section 4.1.2.

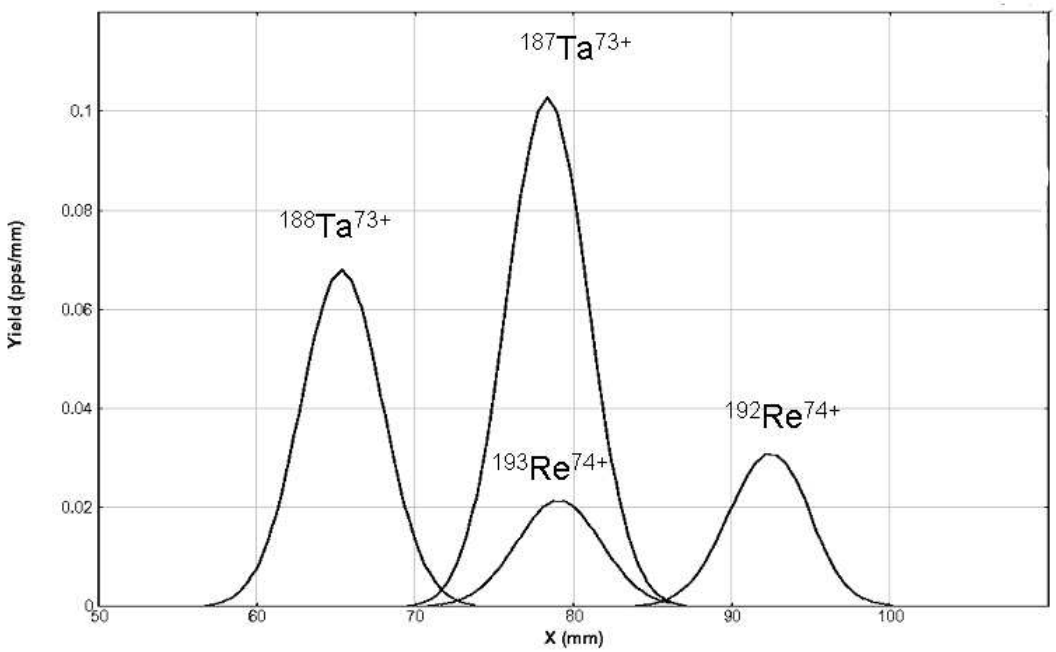

Figure 3.11: Plot showing selected nuclides across the final focal plane of the (passive) stopper. This plot, obtained using a LISE [57] simulation, shows contamination of fully-stripped ^{187}Ta with H-like ^{193}Re. Note that LISE reverses the direction of x compared to the experimental setup.

3.3 Detectors

Several different types of detector are used along the FRS and at the final focus, cf. Fig. 3.4. A SEETRAM (q.v. infra) and current grids measure the intensity and position of the primary beam as it impinges on the target; scintillators and multiwire proportional chambers are used as tracking detectors as the beam travels along the FRS; the time-of-flight is measured using the time differences between signals from scintillators at S2 and

S4; the ions' energy losses are measured by scintillators and MUSICs; ions are implanted in a stopper (a 'passive' plastic stopper in the case of ^{192}W and an 'active' Si stopper in the case of ^{203,205}Au); the RISING γ-ray array surrounds the stopper and detects the gamma rays emitted. These are further described below.

3.3.1 Detectors used for the primary beam

A SEcondary Electron TRAnsmission Monitor (SEETRAM) placed upstream of the target station is used to measure the high beam intensities involved in these experiments. The SEETRAM detects the current caused by secondary electrons emitted from a central thin ($\sim 10 - 15\,\mu$m) Ti foil as the projectile ions pass through it. There are three foils; each having diameter 11.5 cm and mounted perpendicular to the beam axis. The secondary electrons emitted from the middle foil are collected by the two outer foils. The collected current enables measurements of the intensity during the spill structure and the extraction efficiency [60].

In order to centre the beam precisely on the production target, two-dimensional grids, using gas amplification with current readout, are positioned at the entrance of the FRS.

3.3.2 Scintillators

Bicron BC420 scintillation detectors are placed after the wedge degrader at S2 (Sci21), before and after the final degrader at S4 (Sci41 and Sci42), and behind the stopper (Sci43). Distances for each setting are given in Appendix A. They measure particle position and time of detection. Scintillation detectors function by emitting light photons as atoms in the material of the detector de-excite following atomic excitation caused by the passage of the energetic ions. Photons from the scintillator then strike the photocathode of a photomultiplier tube (PMT), releasing electrons. An electric field then causes these photoelectrons to be accelerated towards the first dynode, producing secondary electrons, thus amplifying the number of electrons. This amplification continues with secondary electrons being accelerated via several further dynodes until they reach the anode (a typical photon pulse yielding 10^{10} electrons [56, p.265]). The resulting pulse is then

output to the data acquisition system.

The BC480 detectors are highly efficient in terms of light production and have a fast timing response (the decay constant is 1.5 ns) for areas such as the 200 mm x 80 mm typical beam area. Position is determined from the time difference between signals in fast (Hamamatsu HM2431) photomultiplier tubes placed on either side of the scintillator (left and right for determination of x position, above and below for y); a schematic of the electronics involved is shown in Fig. 3.12. The large refractive index, n_{sci}=1.58 [61], means that total and partial internal reflection at the edges of the scintillator contribute to the efficiency of light transmission to the PMTs; the critical angle for T.I.R. here is:

$$\theta_C = \arcsin(\frac{1}{n_{sci}}) \approx 39^\circ.$$

The position resolution (FWHM) for heavy ions at S2 is 4 mm [62].

Time-of-flight

The signals from scintillators Sci21 and Sci41 are used to determine the time-of-flight. Since the rate of ions at S2 is far higher than at S4, Sci41 is used as the start signal (at actual time T_4). The output pulse at Sci21 (at actual time T_2) is subjected to a delay, T_d such that $T_2 + T_d > T_4$. In this way, the signal from Sci21 serves as the stop signal for the time-of-flight TAC (Time-to-Amplitude Converter). Before the PMT outputs are sent to the TACs, they are input to constant-fraction discriminators (CFDs) which impose a lower threshold. The TAC outputs are digitized using ADCs (Analogue-to-Digital Converters) in order to be written to the data acquisition. This is shown in Fig. 3.12. Note that time is measured in reverse in this system, i.e. the longer the *actual* time-of-flight, the shorter the *measured* time-of-flight. To improve accuracy and remove the position dependence of the scintillator times, the time outputs from the right and left PMTs are averaged at S2 and S4.

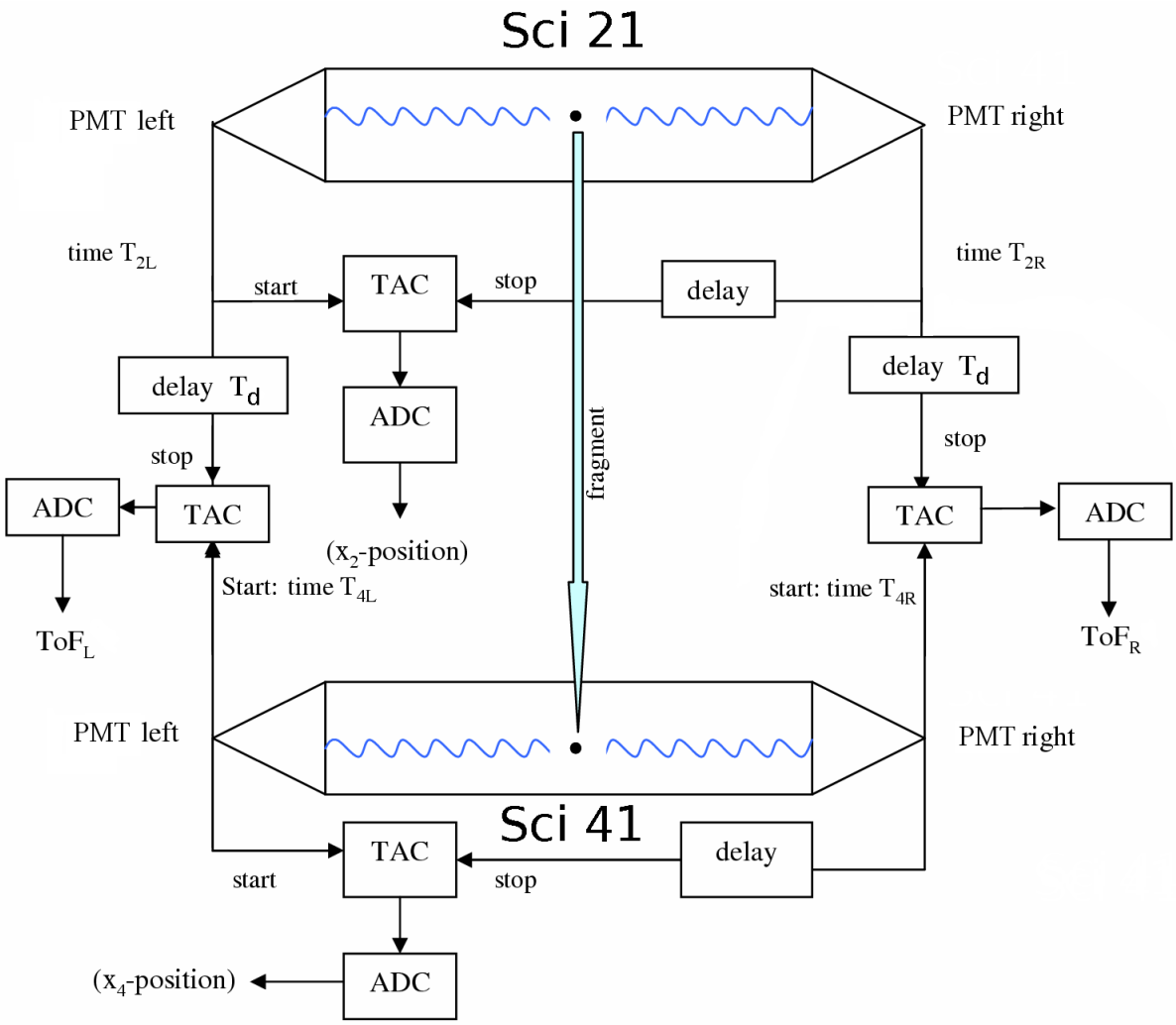

Figure 3.12: Schematic of the scintillator electronics involved in determining the time-of-flight and the x-positions at S2 and at S4. The PMT outputs are first input to CFDs, not shown in this figure. This figure has been slightly adapted from one in [62].

3.3.3 Multiwires

Multiwire proportional counters (MWPCs) are used to measure particle position in the x- and y-directions. They are used before and/or after each dipole in order to tune the beam, then removed during experimental runs in order to avoid decreasing the count rate. Those at the final focal plane (MW41 and MW42) are used, after beam tuning, to determine the trajectory of ions through the two MUSIC chambers (see Section 3.3.4).

The detectors are 20 cm by 20 cm and operate with a mixture of argon, CO_2, and a little alcohol at atmospheric pressure. A schematic diagram of the setup is shown in Fig. 3.13 and the thicknesses of the wires are given in Table 3.1 [63]. There are three anode grids, consisting of thin wires: U_A (at 45° to the two mutually perpendicular cathodes), U_G and U_T. Ions in the beam ionise the MWPC gas. An electric field ($\sim$ 2 kV) causes the electrons produced to be accelerated towards the anode U_A. The electron current is amplified by the avalanche of secondary electrons. The electrical pulse of negative charge on the anode induces a positive pulse on the horizontal and vertical cathode wires closest to the point on the anode at which the charge is collected. Position is determined by the difference in left-right or up-down time delays between the delayed readouts from the cathodes. The MWPCs can resolve position with 0.5 mm precision, enabling the trajectory of an beam ion to be accurately determined [63].

Table 3.1: Geometry and material thickness of the wire planes. The values correspond to one wire plane [63]. The pre-gap is for use only with light ions (Z $<$ 6). It is not, therefore, used in the experiments analysed here.

Plane	**Material**	**Distance**	**Diameter**	**Max. thickness**	**Equiv.max. Al**
(no. of planes)		**[μm]**	**[μm]**	**[mg/cm^2]**	**[mg/cm^2]**
Pregap (4)	PolyNi	86	36	—	9.4
Cathode (2)	Tungsten (W)	1000	50	96.3	67.4
Anode (1)	Tungsten (W)	2000	20	38.5	26.9

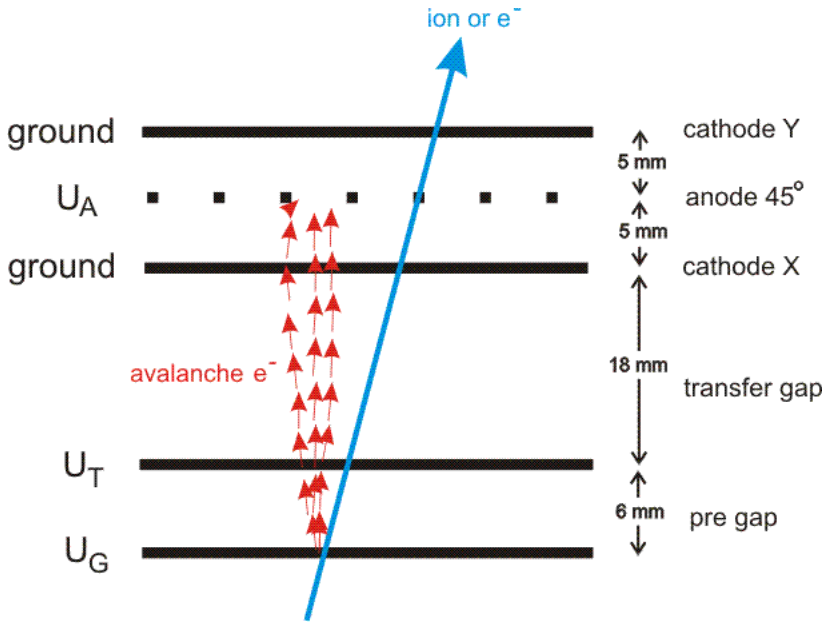

Figure 3.13: Schematic of MWPC, taken from [63].

3.3.4 Ionisation chambers: MUSICs

There are two MUSICs, fast Multi-Sampling Ionisation Chambers, with 8 anode strips of 50 mm active length each, each one filled with 2 bar of P10 gas mixture (90% Ar, 10% CH_4), operated at room temperature and atmospheric pressure. The anode strips are read out with an optimised charge-sensitive preamplifier and shaper combination for particle rates up to 200 kHz. The number of generated electrons in the counting gas is approximately proportional to the square of the charge of the penetrating particle, thus the output voltage can be used to determine the atomic number of the particle [64]. There are many electron transfers (pick-up and loss) in the counting gas. Hence it is not, strictly speaking, the actual charge (Ze for fully-stripped ions) that is measured, but the *effective nuclear charge*, q_{eff}, which, however, depends on the atomic number, Z. Their high energy resolution makes these detectors suitable for determining the small differences in energy loss of the ions through the chamber.

The ions pass through a Ti exit window from the beam line vacuum (0.09 mg/cm^2), a kapton window (from MW41), air, Mylar and glass windows, etc., so the ions have reached charge state equilibium by the time they enter the MUSIC chambers. MUSIC42 is positioned after MUSIC41 (and a Nb foil stripper, cf. Fig 3.4), the best resolution

usually being achieved by combining their outputs. The charge response of the MUSIC chambers is affected by changes in the gas pressure and temperature, such as those due to the atmospheric conditions of the experimental hall, requiring normalisation corrections to the calibration parameters.

3.3.5 Gamma Detectors

In the experimental setup considered here, the RISING (Rare ISotope INvestigations at GSI) array consists of fifteen, seven-element HPGe cluster detectors, placed in three annular groups of five detectors at $51°, 90°$ and $129°$ to the primary beam axis at an average distance from the centre of the array of about 22 cm, forming a 4π arrangement. The array is divided into two unequal 'hemispheres' (9 clusters in one, 6 in the other), allowing the array to be opened and closed mechanically; the right-hand 'hemisphere' is shown in Fig. 3.14. The array has a full peak efficiency of 15% at 662 keV [65] and a maximum resolution of about 2.5 keV at 1.5 MeV. The Compton-suppression shields are removed in order to obtain this 4π setup.

It should be realised that the prompt gamma rays emitted by the nucleus of interest immediately after production cannot be detected in this setup since the time of flight (typically ~ 100 ns) is much greater than that taken for these prompt gammas to decay. Given the flight time and the maximum time gate of 400 μs achievable with the DGF modules (see Section 3.4.1), the setup is sensitive to isomeric γ decays with lifetimes in the range 100 ns to 1 ms [66]. The γ-ray intensity around the production target is several orders of magnitude higher than that of the radiation emitted by the fragments of interest. At the stopper, as the ions are brought to rest, a prompt 'flash' of electromagnetic radiation occurs. This is due to Bremsstrahlung, a result of the rapid deceleration of the highly charged ions, lasting about 30 ns. The high granularity of the array prevents a complete 'blinding' of the RISING Ge array, allowing analysis of the delayed gamma decays immediately after this prompt flash. The correlation of isomerically-delayed γ rays in coincidence with individually identified fragments permits the identification of isomeric decays from specific ions.

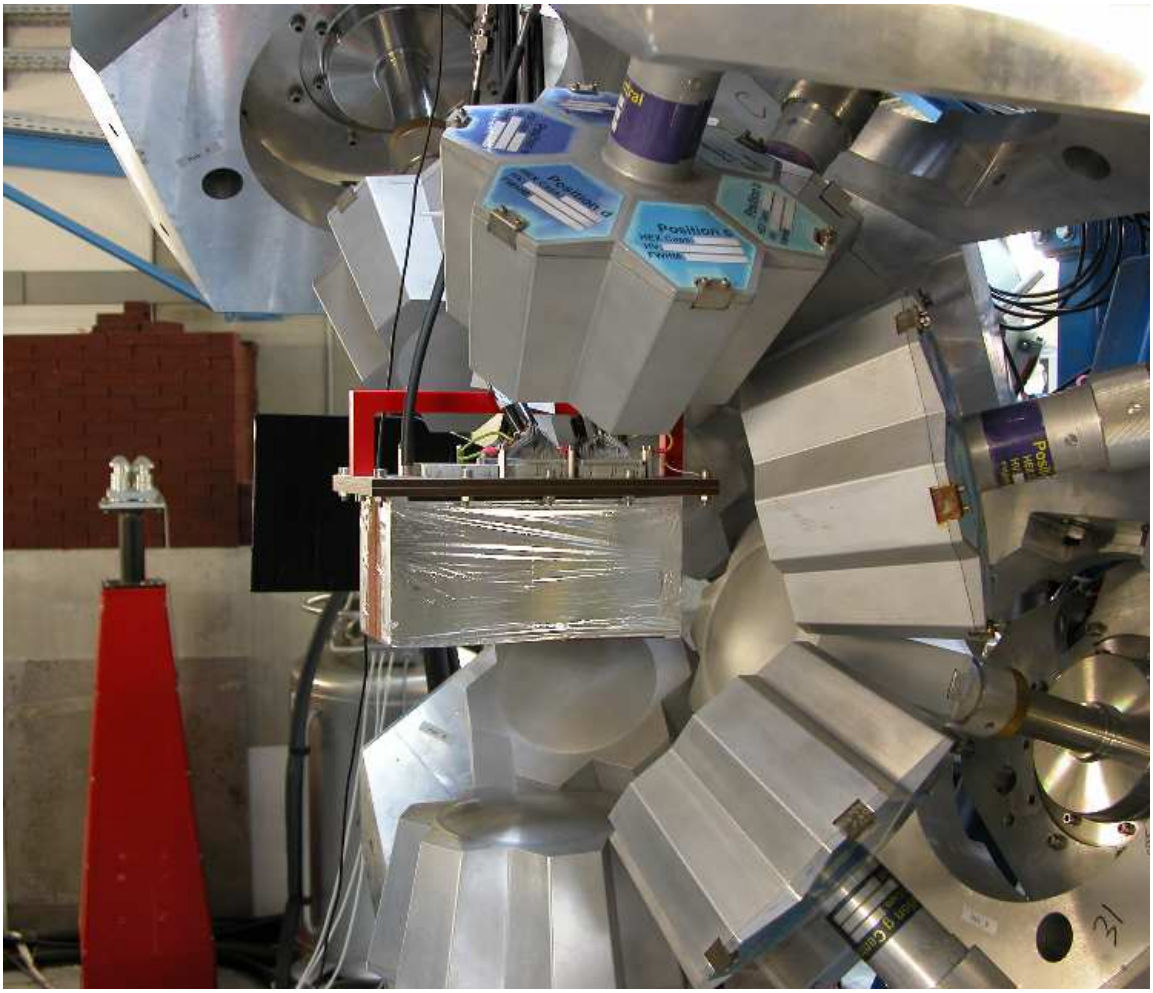

Figure 3.14: The RISING array: 15 clusters of 7 HPGe crystals each in a 4π arrangement with automated liquid nitrogen cooling. This photograph shows the right 'hemisphere'. The active stopper box, covered in Al foil, is visible at the centre of the open array.

Multiplicity

The 'multiplicity' (or 'fold') of the array is defined here as the number of identical Ge crystals/clusters that simultaneously 'fire' during an event. The prompt flash causes large multiplicity events, shown in (a) of Fig. 3.15, the multiplicity being dependent on the energy of the ions as they are implanted in the stopper [67]. Also, the longer the time window for the Ge array, the greater the multiplicity, since there is a larger probability that many different Ge crystals will have fired, cf. Fig. 3.15 (b) and (c). This means that gating on time is related to gating on multiplicity. In practice, time-gating is to be preferred since one can then select precisely the time windows of interest. Gating on a specific nuclide, cf. Fig. 3.15(d), gives far lower statistics and lower crystal multiplicity. In the analysis of the experiments considered here, crystal and cluster multiplicities were chosen to give the optimum peak-to-background ratios for the gamma spectra.

Time Walk

Lower energy ($< 100\,\mathrm{keV}$) gamma photons tend to interact within the surface layer of the Ge detectors, thus the charge takes longer to be collected on average than higher energy events occurring within the active volume; the extra time taken is around 350 ns at 60 keV. This is known, in this context, as the 'time walk' effect [66]. This is evident in Fig. 3.16 where there is a low-energy 'knee' to the prompt flash.

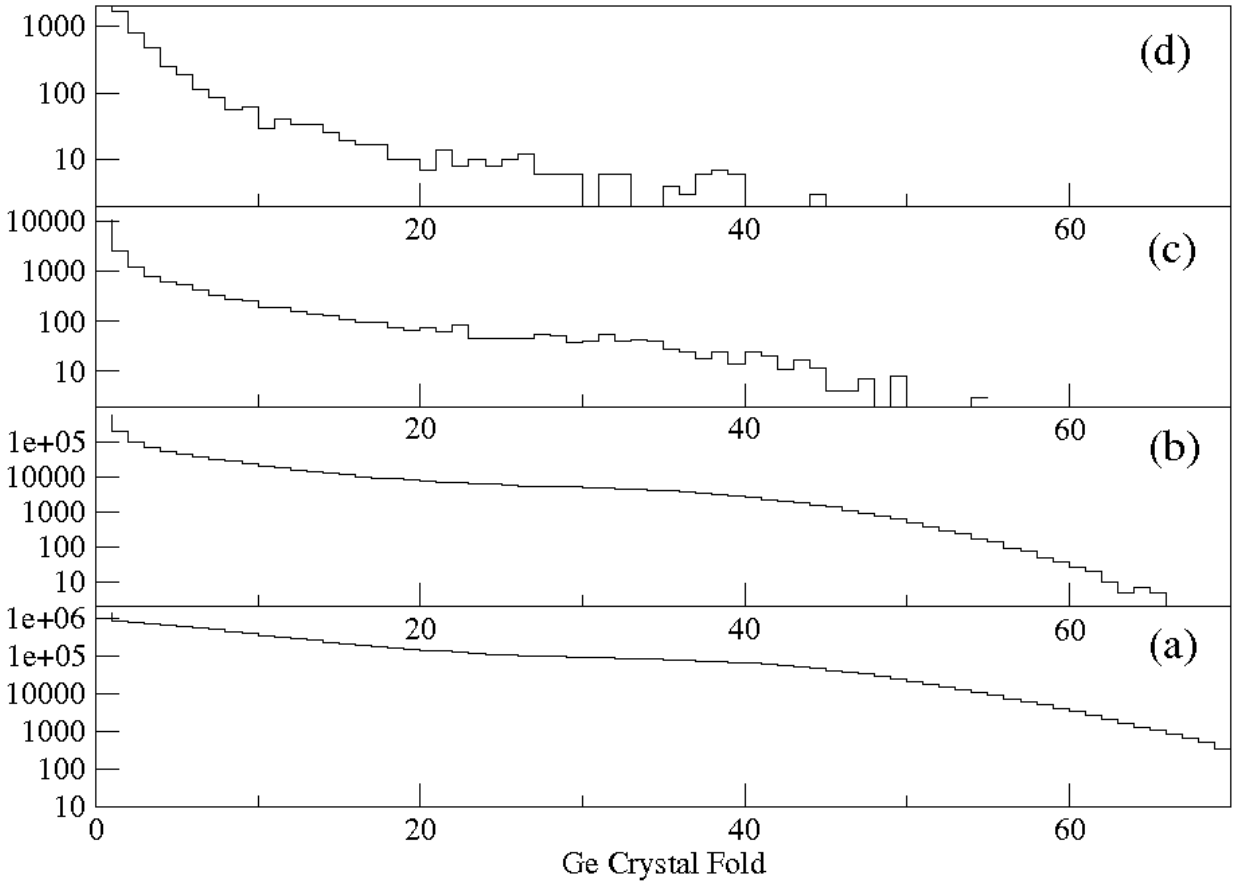

Figure 3.15: Ge crystal multiplicity. (a) is for Δt = 0-100 μs, thus includes the prompt flash, whereas (b)-(d) exclude it. (b) Δt = 2.5-100 μs, (c) Δt = 2.5-3.5 μs, (d) gated on ^{190}W.

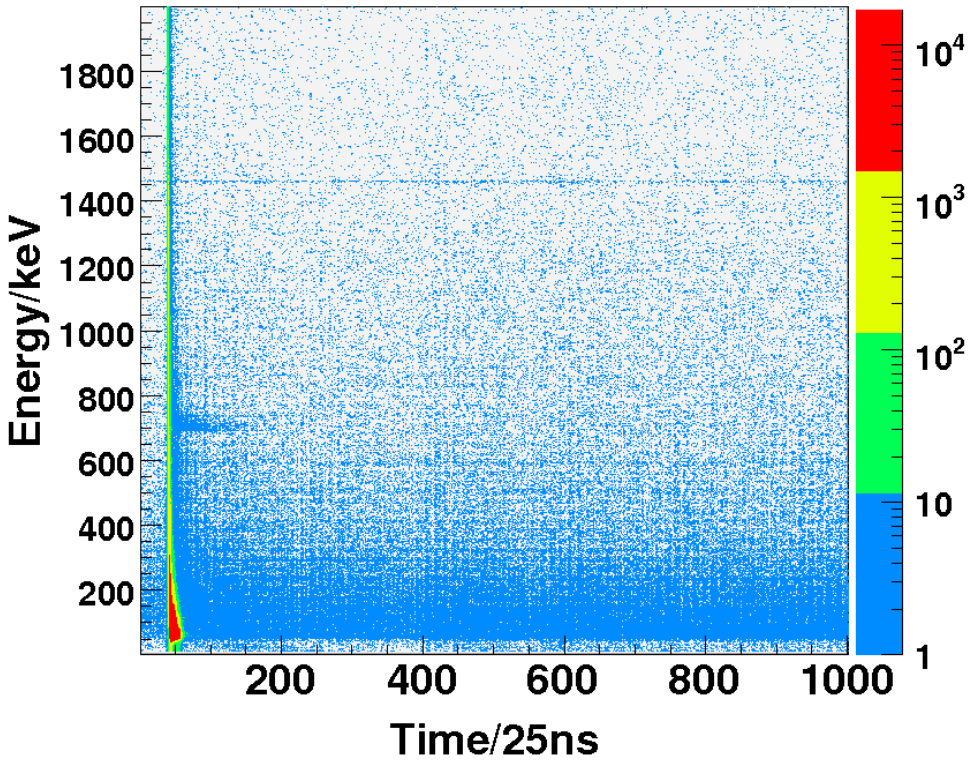

Figure 3.16: Energy-time matrix after gating to reject reactions. The time walk effect is apparent at low energies. The 1460 keV ^{40}K line is clearly visible. The 'finger' around 690 keV is due to (n,n') inelastic scattering in the HPGe detectors. Other 'fingers' are due to isomers in the nuclei populated in this experiment.

3.3.6 Si detectors

Three DSSSDs (Double-Sided Silicon Strip Detectors), cf. Fig. 3.18, were used in the active stopper experiments analysed here. The detectors were Micron Semiconductor Ltd. Model W1(DS)-1000 DC-coupled double-sided silicon strip detectors, measuring 5 cm x 5 cm each, and of thickness 1 mm. This thickness allows efficient implantation of the heavy ions. However, typical β-electron ranges are larger than 1 mm, giving a high probability that these electrons will escape, depositing only a fraction of their energy. The deposited energy depends on the implantation depth; Geant 4 simulations, shown in Fig. 3.17, indicate that implantation in the middle of the strip (i.e. 0.5 mm below the surface) ensures the greatest efficiency, hence accurate implantation by depth is essential, implying operation of the FRS in monochromatic mode, cf. Section 3.2.2.

The DSSSDs have 16 strips at the front and 16 at the back, each of width 3 mm, sufficient to allow detection of β electrons provided that implantation occurs at the correct (central) depth, i.e. 0.5 mm below the surface. The strips are arranged perpendicularly, allowing pixellation. Their purpose was twofold: to detect implantation of the ions of interest, and to detect the subsequent decay events, primarily due to beta electrons. The detectors were not placed in vacuum, nor cooled, but they were protected from light by being mounted within a 2 mm thick Pertinax box (phenolic-formaldehyde cellulose-paper PF CP 2061) with an entrance and exit window covered by a thin black Pocalon C foil of thickness 20 μm and also covered with thin Al foil.

The detectors were run at a bias voltage of 200V to obtain full depletion. A calibration spectrum, using ^{207}Bi, is shown in Fig. 3.19. The inferior resolution of these detectors compared to cooled HPGe detectors is noticeable; peak fitting to the conversion electron peaks by the author yielded FWHM of 18 keV at 482 keV, and 26 keV at 1048 keV.

3.4 Electronics

The event trigger for the passive stopper experiment was from Sci41. For the active stopper experiments two triggers were used: an implantation trigger, using scintillator

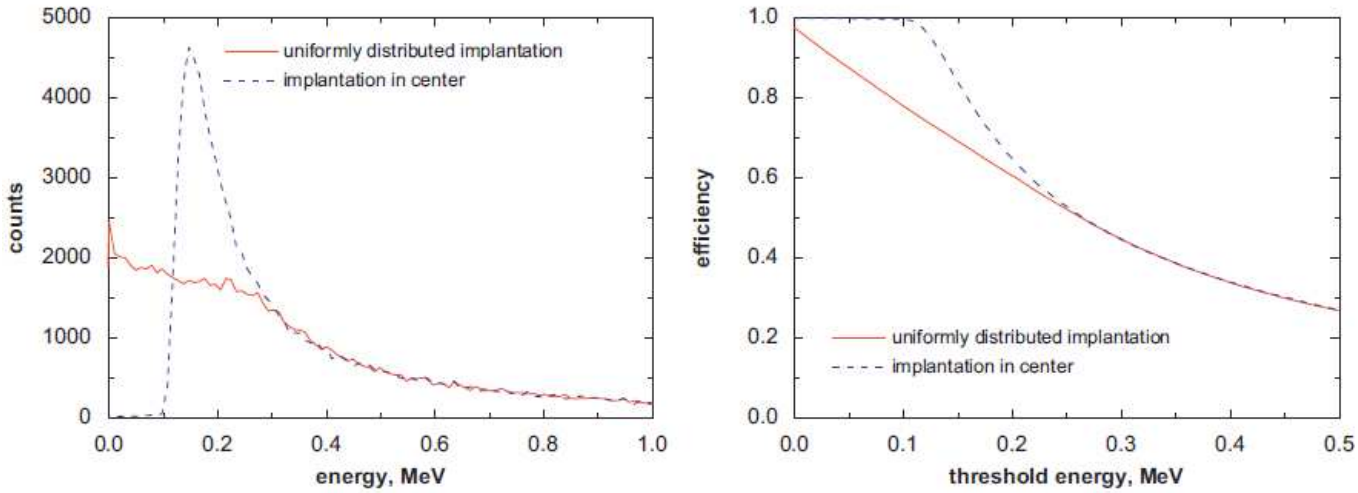

Figure 3.17: Simulated energy spectrum of β electrons emitted from fragments implanted uniformly (solid line), and exactly in the centre (dashed line), of a DSSSD(left). The simulation assumes a Q_β value of 5 MeV with a Fermi-Kurie distribution. The right figure shows the calculated β-detection efficiency as a function of the DSSSD threshold (taken from [68]).

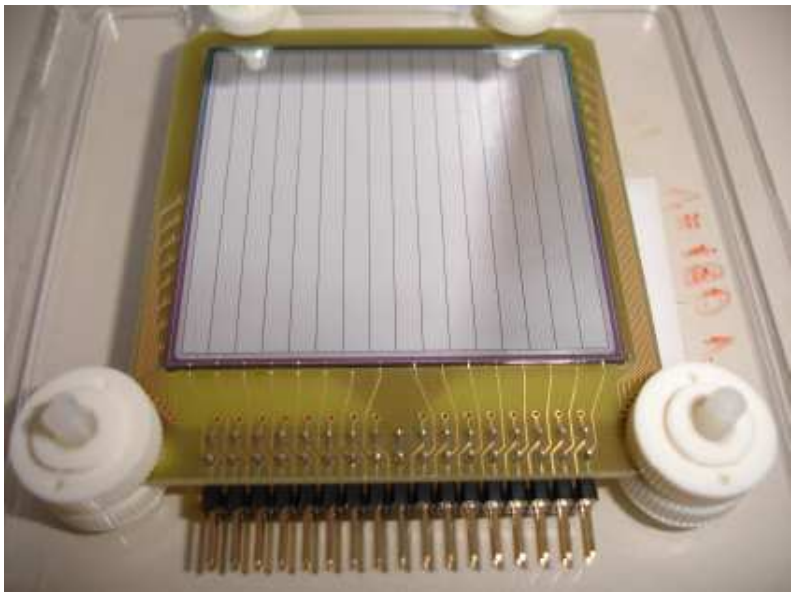

Figure 3.18: Photo of DSSSD.

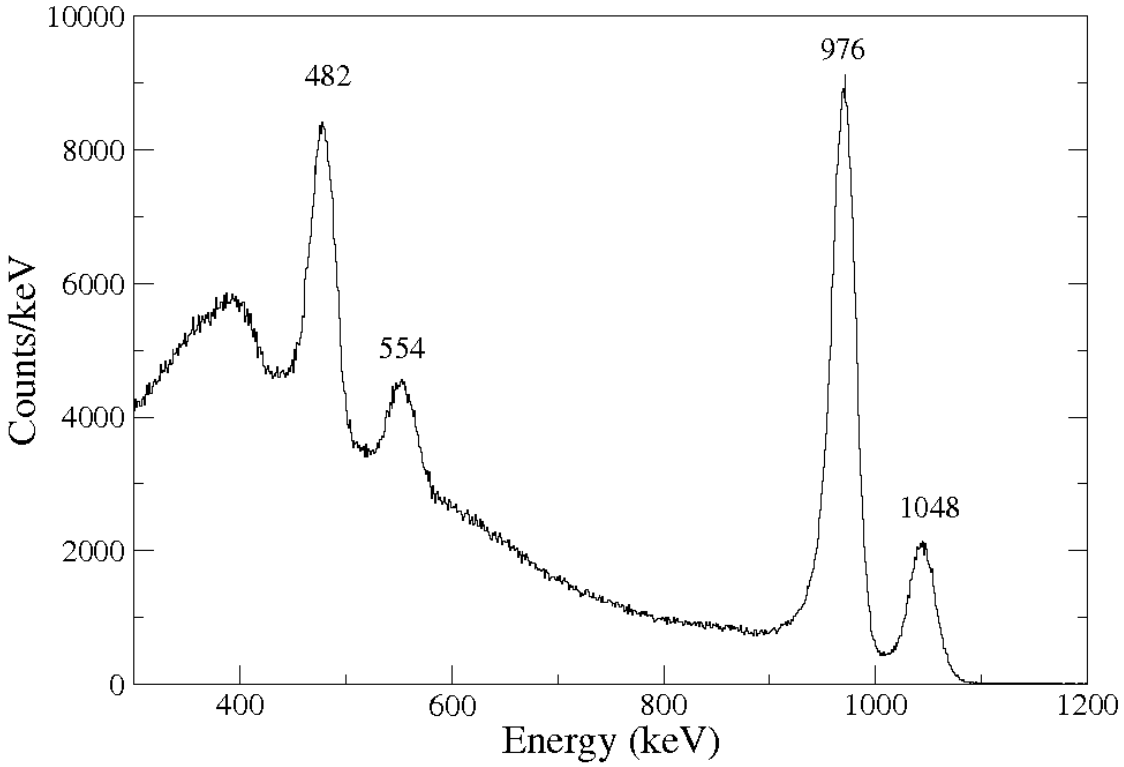

Figure 3.19: Calibration spectrum for DSSSDs using ^{207}Bi conversion electrons.

Sci41, and a decay trigger defined as the presence of a signal from the DSSSDs coincident with no signal from Sci41.

Each Ge detector had two parallel preamplifier outputs sent to two separate branches of the data acquisition. One was for analogue timing (TFA-CFD-TDC) with two types of TDC: one for short-range times: 1.2 μs full-range, 0.293 ns/ch; one for long-range times: 800 μs full-range, 0.763 ns/ch. The other branch was fully digital, providing the input signal for 105 channels within 30 DGF (Digital Gamma Finder) modules, described in Section 3.4.1.

3.4.1 Digital Gamma Finders

Digital Gamma Finders (DGFs) of type DGF-4C produced by XIA electronics [69] were used to digitize, shape and process the signals from the preamplifiers of the HPGe crystals, enabling both the energies and times of signals from the crystals to be recorded efficiently. The DGF-4C is a CAMAC module with four input channels. There are four functional

blocks:

- Analogue signal conditioning

  This adapts the input signals to the (built-in) ADC input voltage with suitable offsets and computer-controlled gain. The 14-bit ADCs digitize the waveform at 40MHz. An anti-aliasing filter is incorporated.

- Real-time processing units

  These consist of a field programmable gate array (FPGA) and FIFO. A pile-up inspector rejects pulses occurring within too short a time interval. Signals are processed at a high rate with digital (trapezoidal) filtering, thus acting as a shaping amplifier. Trapezoidal filtering with short time constants provides a local trigger, used for time-stamping and to feed the pileup inspector. The typical fast filter length of 0.1 μs reduces pile-up. The maximum gate achievable is around 400 μs. A digital copy of the pulse can be buffered into a memory. In the setup at GSI, the individual DGF channel triggers were validated by a master trigger signal generated from scintillator Sci41. This signal provided an internal check of the synchronisation of the DGF clocks and also gave a time-difference measurement between the arrival of an ion in the plastic scintillator and the measurement of a delayed gamma ray via the DGF time signal [66].

  The arrival time of gamma rays is found by comparing the output of the fast filter with an adjustable threshold. This starts a timing counter (dependent on the values of the two filter time constants and the rise time of the ADC pulses) to enable sampling of the output from the slow filter (with long, adjustable time constants), used for the energy measurement. This is shown in Fig. 3.20.

- Digital signal processor (DSP)

  After more complex filtering, if necessary, the DSP formats time/amplitude and waveform data, writes them into a buffer, and increments spectra in its histogram memory. Data is stored in 16 kB output buffers, read-out being triggered by the module which first reports its buffer to be full. Input digitization is inhibited during

readout to avoid electronic interference.

- PCI interface

  Further details of the DGFs are given in [70, 71].

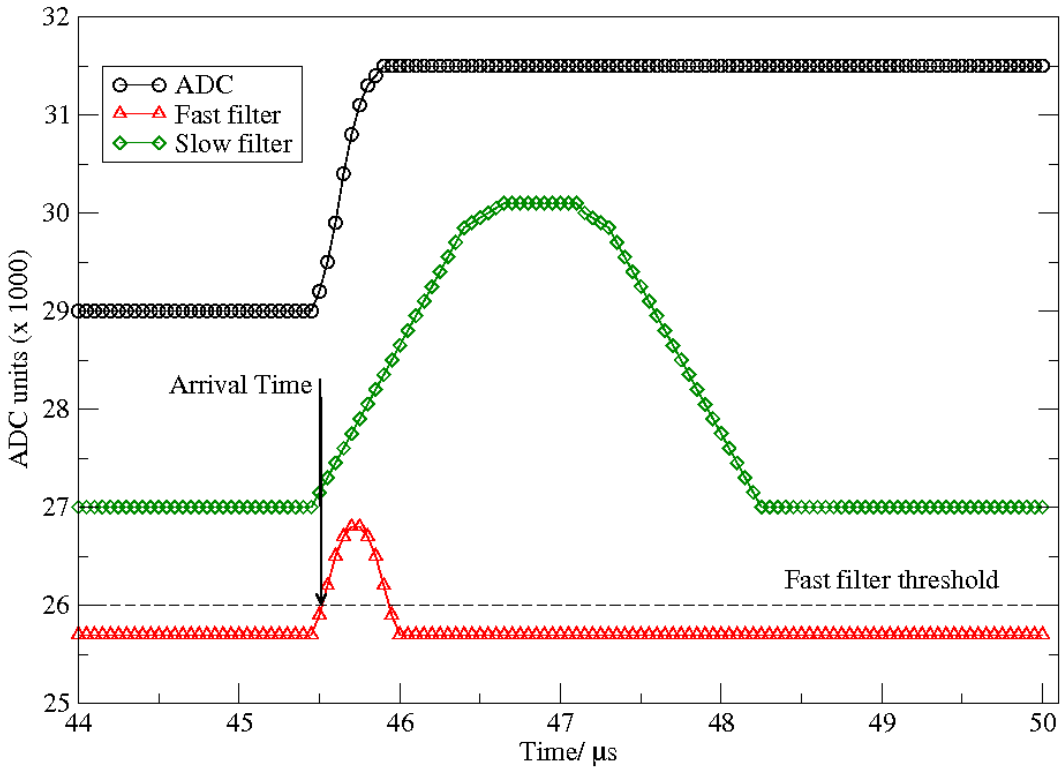

Figure 3.20: DGF pulse filtering and sampling (adapted from [70]).

3.4.2 Mesytec preamplifiers

Implantation of heavy ions involves the deposition of more than 1 GeV energy, followed by β-decay energies of around 1 MeV or less. In order to allow both implantation and decay events to be detected and discriminated correctly, Mesytec MPR-32 multi-channel preamplifiers were used in logarithmic mode. These have a linear range of 2.5 or 10 MeV, covering 70% of the total energy range, and a logarithmic range for the last 30% of the energy range, from 10 MeV to 3 GeV (calibrated using a pulser). Central implantation 0.5 mm below the surface of the Si layer corresponds to a minimum energy deposited by electrons of 0.1 MeV [68]. 150 keV was used as the low energy threshold.

Mesytec STM-16 (Shaping-Timing filter/discriminator Modules), controlled by a NIM-module, were used. A ^{207}Bi conversion electron source was used to calibrate the linear part of the amplifiers, yielding an energy resolution, after exposure to a heavy ion beam, of about 16 keV for the front side and 33 keV for the rear ohmic side at 976 keV [68].

Chapter 4

Analysis techniques

4.1 Particle Identification (PID)

Identification of the transmitted nuclides is carried out as follows:

1. Suppression of unwanted events, i.e. 'clean-up' of the data
2. Identification and selection of charge states
3. Identification of specific nuclides

4.1.1 Clean-up

In order to obtain 'clean' gamma (and beta) spectra correlated to the ions of interest, it is necessary to remove 'bad' events, i.e. those events that appear as correlated but in fact are due to reactions in the materials of the degraders, the MUSIC chambers, the stripping foils, etc. It is also necessary to remove those events in which the detectors did not give output signals that could be considered suitable for 'good' events. The clean-up procedure involved in the analyses presented here consists of:

- Selecting only those events in which there has been a suitable charge collection using the intermediate scintillator, Sci21. Although the beam is focussed at the intermediate focal plane, the ions of interest are not necessarily focussed at the centre, thus scintillations may occur preferentially on one side, as shown in Fig. 4.1.

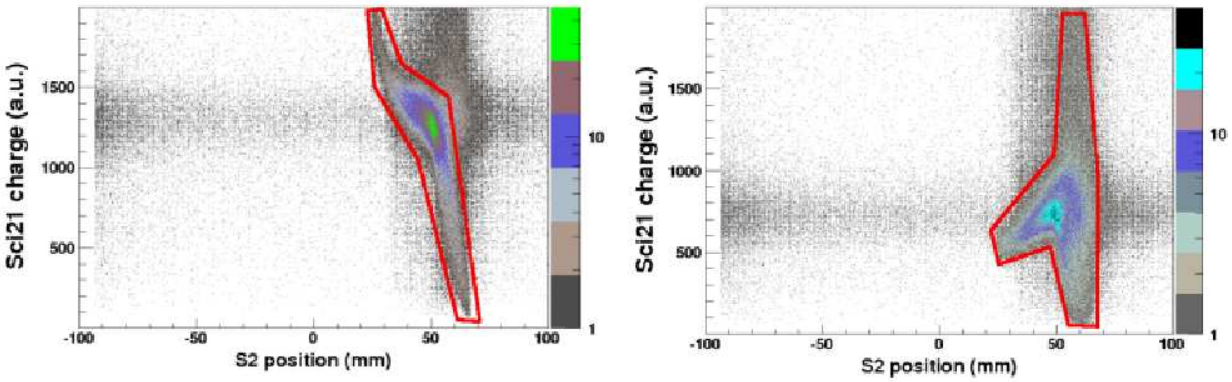

Figure 4.1: Collected charge vs. horizontal position from Scintillator Sci21 with gates showing selected 'good' events a) using left PMT, b) using right PMT.

'Good' charge collection at this scintillator, using both left and right photomultiplier tubes, is defined by the gates shown in the figure. This is essential for time-of-flight calculations. In the set of experiments of which the ^{192}W setting formed part, there was a problem with the timing output from the right PMT of scintillator Sci21, cf. Fig. 4.1, so the time-of-flight was determined from the left PMT outputs of this scintillator and scintillator Sci41 only, applying an appropriate correction.

- Selecting only those events in which the multiwire proportional counters fire correctly for the ions being considered. The 'bad' events are due to the detection of lighter ions formed in reactions in the intermediate degrader, and also from multiple firing. The 'good' events are shown between the vertical lines in Fig. 4.2.

- Selecting only those events in which there is a correct correlation between MUSIC 41 (before the final degrader) and scintillator Sci42 (after the final degrader, cf. Fig 3.4). This 'gate' is shown in Fig. 4.3. Events with the lower Sci42 energies consist of both lighter fragments from the beam and reaction products formed in the final degrader. Here, 'bad' events are those in which the energy losses in MUSIC 41 indicate that these events correspond to the ions in the region of interest but whose Sci42 energy losses are too low, indicating that these are reaction products.

- Selecting only those events in which there is a correct positive correlation between

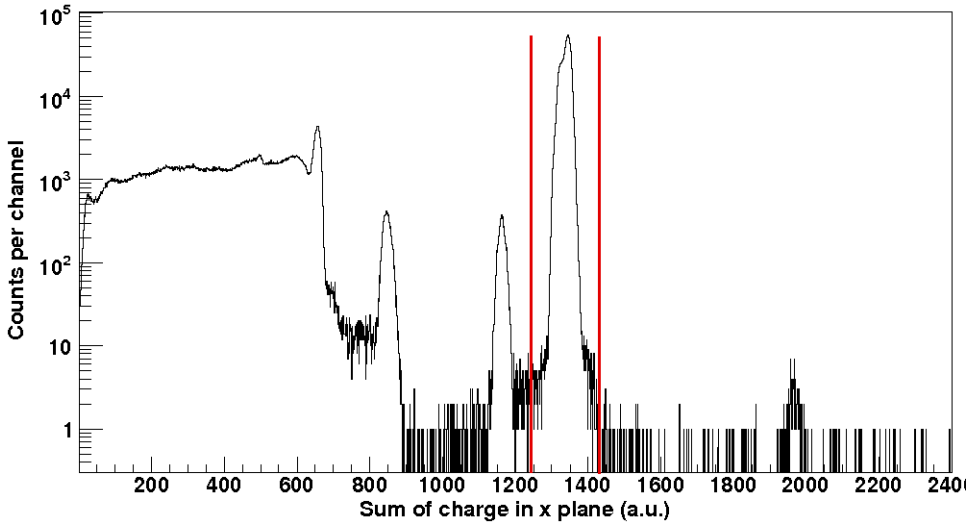

Figure 4.2: Sum charge collection in the horizontal plane of multiwire MW41. Data outside the red lines in removed in the off-line analysis. This is also done for the vertical plane of MW41 and for both planes of MW42.

MUSIC 41 and MUSIC 42. This 'gate' is shown in Fig. 4.5. 'Bad' events here are those in which ions react in the gas of the first MUSIC chamber, or in the Nb stripper foil between MUSIC 41 and MUSIC 42. These bad events will be ones in which there is a different energy loss in the second MUSIC chamber due to the reaction in the first, thus they will lie off the diagonal line of correlation.

- Excluding any events detected by the veto detector, scintillator Sci43, behind the stopper, cf. Fig. 4.4. This suppresses events in which fragments have been destroyed in the slowing down process as well as those which were not stopped in the catcher (about 2% of all ions produced are detected at Sci43). The secondary beam is tuned, using the final degrader, so that the ions stop in the stopper, but lighter reaction or fission products travel further (since they have lower Z, cf. Equation (3.4)) and thus reach the veto detector. Most of these products will have been created in the final degrader or in the stopper itself. A pulser is used to ensure that this scintillator is functioning correctly, giving the sharp initial peak in the energy spectrum for this scintillator, but all other events (i.e. those of higher energy) are vetoed.

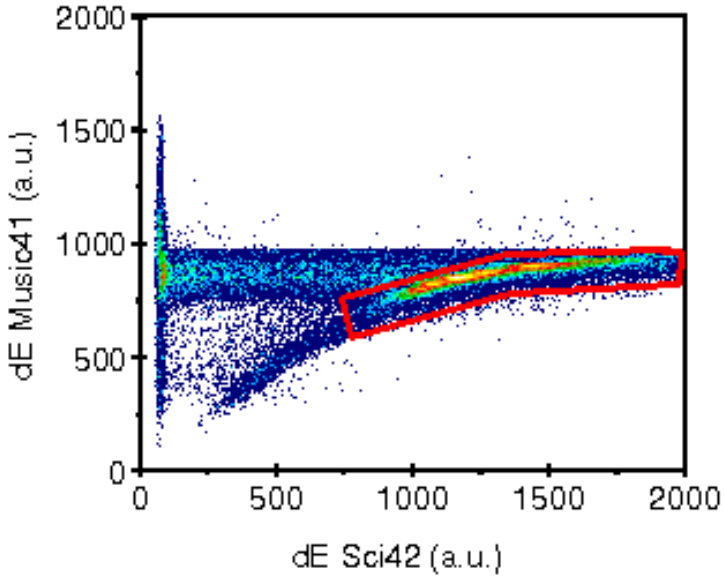

Figure 4.3: Plot of energy loss in MUSIC 41 vs. energy loss in Sci42 (arbitrary units). The gate for 'good' events is shown.

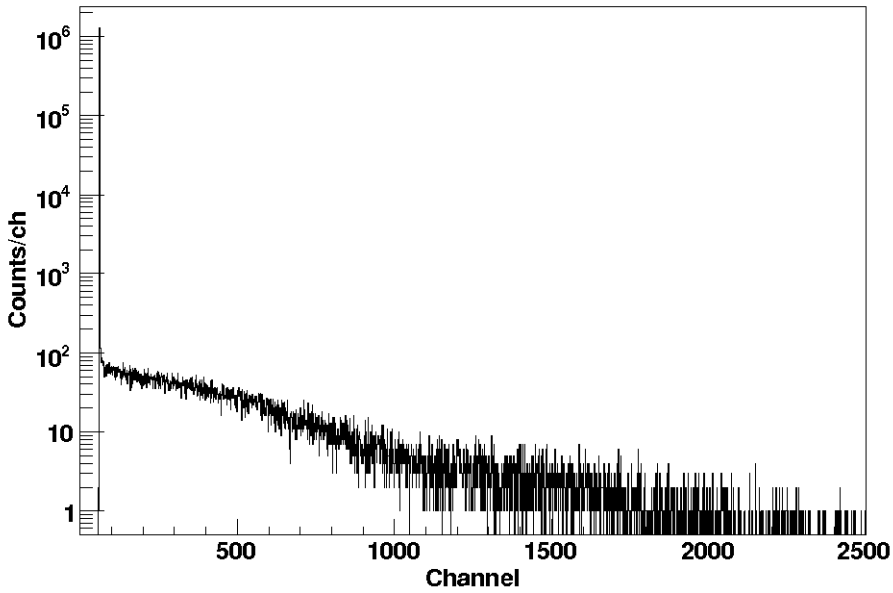

Figure 4.4: Scintillator Sci43 energy loss spectrum. The vertical line (at channels 58-62) is from the pulser.

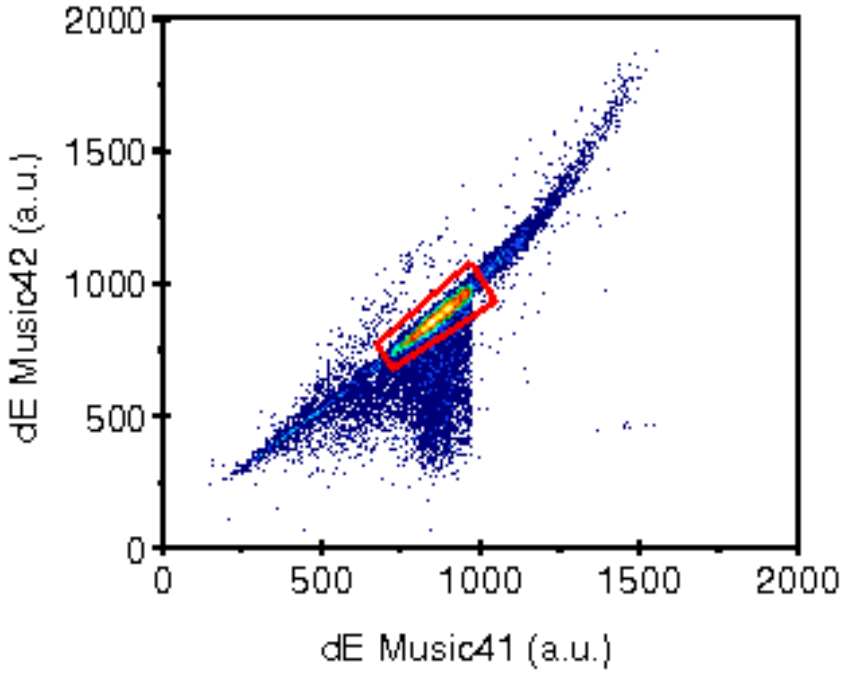

Figure 4.5: Energy loss in MUSIC 42 vs. energy loss in MUSIC 41, with gate for 'good' events.

Additional clean-up conditions for the active stopper experiments

In addition to the clean-up conditions described above, extra conditions are applied for the active stopper experiments:

- **Scintillator Sci42**

  Events detected by Sci42 (after the final degrader) after the decay trigger has 'fired' are vetoed, i.e. when there is essentially no beam but electrons are detected in the DSSSDs. These events may be due to the delayed arrival of lighter ions, etc., following reactions, chiefly in the degraders. There are few such events detected above the threshold of this scintillator, cf. Fig. 4.6.

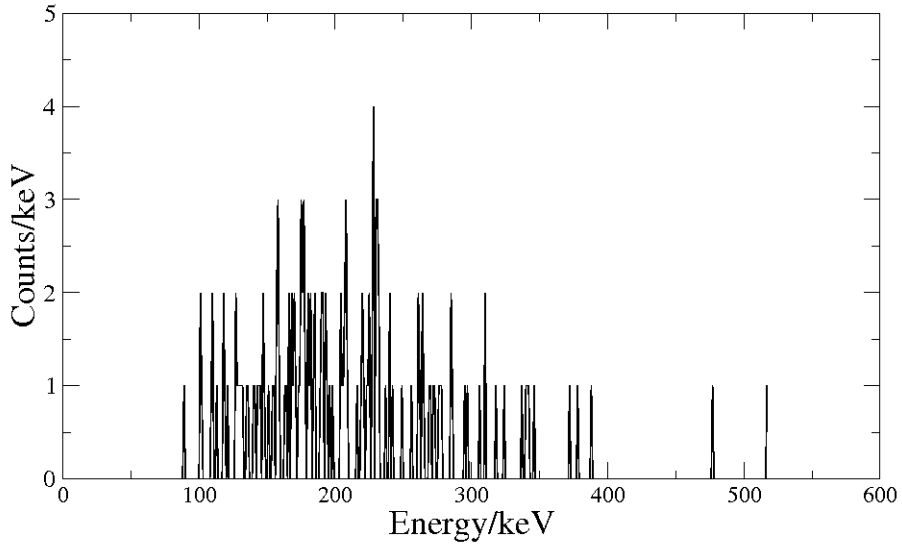

Figure 4.6: Energy spectrum from scintillator Sci42 following the decay trigger. This is used as a veto during decay.

- **Scintillator Sci43**

  Sci43 is used as a veto detector both for implantation and decay events. Beta (and delta) electrons produced in the DSSSD detectors can move through air, reaching this scintillator (a 1 MeV electron has a range of about 400 cm in air [72] and the distance between the active stopper box and scintillator Sci43 is about 58 cm). Although initially all such events were vetoed on the basis that these electrons

will obviously not have deposited their full energy in the DSSSDs, it was later realised that these electrons are not necessarily those from correlated events in the DSSSDs. A comparison of the spectra from Sci43 for implantation and decay, shown in Fig. 4.7, reveals that the events to be rejected are the higher energy events during implantation, corresponding to the lighter fragments depositing their energy in the scintillator. The lower portion of the spectra, beyond the pulser signals (shown in Fig. 4.8), is characteristic of beta electrons and thus should not be vetoed.

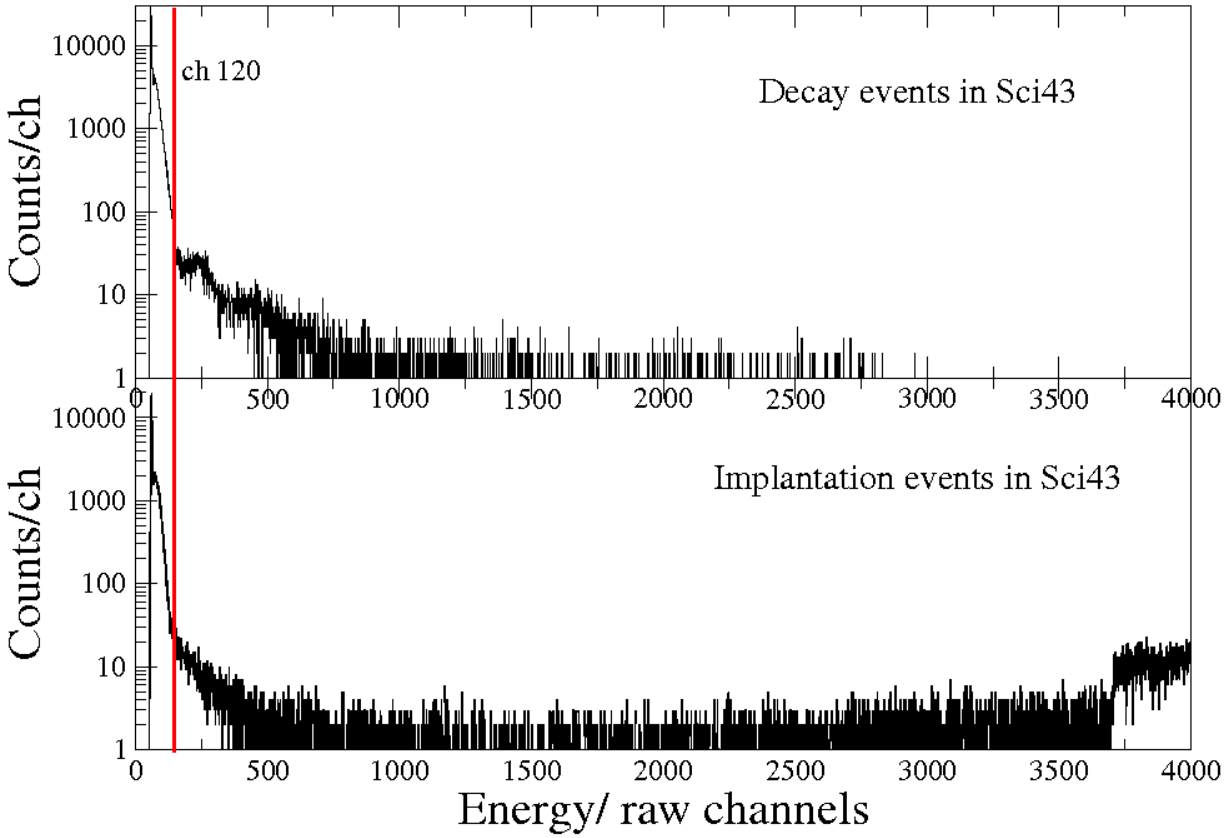

Figure 4.7: Energy spectrum from scintillator Sci43 following a) the implantation trigger (bottom), b) the decay trigger (top). Channel 120 marks the threshold chosen for vetoing events.

The results presented below for the ^{203}Au setting are from the initial analysis, i.e. all events beyond the pulser in Sci43 are vetoed, thus reducing the statistics somewhat. However, an initial analysis of the γ-γ coincidence spectrum and the beta electron spectrum for ^{203}Au obtained by vetoing only events beyond channel 120 yielded no new peaks, thus the conclusions and discussion concerning the ^{203}Au setting are

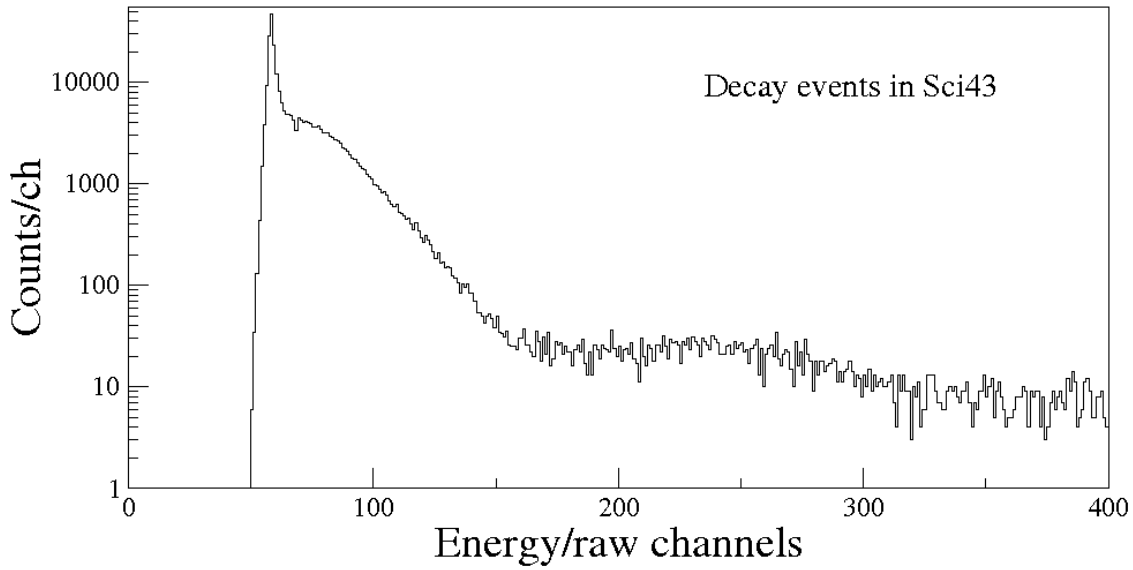

Figure 4.8: Energy spectrum from scintillator Sci43 following the decay trigger, showing the pulser signals followed by a typical beta continuum up to approximately channel 120.

unaffected. The results presented below for the ^{205}Au setting, however, use channel 120 in Sci43 as the veto threshold.

A similar spectrum for decay events in Sci43 is obtained by gating backwards from 'good' events, i.e. after rejecting 'bad' events using the reactions gates for Sci42 and for the two MUSIC chambers described above, thus confirming the interpretation that the lower energy events (below channel 120, approximately) are due to beta and delta electrons rather than light fragments.

- **DSSSD energies**

  The spectrum for the average of the energies for all the strips in the DSSSDs is shown in Fig. 4.9. It is here assumed that light particles/fragments passing through the DSSSDs are responsible for the second 'peak' around 1500 keV. Although this region will include β electrons with these higher energies, use of this part of the DSSSD decay energy spectrum would involve the possible contamination of events involving β decay with those resulting from light particles/fragments, so events with energies above 1300 keV in the DSSSDs were rejected.

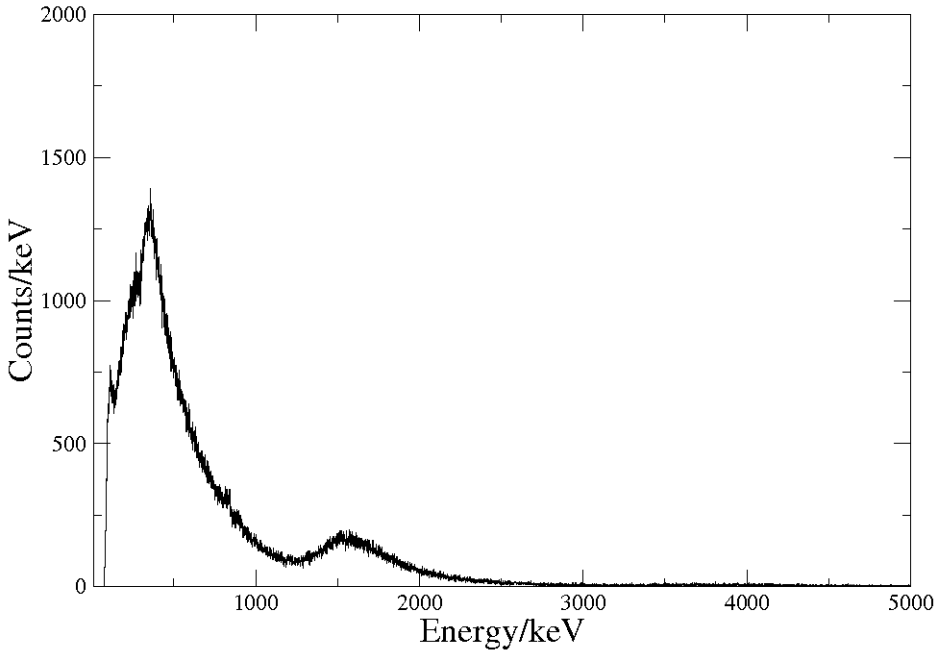

Figure 4.9: Decay energy spectrum for DSSSDs showing a second peak around 1500 keV due to light particles. Decay events with energies greater than 1300 keV were vetoed.

4.1.2 Charge states

As mentioned in Section 3.2.2, although most of the ions enter the FRS fully stripped of electrons, the ions may pick up one or more electrons, although the probability of acquiring each extra electron decreases rapidly. Niobium foils are used to strip electrons from the transmitted ions. If the magnetic rigidity of a low-probability charge state is within the Bρ acceptance, its intensity is very much reduced by using stripper foils in the intermediate focal plane.

To avoid mixing different charge states of different nuclei with the same A/Q, the charge states have to be identified before the nuclides themselves can be identified unambiguously. This is achieved by plotting a measure of the energy loss through the degrader in the intermediate focal plane (S2) against the energy loss in one of the MUSICs. The calculated energy loss through the wedge degrader, described below, depends on the charge state of each ion, whereas the energy loss in the MUSIC chambers is related to the atomic number of each ion, cf. Section 3.3.4, irrespective of charge state. This means that different charge states for the same element will appear in different positions on such

a plot. Fig. 4.10 shows such a plot for the ^{192}W passive stopper setting.

The energy loss through the intermediate degrader is calculated from the difference in the values of γ, the Lorentz factor, between the two halves of the FRS for ions of a given A/Q. Since the kinetic energy of an ion is: $T = (\gamma - 1)mc^2 = (\gamma - 1)Auc^2$, this implies that the energy loss through the degrader is:

$$\Delta T = \Delta\gamma Auc^2 \tag{4.1}$$

Now (cf. Equation (3.2))

$$\beta\gamma = \frac{B\rho eQ}{Auc} \Rightarrow \beta^2\gamma^2 \propto \frac{(B\rho)^2}{(A/Q)^2} \tag{4.2}$$

but $\beta^2\gamma^2 \equiv \gamma^2 - 1$, thus

$$\gamma \propto \sqrt{1 + k\frac{(B\rho)^2}{(A/Q)^2}} \tag{4.3}$$

where k is the constant of proportionality involved in Equation (4.2).

The γ factor for ions in the second half of the FRS can be determined directly from the time-of-flight from S2 to S4 (see Section 3.3.2). Since the magnetic rigidities are known, A/Q can then be determined from Equation (3.2) and, since A/Q for the ion in question is now known, we can use Equation (4.3) to determine γ for ions in the first half of the FRS and hence find the energy loss through the degrader from Equation (4.1).

For the ^{192}W setting, the two most populated regions of Fig. 4.10 correspond to ions that are fully stripped (42% of the total ions produced) and hydrogen-like (36%) at the S2 position. Strictly speaking, Fig. 4.10 indicates regions of *change* in the charge state, e.g. the $dQ = -1$ region refers to those ions which have acquired an electron, e.g. fully-stripped to H-like, H-like to He-like, etc. This explains the (unlabelled) region below $dQ = 0$: these are ions which have lost an electron, mainly H-like ions that have become fully-stripped.

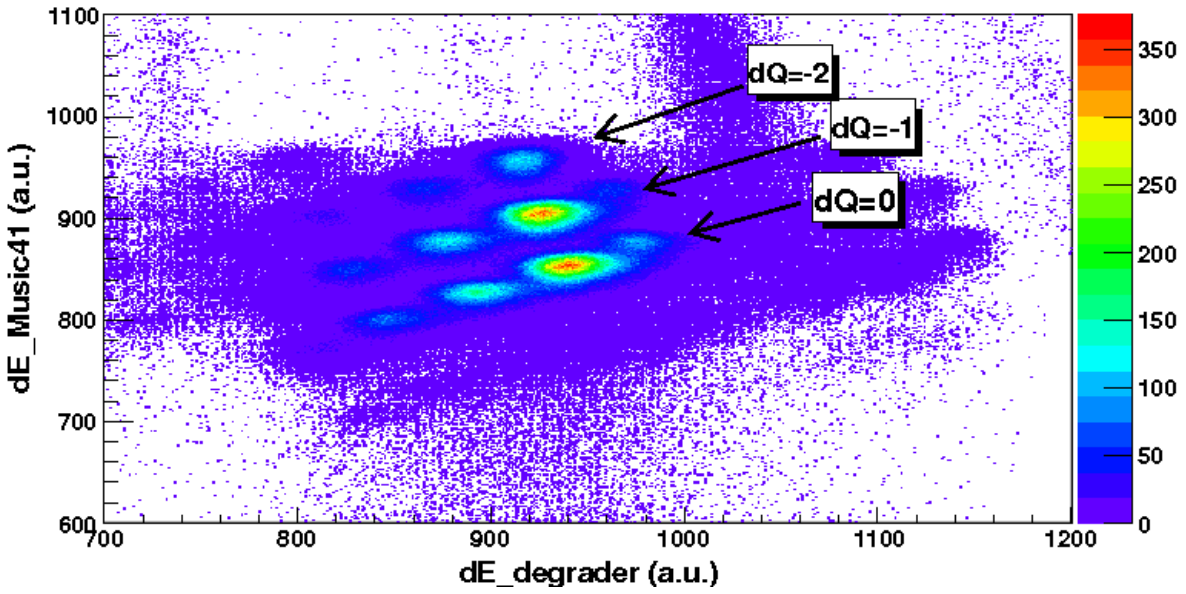

Figure 4.10: Charge states of ions for the ^{192}W setting. $dQ = 0$ refers primarily to fully-stripped ions, $dQ = -1$ to H-like ions, and $dQ = -2$ to He-like ions.

Charge state selection for the active stopper experiments

In the case of the active stopper experiments investigated here, the standard charge state plots, described in Section 4.1.2, viz. energy loss in the wedge degrader vs. energy loss in MUSIC 41 (or 42), were not sufficiently clear to enable the charge states to be identified, cf. Figs. 4.11 and 4.12. This was linked to the fact that the FRS setup for ^{203}Au and ^{205}Au used restrictive slits and had H-like ions in the first half but fully-stripped ions in the second half. A different algorithm based on the change in the *square* of the energy of the ion before and after the intermediate degrader gave a better separation for the ^{203}Au setting (cf. Fig. 4.13), though not for the ^{205}Au setting (cf. Fig. 4.14), so charge state selection was not performed for the latter.

This revised algorithm enhances the differences in energy losses, giving a value proportional to the square of the energy loss:

$$E^2 = p^2c^2 + (m_0c^2)^2 \Rightarrow \Delta E^2 = \Delta(p^2)c^2 \tag{4.4}$$

For a specific nuclide, Equation (3.2) implies that $\Delta E^2 \propto \Delta(B\rho)^2$, so the difference in the

squares of the average magnetic rigidities before and after the wedge degrader was used to estimate ΔE^2.

The improved charge state plot for the ^{203}Au setting, shown in Fig. 4.13, enables charge state separation to be carried out: gates for $dQ = 1$, i.e. H-like ions in the first half of the FRS but fully stripped in the second half, and $dQ = 0$, i.e. those fully stripped or H-like in both halves, are shown. Charge state probabilities for ^{205}Au and ^{203}Au are given in Table 4.1.

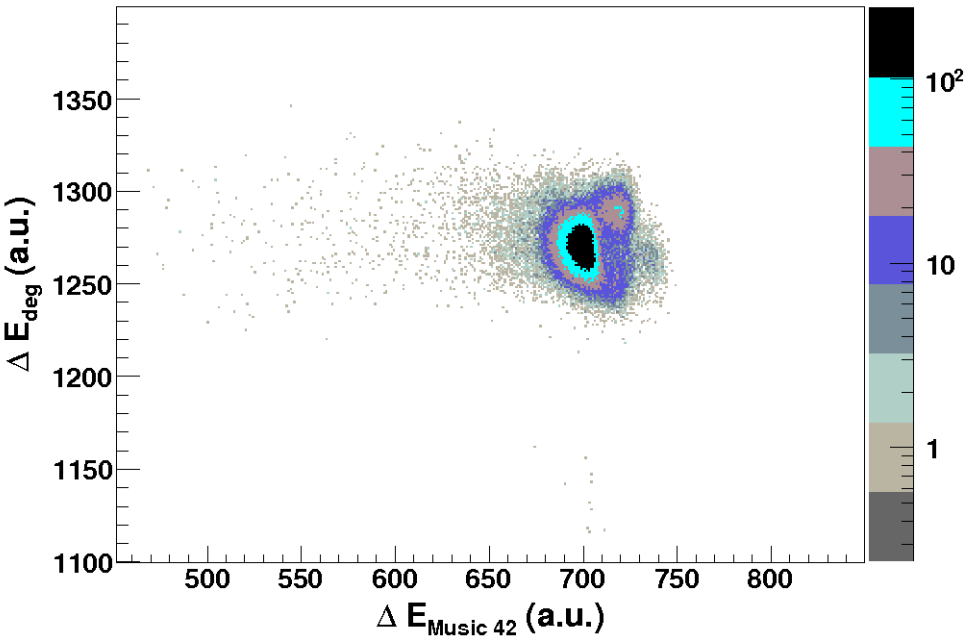

Figure 4.11: Standard charge state plot of ΔE_{deg} vs. $\Delta E_{MUSIC42}$ for ^{203}Au.

Having selected the charge state, particle identification can be carried out.

4.1.3 Nuclide identification

The principles of particle identification have been described in Section 3.2.2 above. For the active stopper settings the FRS is in monochromatic mode, so particle identification was carried out by using a plot of Z against time-of-flight, i.e. the Z value obtained from MUSIC 42 (after correcting the calibrated signal for velocity and position) vs. the time-of-flight in the second half of the FRS, as shown in Fig. 5.16. Preparatory calculations

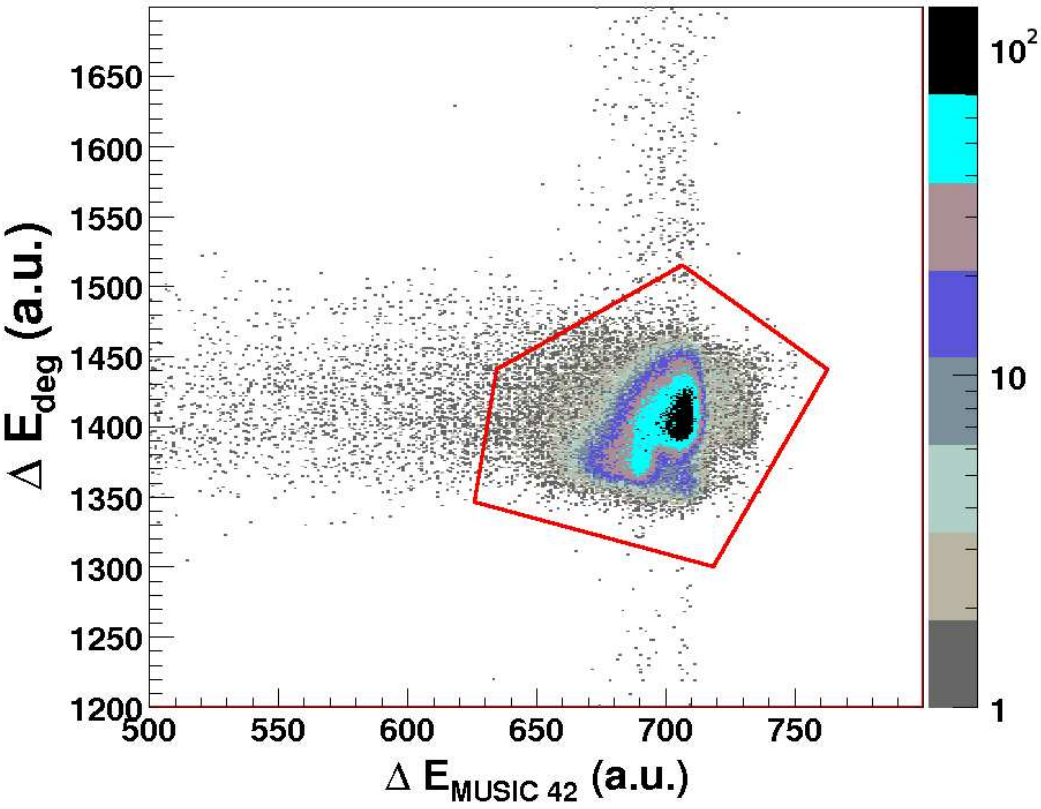

Figure 4.12: Standard charge state plot of ΔE_{deg} vs. $\Delta E_{MUSIC42}$ for ^{205}Au. The gate shown does not select charge states but merely excludes unwanted events.

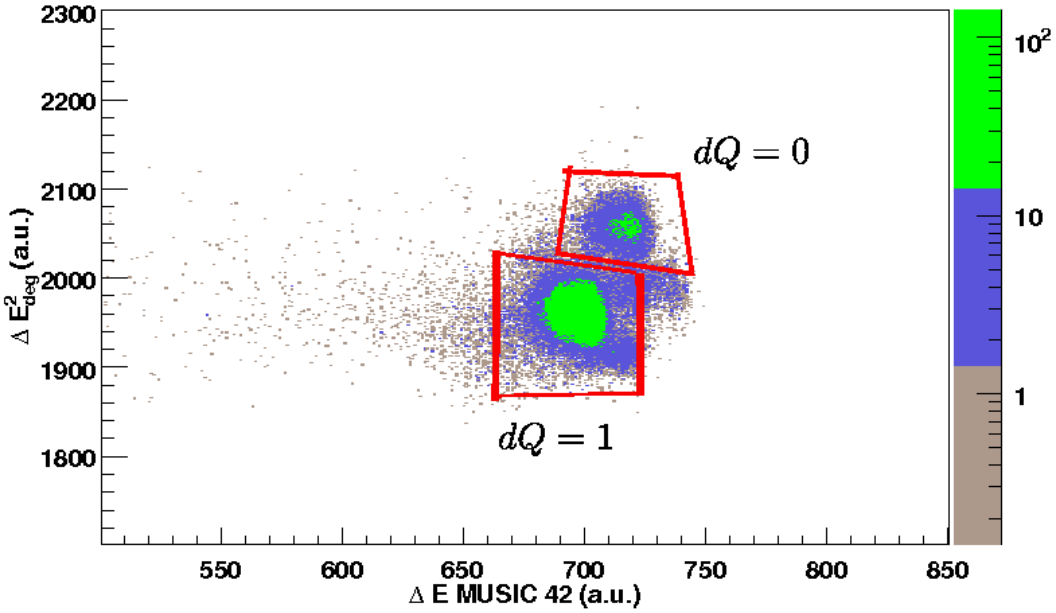

Figure 4.13: Charge state plot for ^{203}Au using ΔE^2. The $dQ = 1$ gate selects ions that are H-like in the first half of the FRS but fully stripped in the second half; the $dQ = 0$ gate selects ions that are fully stripped or H-like in both halves.

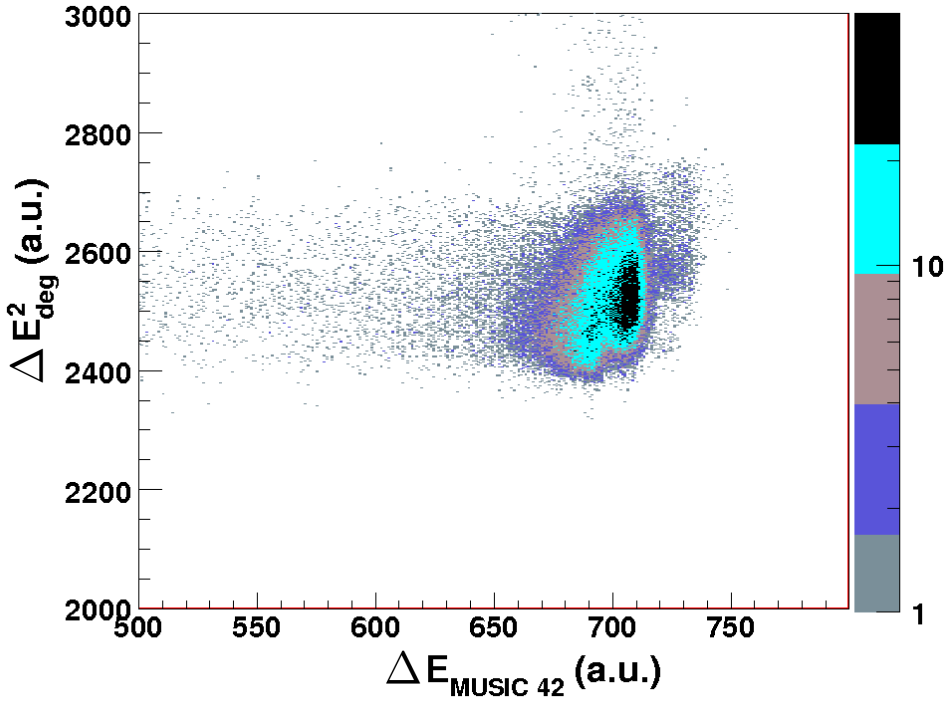

Figure 4.14: Charge state plot for ^{205}Au using ΔE^2.

Table 4.1: Cross sections and charge states after the Nb stripper behind the target. Charge state percentages were calculated using the code GLOBAL [73] and cross sections are from LISE simulations [57]. Bρ_1 refers to the average magnetic rigidity in the first half of the FRS and was calculated using the code MOCADI [74].

	Fully-stripped	**H-like**	**He-like**	**Li-like**
208Pb				
A/Q	2.537	2.568	2.600	2.633
Bρ_1 (Tm)	12.6685	12.8226	12.9860	13.1489
Percentage in charge state	91.5	8.34	0.203	2.84 x 10^{-4}
205Au				
A/Q	2.595	2.628	2.662	2.697
Bρ_1 (Tm)	13.1767			
σ (mb)	0.0108			
Percentage in charge state	93	6.54	0.122	1.30 x 10^{-4}
203Au				
A/Q	2.570	2.603	2.636	2.671
Bρ_1 (Tm)	13.0388			
σ (mb)	0.07			
Percentage in charge state	93	6.58	0.122	1.30 x 10^{-4}

for experimental runs use a Monte-Carlo code, MOCADI, specifically developed for the FRS at GSI.

The mass-to-charge ratio of the ions, A/Q, is determined from their time of flight and the magnetic rigidity from S2 (the intermediate focal plane) to S4 (the final focal plane). The time of flight is found by comparing the time signals from the scintillators at S2 and S4, thus giving the speed, v. In the case of the ^{192}W setting, the magnetic field strength, B, was 1.16 T and the dipole radius, ρ, 11.25 m, giving a magnetic rigidity, $B\rho$, of around 13 Tm. This is the magnetic rigidity for a central trajectory. The actual path taken by the nuclide of interest is determined by the positions (using the difference in times between signals from the PMT outputs of scintillators) at S2 and S4. This enables the true magnetic rigidity to be calculated [75]. The ions travel at around 85% of the speed of light, so relativistic corrections have to be applied. The magnetic rigidity for individual ions in the first half of the FRS is not measured, since there is no position detector at the target, but is calculated with the assumption that the beam is correctly focussed on the target at the centre of the beamline using Equation (4.5):

$$B\rho_1 = \left(1 - \frac{(x_{S2} - M_{12} \times 1)}{1000 \times D_{12}}\right)\left(\frac{B_1 + B_2}{2}\right)\left(\frac{\rho_1 + \rho_2}{2}\right) \tag{4.5}$$

The magnetic rigidity for ions in the second half of the FRS is given by Equation 4.6 using the horizontal position measurements given by the scintillators at S2 and S4.

$$B\rho_2 = \left(1 - \frac{(x_{S4} - M_{34} \times x_{S2})}{1000 \times D_{34}}\right)\left(\frac{B_3 + B_4}{2}\right)\left(\frac{\rho_3 + \rho_4}{2}\right) \tag{4.6}$$

In Equations (4.5) and (4.6), M_{12} and D_{12} are the magnification and dispersion factors, respectively, for the first stage of the FRS, i.e. dipoles 1 and 2, B_1 and B_2 their respective magnetic field strengths, and ρ_1 and ρ_2 their respective radii. The subscripts 3 and 4 refer to the corresponding dipoles. These values are given in Appendix A.

Having gated on the charge state, for achromatic mode the different nuclides are identified from a plot of longitudinal position at the final focal plane of the FRS (S4x) against A/Q, cf. Fig. 4.15. The longitudinal position, S4x, is calculated from signals given

by the multiwire proportional chamber just before S4, the final focal plane. Identification can be confirmed for nuclides in which there are known isomers. Once one such nuclide is positively identified, the others are determined by their (relative) positions on the S4x vs A/Q plot.

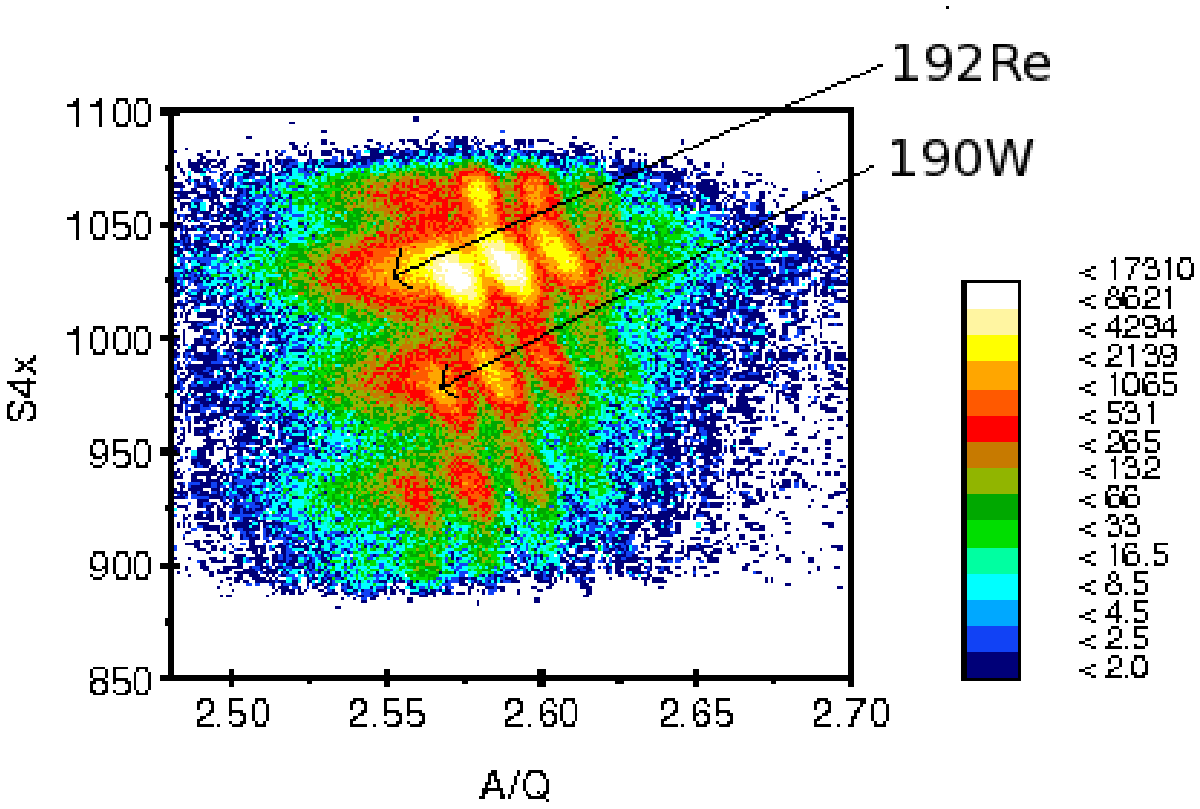

Figure 4.15: Particle Identification (PID) plot for fully stripped ions in the ^{192}W setting.

4.2 Identification of Isomeric States

Isomeric states are indicated by the horizontal lines or 'fingers' on the energy-time plots, cf. Fig. 4.16. The background gamma radiation at 1460 keV from the decay of ^{40}K to ^{40}Ar is clearly visible in all such spectra and, since it is very long-lived, may be used to normalise the intensities of the observed gamma transitions from different experimental runs. Since the time of flight through the FRS is approximately 230 ns, this setup permits the detection of isomeric decays with half-lives in the range of 100 ns to several hundred microseconds. Shorter lifetimes can also be detected if there exists a decay branch by

electron conversion, this branch being hindered due to the fact that the ions have no (or very few) atomic electrons [76].

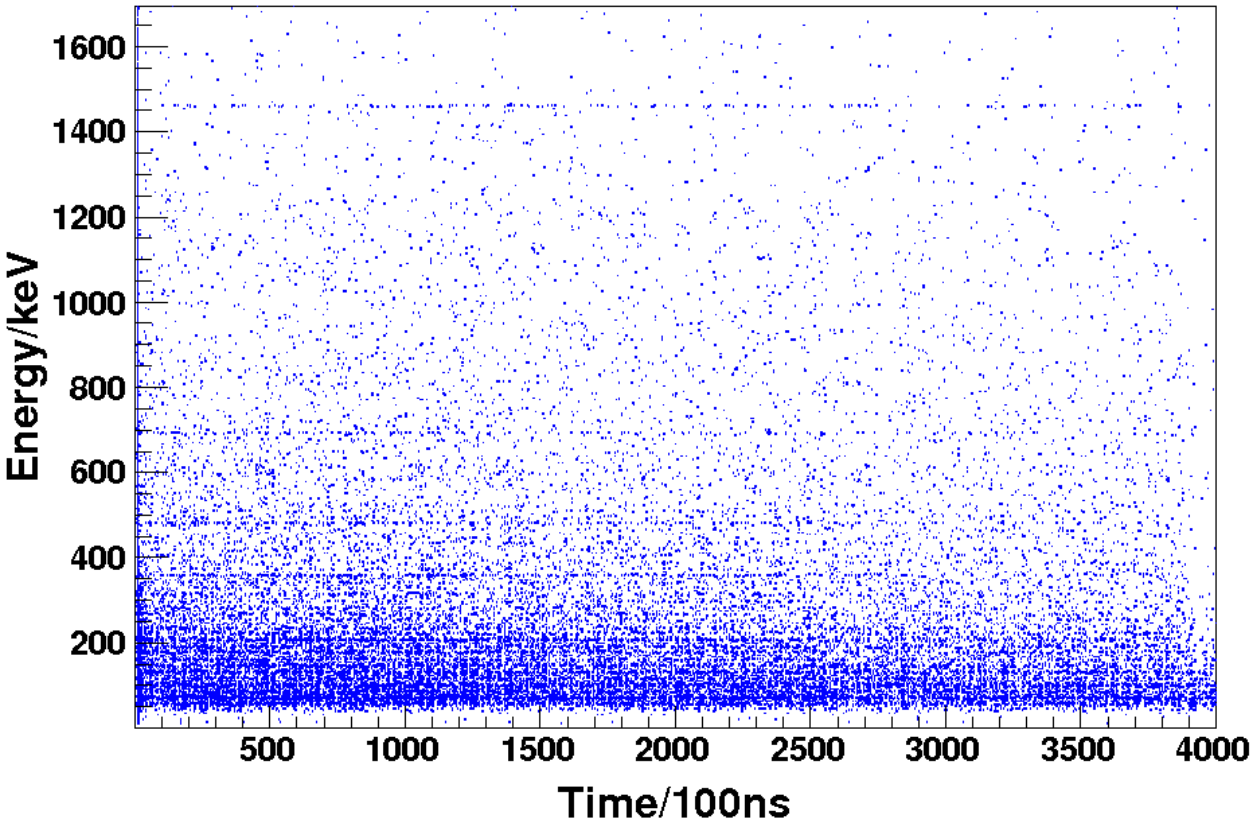

Figure 4.16: Energy-time matrix for ^{190}W for 0-400 μs after implantation. Horizontal 'fingers' indicate gamma decays from isomeric states.

4.3 Lifetime fitting

Half-lives for isomeric transitions are determined by slicing the relevant energy-time matrix for the energies required and projecting onto the time axis. Additional slices and projections are taken for energies below and above the transitions of interest to enable background subtraction to be carried out, normalising as required. If the statistics are sufficiently high, an exponential line of best fit can be obtained, weighting in inverse proportion to the squares of the vertical error bars, the latter being considered to be $\sqrt{N}$ where N is the number of counts (after subtracting background). A two parameter exponential fit, $N = N_0 \exp(-\lambda t)$, was used for the passive stopper experiment, except

where feeding of an isomeric state (as well as decay) was being investigated. Different time regions of the data to be fitted are chosen to ensure that the fit includes only the decay period under consideration. This is particularly important in the active stopper analysis (see Section 4.3.1).

4.3.1 Lifetime fitting for the active stopper experiments

As noted above, two-parameter exponential fits were used to obtain gamma lifetimes from the passive stopper experiment, but for the active stopper a three-parameter exponential fit was used:

$$N = N_0 \exp(-\lambda t) + c \tag{4.7}$$

where c is a constant determined for each time region selected for fitting. The justification for using a three-parameter fit is that there are false correlations between implantation and electron decay events in the DSSSDs. The algorithm for correlation is fairly crude, though effective (see Section 4.4.1). These false correlations will, of course, not decay with the same half-life as correctly correlated events. Equation (4.7) implies that there is a constant background, but analysis of time spectra with long implant-decay time correlation periods shows that this background decreases with time. In addition, the spill structure is visible on the gamma decay time spectra when gated on specific ions, cf. Fig. 4.17 top; a similar time spectrum is obtained for the conversion electrons. The lower part of Fig. 4.17 indicates that there is a considerable statistical variation of counts with time when gating on particular energies, thus the removal of data immediately after each spill is not necessary. Although various other types of fit were attempted to model this decreasing false correlation background, Equation (4.7) gives the best results, provided that the time region chosen is that for which the points (on a semi-log scale) show the typical simple exponential decay.

For beta lifetimes, if the gamma transitions to the ground state are known, one may gate on these gamma peaks and apply the three-parameter fit noted above. Alternatively, for conversion electrons, the peak-to-total ratio of their peaks can be used to normalise the time spectrum background before subtracting it. In this case, a two-parameter fit

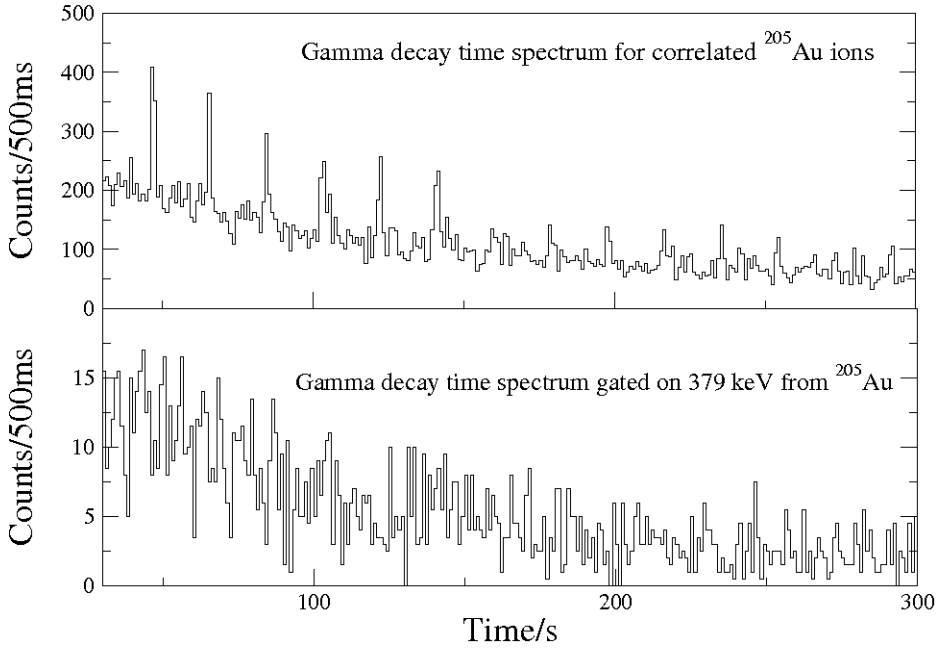

Figure 4.17: Time spectrum from the prompt gamma rays emitted during the beta decay of ^{205}Au ions using an implant-decay time correlation of 300 s. The spectrum at the top clearly shows the spill structure. The spectrum at the bottom is further gated on the 379 keV transition; the spill structure is less evident here.

may be applied, although it must be restricted to the time region of interest in order to reduce the influence of false correlations, and to remove or reduce the effect of the increase in counts during and immediately after a spill. In the case of ^{205}Au, with a spill period of approximately 10 s, the time region for fitting was chosen to be less than this since the half-life was evidently less than the spill period.

4.4 Production and Particle Identification for ^{203}Au and ^{205}Au

Table 4.1 indicates that the calculated magnetic rigidities of fully stripped ^{205}Au and ^{203}Au ions are very close to those of the primary beam, ^{208}Pb, in its He-like and Li-like charge states. Fig. 4.18 shows the yield of He-like ^{208}Pb ions, fully stripped ^{205}Au ions and H-like ^{205}Au ions against horizontal position just before the S1 slits. This clearly shows that the He-like ^{208}Pb ions contaminate the fully stripped ^{205}Au ions, the former being

about four orders of magnitude greater in yield than the latter at the focal position. The situation for ^{203}Au ions is similar.

The problem of contamination by He-like Pb ions was solved by choosing a magnetic rigidty and slit settings in the first half of the FRS to preferentially transmit H-like ^{205}Au ions.

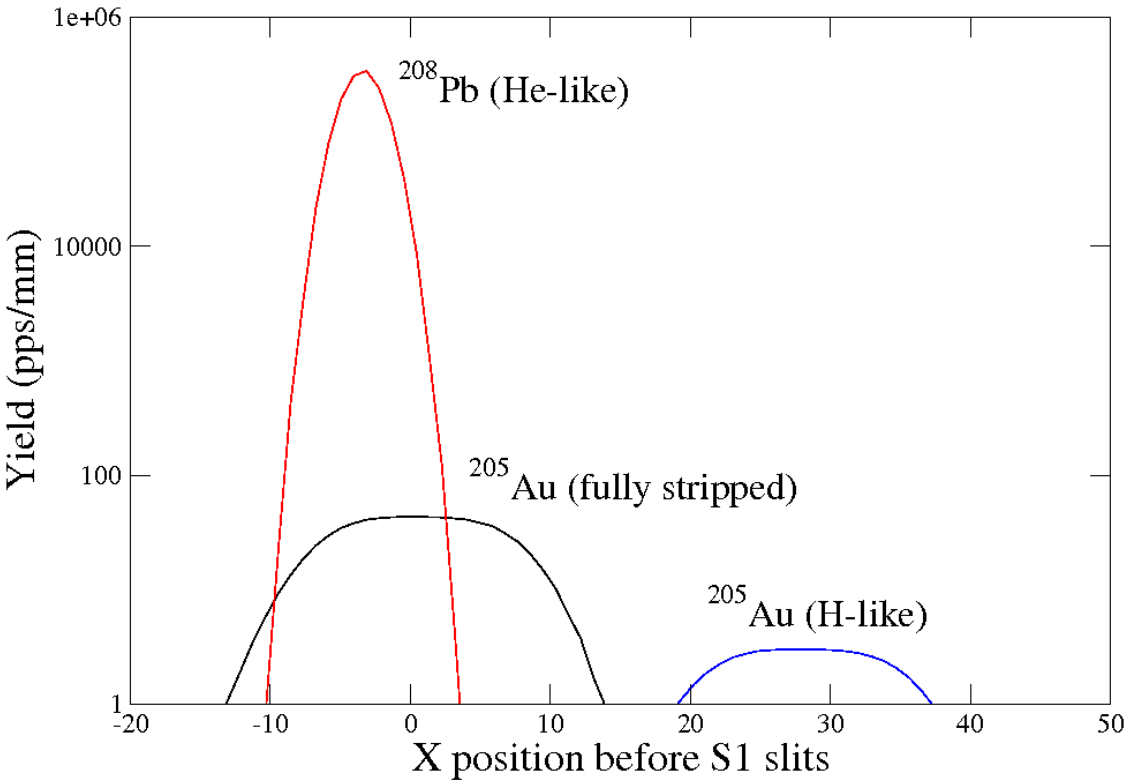

Figure 4.18: LISE simulation of the yield of He-like ^{208}Pb ions, fully stripped ^{205}Au ions and H-like ^{205}Au ions against horizontal position just before the S1 slits. The H-like ^{205}Au ions were selected by use of the slits, thus avoiding contamination of the ions of interest by the He-like ^{208}Pb ions. Note that LISE reverses the direction of x compared to the experimental setup.

4.4.1 Correlation of implanted ions with beta electrons

The DSSSDs, as explained in Section 3.3.6, give signals both on implantation of the ions and from electrons following implantation, primarily beta electrons. The horizontal and vertical strips that collect the greatest amount of charge enable the pixel in which the ion was implanted to be determined. A subsequent beta electron produced in the same

pixel within a time related to the known beta half-life for the implanted ion is considered to be due to decay of the implanted ion in that pixel. However, due to straggling of the electrons there is always a degree of uncertainty in assigning an electron detected in the same pixel as that in which implantation occurred as an electron from the beta decay of the implanted ion; it could be due to the decay of an ion implanted earlier in a neighbouring pixel. For this reason, the algorithm used in the sorting code was such that implanted ions were correlated with electrons detected in the same pixel or, failing such correlation, in the immediately neighbouring pixels of the same DSSSD, cf. Fig. 4.19, within the time gate assigned to the ion of interest. The results of matching, using this algorithm, can be seen in Fig. 4.20.

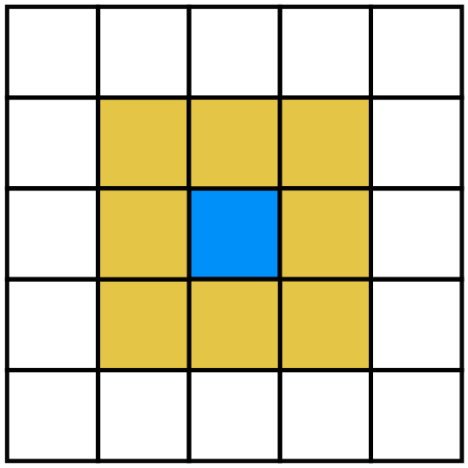

Figure 4.19: DSSSD pixels: Pixel with implanted ion in blue; decay events within the required implant-decay correlation time in the nearest neighbours are shown in brown.

Spectra from the DSSSDs show the characteristic continuous beta energies with a considerable degree of noise. The primary purpose of these spectra, however, was for the detection of conversion electrons. Therefore, the peak-to-background ratio for conversion electron peaks was enhanced by changing the implant-decay correlation time to be close to that of the half-life of the state from which they are produced.

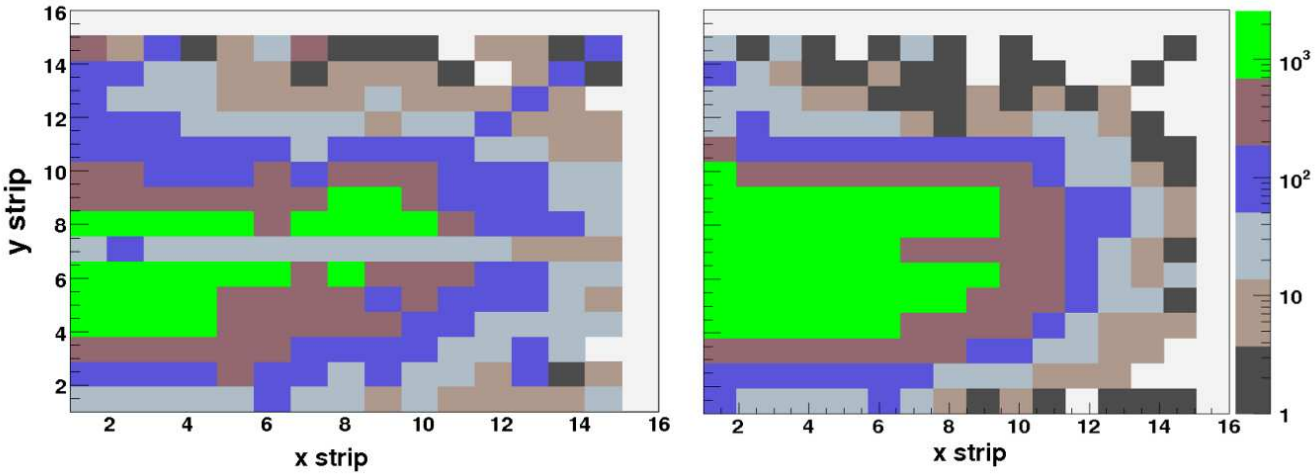

Figure 4.20: These diagrams show the intensity of events in each pixel of the main DSSSD used in this experiment. In the left diagram are shown implantation events; the right diagram shows decay events matched to the former using the algorithm described in the text.

4.4.2 Beta-delayed gamma spectra

The gamma spectra for the implanted ions here, as in the case of the passive stopper experiment, show gamma rays emitted immediately after implantation, thus (in addition to background) they show isomerically delayed gammas. However, the signals from the DSSSDs indicating the beta decay of the implanted ion are used as a trigger to enable the detection of the prompt gammas produced in such decay. This also confirms (or refutes) the prior identification of the implanted ions if the beta-delayed gamma energies are known.

Chapter 5

Results and Discussion

5.1 ^{190}W

5.1.1 Production and Identification of ^{190}W

In this experiment, a 1 GeV/u ^{208}Pb beam with average intensity 1 x 10^9 pps impinged on a Be target of thickness 2.446 mg/cm^2. The setting was for the production of ^{192}W and ran for about 40 hours. Magnetic rigidities and further details are given in Table A.1 in Appendix A. Analysis of the H-like and He-like charge states indicated that there were no ^{190}W ions present in these charge states. A total of about 20 000 ^{190}W ions (fully-stripped) were collected at a rate of approximately 8 per minute, of which about 1000 (calculated from the intensity of the 693 keV gamma transition) were implanted in the stopper in the isomeric state investigated below.

5.1.2 Gamma spectra

Singles

The γ-ray spectrum observed in delayed coincidence with ^{190}W ions, obtained using the DGFs with a time gate of 2-380 μs, is shown in Fig. 5.1. The intensities of the the 58 keV tungsten K_α X-ray and the four intense gamma peaks, corrected for efficiency and internal conversion, are given in Table 5.1. The intensities of the 357, 483 and 693 keV

gamma rays balance within one standard deviation, but it is evident that the intensities for the 58 keV X-ray and the 206 keV γ ray are higher than those of the other gamma transitions. The intensities relative to the highest intensity, that of the 206 keV transition, indicate that the 58 keV X-ray intensity is much greater than would be expected from internal conversion alone (internal conversion would give an intensity of 5(2)% relative to the 693 keV intensity). The (total) internal conversion coefficients, α_t have been calculated from B.R.I.C.C. [77], under the assumption that the gamma transitions are of multipolarity E2.

Table 5.1: Internal conversion coefficients and intensities for gamma transitions in ^{190}W, corrected for efficiency and internal conversion, relative to the highest intensity.

Energy (keV)	**Area**	$\alpha_\mathbf{t}$	**I**	**Rel. I**
58.8(28)	1513(246)	N/A	1513(246)	77(13)%
205.8(17)	1535(142)	0.279(6)	1963(182)	100(9)%
357.2(22)	1070(100)	0.0513(9)	1125(106)	57(5)%
484(1)	1213(117)	0.0229(4)	1240(120)	63(6)%
693.6(22)	1050(105)	0.00975(14)	1060(106)	54(5)%

$\gamma - \gamma$ coincidences

The high efficiency of the RISING array and the large number of ^{190}W nuclei allowed the determination of coincidence relationships between the observed γ rays. $\gamma-\gamma$ coincidences, gating on each of the transitions, are shown in Fig. 5.2. It is evident that the K_α X-ray and the four γ rays are in prompt ($\Delta t < 300\,ns$), mutual coincidence. A peak at 280 keV is visible in the 206 keV gated spectrum and is present (with low intensity) in the 357 and 693 keV gated spectra. Gating on this 280 keV peak to find prompt coincidences resulted in a poor spectrum due to low statistics, but the 206, 357 and 693 keV may be

in prompt coincidence with it. Some discussion of this is given in the concluding remarks of Section 5.1.4.

Short-lived isomer in ^{190}W

The energy-time matrix for fully-stripped ^{190}W ions, shown in Fig. 5.3 reveals the presence of intense X-rays at 58 and 68 keV. The horizontal 'fingers' on the matrix at these energies extend for only a short time, about 1 μs, indicating that there may be another isomer, much shorter in lifetime than the isomer which gives rise to the gamma transitions. The X-rays are quite distinct from the background and have energies in accordance with the characteristic K_α and K_β X-rays for tungsten. The 'fingers' are not a result of the time-walk effect (see Section 3.3.5). This is clear from Fig. 5.4, which shows the decay curve for energy channels corresponding to 58 keV, starting within the prompt flash (which at this energy has a duration of about 500 ns). This figure shows that immediately after the prompt flash there is a separate decay curve, corresponding to the 'fingers'. A short-lived ($\sim 1\,\mu$s) component of all the transitions was observed in the ^{190}W experiment reported by Lane *et al.* [78], indicating the existence of an isomer with this short lifetime. There also appear to be similarly short-lived transitions, leading to the same characteristic tungsten X-rays, in ^{191}W, cf. Figs. 5.5 and 5.6. Steer [79] investigated ^{191}W in an similar series of experimental runs at GSI and obtained a gamma spectrum similar to that shown in Fig. 5.6, with a strong gamma ray at 167 keV and intense characteristic tungsten X-rays. Steer was (also) unable to balance the intensities of the gamma and X-ray transitions, but he obtained a half-life of 0.36(2)μs. A short discussion of the short-lived intense X-rays in ^{190}W is given in Section 5.1.4.

Singles spectra for ^{190}W, gated 2 μs and 20 μs after the prompt flash, are shown in Fig. 5.7. This clearly shows the contribution to the X-ray intensities of the short-lived isomeric state. The raw counts for the K_α and K_β tungsten X-rays relative to the 357 keV gamma ray for these time gates is shown in Table 5.2, in which it is evident that the X-rays have a different (shorter) half-life than the gamma rays.

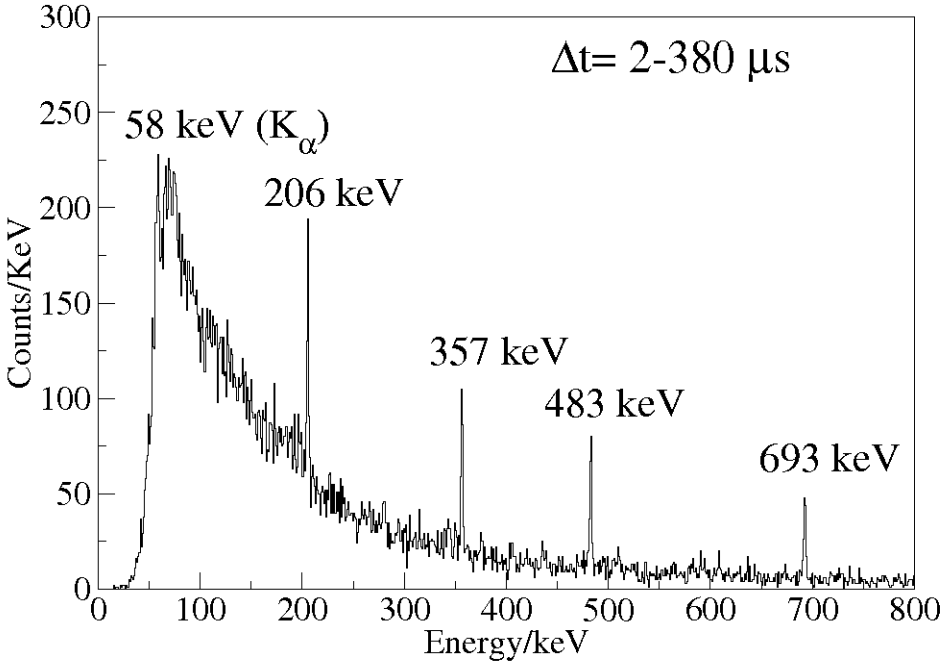

Figure 5.1: Delayed gamma spectrum for ^{190}W.

Table 5.2: Time-gated X-ray counts relative to the 357 keV gamma ray in ^{190}W. These show background-subtracted raw areas for X-ray and gamma peaks using two different time gates: 2 μs and 20 μs after the prompt flash.

Energy (keV)	**Area**	**Area rel. to 357 keV area**
X-rays within 2 μs		
58.1(2)	60(8)	12(9)
67.0(3)	39(7)	8(6)
206.0(4)	5(3)	1(1)
356.8(4)	5(3)	1(1)
483	absent	
693.0(1)	2(22)	0.4(464)
X-rays within 20 μs		
58.1(1)	99(11)	4.0(12)
67.0(2)	56(9)	2.2(8)
205.0(9)	18(6)	0.72(38)
357.2(2)	25(5)	1.0(4)
483.2(4)	16(5)	0.64(33)
693.4(5)	17(5)	0.68(34)

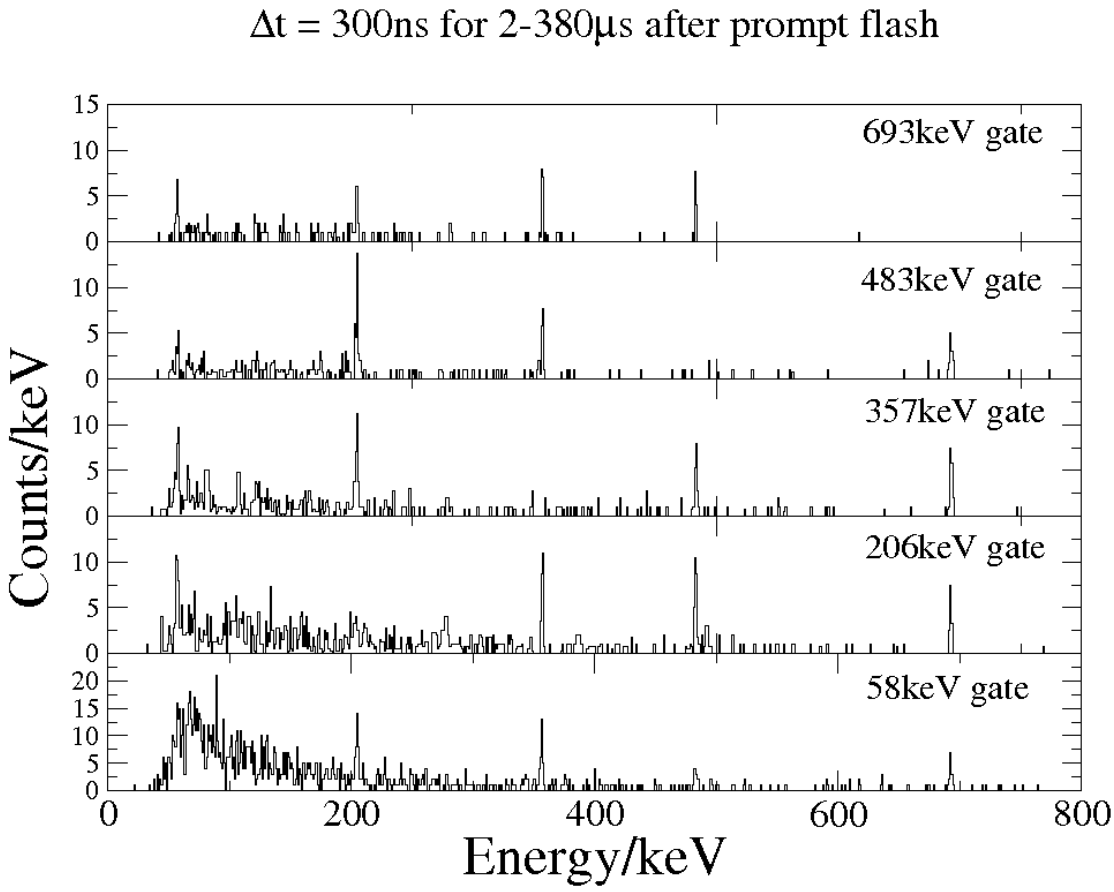

Figure 5.2: Prompt ($\Delta t < 300$ns) $\gamma - \gamma$ coincidence spectra obtained by gating on individual transitions in ^{190}W.

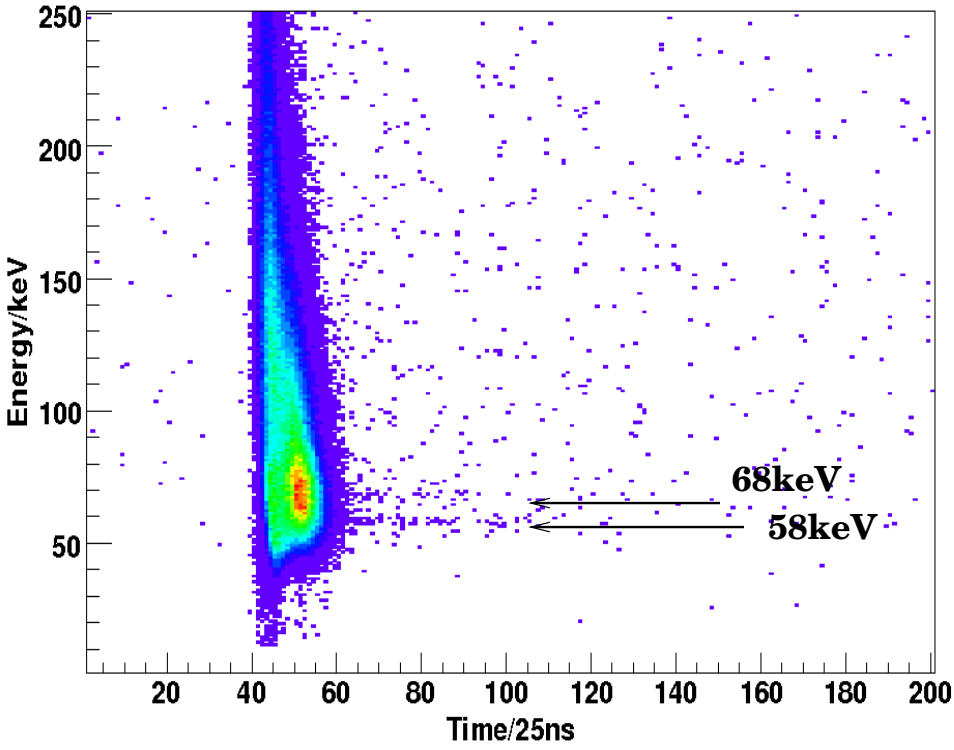

Figure 5.3: Delayed gamma energy-time matrix for ^{190}W, showing short-lived characteristic X-rays.

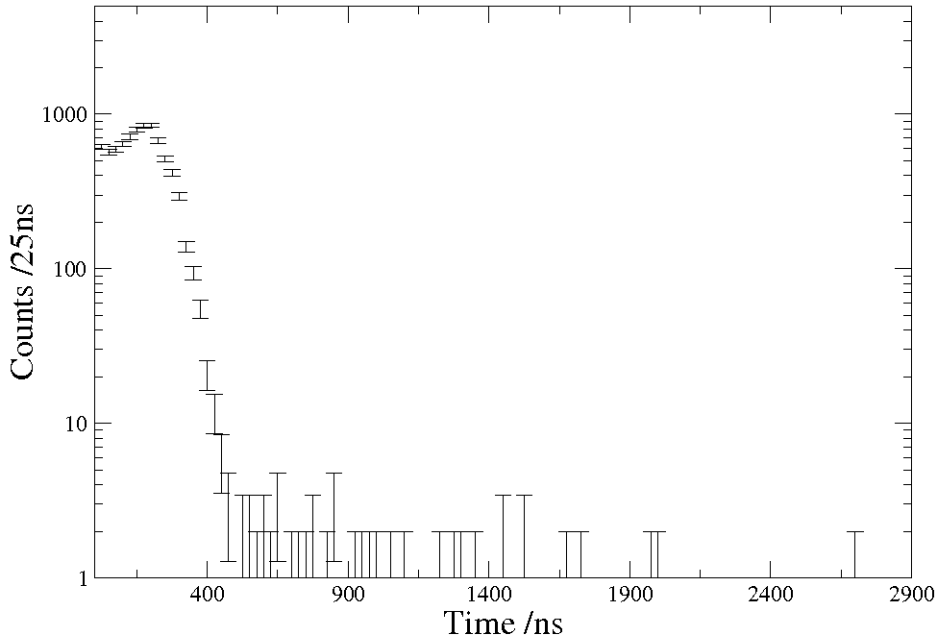

Figure 5.4: Time decay curve gated on the 58 keV K_α X-ray in ^{190}W, starting from the prompt flash.

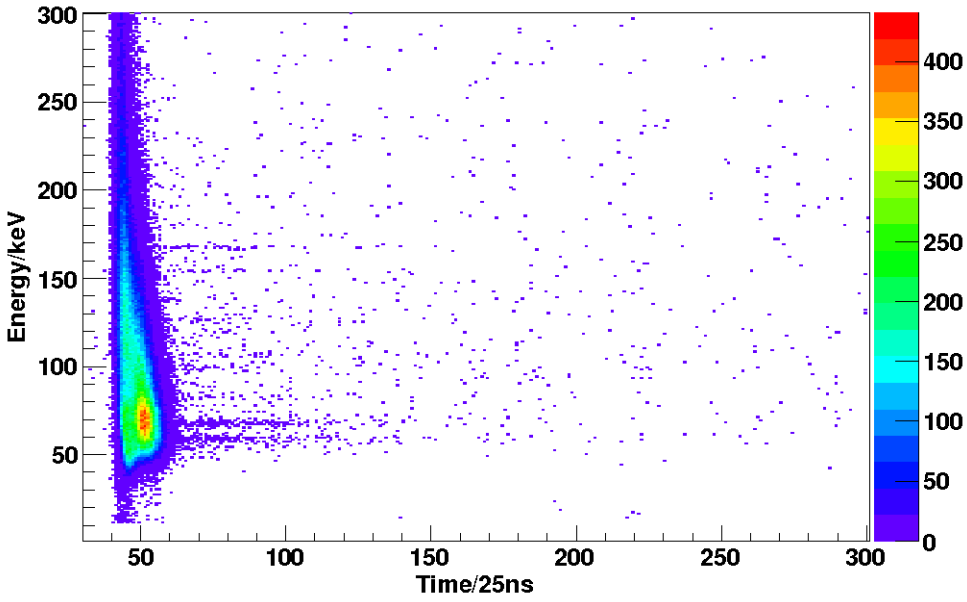

Figure 5.5: Delayed gamma-ray energy-time matrix for ^{191}W showing short-lived X-rays and gamma transitions as horizontal 'fingers'.

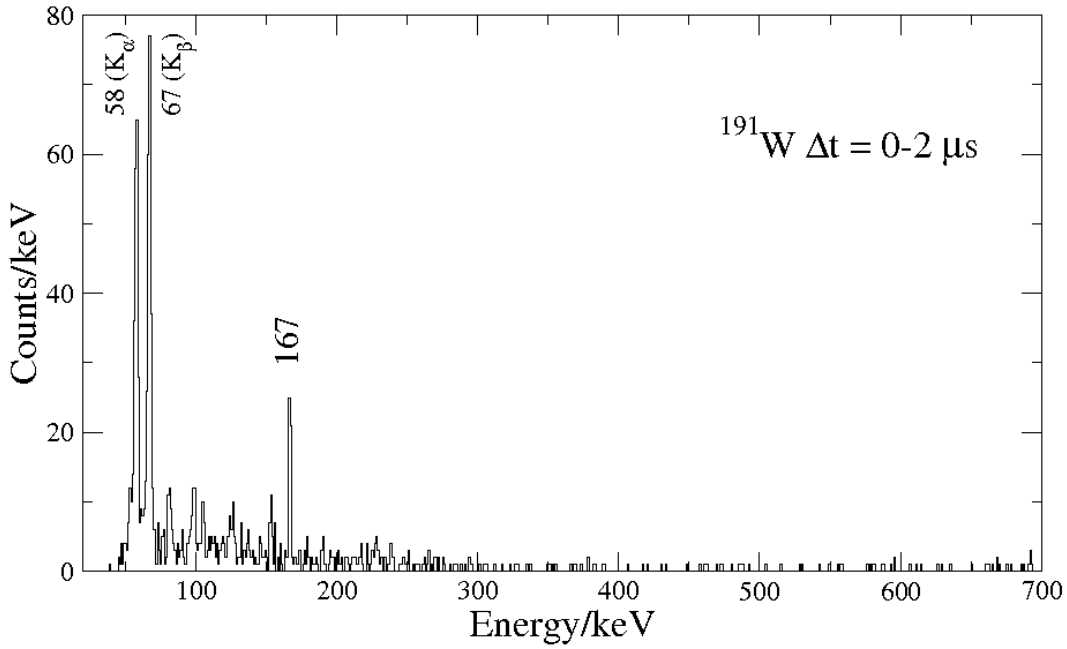

Figure 5.6: Delayed gamma spectrum for ^{191}W showing short-lived X-rays and gamma transitions using Δt=0-2 μs.

5.1.3 Lifetimes

As shown in Fig. 5.8, the 206 keV time decay curve shows a distinct rise in counts for the initial $\sim 50\,\mu$s. Fitting the points with a parent-daughter decay equation of the form:

$$A_2 = N_0 \frac{\lambda_2 \lambda_1}{\lambda_2 - \lambda_1}(e^{-\lambda_1 t} - e^{-\lambda_2 t}) \tag{5.1}$$

gives a parent half-life of 22(9) μs and a daughter half-life of 77(18) μs. This is discussed below in Section 5.1.4.

The 357 keV transition has a fairly constant count rate for the first $\sim 50\,\mu$s before decaying with a half-life of 57(11)μ s. The 483 and 693 keV transitions have simple decay curves. The lifetimes of all the transitions (using a simple single exponential decay function and gating only on 100-400 μs so as to avoid the complications of any initial rises and the effect of the short-lifetime X-rays) are given in Table 5.3 and their decay curves, using semi-log graphs, are shown in Fig. 5.9. The lifetime of the sum of the gamma transitions only, gated on $\Delta t = 100 - 400\,\mu$s, is 86(10) μs, an improvement in its precision compared with the previously determined value of the mean life, $\tau = 390^{+\infty}_{-255}\,\mu$s in reference [7]. The

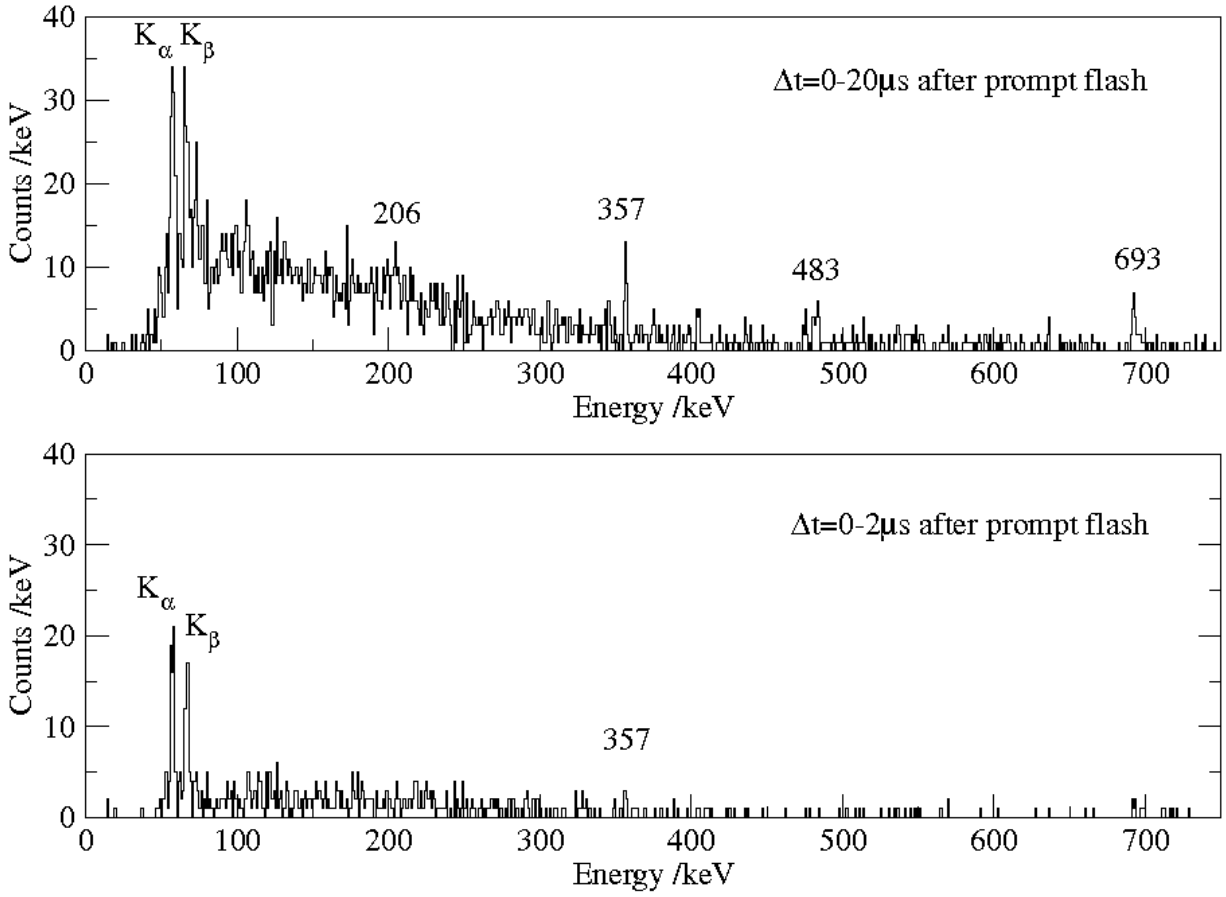

Figure 5.7: Delayed gamma spectra for ^{190}W using time gates 0-2 μs and 0-20 μs after the prompt flash.

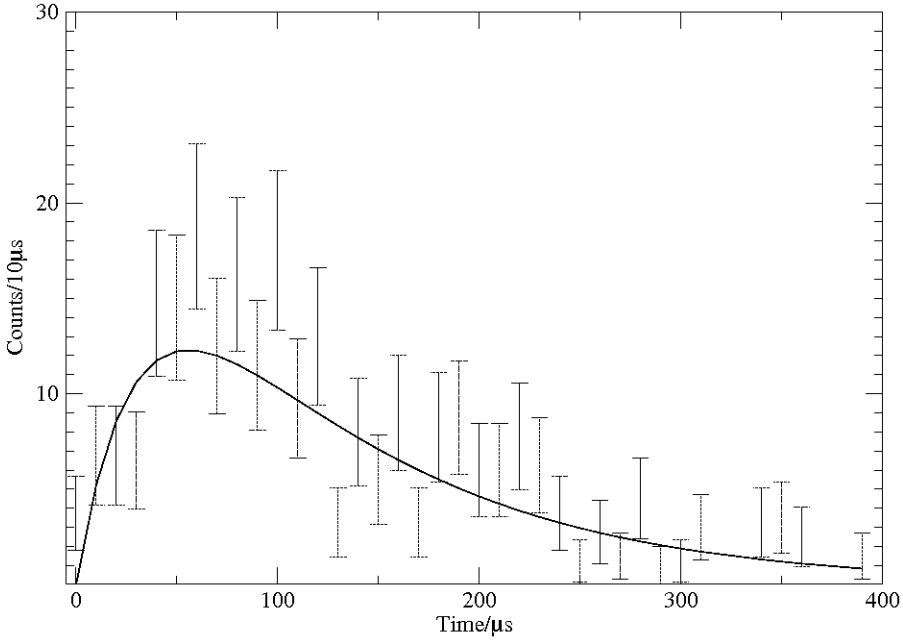

Figure 5.8: Decay curve for the 206 keV gamma transition in ^{190}W, fitted using parent-daughter decay, cf. Equation (5.1).

decay curve is shown in Fig. 5.10.

Table 5.3: Lifetimes of transitions for ^{190}W

Energy (keV)	**Lifetime (gated on 100-400 μs)**
58	89(37)
206	88(28)
357	57(11)
483	106(14)
693	99(37)

The decay curve for the K_α X-ray at 58 keV with $\Delta t = 2\,\mu$s, i.e. from the supposed short-lived isomer, is shown in Fig. 5.11. The fitted half-life is 440(80) ns. The half-life for the K_β X-ray at 67 keV over the same time interval is 790(410) ns, the higher error being due to the poorer statistics.

Time difference spectra

In addition to the time-gated coincidence measurements above, one can find the actual differences in the time between specific gamma transitions although, as with $\gamma - \gamma$ coincidence matrices, this results in low statistics. The time differences for the gamma

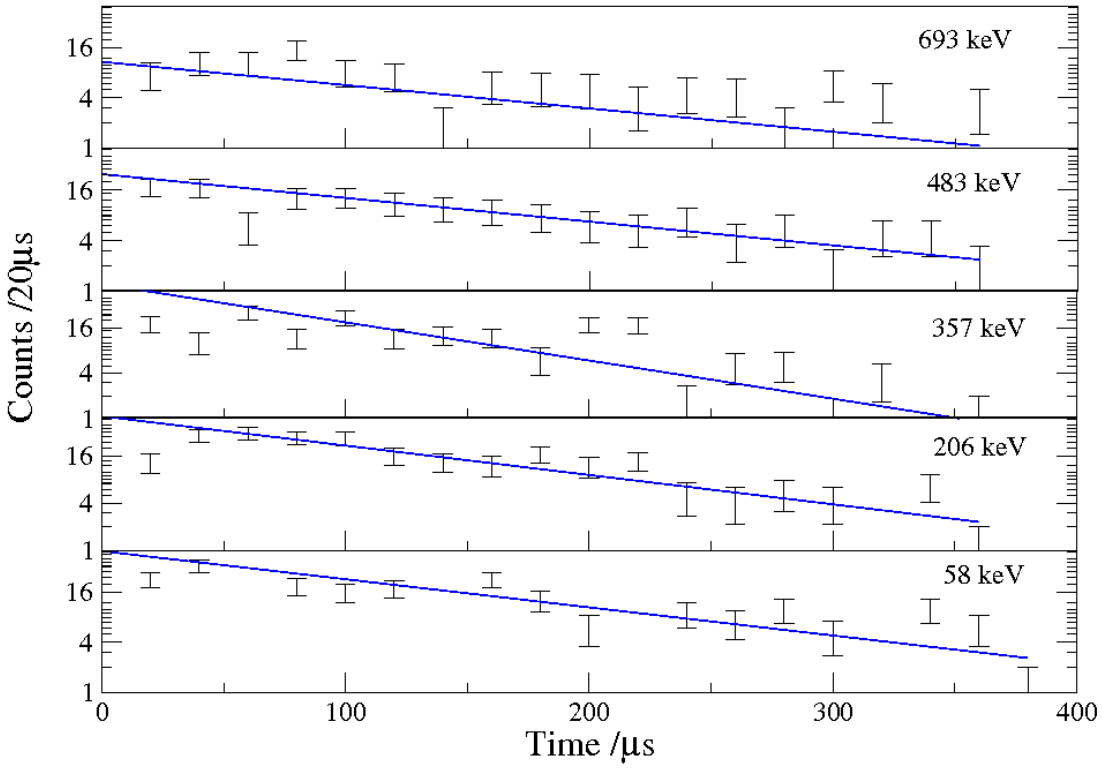

Figure 5.9: Decay curves for transitions in ^{190}W fitted using a single exponential decay function.

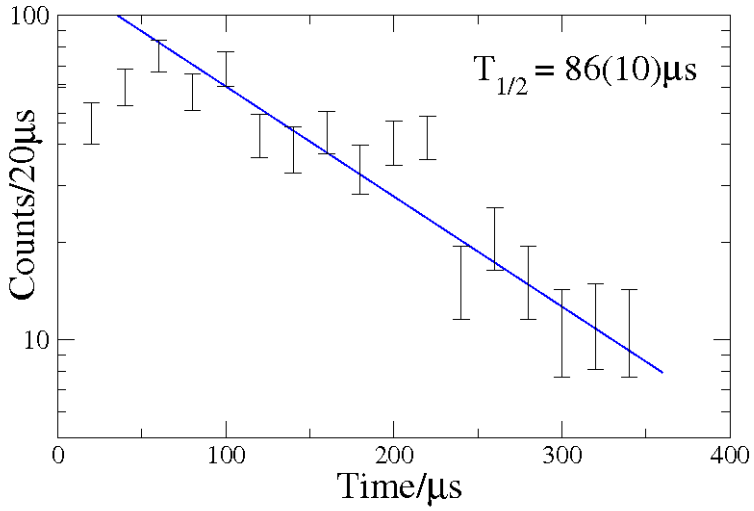

Figure 5.10: Decay curve for the sum of the gamma transitions in ^{190}W with $\Delta t = 100 - 400\,\mu$s.

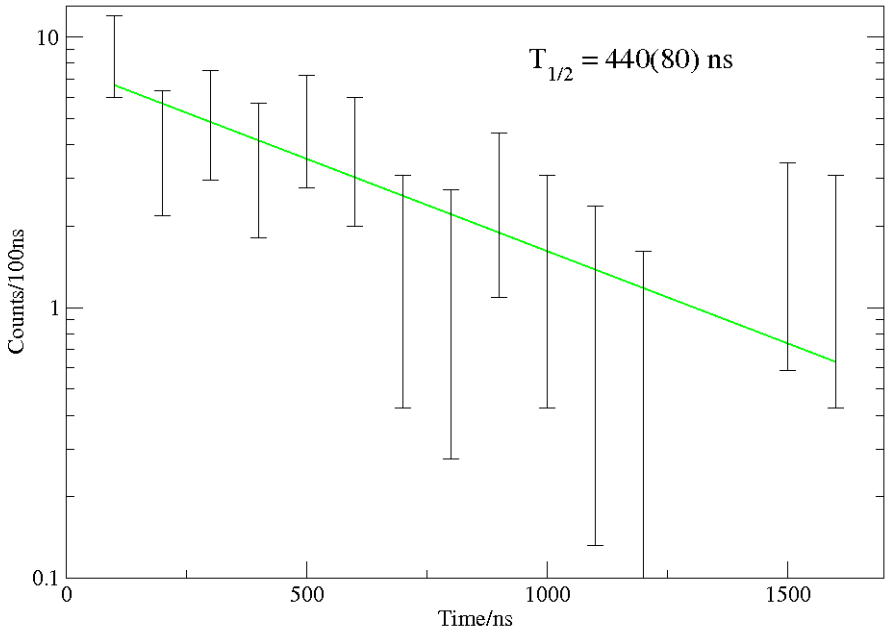

Figure 5.11: Decay curve for 58 keV transition in ^{190}W for the first 2 μs after the prompt flash, fitted using a single exponential decay function.

transitions and the 58 keV X-ray, gated on the 693 keV γ ray, using $\Delta t = 0 - 400\,\mu s$ after the prompt flash, are shown in Fig. 5.12. Although the statistics are low, the gamma transitions are clearly in prompt coincidence with the 693 keV transition. The 58 keV transition has some coincidences with the 693 keV γ ray that are not prompt, although these could be random coincidences.

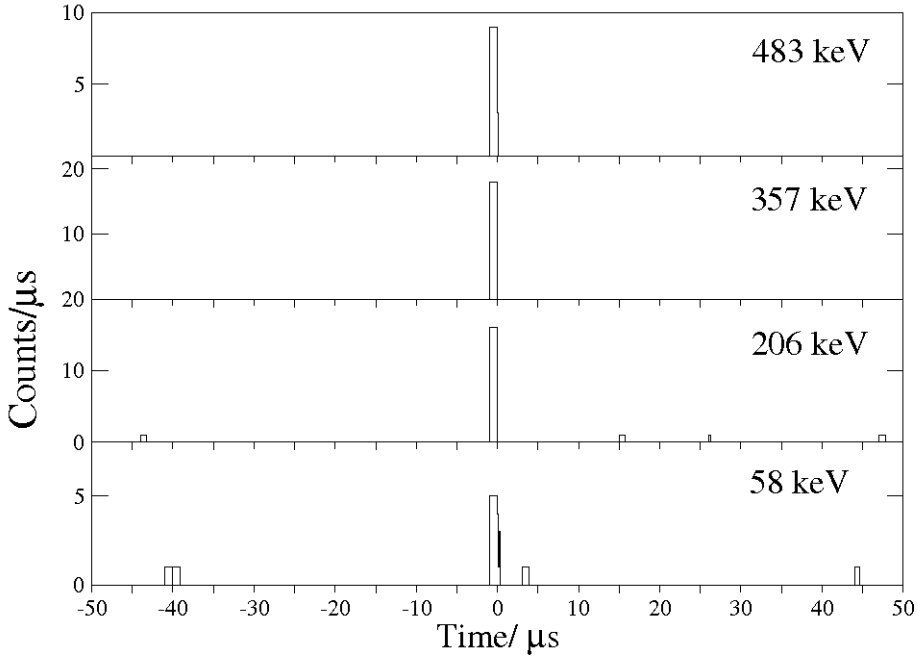

Figure 5.12: Time differences for transitions in ^{190}W gated on the 693 keV transition.

5.1.4 Discussion and Conclusions

Unobserved transition

The decay of a rotational band from a K-isomer in ^{190}W at an energy of 2381 keV has previously been reported [7, 76]. A 591 keV transition, with an intensity close to the observation limit, was observed in this previous fragmentation experiment and, more recently, from deep-inelastic reactions using Gammasphere [78]. This is absent in both the singles and the coincidence spectra in this experiment (cf. Figs. 5.1 and 5.2).

When a γ-ray transition that de-excites an isomer is not observed, the upper limit of the area of a possible gamma peak at the required energy is given by [80]:

$$A_\gamma < N\sqrt{2A_{bgnd}} \tag{5.2}$$

where $\sqrt{2A_{bgnd}}$ is the standard deviation of the area for an unobserved peak and N is the number of standard deviations [80]. Using a 2σ limit, and assuming that the decay scheme in this case is as shown in Fig. 5.13, i.e. with the 102 keV transition depopulating the isomeric level, leading to a 591 keV $8^+ \rightarrow 6^+$ transition, the maximum possible branch-

ing ratios are shown in Table 5.4. Since the 591 keV transition must proceed from the 102 keV transition in this scheme, the maximum branching ratio is given by the smaller of these two decay branching ratios; the table thus indicates a maximum branching ratio of 6(1)% (for an isomeric level with spin-parity 8^+) or less.

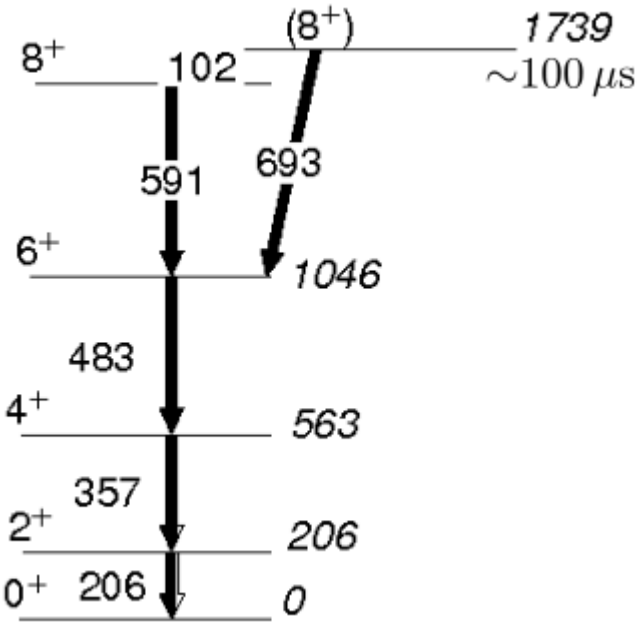

Figure 5.13: Decay scheme for ^{190}W used to investigate the maximum branching ratio for the unobserved 591 keV transition.

Table 5.4: Maximum branching ratios (%) for the proposed, unobserved transitions from the isomer in ^{190}W using a 95% confidence interval.

Energy (keV)	$\mathbf{8^+}$	$\mathbf{8^-}$	$\mathbf{7^+}$	6^+	$\mathbf{6^-}$
102	24(4)	3(1)	6(2)	5(1)	14(4)
591	6(1)	2(1)	2(1)	2(1)	2(1)

The absence of a γ peak at around 591 keV, from the reported 10^- isomeric state to the 8^+ yrast state, suggests a preferential decay from the isomeric state directly to the 6^+ state.

Reduced transition factors

Calculations have been carried out to determine the reduced transition probabilities and the reduced hindrance factors for the transition from an isomeric state to the yrast 8^+ and 6^+ states to enable the possible spins and parities of the isomeric state to be compared with theoretical calculations and then tentatively assigned. The calculations for a branching ratio of 10% to the 8^+ and 90% to the 6^+ state are shown in Table 5.5. The 1176 keV energy is included in the table for those isomeric states that would have reasonably probable gamma transitions to the 4^+ level of the g.s. rotational band. The maximum possible branching ratio for the 1176 keV gamma rays relative to the 693 keV gamma ray is 7%. In fact, the reduced hindrances generally show little dependence on the branching ratio. It should also be noted that E1 reduced hindrance factors are generally up to two orders of magnitude higher than for other transitions, requiring prior multiplication of B(E1) by a factor of 10^4 [41] since an unhindered E1 transition has $B(E1) \sim 10^{-4}$ rather than 1 W.u.. This enhancement has been applied for the E1 transitions in Table 5.5.

Table 5.5: Reduced hindrance factors, f_ν, for the 693 and 1176 keV transitions with a branching ratio of 90% from an isomeric state to the 6^+ state.

Isomeric state	E_γ **(keV)**	**Mult.**	$\boldsymbol{\nu}$	$\mathbf{f}_\nu$
5^+	693	M1	4	194(13)
5^-	693	E1	4	62(4)
5^-	1176	E1	4	180(59)
6^+	693	M1	5	72(4)
6^+	1176	E2	4	149(48)
6^-	693	E1	5	37(2)
6^-	1176	M2	4	62(20)
7^+	693	M1	6	35.5(16)
7^-	693	E1	6	15.8(7)
8^+	693	E2	6	11.6(5)
8^-	693	M2	6	5.1(2)
9^+	693	M3	6	0.75(2)
9^-	693	E3	6	1.54(3)
10^+	693	E4	6	0.21(1)
10^-	693	M4	6	0.119(3)

Typical reduced hindrances for K-isomers are in the region $f_\nu = 30 - 200$, although they generally decrease with increasing neutron number, a result of the trend towards γ-softness in this transitional region. Reduced hindrance factors greater than 100 are highly unlikely, thus the 5^+, 5^- (E1, 1176 keV) and 6^+ (E2, 1176 keV) states may be excluded. By contrast, the reduced hindrance factors for 9^+, 10^- and 10^+ are below 1, and the 9^- state is barely hindered, indicating that these are unlikely as possibilities for the isomeric state.

BCS calculations

Blocked BCS calculations with residual interaction were performed using a code developed by K. Jain [44]. The deformation parameters used were $\epsilon_2 = 0.145$ and $\epsilon_4 = 0.056$, and pairing strengths G_π=22.50/A MeV and G_ν=21.50/A MeV, cf. Section 2.1.4. The residual interaction has been taken as a correction of 100 keV, favouring the anti-parallel alignment of like particles. The results, showing energy against K(K+1) for several multi-quasiparticle (mqp) configurations, are shown in Fig. 5.14. The high population of 2 quasiparticle states close to the yrast line below 2 MeV is evident. Those multi-quasiparticle states closest in energy to the proposed energy of the isomeric state (found by adding the energies of the coincident gamma transitions, giving a state at 1739 keV) are shown in Table 5.6. These calculations, combined with the table of reduced hindrance factors, further enable the elimination of some isomeric states. The 9^- state is at least 569 keV too high in energy and the 7^+ has no 2 quasiparticle yrast state.

Calculations recently carried out by Furong Xu, using configuration-constrained Potential-Energy-Surface (PES) techniques, are shown in Table 5.7. These calculations, briefly described in Section 2.1.2, assumed G_π=1.05 G^0_π and G_ν=1.14 G^0_ν.

This leaves a number of possible candidates: 8^+ ($\nu\, 9/2^-$ [505] $\otimes\, \nu\, 7/2^-$ [503]) and 7^- ($\nu\, 11/2^+$ [615] $\otimes\, \nu\, 3/2^-$ [512]). It should be noted that although Table 5.7 predicts an yrast 10^- isomeric state at energy 1660 keV, close to the energy of the isomer observed here, this was excluded earlier (see Section 5.1.4) on the basis of its very small reduced hindrance factor, 0.119(3).

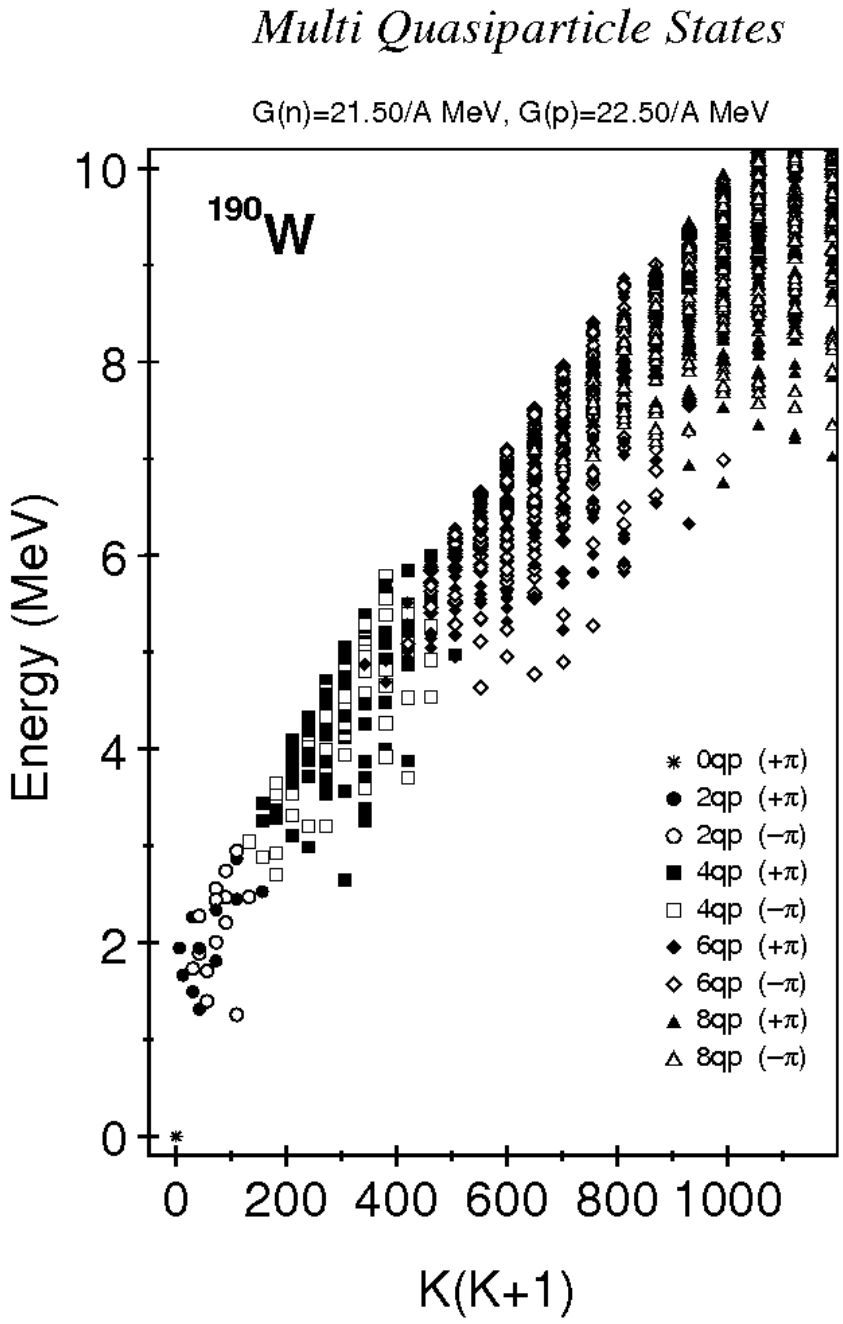

Figure 5.14: Blocked BCS calculated energies for ^{190}W using different mqp configurations.

Table 5.6: Blocked BCS calculated energies for 2 quasi-particles in ^{190}W. E_{res} is +100 keV for parallel intrinsic spins and -100 keV when antiparallel [27]. E_{res} has been assigned as 0 where $\Lambda = 0$. ΔE is the difference between the calculated energy and 1739 keV, the supposed energy of the isomeric state.

K^{π}	Configuration	Energy (keV)			
		E_{qp}	E_{res}	E_{calc}	ΔE
	2 Neutrons				
5^+	$9/2^-$ [505] $\otimes$ $1/2^-$ [510]	1494	0	1494	-245
6^-	$11/2^+$ [615]$\otimes$ $1/2^-$ [510]	1890	0	1890	151
6^+	$9/2^-$ [505]$\otimes$ $3/2^-$ [512]	1312	100	1412	-327
7^-	$11/2^+$ [615]$\otimes$ $3/2^-$ [512]	1708	-100	1608	-131
8^-	$3/2^-$ [512]$\otimes$ $13/2^+$ [606]	2560	-100	2460	721
8^+	$9/2^-$ [505]$\otimes$ $7/2^-$ [503]	1812	-100	1712	-27
9^-	$11/2^+$ [615]$\otimes$ $7/2^-$ [503]	2208	100	2308	569
	2 Protons				
5^-	$9/2^-$ [514]$\otimes$ $1/2^+$ [411]	1732	-100	1632	-107
6^-	$5/2^+$ [402]$\otimes$ $7/2^-$ [523]	2277	100	2377	638
6^+	$5/2^+$ [402]$\otimes$ $7/2^+$ [404]	1942	-100	1842	103
7^-	$5/2^+$ [402] $\otimes$ $9/2^-$ [514]	1395	100	1495	-244
8^-	$9/2^-$ [514]$\otimes$ $7/2^+$ [404]	2006	-100	1906	167
8^+	$9/2^-$ [514] $\otimes$ $7/2^-$ [523]	2338	100	2438	699
9^-	$7/2^+$ [404] $\otimes$ $11/2^-$ [505]	2742	-100	2642	903

Proposed level scheme

Based on the γ-ray intensities (corrected for internal conversion and efficiency), the coincidence relations, the reduced hindrance factors, and the results of the BCS and PES calculations, a level scheme can be proposed for the decay from the isomer populated in this experiment; this is shown in Figure 5.15. If, however, the reported *experimental* results are from the population of a different isomer, at an energy of around 2330 keV (the sum of its gamma transition energies), the blocked BCS calculations indicate that the state could have spin-parity 8^-.

The 102 keV transition is not observed. If the branching ratio is around 10% for the 102 keV transition and 90% for the 693 keV transition, then (before correcting for efficiency and internal conversion) one would expect about 25 counts above background in the 102 keV peak, compared with the 110 counts seen for the 693 peak. Given that the background is at about 100 counts per keV in this energy region, it is unsurprising that

Table 5.7: PES calculated energies for 2 quasi-particles in ^{190}W [33].

$\mathbf{K}^{\pi}$	**Configuration**	β_2	γ	β_4	$E_{calc}\,(keV)$
$\mathbf{7}^{-}$	$\nu\,11/2^{+}\,[615] \otimes \nu\,3/2^{-}\,[512]$	0.16	-25^{0}	-0.04	1729
$\mathbf{8}^{+}$	$\nu\,9/2^{-}\,[505] \otimes \nu\,7/2^{-}\,[503]$	0.17	0^{0}	-0.07	1835
$\mathbf{10}^{-}$	$\nu\,11/2^{+}\,[615] \otimes \nu\,9/2^{-}\,[505]$	0.16	0^{0}	-0.06	1660
$\mathbf{7}^{-}$	$\pi\,9/2^{-}\,[514] \otimes \pi\,5/2^{+}\,[402]$	0.16	0^{0}	-0.05	1486
$\mathbf{8}^{-}$	$\pi\,9/2^{-}\,[514] \otimes \pi\,7/2^{+}\,[404]$	0.17	0^{0}	-0.06	2270
$\mathbf{6}^{-}$	$\nu\,11/2^{+}\,[615] \otimes \nu\,1/2^{-}\,[510]$	0.15	0^{0}	-0.04	2114
$\mathbf{6}^{+}$	$\nu\,9/2^{-}\,[505] \otimes \nu\,3/2^{-}\,[512]$	0.16	12^{0}	-0.05	1859

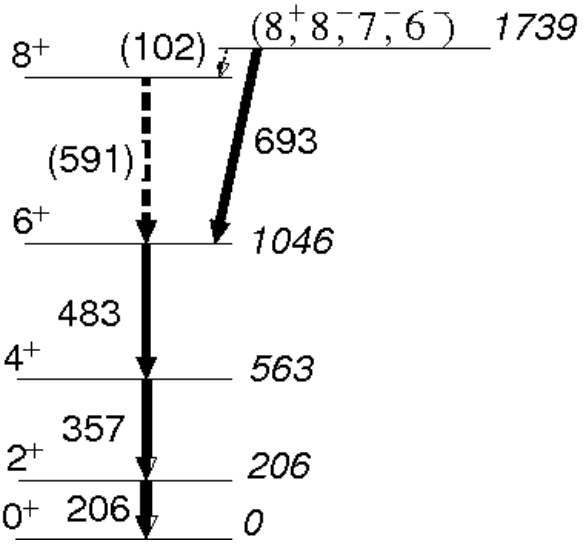

Figure 5.15: Proposed level scheme for the decay of the isomer in ^{190}W.

the 102 keV peak is not detected.

Concluding remarks

The 280 keV peak, observed initially on the gamma-gamma coincidence spectrum, principally for the 206 keV gate, is only noticeable (compared to the other gamma transitions and characteristic X-rays) on a singles spectrum using a gate with Δt=100 μs after the end of the prompt flash. Its intensity, corrected for efficiency, relative to that of the 206 keV peak is 29(12)% using Δt=100 μs and 17(8)% using Δt=400 μs. Although there were insufficient counts in the 280 keV peak to obtain an accurate half-life, the reduction of counts under the peak with increasing time gates is consistent with a half-life of the

order of 50 μs. This half-life is close to the 'parent' half-life of the 206 keV transition, cf. Section 5.1.3. If the 280 keV transition is from an isomer with half-life $\sim$ 50 μs, it might be responsible for the initial rise in the 206 keV time decay curve but, since it is also in coincidence with the 357 keV transition, it should feed this decay as well. Lack of statistics prevented any further analysis, so the existence of a $\sim$ 50 μs isomer, feeding the 2^+ and possibly the 4^+ states in the ground state bound, is unverified.

The existence of a shape isomer, namely an oblate, rotational-aligned state, is also a possibility [10]. Indeed, the intense X-rays observed in the present analysis of ^{190}W were investigated with regard to an oblate-prolate shape transition, since in this case, one might have a $0^+ \rightarrow 0^+$ transition which would decay entirely by internal conversion, thus yielding a relatively high intensity of the characteristic tungsten X-rays. However, Walker [81] had already proposed that there was a $\sim$ 1 ms shape isomer, of lower energy than the K-isomer investigated here, and thus with longer lifetime, making it inaccessible using the present experimental procedure [81]. In this context, it is interesting to note that Xu's PES calculations predict an yrast 10^- isomeric state from two neutrons with configuration $\nu\, 9/2\,[505] \otimes \nu\, 11/2[615]$ at an energy of 1256 keV, much lower in energy than the isomer observed here.

The intense X-rays, of half-life $\sim$ 1 μs are also present in ^{191}W and careful comparison of relative intensities using different time gates for both ^{190}W and ^{191}W was inconclusive. There was a previously reported problem regarding the performance of scintillator Sci21, used to calculate the time-of-flight and hence A/Q (see Section 3.3.2). This could have the effect of causing a cross-contamination of neighbouring isotopes in the PID, e.g. the ^{190}W PID 'blob' may include events that properly belong to ^{191}W, etc. The high intensity of these short-lived, characteristic X-rays in both ^{190}W and ^{191}W are consistent with this. At all events, no conclusions can be drawn regarding these X-rays.

In conclusion, the 591 keV transition reported previously for ^{190}W is not observed, but, in this improved experimental setup with higher statistics, $\gamma - \gamma$ coincidences were obtained, indicating that the 206, 357, 483 and 693 keV transitions are in mutual, prompt coincidence. Reduced hindrances, BCS and PES calculations indicate a possible new de-

cay scheme. However, several issues are unresolved: the rise in the time decay curve for the 206 keV transition, the probable leakage of ^{191}W ions into the ^{190}W PID, possibly explaining the short-lived, intense characteristic tungsten X-rays, and the 280 keV transition observed for the first time in the coincidence spectra.

5.2 Production and Particle Identification for the ^{205}Au and ^{203}Au settings

Beta spectroscopy and beta-delayed gamma-spectroscopy were carried out for both of these Au isotopes at GSI for the first time during the initial experimental runs using the active stopper in 2007. The specific settings for these experimental runs are given in Appendix A.

5.2.1 Identification of ^{205}Au

As noted above, in Section 4.1.2, charge states could not be identified easily for ^{205}Au, so particle identification was performed without prior selection of charge state, using the gate shown in Fig. 4.12 to eliminate unwanted events. Particle identification was carried out using a plot of Z (from MUSIC 42) vs. time-of-flight, shown in Fig. 5.16. The numbers of ions identified are shown in Table 5.8. The gate labelled '^{205}Au' includes ^{203}Pt ions (in the lower part) since these two nuclides have approximately the same time-of-flight (having approximately the same A/Q). The gamma spectrum for implanted ions from this gate, shown in Fig. 5.21, does not show the peak at 1104 keV from ^{203}Pt reported by Steer [79], but a peak is discernible using Δt= 0.7-90 μs with the DGF TDCs, giving 10(4) raw counts. Using Steer's branching ratio for ^{203}Pt, the 1104 keV peak indicates that there are 10500(4400) such ions in the ^{205}Au gate shown in Fig. 4.12, i.e. a contamination of around 20%. The isomerically delayed 1104 keV gamma ray from ^{203}Pt has a very different half-life (641(55) ns [79]) from the ground state and isomeric state investigated here for ^{205}Au (34 and 6 s respectively, cf. Section 5.3.1), and its energy is not very close to the gamma transitions in ^{205}Au, implying no mis-identification in the gamma or beta spectra. A LISE simulation of the implantation of ions in this setting is shown in Fig. 5.17, indicating that the ^{203}Pt ions are implanted towards the back of the DSSSDs, further reducing any effect they might have on the beta spectra. The daughter nuclei are ^{203}Au, having an isomer at 563 keV (described in Section 5.4.2) with half-life $\sim$ 140 μs, and ^{205}Hg with a 1.09 s isomer [82], undetectable in this setup. Therefore, there is no

discernible contamination of the ^{205}Au beta or gamma spectra by the ^{203}Pt ions analysed here.

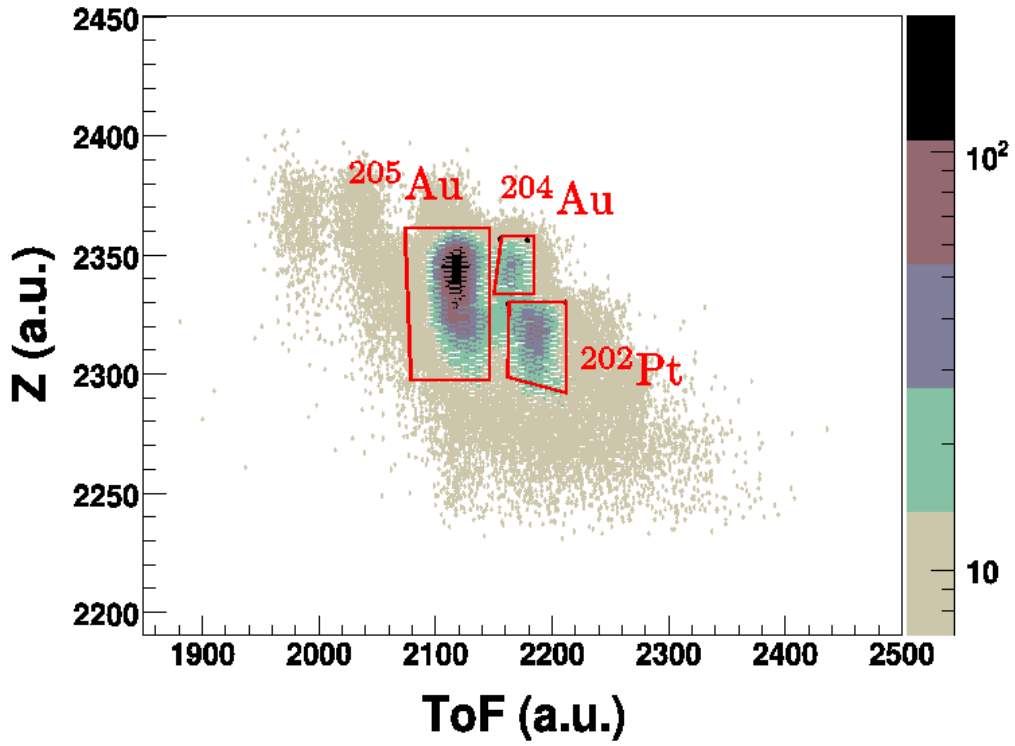

Figure 5.16: Particle I.D. for ^{205}Au using Z vs. time-of-flight.

Table 5.8: Number of ions for each nuclide identified, after 'clean-up', in the ^{205}Au setting.

Nuclide	No.of ions	Percentage of total
^{205}Au	56720	71%
^{204}Au	6545	8%
^{202}Pt	14348	18%

5.2.2 Identification of ^{203}Au

Having selected the charge states (cf. Fig. 4.13), particle identification was carried out using plots of Z (from MUSIC 42) vs. time-of-flight, shown in Figs. 5.18 and 5.19. The numbers of ions identified are shown in Table 5.9, the identification being confirmed by the detection of known gamma rays.

A LISE simulation of the implantation of ions in this setting is shown in Fig. 5.20.

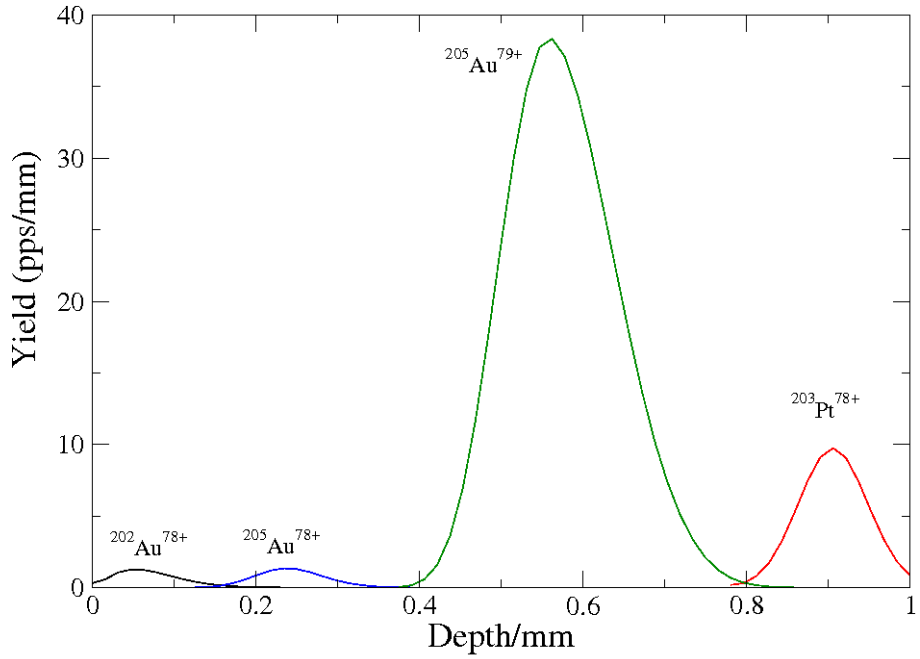

Figure 5.17: Simulated implantation profile in the DSSSD, using LISE [57], for ions from the ^{205}Au setting. This assumes a single DSSSD of thickness 1 mm at the final (stopper) focus.

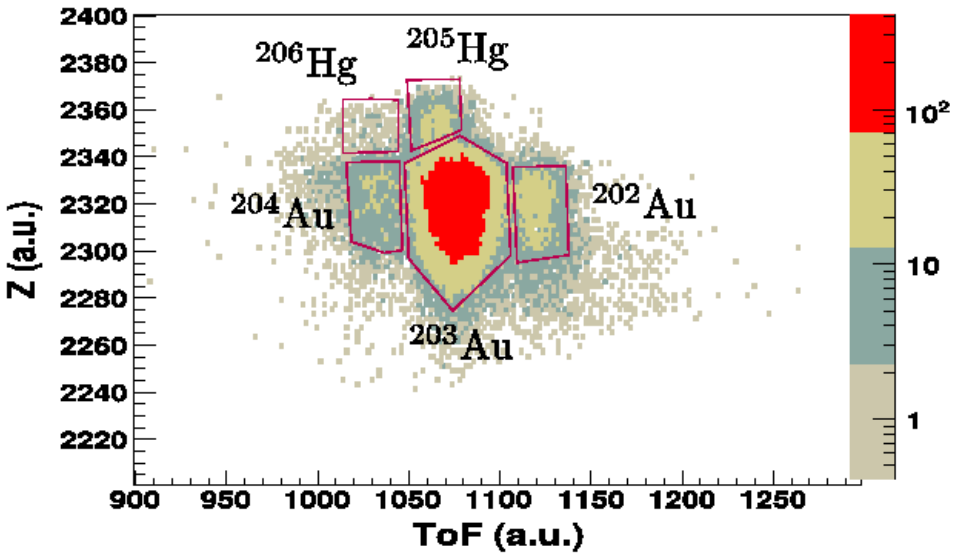

Figure 5.18: PID for $dQ = 1$ charge states in the ^{203}Au setting.

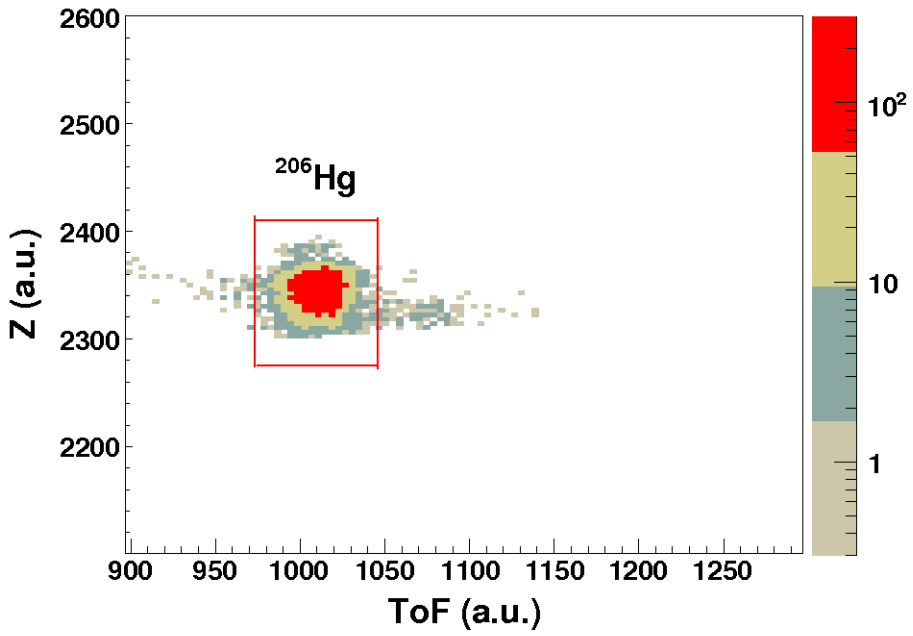

Figure 5.19: PID for $dQ = 0$ charge states in the ^{203}Au setting. The gate shown was used to remove unwanted events.

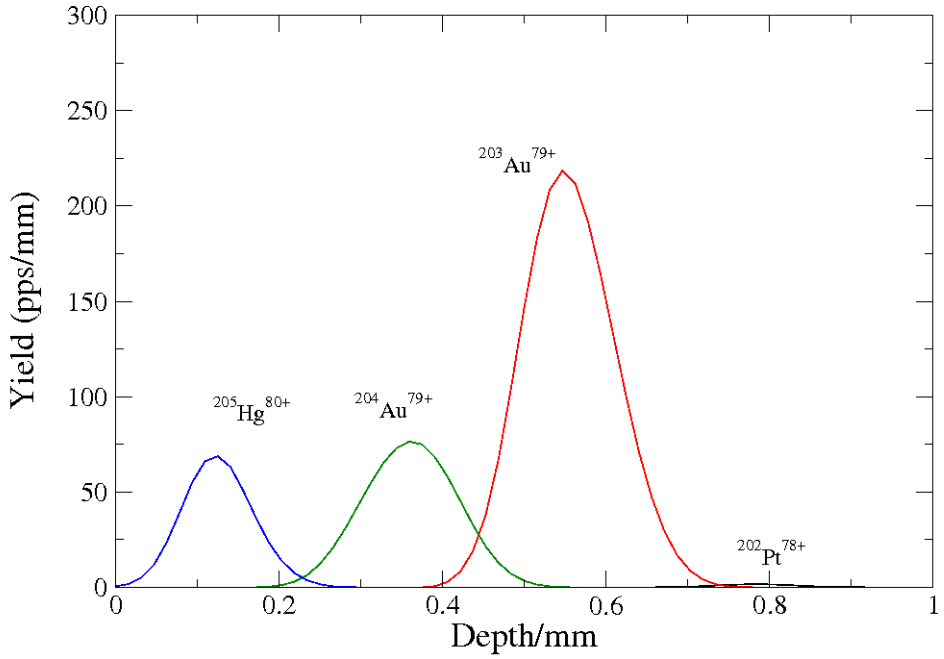

Figure 5.20: Simulated implantation profile in the DSSSD, using LISE [57], for ions from the ^{203}Au setting. This assumes a single DSSSD of thickness 1 mm at the final (stopper) focus.

Table 5.9: Number of ions for each nuclide identified, after 'clean-up', in the ^{203}Au setting.

Nuclide	**Charge State**	**No.of ions**	**Percentage of total**
^{204}Au	dQ=1	6964	3%
^{203}Au	dQ=1	169943	77%
^{202}Au	dQ=1	11080	5%
^{206}Hg	dQ=0	27961	13%

5.3 ^{205}Au setting

5.3.1 ^{205}Au

^{205}Au has a ground state of spin-parity $(3/2^+)$ [83] with half-life 31(2) s [14].

Gamma spectrum from isomeric decays on implantation

Excited states in ^{205}Au were first reported by S. Steer *et al.* [84, 79]. Seven transitions were observed in the gamma-ray spectrum (at 243, 737, 928, 946, 962, 980 and 1172 keV), all but the 243 keV transition having a measured half-life of 163(5) ns. The spectrum obtained in this experiment, shown in Fig. 5.21, uses the short-range TDCs and confirms the reported results. Although the 243 keV transition is not visible on this spectrum, it is just visible on a similar spectrum using $\Delta t = 1\,\mu s$ with the DGF TDCs (its intensity is included in Table 5.10, although its peak-to-total ratio of 0.14 is too low for it to be properly considered a peak here). Steer *et al.* had a total of approximately 342 000 ^{205}Au ions, compared with about 56 720 in this experiment. The reduced statistics in this experiment meant that $\gamma - \gamma$ coincidence spectra could not be produced in the present analysis. Since the present statistics are far lower than those obtained by Steer *et al.* in an experimental setup identical except for the presence of an active stopper, and since no new peaks have been detected here, no further study of the isomerically-delayed gamma decay of ^{205}Au *on implantation* is presented here, but the subsequent beta-delayed gamma rays and conversion electrons are discussed below.

Beta electron spectrum

The energy spectrum for electrons following the implantation of ^{205}Au ions in the DSSSDs is shown in Fig. 5.22, using a 5 s correlation time between implantation and β decay. There is a clear doublet above the beta energy background at 824(10) and 897(10) keV, indicating that these two peaks are from K and L conversion electrons. The observed γ spectrum, gating on the K-electron peak, is shown in Fig. 5.23, confirming that the K conversion electron gives rise to characteristic K X-rays; the resolution is insufficient to

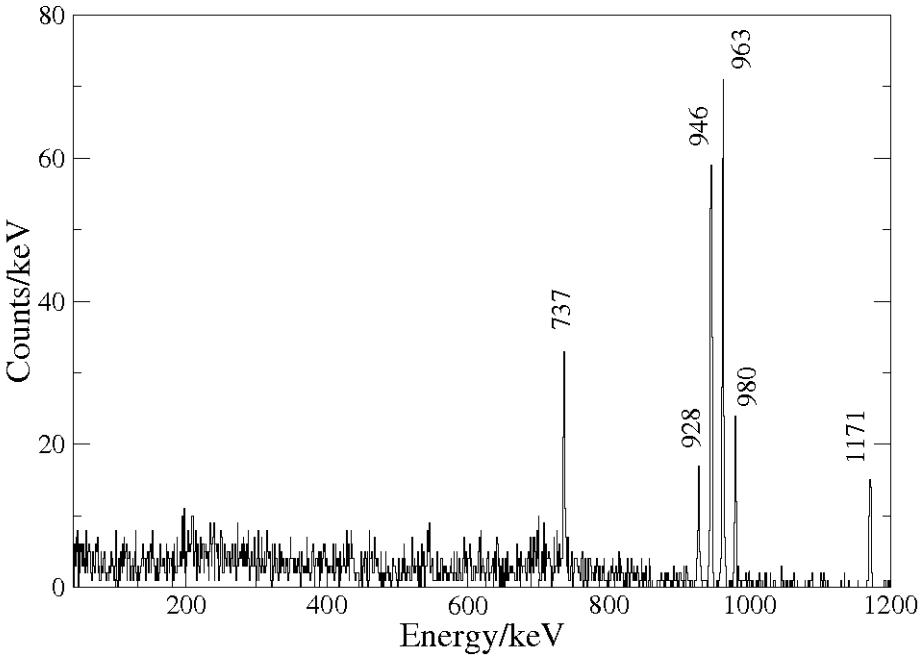

Figure 5.21: Gamma spectrum for implanted ^{205}Au ions using short-range TDCs with Δt =15-900 ns after the prompt flash.

Table 5.10: Intensities (corrected for efficiency), normalised to 100 for the strongest peak, for gamma rays on implantation of ^{205}Au; Δt=15-900 ns.

E_γ (keV)	**FWHM (keV)**	**Intensity**
242	2	3(1)
737	2.8	39(5)
928	3.0	20(4)
946	2.8	93(9)
963	2.5	100(9))
980	2.3	26(4)
1171	2.8	26(4)

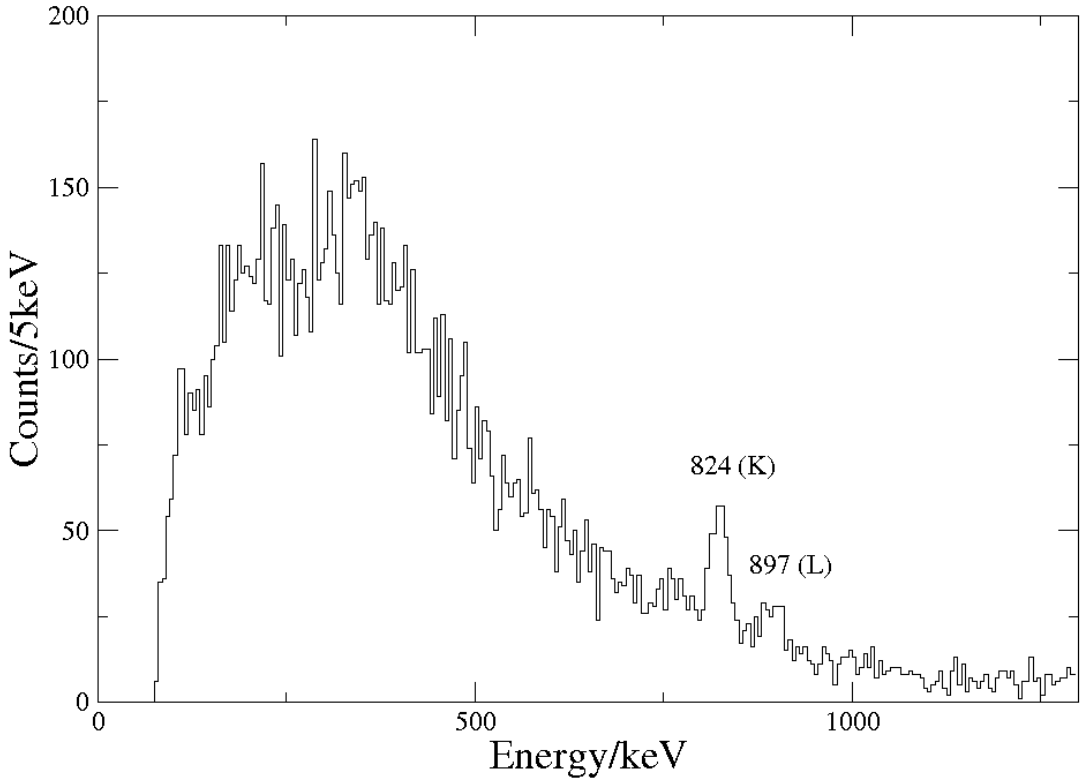

Figure 5.22: Electron spectrum for ^{205}Au using a 5 s implant-decay correlation time.

distinguish the $K_{\alpha 1}$ X-ray at 68.8 keV (46.4(10)% branching ratio per 100 K-shell vacancies) from the $K_{\alpha 2}$ X-ray at 67.0 keV (27.5(6)% branching ratio) [85]. Unlike Fig. 5.21, this spectrum does not show the gamma transitions on implantation of ^{205}Au, described above, further confirming the assignment of the peaks in the DSSSD electron spectrum as K and L conversion electrons from an isomeric state. Since the binding energy of the K electrons is 80.7 keV (that of the L1 and L2 electrons is around 14 keV), this indicates that the converted transition has an energy of 824+81=905(10) keV. It should be noted that the width of the peak labelled 'L' in Fig. 5.22 will contain components from M, N, etc. transitions. The lifetime of the converted transition is difficult to establish exactly since the statistics are relatively low and there are many false correlations (as noted in Section 4.3.1). The use of the improved charge state algorithm (see Section 4.1.2) and a more restrictive PID gate in this setting compared with that used for the analysis carried out immediately before publication of the paper on ^{205}Au, printed in the Appendix, yielded a shorter half-life, 4(2) s, than the published value of 6(2) s, although with lower statistics. The lifetime fits are shown in Fig. 5.24.

The internal conversion coefficient for the observed 905 keV transition, assuming M4 multipolarity, is 0.178(5) [77]. Its high energy and relatively high internal conversion coefficient were favourable for the detection of conversion electrons in this experimental setup, but the measured half-life of this isomeric state, 6(2) s, implies that gamma decays from this state to the ground state could not be correlated to such a long-lived isomer in this setup, cf. Section 3.3.5.

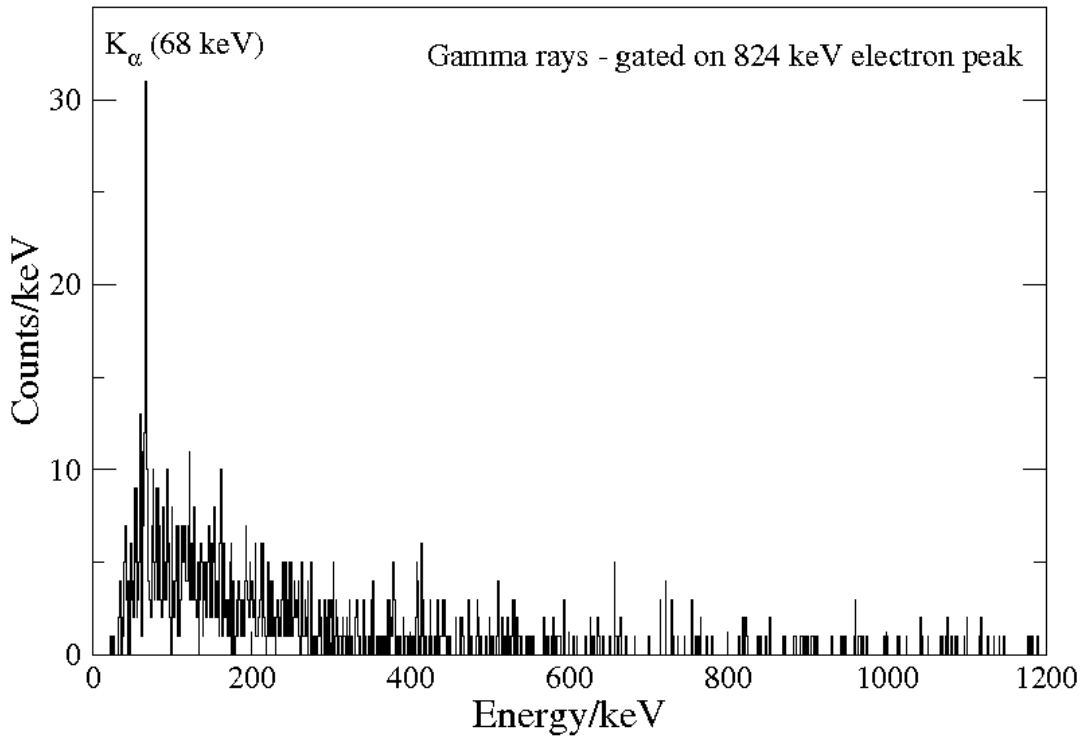

Figure 5.23: Gamma spectrum gated on the ^{205}Au K-electron detected by the DSSSDs.

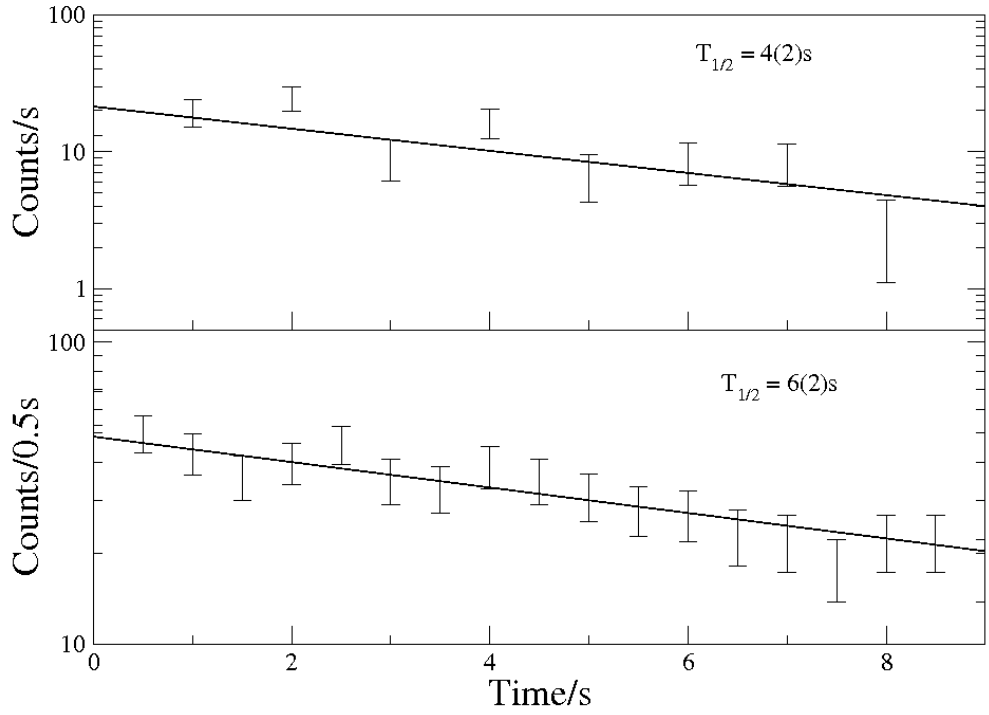

Figure 5.24: Lifetime fits for the K conversion electron in ^{205}Au. The upper spectrum was obtained by using the charge state algorithm and PID described in the text. The lower spectrum was obtained without selecting charge state and with a less restrictive PID gate for ^{205}Au.

Beta-delayed gamma spectrum

The prompt beta-delayed gamma spectrum, using a 5 s time correlation between implantation and decay, is shown in Fig. 5.25. There are noticeable peaks at 68 keV (the energy,

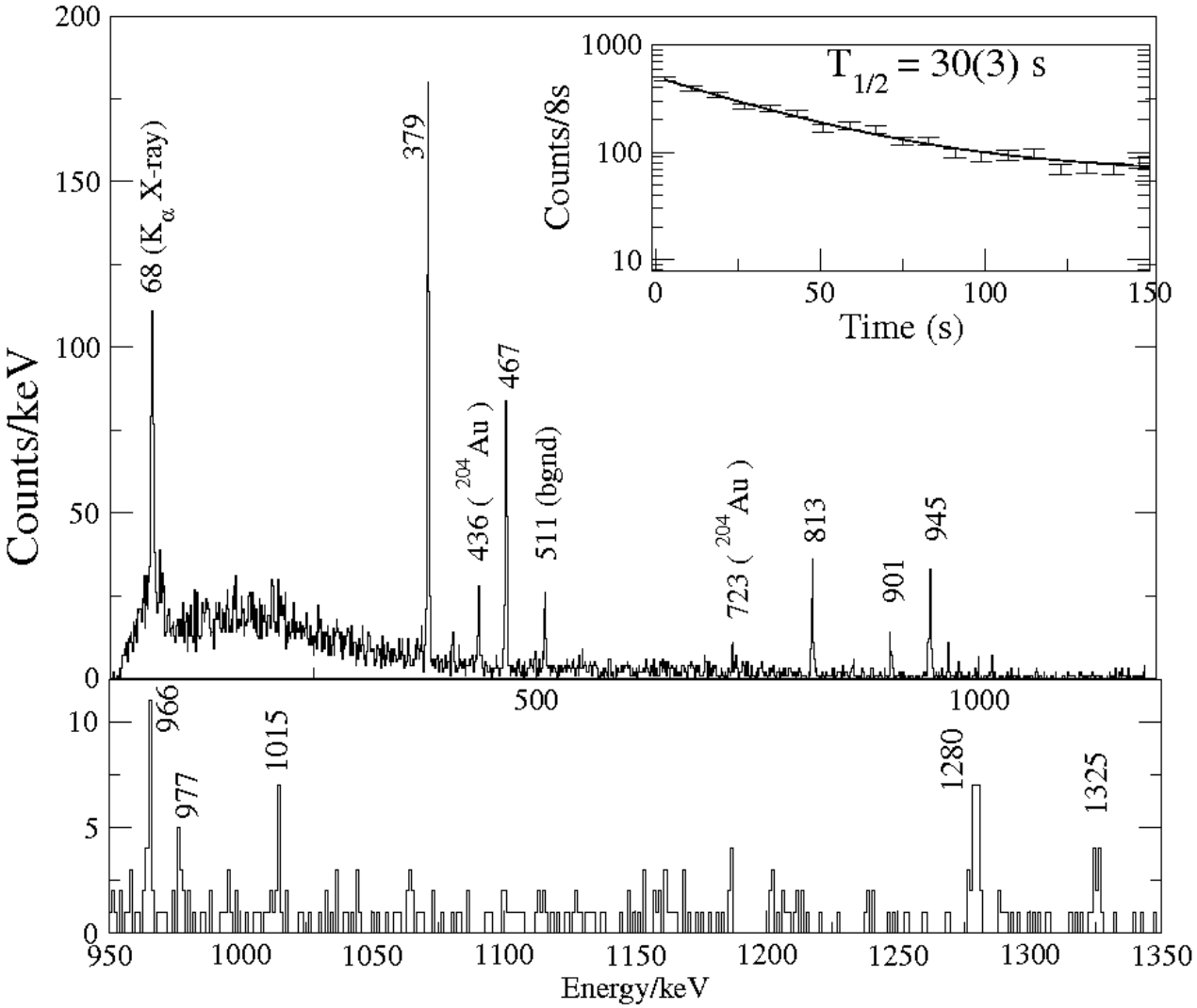

Figure 5.25: ^{205}Au beta-delayed, prompt ($\Delta t = 0 - 0.35\,\mu$s) gamma spectrum using an implant-decay time correlation of 5 s. The lower graph shows the 950-1350 keV region more clearly. The decay curve is shown inset on the upper graph.

within experimental error, of the K_α X-ray) and at 379, 467, 813, 901 and 945 keV from the decay of ^{205}Hg [82]. In addition, peaks at 1280 and 1325 keV confirm that these gamma rays are from the beta decay of ^{205}Au to ^{205}Hg (see the level scheme shown in Fig. 5.26). The intensities are shown in Table 5.12. In addition, low intensity peaks at 966, 977 and 1015 keV are observed. Gamma transitions from states with spin-parity

$7/2^-$ and $9/2^-$, with energies 966 and 1015 keV respectively, are known from the decay of ^{205}Hg [86], but not as arising from the prior beta-decay of ^{205}Au. Table 5.11 shows the gamma intensities and log ft values obtained by Wennemann [14]. Note that ^{205}Au decays 100% by β^- decay.

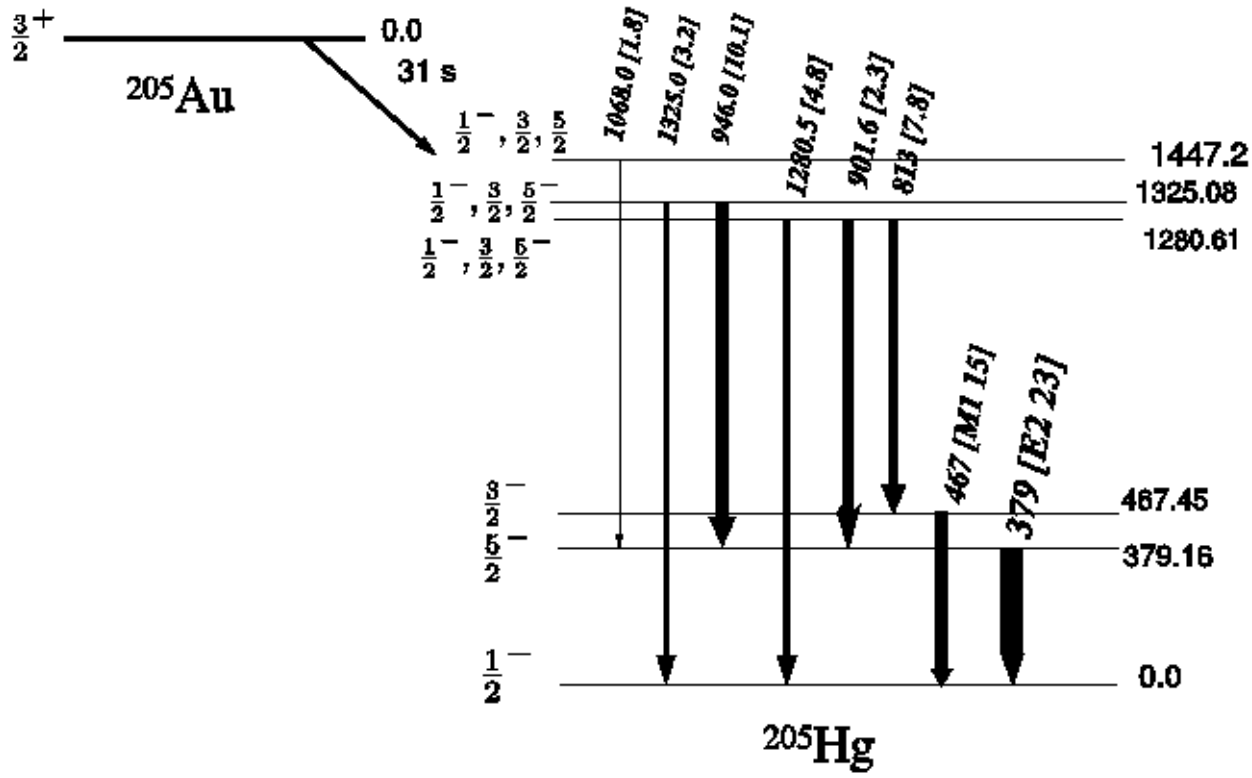

Figure 5.26: Level scheme for the beta decay of ^{205}Au (cf. ENSDF - Wennemann [14]).

These spins ($7/2^-$ and $9/2^-$) are high when compared to that of the $3/2^+$ ground state of ^{205}Au, indicating that these transitions are unlikely to arise from the beta decay of ^{205}Au but may be due to the decay of the same isomeric state that produces the conversion electrons described above. This would imply that ^{205}Au has an isomeric state that decays to the ground state by internal conversion and γ decay, but in addition, given its long half-life, undergoes β^- decay to excited states in ^{205}Hg which are forbidden in the case of beta decay of the ground state.

The gamma peaks at 966 and 1015 keV reduce in intensity relative to the peaks arising from the ground state beta decay of ^{205}Au as the implant-decay correlation time is

Table 5.11: Beta intensities (calculated using a calibrated β^- singles spectrum after subtracting the feedings from excited-states) and log ft values for ^{205}Au, taken from Wennemann [14, 82].

Energy level (keV)	β^- **Intensity**	**log ft**
1447.2	1.8(6)	6.29(15)
1325.08	13(3)	5.53(11)
1280.61	15(4)	5.51(12)
467.45	6.7(16)	6.43(11)
379.16	8.7(22)	6.37(12)
0	54(10)	5.79(9)

increased, as shown in Fig. 5.27; the raw intensities are given in Table 5.13. This is further evidence that these transitions arise from the isomeric state, as is the fact that their lifetimes are inconsistent with that of the ground state, viz. 34(2) s, but consistent with that of the isomeric state as determined from the 6(2) s half-life via internal conversion decay.

Table 5.12: Gamma intensities, corrected for efficiency and normalised to 100 for the strongest peak, following the beta decay of ^{205}Au using a 5 s implant-decay time correlation. For absolute intensities multiply by 0.04175.

$\mathbf{E_\gamma}$ **(keV)**	**FWHM**	**Intensity**
68	3.9	43(4)
379	2.4	100(7)
467	2.7	51(5)
813	2.7	32(4)
901	2	11(3)
945	2.9	41(5)
966	2.5	7(2)
977	2.1	3(1)
1015	1.4	3(1)
1280	2.1	10(3)
1325	1.7	4(2)

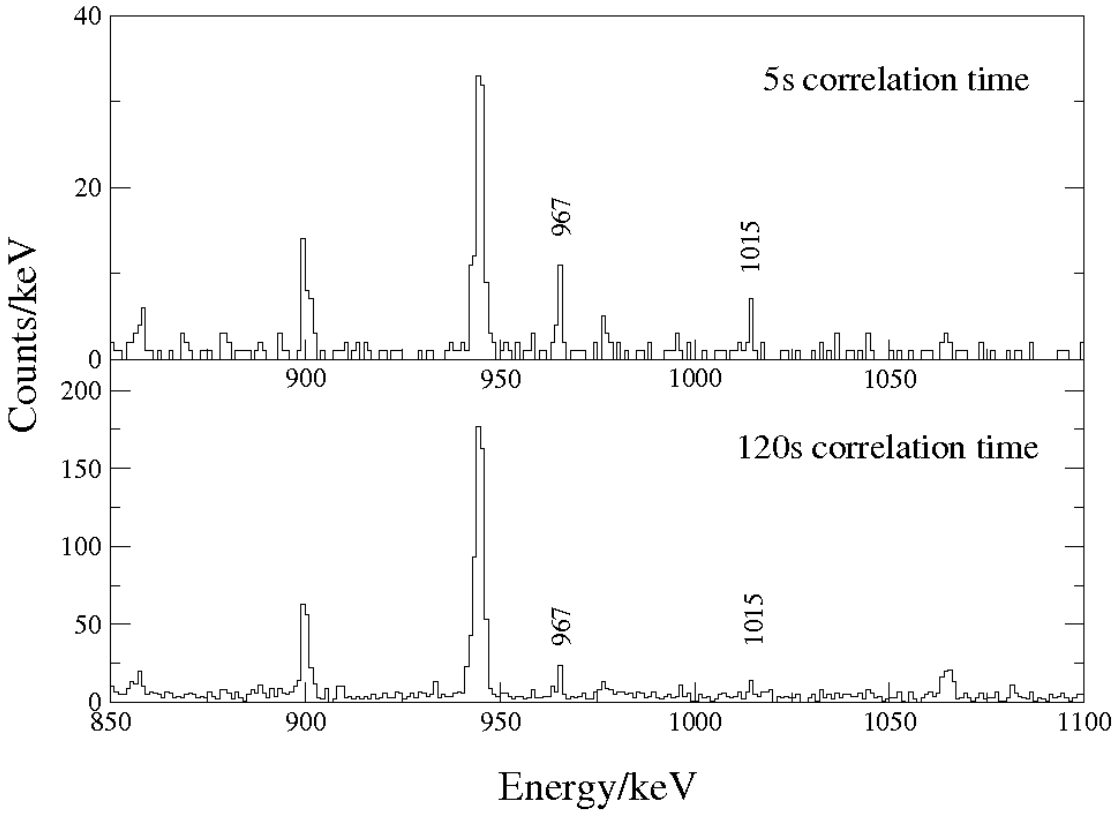

Figure 5.27: ^{205}Au beta-delayed, prompt (Δt=0-0.35 μs) gamma spectra showing the reduction in intensity of the 967 and 1015 keV peaks relative to the 901 and 945 keV peaks.

Table 5.13: Raw intensities of the 966 and 1015 keV peaks relative to the 966 keV peak.

Imp-dec time (s)	**Energy (keV)**	**Intensity**	**Int. rel. to 945 keV**
5	945	94	100%
	966	15	16(4)%
	1015	7	7(3)%
120	945	523	100%
	966	30	6(1)%
	1015	15	3(1)%

5.3.2 ^{204}Au

Gamma spectrum from isomeric decays on implantation

This nuclide was also obtained in the ^{203}Au setting and its spectra are described there (see Section 5.4.1). There are no obvious 'new' peaks evident in the gamma spectrum obtained in this setting compared to those from the ^{203}Au setting, shown in Fig. 5.32, and the statistics are roughly the same. Combining the data from the two experiments increases the statistics but reveals no definite new peaks compared with those mentioned in section 5.4.1.

Beta-delayed gamma spectrum

The prompt, beta-delayed gamma spectrum, using a 60 s time correlation between implantation and β decay, is shown in Fig. 5.28. This has intense peaks at 436, 691 and 722 keV, known to be from the decay of ^{204}Hg [82]. These were also observed in the ^{203}Au setting (see Section 5.4.1). The intense peak at 436 keV corresponds to the decay from the 2^+ to the 0^+ ground state in ^{204}Hg. The peak at 691 keV is that corresponding to the $4^+ \rightarrow 2^+$ transition and the 722 keV transition is due to decay from a 2^+ state to the yrast 4^+ level [82]. The characteristic K_α and K_β X-rays are also clearly visible. Unlike the beta-delayed gamma spectrum from the ^{203}Au setting, shown in Fig. 5.33, here there are several strong peaks from the decay of ^{205}Hg.

Beta electron spectrum

The beta electron spectrum, using a 60 s time correlation, is shown in Fig. 5.29. Although there are apparent peaks here (at 436 and 543 keV), it is difficult here to identify any conversion electron K-L doublets since such doublets should be about 66 keV apart (the difference between 80 keV, the binding energy of the K-electron, and 14 keV, the binding energy of the L-electron) and should be such that the area under the L-peak is considerably less than that under the K-peak (the precise relative areas depending on multipolarity and type of transition). The peak around 825 keV is due to correlation with the K conversion electron from ^{205}Au, described above.

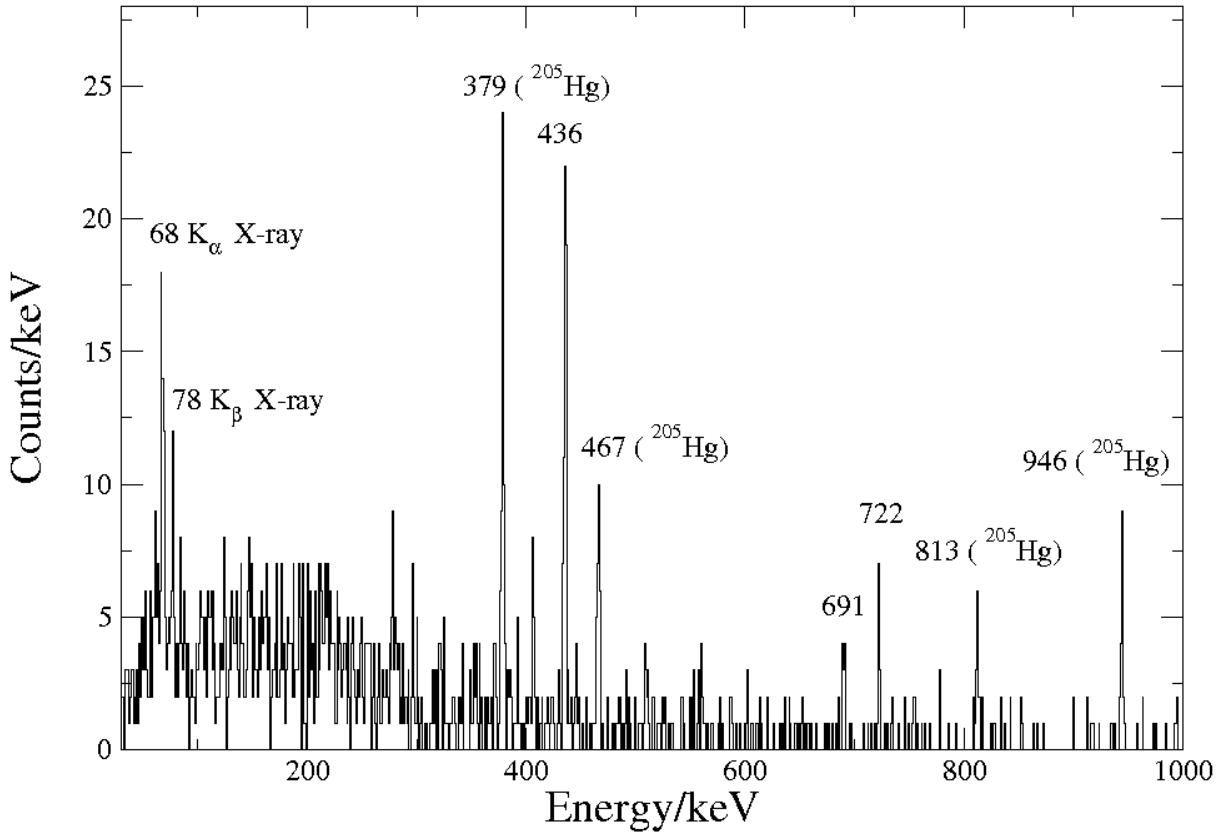

Figure 5.28: ^{204}Au beta-delayed, prompt (Δt=0-0.35 μs) gamma spectrum using an implant-decay time correlation of 60 s.

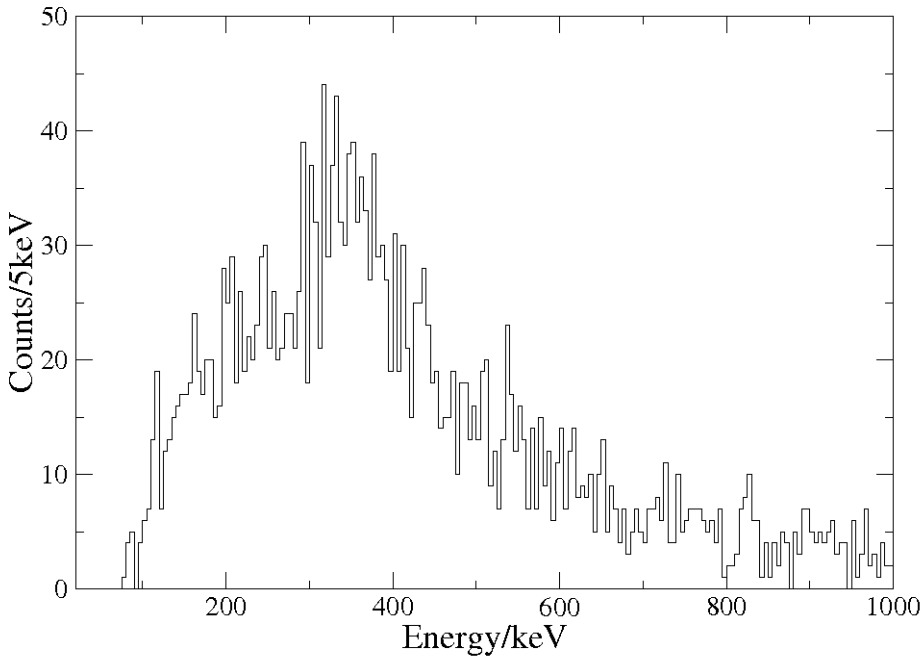

Figure 5.29: ^{204}Au beta electron spectrum.

5.3.3 ^{202}Pt

Gamma spectrum from isomeric decays on implantation

The gamma spectrum for ^{202}Pt obtained in the present experiment, using $\Delta t = 0.3 - 93\,\mu$s, is shown in Fig. 5.30.

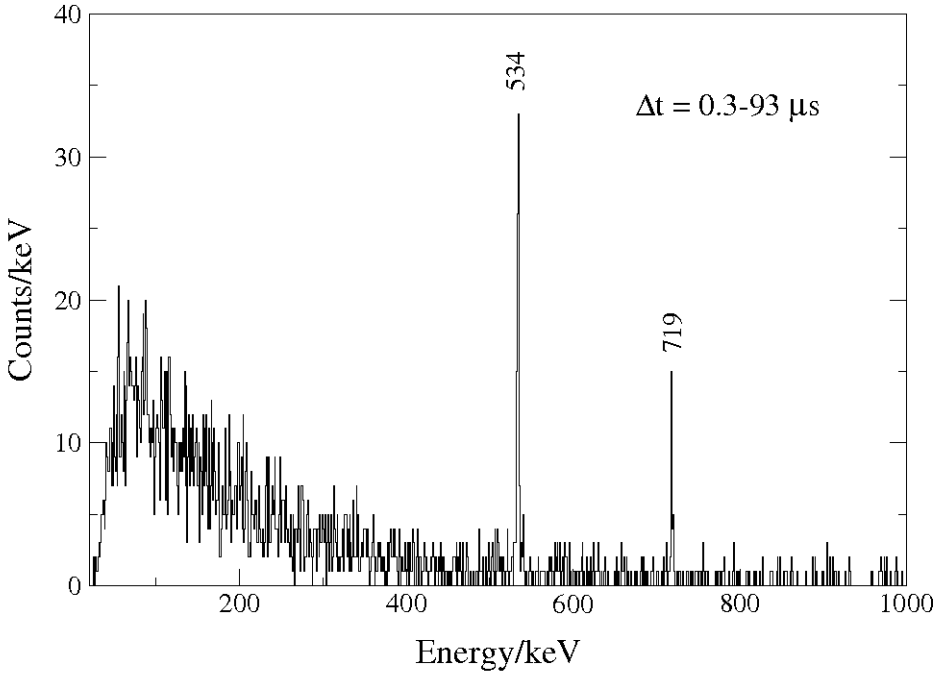

Figure 5.30: Gamma spectrum for implanted ^{202}Pt ions.

There are clear gamma peaks at 534 and 719 keV. These correspond to previously reported gamma transitions from an isomeric state at 1788.5 keV of spin-parity 7^- with possible configuration $\pi h_{11/2}^{-1} \otimes \pi d_{3/2}^{-1}$ [76]. The intensities of the 534 and 719 keV peaks, corrected for efficiency, are 460(65) and 258(52) respectively, consistent with the level scheme proposed by Caamaño *et al.*, shown in Fig. 5.51, in which the 534 keV transition is a doublet, thus having approximately double the intensity of the 719 keV transition. Steer confirmed the structure proposed by Caamaño and obtained an improved half-life of 141(7) μs [79]. The present experiment resulted in about 14 000 ^{202}Pt ions, cf. Table 5.8, compared with about 300 000 in Steer's analysis, so no further analysis of the isomeric decay has been performed.

Given the very long half-life of ^{202}Pt (44(15) h [82]), it is impossible to obtain a spec-

trum for beta-delayed gammas for this nuclide in this analysis, thus no information on the levels in ^{202}Au can be deduced. However, the gamma rays from an isomeric level in ^{202}Au were detected and are described in Section 5.4.3. Similarly, it was impossible to produce a spectrum for the beta electrons since the required correlation time is too long for this experimental setup.

5.3.4 Discussion of ^{205}Au

Although the shape of this nuclide is essentially spherical, there is a very small quadrupole deformation, ϵ_2=0.008 [87], indicating that there are several possible energies for the various excited states, depending on the value of Ω, the projection of **j** on the axis of symmetry, cf. Fig 2.7. From the relevant Nilsson diagram, Fig. 2.8, one would expect the ground state of ^{205}Au to have spin-parity $3/2^+$, since it has three proton holes, i.e. the $s_{1/2}$ state is empty and there is one hole in the $2d_{3/2}$ state. A level scheme for ^{205}Au, calculated using the OXBASH code [88] by the author, is shown in Fig. 5.31. The khhe interaction invoked for these OXBASH calculations involves TBMEs (two-body matrix elements) as described by Rydström [89], being based on the Kuo-Brown interaction, including core polarisation [90]. The proton-hole energies were taken from the experimental level scheme of ^{207}Tl [91, 92]. This parameterisation gives a good description of the reported excited states in the two proton-hole ^{206}Hg and a reasonable description for the four proton-hole nucleus ^{204}Pt. Although further modifications to the TBMEs were made by H. Grawe in order to describe better the N = 126 isotones below lead (the results being published and presented in reference [13], also in the Appendix), this author did not apply such modifications to the interaction in the calculations described here.

The level scheme of Fig. 5.31 indicates that there is a $\pi h^-_{11/2}$ excited state at an energy of 921 keV. Since this state has a high spin relative to the lower states, it can only decay by high multipolarity transitions (E3 to the $5/2^+$, M4 to the $3/2^+$ states, E5 to the $1/2^+$state), implying that it should have a relatively long half-life, thus that it should be isomeric. Of the two possible M4 transitions, that to the ground state is more likely since it has a higher energy, thus lower half-life; Weisskopf estimates for the half-lives of

decay transitions from the $h^{-}_{11/2}$ state are given in Table 5.14, confirming M4 decay to the ground state as the most likely explanation for the detection of the conversion electrons in this experiment.

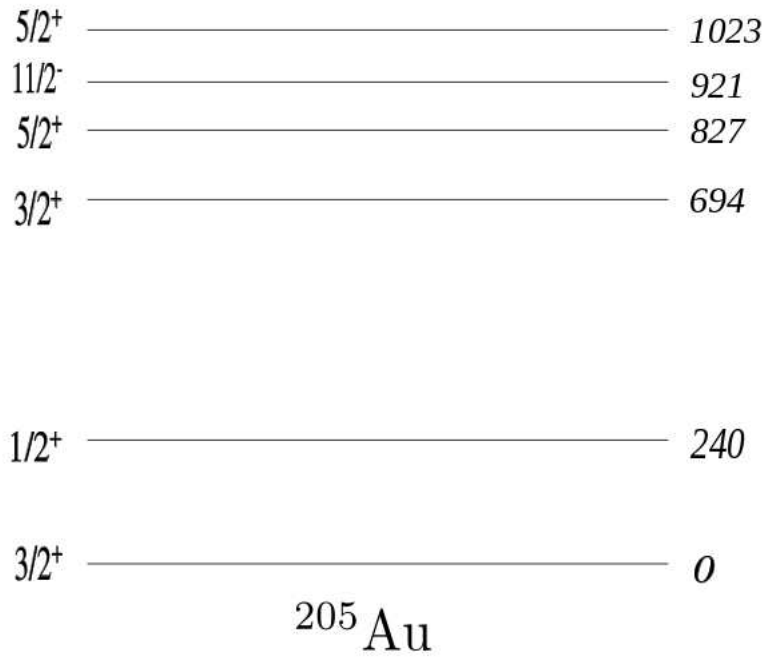

Figure 5.31: Shell model levels for ^{205}Au constructed using the OXBASH code.

Table 5.14: Weisskopf half-life estimates for decay from the $\frac{11}{2}^{-}$ state in ^{205}Au.

Transition	$\mathbf{E_\gamma}$ **(keV)**	**Type**	$\mathbf{T^\gamma_{W1/2}}$ **(s)**
$11/2^-$ to $5/2^+$	78	E3	28(4)
$11/2-$ to $3/2^+$ at 694 keV	227	M4	3.2(2) x 10^6
$11/2-$ to $1/2^+$	681	E5	3.89(9) x 10^5
$11/2-$ to $3/2^+$ g.s.	905	M4	12.4(2)

5.4 ^{203}Au setting

5.4.1 ^{204}Au

Gamma spectrum from isomeric decays on implantation

^{204}Au undergoes β decay with a half-life of 39.8(9) s and has a ground state of 2^- [82]. A number of prompt γ rays have been previously observed; Steer *et al.* [79, 84] analysed data from passive stopper experiments at GSI, observing gamma peaks at 839 and 977 keV from an isomer with a half-life of 2.1(3) μs using a $\Delta t = 0.5 - 6.5\,\mu$s time window. The gamma spectrum for ^{204}Au obtained in the present experiment, using $\Delta t = 0.1 - 90\,\mu$s, is shown in Fig. 5.32.

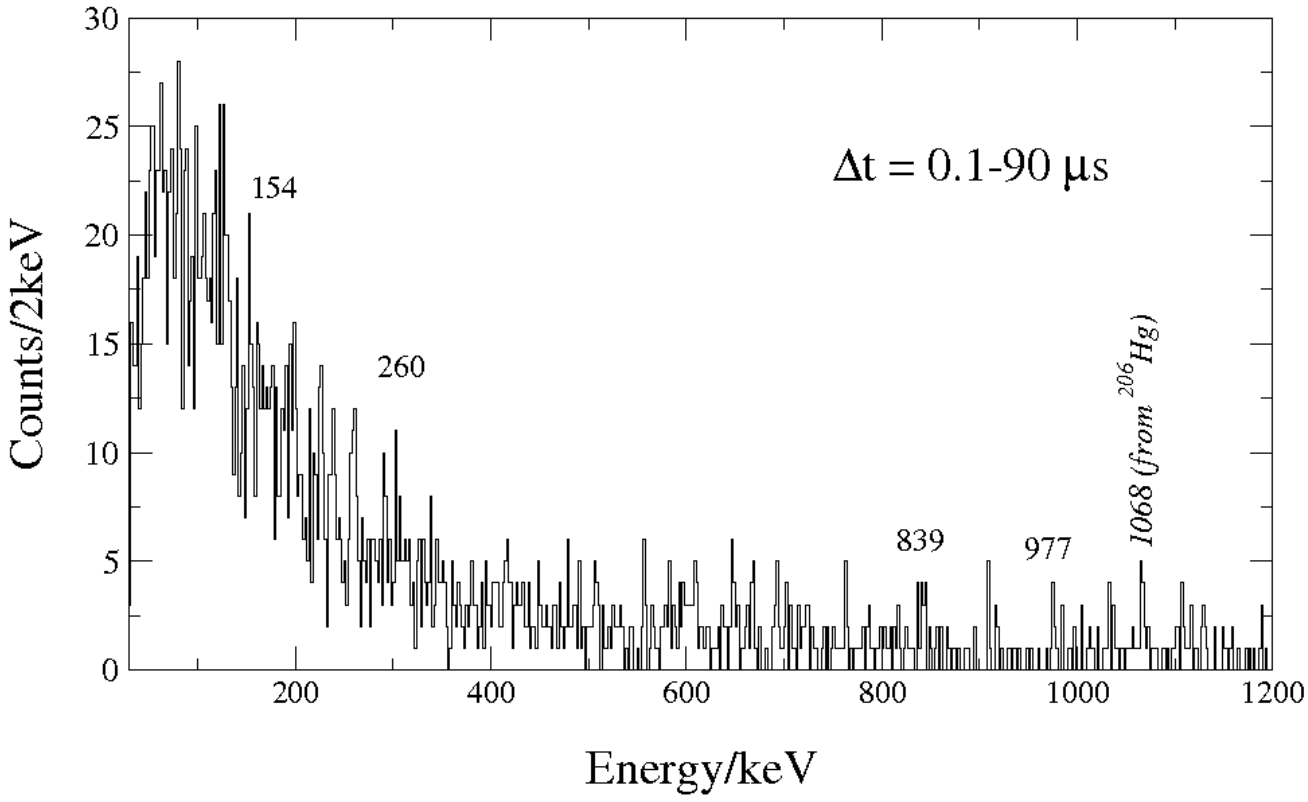

Figure 5.32: Gamma spectrum for implanted ^{204}Au ions.

The gamma peaks with the greatest intensities here, after correcting for efficiency, are at 154, 260 and 1068 keV (due to contamination from ^{206}Hg). The 839 and 977 keV peaks are just observable. Use of a shorter time gate of $\Delta t = 0.1 - 10\,\mu$s, similar to that

employed by Steer, revealed no extra peaks. This is not surprising, given that Steer had about 135 000 ^{204}Au ions in his analysis, whereas in this experiment there were about 7000 (cf. Table 5.9).

Beta-delayed gamma spectrum

The prompt, beta-delayed gamma spectrum, using a 60 s time correlation between implantation and β decay, is shown in Fig. 5.33 and may be compared with that of Fig. 5.28 for the ^{205}Au experimental run. There is some contamination from the decay of ^{203}Au, giving gamma rays at 318 and 368 keV. There is also a small peak (not shown in Fig. 5.33) at 1511 keV, from the decay of a state at 1947.68 keV with spin-parity 1^+ or 2^+ [82]. The normalised intensities are listed in Table 5.15.

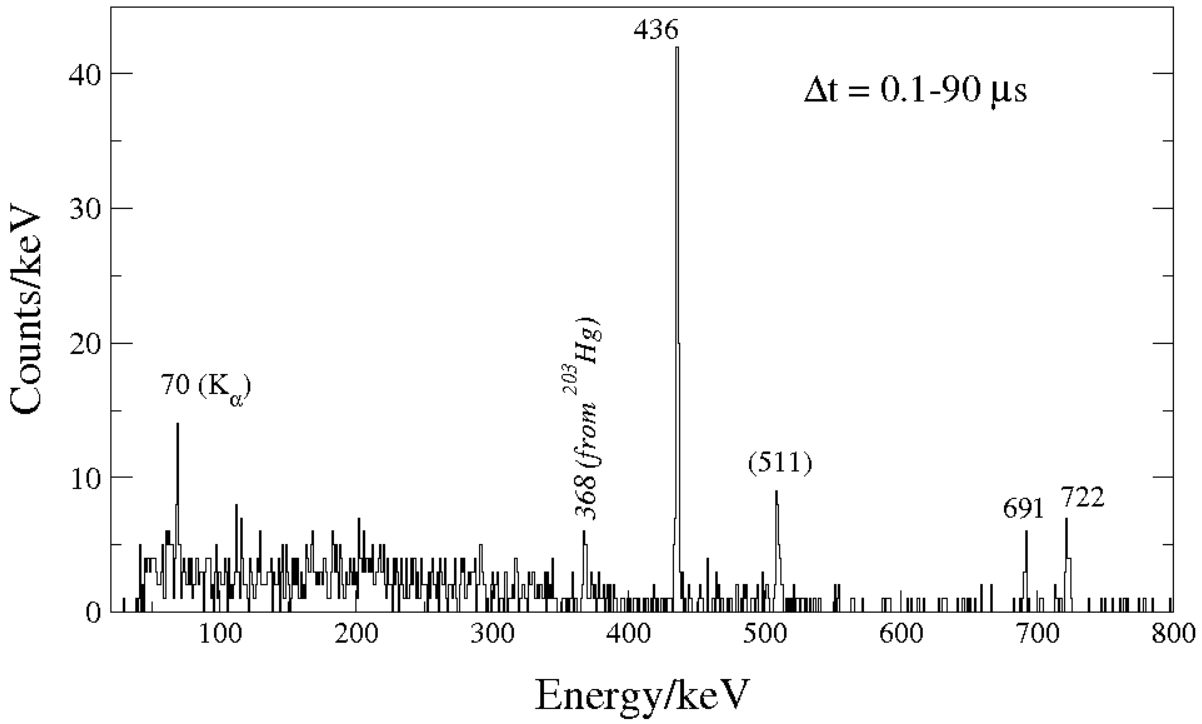

Figure 5.33: ^{204}Au beta-delayed, prompt($\Delta t = 0 - 0.35\,\mu$s) gamma spectrum using a 60 s implant-decay correlation time with DGF time window of $\Delta t_{DGF} = 0.1 - 90\,\mu$s. The 511 keV peak is from background.

The statistics were low in this spectrum, but summing the $\gamma - \gamma$ coincidence spectra gated on the ^{204}Hg decays at 436, 691 and 722 keV, shown in Fig. 5.34, indicates that these three decays are in mutual coincidence.

Table 5.15: Intensities of beta-delayed gamma peaks for ^{204}Hg, corrected for efficiency and normalised to 100 for the strongest peak. To obtain the absolute intensities, multiply by 4.177.

E_γ (keV)	**FWHM**	**Intensity**
70	2.3	15(5)
318	1.9	9(3)
368	1.9	12(5)
436	1.2	100(14)
510	3.9	34(8)
691	1.0	14(6)
722	2.8	28(8)
1511	5	12(9)

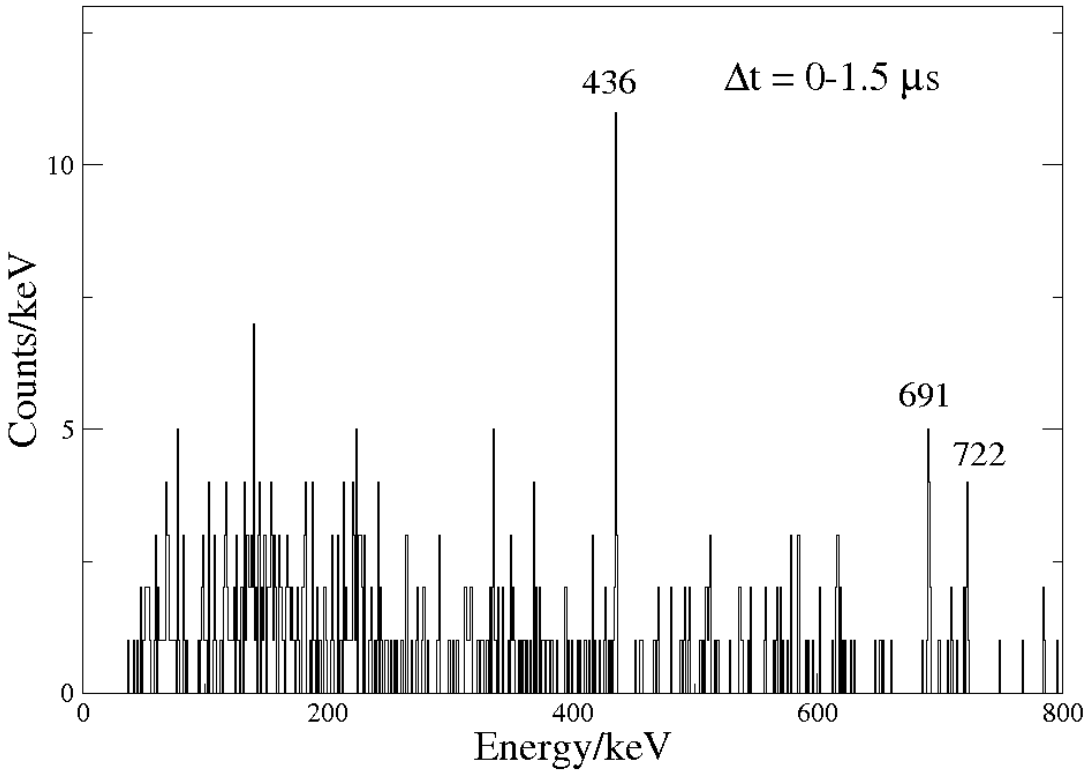

Figure 5.34: ^{204}Au beta-delayed $\gamma - \gamma$ coincidence ($\Delta t = 0 - 1.5\,\mu$s) spectrum using an implant-decay time correlation of 60 s.

The beta electron spectrum, using the same time correlation of 60 s, is, unsurprisingly, very similar to that of Fig. 5.29, so it is omitted here.

5.4.2 ^{203}Au

Gamma spectrum from isomeric decays

^{203}Au has a ground state of spin-parity $3/2^+$ with a half-life of 60(6) s; several low-lying energy levels are known [82]. Caamaño *et al.* [76], and more recently Steer [79], observed a gamma transition at 563 keV in this nuclide with a half-life of 140(44) μs, although no assignment of spin or parity for the isomeric state was made.

The gamma spectrum from the present experiment for isomeric decay from implanted ^{203}Au ions, shown in Fig. 5.35, shows clear peaks at energies 75, 198, 269, 352 and 563 keV, and smaller peaks at 383 and 833 keV. The peak at 198 keV is due to background, ^{19}F(n,n'γ)^{19}F, as are those at 583 keV (from ^{212}Po, not labelled), 596 keV (not labelled) and 609 keV, the latter two being peaks from ^{74}Ge(n.n'), and 911 keV (from ^{228}Ac). The gamma intensities, corrected for efficiency and normalised to 100 for the strongest peak, are given in Table 5.16. The lifetime obtained for the 563 keV transition, 500(120) μs (cf. Fig. 5.36), is somewhat longer than that obtained by Steer, despite similar statistics.

Table 5.16: Gamma intensities, corrected for efficiency and normalised to 100 for the strongest peak, for implanted ^{203}Au ions. To obtain the absolute intensities, multiply by 54.86.

E_γ (keV)	**FWHM**	**Intensity**
75	2.4	29(4)
198	1.5	15(3)
269	0.7	6(2)
352	2.7	17(3)
383	1	7(2)
511	4.1	42(4)
563	2.2	100(7)
609	1.8	20(3)
833	2	13(3)
911	3.2	160(18)

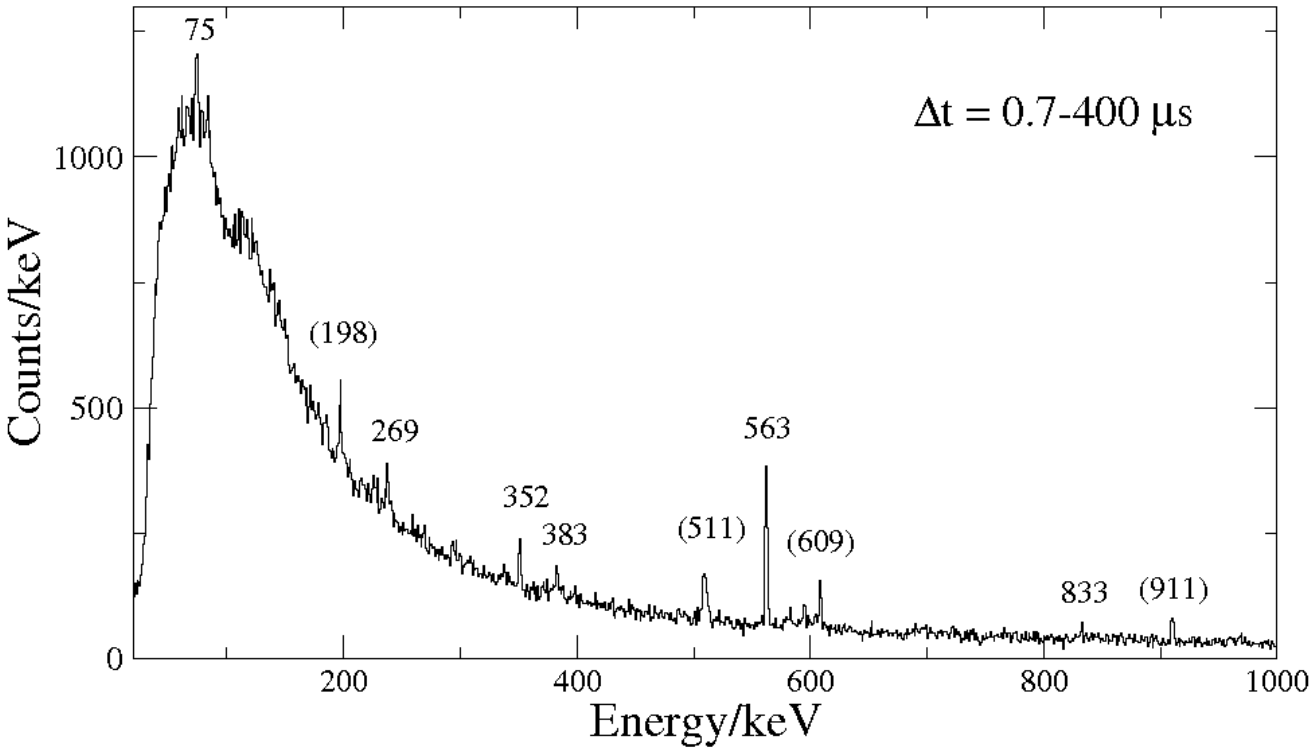

Figure 5.35: Gamma spectrum from isomeric decays in ^{203}Au. Background peaks are enclosed in brackets.

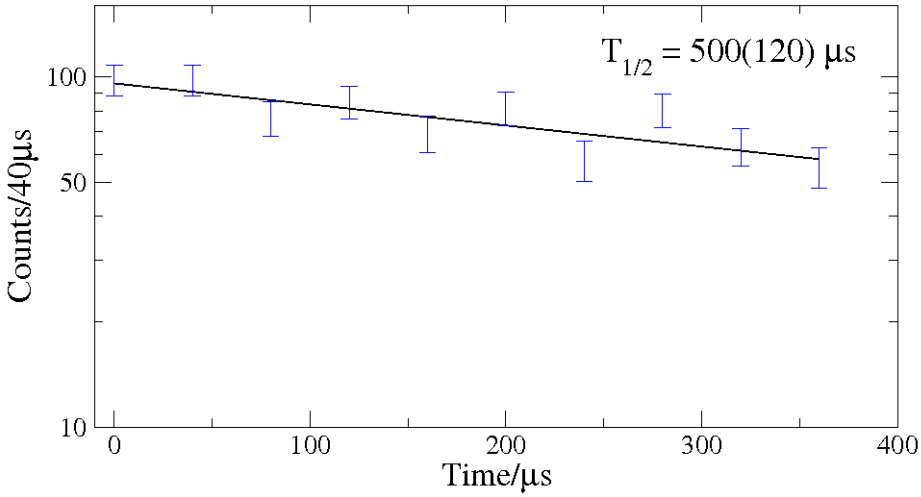

Figure 5.36: Lifetime fit for the 563 keV transition from an isomer in ^{203}Au.

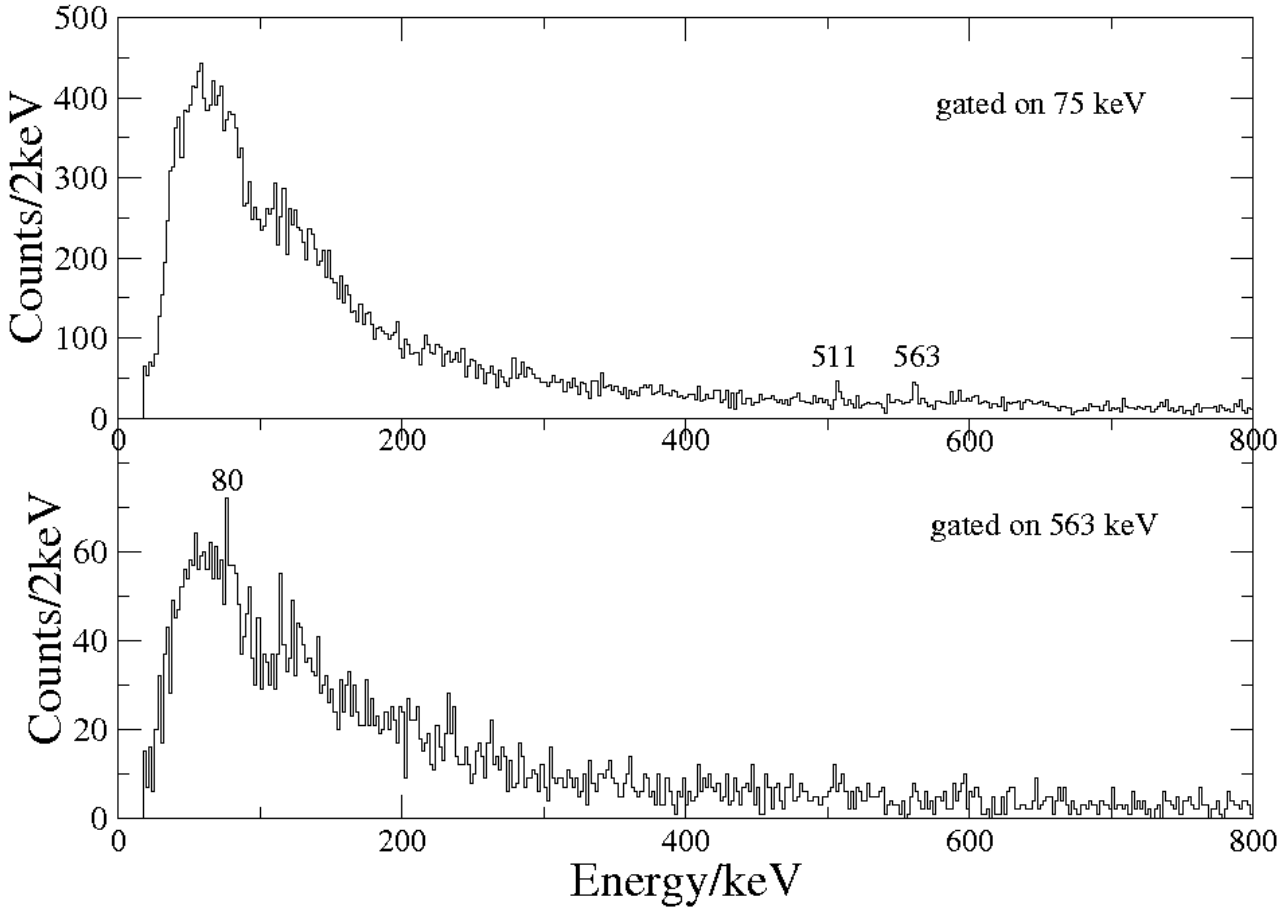

Figure 5.37: $\gamma - \gamma$ coincidence spectra for implanted ^{203}Au ions gated on the 75 and 563 keV transitions.

Beta-delayed gamma spectrum

The beta-delayed, prompt gamma spectrum, using a 60 s time correlation between implantation and β decay, is shown in Fig. 5.38. This has a very intense peak at 436 keV due to the decay of ^{204}Hg. The 691 and 722 keV peaks are also from this decay (as noted above in Section 5.3.2). Also from this decay are low intensity peaks at 1392 keV (from decay from a state at 1828.8), 1415 keV (from decay from a state at 1851 keV), 1512 keV (from decay from a state at 1947.7 keV) and 1704 keV (from a state at 2140.8 keV, not shown on Fig. 5.38), all decaying to the 2_1^+ state at 436.6 keV [82].

The peaks proper to the gamma decay of ^{203}Hg evident in Fig. 5.38 are 217, 318 and 369 keV from the states shown in Fig. 5.39. The K_α X-ray at 69 keV is clearly visible; the K_β at 77 keV has a lower intensity and is not visible on Fig. 5.38. The intensities, corrected for efficiency and normalised to 100 for the strongest peak, are shown in Table 5.17.

It is evident that there is considerable contamination of beta-delayed gammas from ^{204}Au into the ^{203}Au gate. The reason for this is that the correlation algorithm (cf. Section 4.4.1) is rather crude; any gamma rays emitted from the same pixel or neighbouring pixels as that pixel in which the ^{203}Au ion was implanted are considered as correlated, even though they may be due to the decay of other implanted ions within the selected implant-β decay correlation time (60 s here). It may be recalled that there was a similar contamination from the decay of ^{203}Au in the beta-delayed gamma spectrum of ^{204}Au, described above.

The reason that the intensity of the ^{204}Hg peaks is greater here, gated on an implantation of ^{203}Au, than in the spectrum gated on an implantation of ^{204}Au, shown in Fig. 5.33, is that there are far more implanted ^{203}Au ions than ^{204}Au ions (cf. Table 5.9), thus for each implanted ^{204}Au ion there is a very high probability that electrons in the same pixel or neighbouring pixels will in fact be from the beta decay of ^{203}Au into ^{203}Hg, thus the gammas associated with the beta decay of ^{204}Au will appear as correlated to the implantation of ^{203}Au. The half-lives of these two nuclides are very similar, at 40 and 60 s [82], so it is impossible to separate their gamma decays using the algorithm described above simply by applying different implant-β decay correlation times.

The intensities of the ^{204}Hg peaks in the ^{203}Au beta-delayed gamma spectrum were sufficient to allow a $\gamma - \gamma$ coincidence spectrum to be created, cf. Fig. 5.40, showing the sum of the gamma spectra gated on the transitions at 436, 691 and 722 keV in ^{204}Hg. This shows that these transitions are in mutual, prompt coincidence and that they are not in coincidence with the ^{203}Hg transitions mentioned above. $\gamma - \gamma$ coincidence spectra were created for the ^{203}Hg transitions but, the statistics being low, were inconclusive.

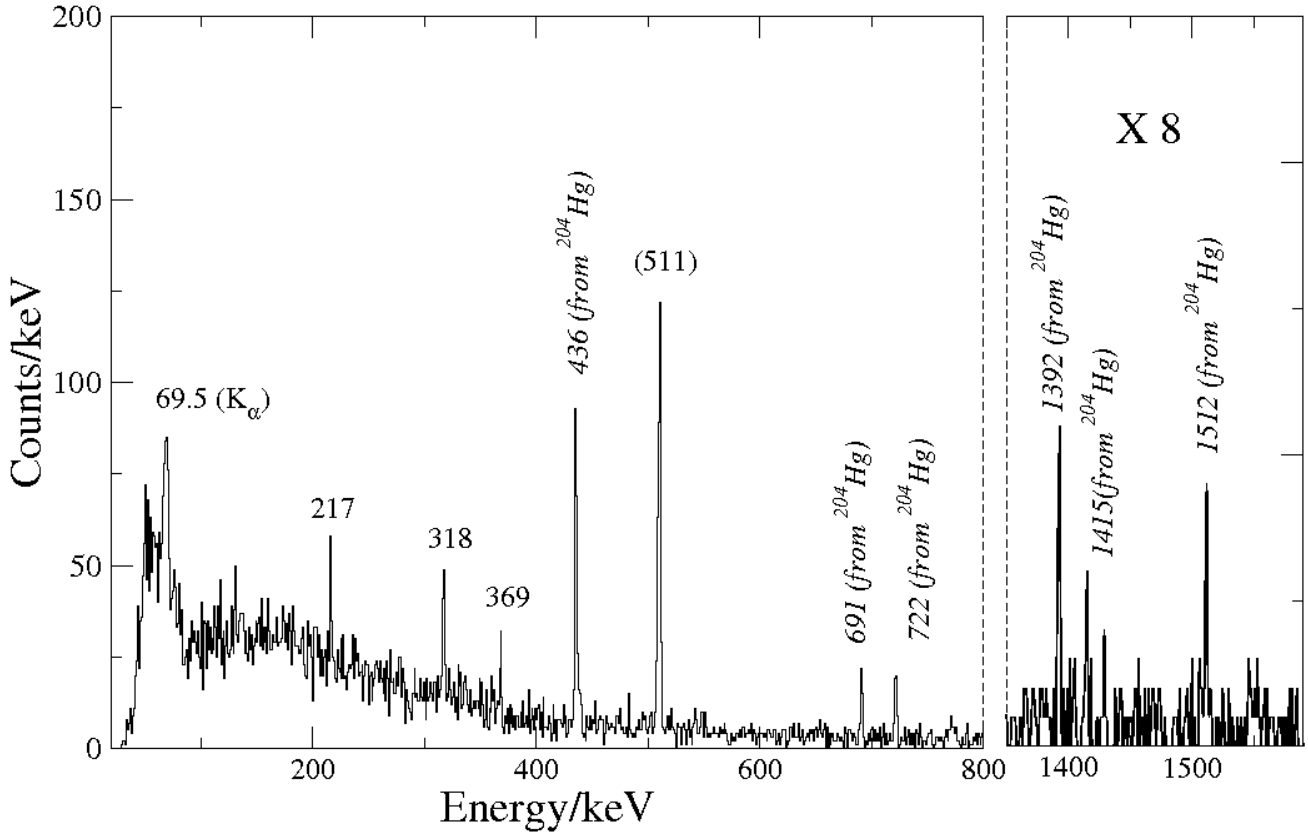

Figure 5.38: ^{203}Au beta-delayed, prompt ($\Delta t = 0 - 0.35\,\mu$s) gamma spectrum using a 60 s implant-β decay correlation time.

Beta electron spectrum

The beta electron spectrum for ^{203}Au, using the same time correlation, is shown in Fig. 5.41. There are no obvious peaks and a reduction of the time correlation neither produces new peaks nor enhances existing ones.

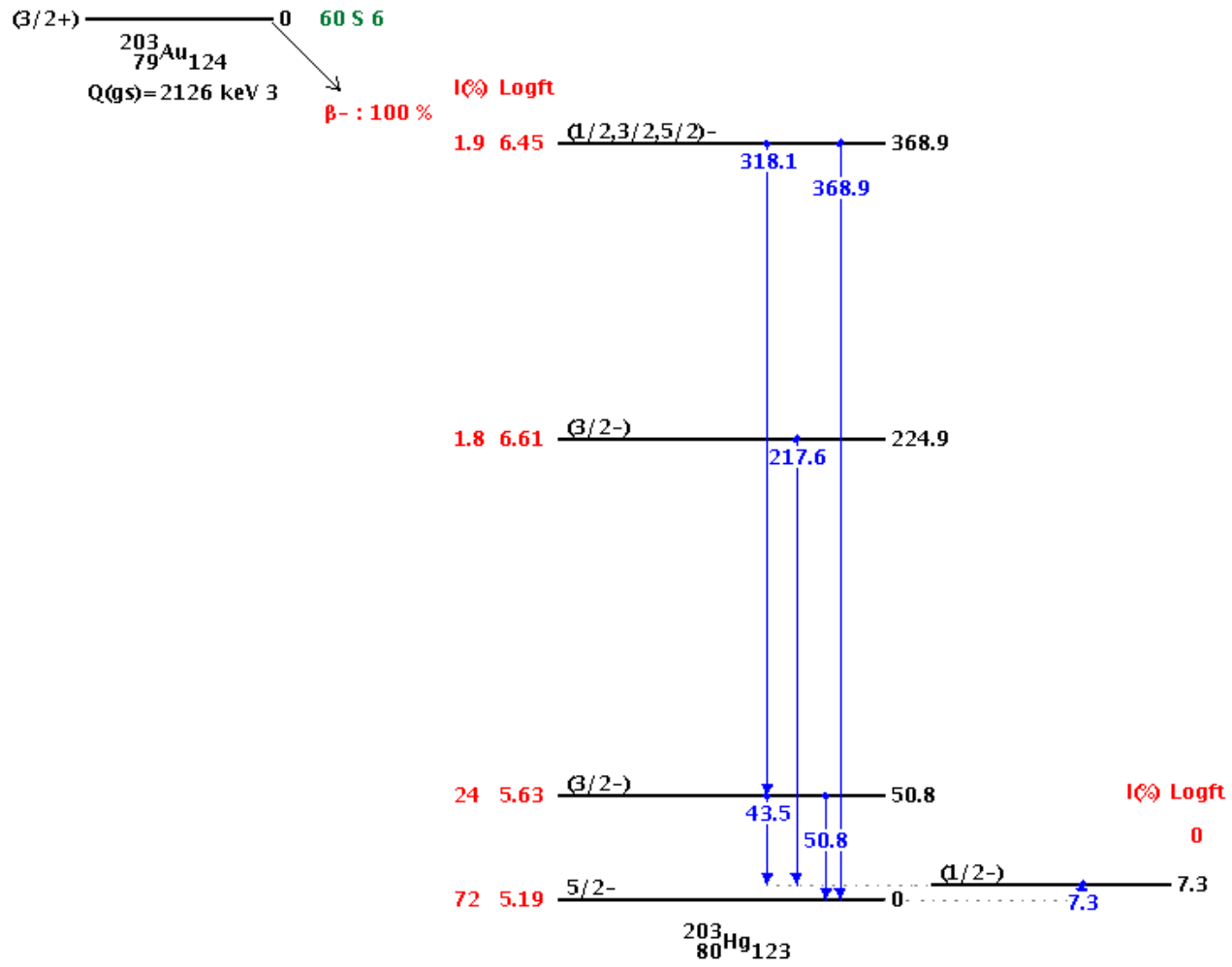

Figure 5.39: ^{203}Au–^{203}Hg decay scheme, taken from the National Nuclear Data Center database (http://www.nndc.bnl.gov/).

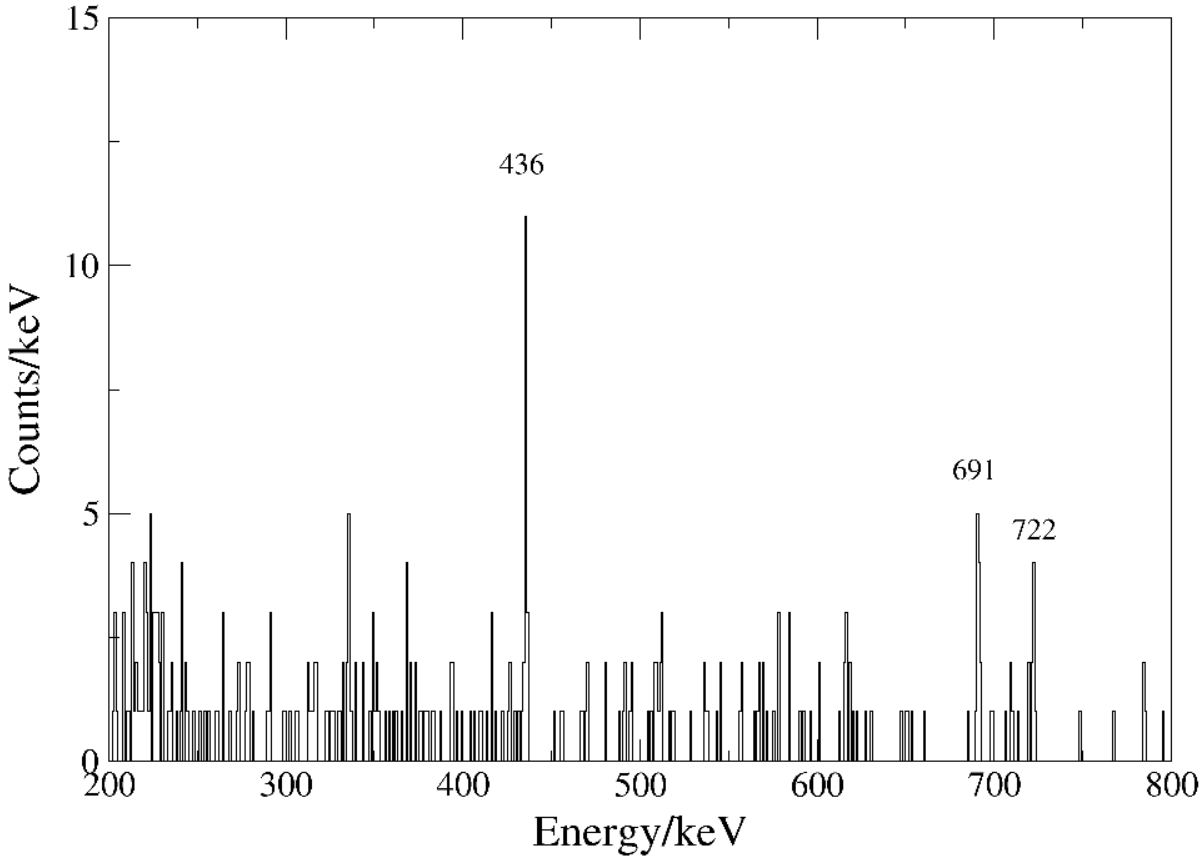

Figure 5.40: ^{203}Au beta-delayed, prompt ($\Delta t = 0 - 0.35\,\mu$s) $\gamma - \gamma$ coincidence spectrum using a 60 s implant-decay correlation. This spectrum is the sum of individual coincidence spectra gated on the transitions at 436, 691 and 722 keV in ^{204}Hg.

Table 5.17: Intensities of beta-delayed gamma peaks, corrected for efficiency and normalised to 100 for the strongest peak, for ^{203}Hg. To obtain the absolute intensities, multiply by 23.42.

E_γ (keV)	FWHM (keV)	Intensity
44	1	6(2)
50	1	12(3)
69.5	3	21(3)
77	2	4(2)
217	1.7	10(2)
318	1.7	14(2)
369	1.5	9(2)
436	2.8	53(5)
511	3.2	100(8)
691	2.5	20(3)
722	2.6	22(3)
1392	1.9	12(3)
1415	2	5(2)
1512	2	8(2)
1704	3	3(2)

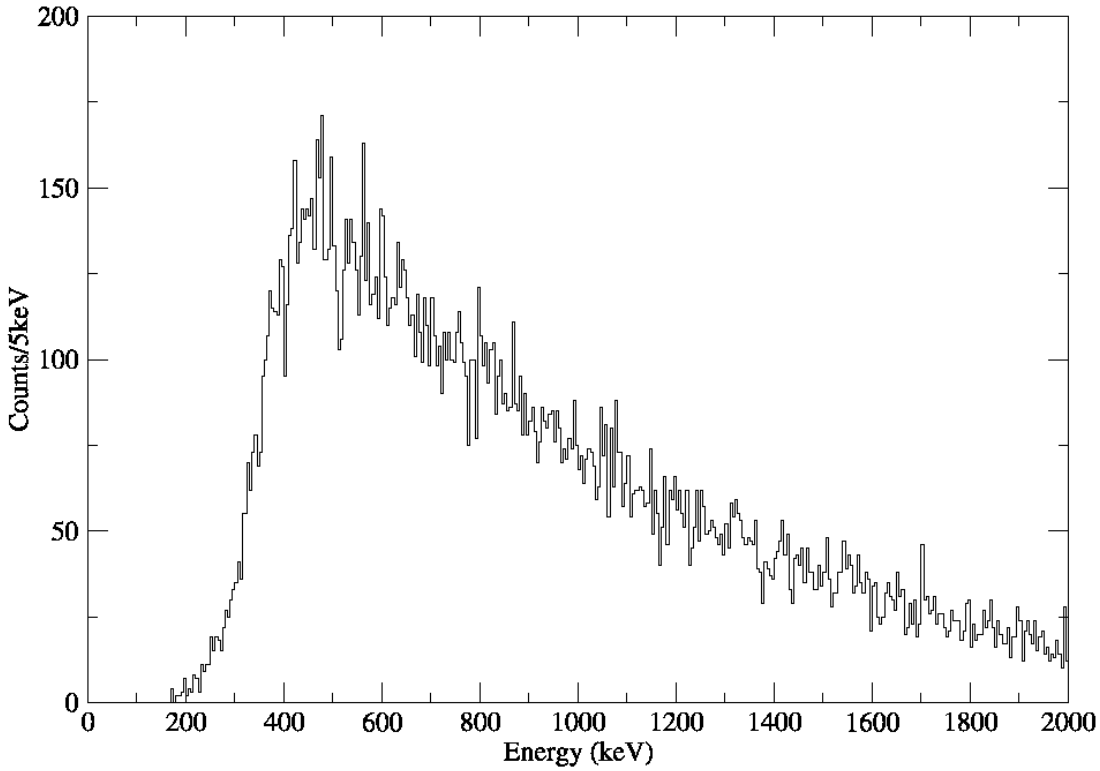

Figure 5.41: ^{203}Au beta electron spectrum using a 60 s implant-decay correlation time.

5.4.3 ^{202}Au

Gamma spectrum from isomeric decays

As with ^{204}Au, relatively few ions (around 11 000) of ^{202}Au were produced. The ground state is reported to be of spin-parity 1^- with half-life 28.4 s [82]. Steer found gamma peaks at 138 and 414 keV in mutual coincidence from an isomer with half-life 13.1(5) ns [79]. These peaks are confirmed in this experiment. The gamma spectrum for implanted ions using the short-range TDCs is shown in Fig. 5.42. The intensities, corrected for efficiency and normalised to 100 for the strongest peak, are shown in Table 5.18.

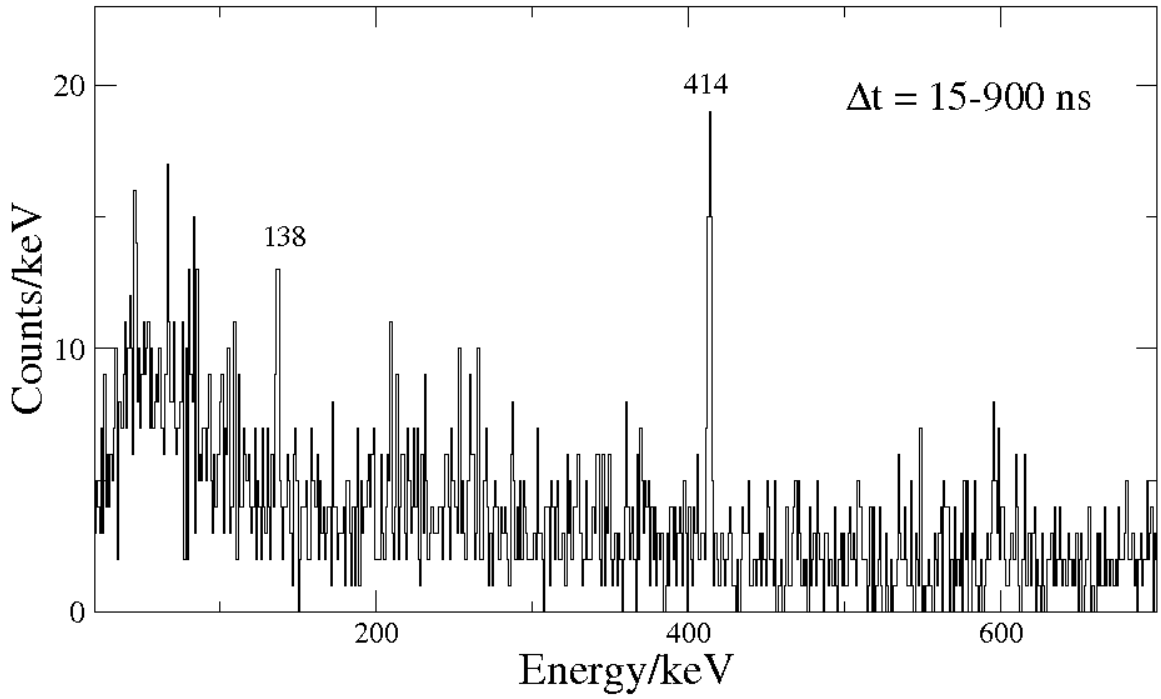

Figure 5.42: Gamma spectrum for implanted ^{202}Au ions for $\Delta t = 15 - 900$ ns using short-range TDCs.

Table 5.18: Intensities of gamma peaks, corrected for efficiency and normalised to 100 for the strongest peak, for ^{202}Au.

E_γ (keV)	FWHM (keV)	Intensity
137	2.1	30(8)
414	2.7	100(16)

Beta-delayed gamma spectrum

The beta-delayed gamma spectrum, using an implant-β decay time correlation of 60 s, is shown in Fig. 5.43. The statistics are so low that no obvious peaks are visible. However, isomeric decays in the daughter, ^{202}Pt, have already been described in Section 5.3.3.

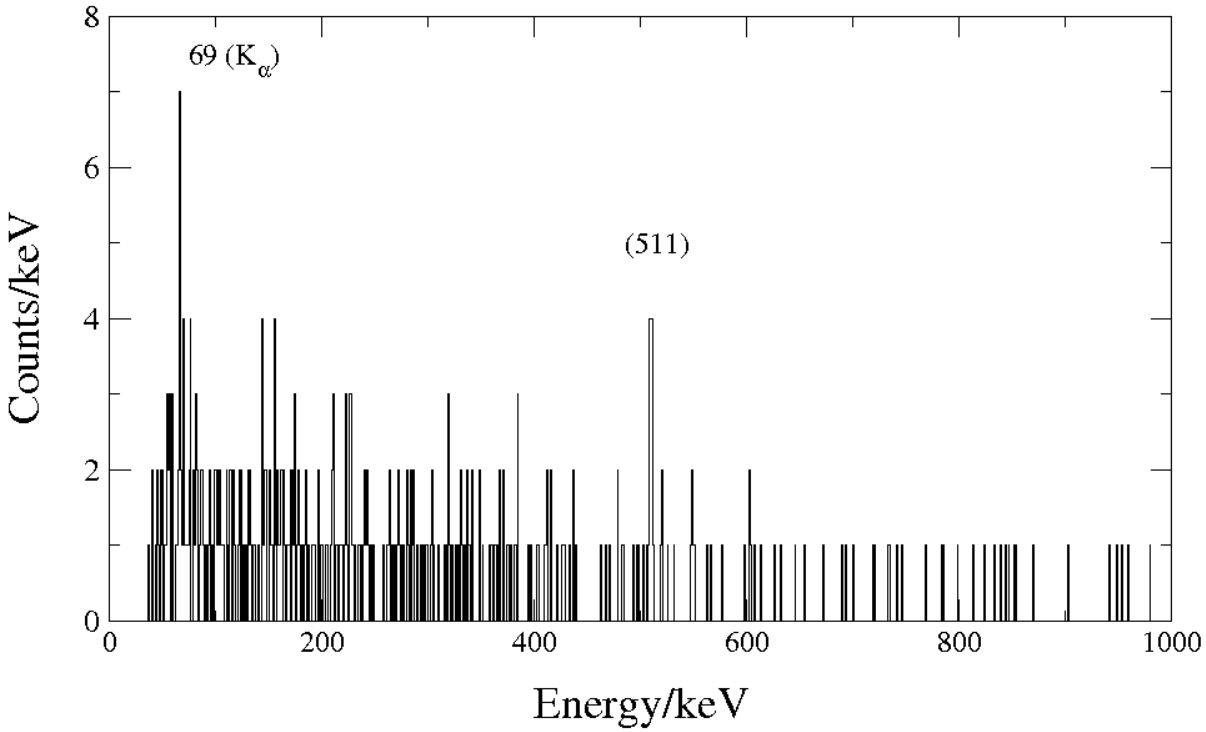

Figure 5.43: Beta-delayed gamma spectrum, using 60 s implant-decay correlation time, for implanted ^{202}Au ions for $\Delta t = 0 - 370\,\mu$s.

Beta electron spectrum

The beta electron spectrum, using the same 60 s time correlation, is shown in Fig. 5.44 but reveals nothing of interest.

5.4.4 ^{205}Hg

Gamma spectrum from isomeric decays on implantation

The gamma spectrum for implanted ions gated on the ^{205}Hg region of the PID, using $\Delta t = 0.1 - 90\,\mu$s, is shown in Fig. 5.45. There are gamma peaks at 810, 950 and 1015 keV.

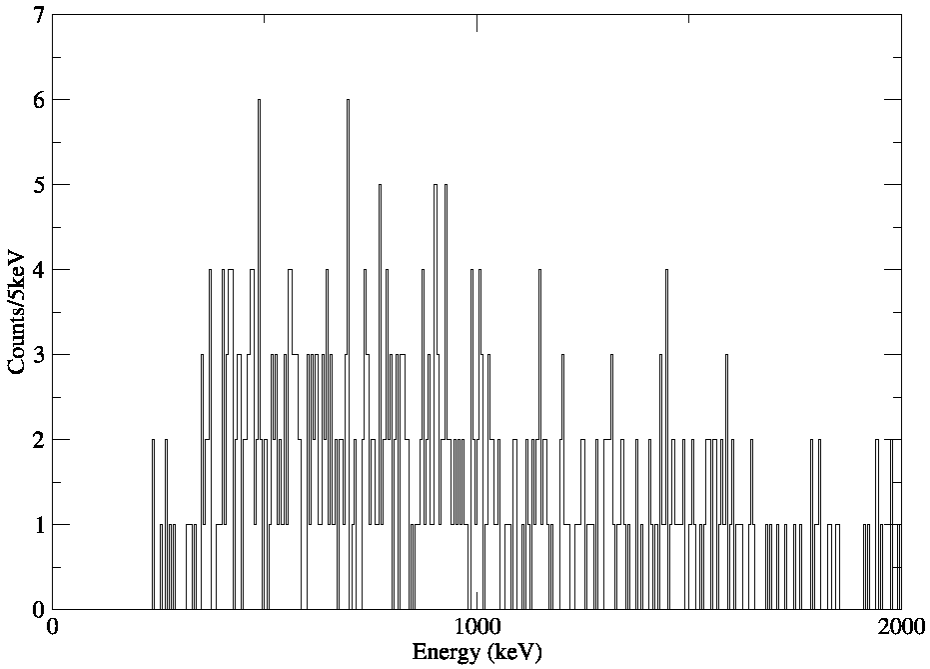

Figure 5.44: ^{202}Au beta electron spectrum using an implant-decay time correlation of 60 s.

The first two confirm the results of Steer [84], who reported a new isomer with a half-life of $\sim 6\,\mu$s in this nuclide with four identified transitions: 227, 723, 810 and 950 keV, all in mutual coincidence. Steer's proposed scheme places the 227 and 723 keV transitions as M1 decays in cascade, parallel to an E2 950 keV decay which would be expected to be more intense, cf. Fig. 5.46. It is not surprising, then, that the results of this experiment, with lower statistics, show no evidence of the 227 and 723 keV transitions. The 1015 keV transition was already known to be a decay from an isomer with a half-life around 1 ms [93]. Steer [79] measured the half-life of this $13/2^+$ isomer to be 1.09(4) ms. A proposed scheme is shown in Fig. 5.47. The intensities, corrected for efficiency and normalised to 100 for the strongest peak, are shown in Table 5.19. Using a longer time gate, $\Delta t = 0.7 - 400\,\mu$s, showed the transition at 379 keV as a peak with the same intensity, after correcting for efficiency, as the 1015 keV peak, both having about 30 counts.

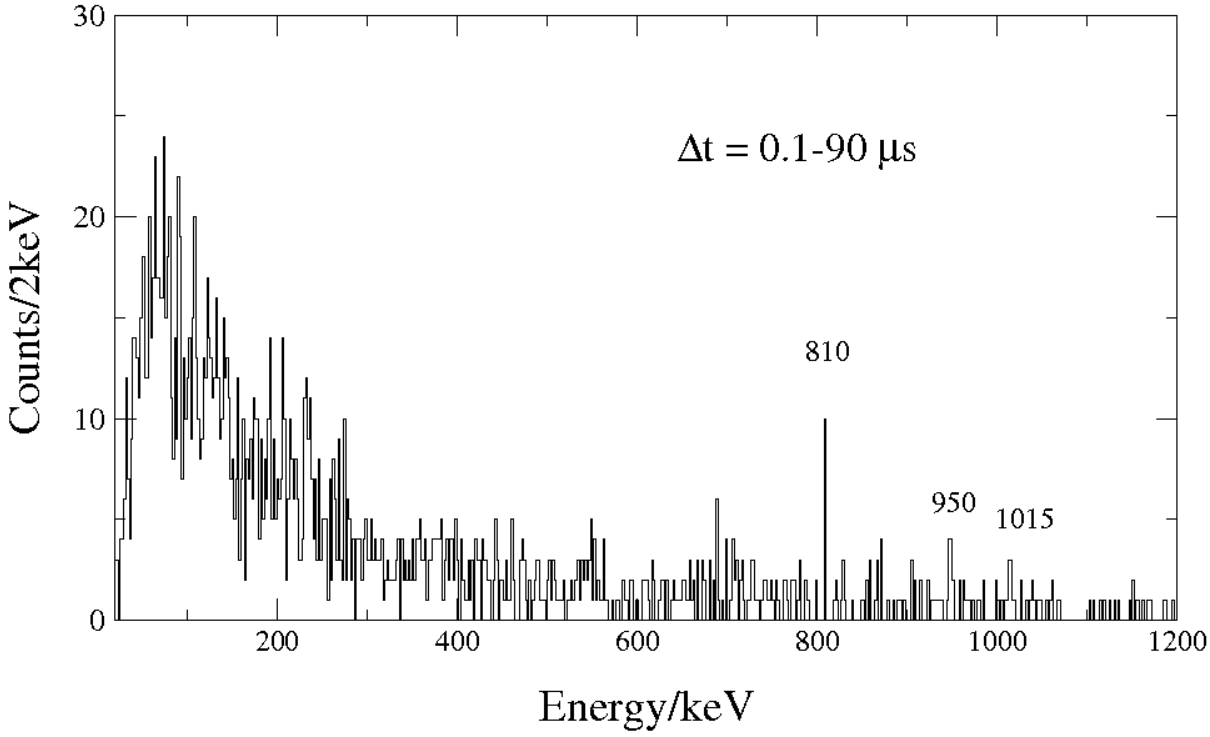

Figure 5.45: Gamma spectrum from isomeric decays on implantation of ^{205}Hg.

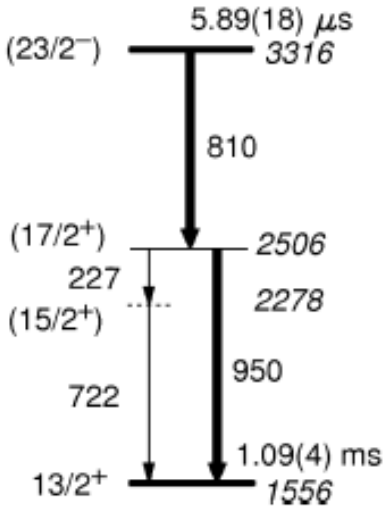

Figure 5.46: A partial decay scheme for ^{205}Hg from a shell model calculation, taken from Steer [79].

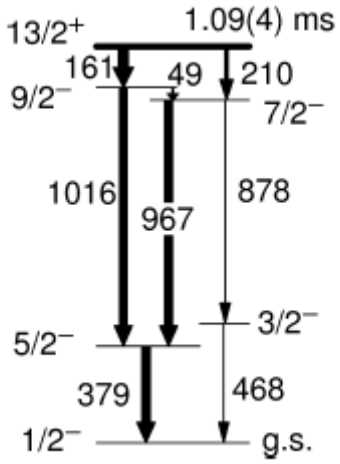

Figure 5.47: A partial decay scheme from a 6 μs isomer in ^{205}Hg, taken from references [93, 94, 95].

Table 5.19: Intensities of gamma peaks, corrected for efficiency and normalised to 100 for the strongest peak, for ^{205}Hg. To obtain the absolute intensities, multiply by 0.636.

E_γ (keV)	**FWHM (keV)**	**Intensity**
810	2	100(43)
950	4	99(50)
1015	2	70(53)

5.4.5 ^{206}Hg

Gamma spectrum from isomeric decays

^{206}Hg has a ground state of spin-parity 0^+ with a half-life of 8.32(7) m [82]. It has two very intense, known, gamma transitions which depopulate a 5^- isomeric state at about 2102 keV with half-life 2.15 μs. These transitions (cf. Fig. 5.48) are at 1034 keV ($5^- \rightarrow 2^+$) and 1068 keV ($2^+ \rightarrow 0^+$ ground state) [96]. Also present is a transition at 363 keV, from decay of the state above the isomer: $7^- \rightarrow 5^-$. The reason for its presence is due to an isomeric state at 3723 keV with half-life 92 ns, assigned as 10^+ with $\pi h_{11/2}^{-2}$ [97]. The 1257 keV decay from this isomer to the 7^- state is just visible using the short-range TDCs with a $\Delta t = 15 - 200$ ns gate. The intensities, corrected for efficiency and normalised to 100 for the strongest peak, are shown in Table 5.20.

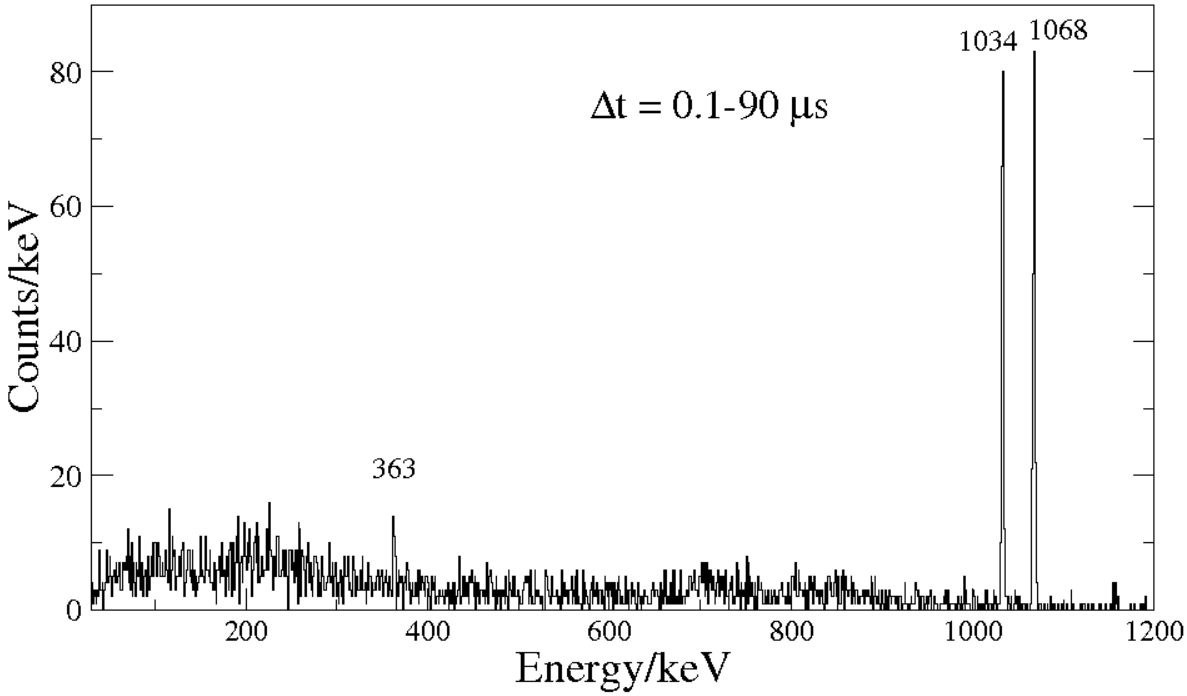

Figure 5.48: Gamma spectrum from isomeric decays in ^{206}Hg.

Table 5.20: Intensities of gamma peaks, corrected for efficiency and normalised to 100 for the strongest peak, for ^{206}Hg. To obtain the absolute intensities, multiply by 27.78.

E_γ (keV)	FWHM (keV)	Intensity
363	2.1	6(1)
1034	2.8	88(8)
1068	2.9	100(8)
1257	1	1(10)

5.4.6 Discussion of ^{203}Au

Isomerically delayed gamma decay

As noted above, in Section 5.4.2, a 563 keV isomer was observed on implantation of ^{203}Au ions, confirming the results of Caamaño *et al.* [76] and Steer [79]. Caamaño suggested that if this gamma ray is from the depopulation of an isomeric state with spin-parity $11/2^-$ at about 640 keV, it would most probably have E3 multipolarity, with hindrance $F_W \approx 1$. Steer obtained a half-life of 140(44) μs, which gives $F_W \approx 5$. The Weisskopf single particle half-lives are 2.8×10^{-5} s and 9.1×10^{2} s for E3 and M4 transitions respectively. If the 563 keV transition reported by Caamaño is, as she suggests, an E3 transition, and if it is due to decay from the 640 keV $11/2^-$ state, this would imply decay to a $5/2^+$ state, hitherto neither observed experimentally nor predicted by shell model calculations. If this is the case, the state into which it decays would have an energy of around 78 keV above the g.s. and decay via E2 to the $1/2^+$ state at 39 keV and thence via M1 to the $3/2^+$ground state; 39 keV is below the threshold at which gamma rays could be detected in this experiment, but a competing 78 keV M1 transition would be detectable. In fact, as noted above, a 75 keV peak is observed and has the same intensity within experimental error (after correcting for efficiency) as the 563 keV intensity only if it is of M1 character. However, the $\gamma-\gamma$ coincidence spectrum, shown in Fig. 5.37, shows no obvious coincidence peaks for the spectrum gated on 563 keV, although the 563 keV gamma peak is clearly in

coincidence with the 75 keV transition when gated on the latter. This implies that the decay scheme is unlikely to consist of a simple cascade consisting only of 563 and 75 keV decays as a unique decay branch.

The accepted levels indicate that there is a $3/2^+$ state at 389 keV and a $1/2^+$ state at 39 keV [82], suggesting that the 352 keV transition observed here might be from decay of the $3/2^+$ state to the $1/2^+$ state following an isomeric decay, but the coincidence spectrum again sheds no light on the relationship between this decay and the 563 keV transition.

Comparison of the beta decay of ^{205}Au and ^{203}Au.

Internal conversion electrons from a highly converted transition, of assumed M4 character, from the $11/2^-$ state to the ground state, were observed in ^{205}Au (see Section 5.3.1), yet the beta spectrum for ^{203}Au, cf. Fig. 5.41, shows no such internal conversion electrons, despite having a very similar shell structure. Given the number of ^{203}Au ions compared to the number of ^{205}Au ions, cf. Tables 5.8 and 5.9, it is unlikely that a highly converted isomeric transition in ^{203}Au would remain undetected while that in ^{205}Au was observed.

The binding energy of the K-electron in Au is 80 keV, thus a K conversion electron from the decay of the 640 keV $11/2^-$ state would have an energy of 560 keV. The competing M4 transition to the higher $3/2^+$ state at 389 keV would be even less likely since of lower energy. The internal conversion coefficients for an M4 transition of energy 640 keV are $\alpha_K = 0.44(1)$ and $\alpha_L = 0.14(1)$, giving conversion electrons at energies 559 and 626 keV respectively. Unambiguous peaks in the beta spectrum at these energies are not seen, nor are they evident in a beta spectrum made in anti-coincidence with the 563 keV gamma decay, shown in Fig. 5.49, the latter using a 15 s time correlation between implantation and β decay (as in the case of ^{205}Au). Although there does exist a peak at around 560 keV, there is no obvious L-peak at around 626 keV, nor do different time correlations enhance the peak-to-background ratio of the 560 keV peak as might be expected if it were indeed due to a K conversion electron. This is contrary to what might be expected given that shell model calculations indicate that the level structures of ^{203}Au and ^{205}Au are the same, apart from their energies, and that the lower energy of the $11/2^-$ state in ^{203}Au implies

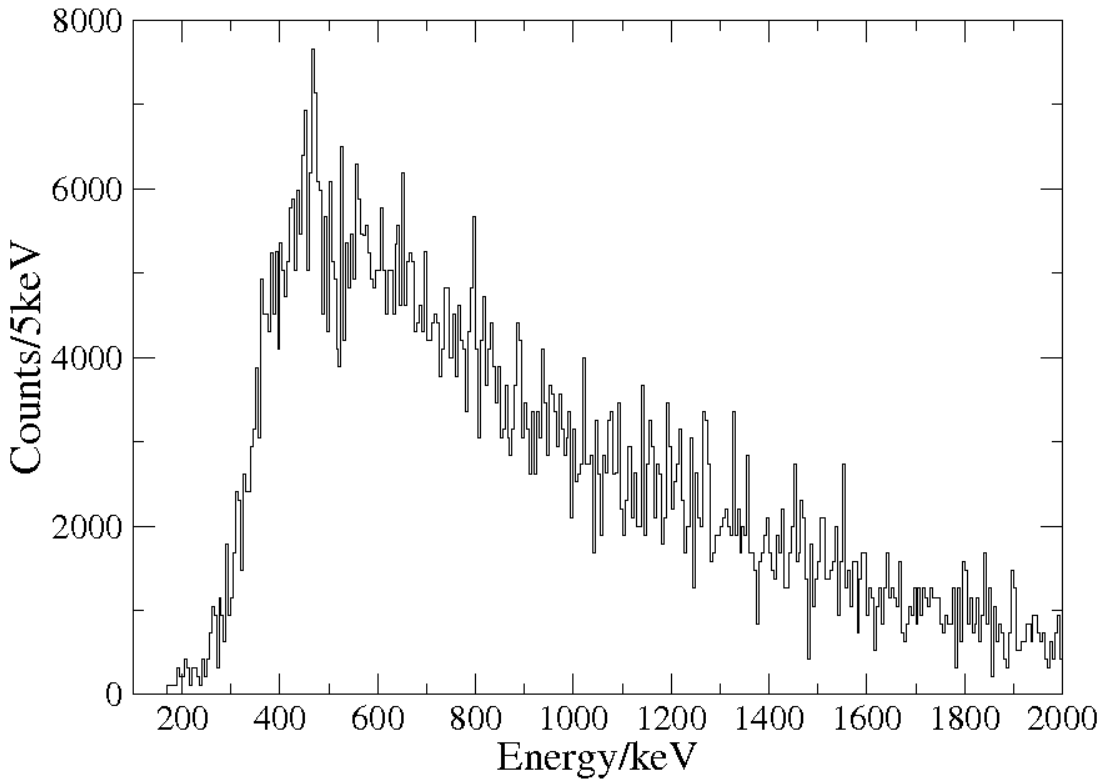

Figure 5.49: ^{203}Au beta electron spectrum for electrons when not in coincidence with the 563 keV gamma transition. A 15 s implant-β decay time correlation was used.

that the decay of this state to the ground state should be even more highly converted than the equivalent transition in ^{205}Au since it is lower in energy.

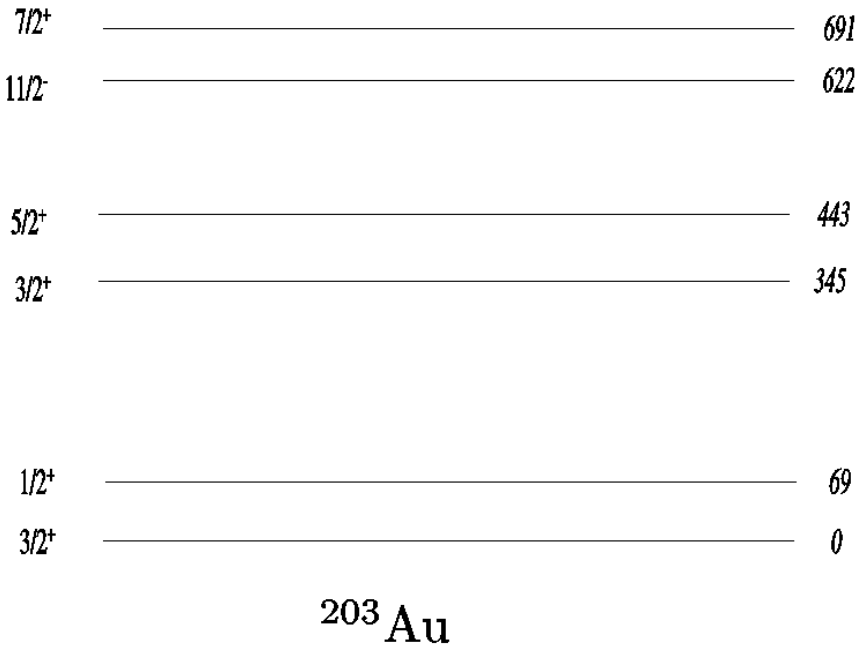

Figure 5.50: Shell model levels for ^{203}Au constructed using the OXBASH code.

OXBASH shell model calculations, as described in Section 5.3.4, performed by the author for ^{203}Au are shown in Fig. 5.50. According to these calculations, depopulation of the $11/2^-$ state could be by M4 decay to the ground state, or by E3 decay to the $5/2^+$ state, both implying an isomeric nature of this level since these decays are relatively slow. The transition rates for M4 and E3 are highly sensitive to the energy differences between the levels, $(\Delta E)^9$ and $(\Delta E)^7$ respectively (cf. Equation (2.28)). Also, these high multipolarity transitions are highly converted, especially at lower energies. If the $5/2^+$ state in ^{205}Au is in fact only 60 keV below the $11/2^-$ state, the E3 transition would then be an order of magnitude less probable than the M4 transition to the g.s., as shown by the Weisskopf half-life estimates in Table 5.21. This would then account for the absence of any detected E3 decay by internal conversion (the internal conversion coefficient for an E3 decay at 60 keV is 2.39 x 10^3 and the gamma branch would in any case be unobservable due to the long half-life of this transition).

Table 5.21: Weisskopf estimates for half-lives for selected transitions in ^{203}Au and ^{205}Au. The $11/2^-$ state in ^{205}Au is here taken to have the energy found from the detected K conversion electron, 905 keV, cf. Section 5.3.1.

Nuclide	**Transition**	**Energy (keV)**	$\mathbf{T_{1/2,W}}$ **(s)**
^{205}Au	$11/2^- \rightarrow 3/2^+$ (M4)	905	12.0(2)
^{205}Au	$11/2^- \rightarrow 5/2^+$ at 827 keV (E3)	78	27.6(37)
^{205}Au	$11/2^- \rightarrow 5/2^+$ at 845 keV (E3)	60	173(30)
^{203}Au	$11/2^- \rightarrow 3/2^+$ (M4)	622	369(8)
^{203}Au	$11/2^- \rightarrow 5/2^+$ (E3)	179	0.084(5)

The Weisskopf estimate for the half-life of the 622 keV M4 transition in ^{203}Au from $11/2^-$ to the g.s. is very long (for clear detection in this setup) at 369(8) seconds, and the competing E3 decay ($11/2^-$ to $5/2^+$ at about 180 keV), although highly converted (α_{total} = 5.62(8), is very short, with a half-life of about 80 ms. The energies of the conversion electrons are barely above the threshold (150 keV) of the DSSSDs. This could explain the fact that no conversion electrons were observed in ^{203}Au.

Alternatively, the absence of a converted M4 transition in ^{203}Au may imply that the level structure in ^{203}Au is different from that predicted by the shell model calculations. A difference between the shell structures of ^{203}Au and ^{205}Au, cf. Figs. 5.50 and 5.31, is that the former has a $7/2^+$ level immediately above the $11/2^-$ state, whereas the latter has a $5/2^+$ state above it. If the $7/2^+$ level in ^{203}Au is in fact *below* the $11/2^-$ state, this would allow depopulation of the $11/2^-$ level by a fast E2 gamma decay, thus accounting for the non-detection of the M4 decay. Such an argument is similar to that proposed by M.Caamaño *et al.* for ^{202}Pt [76]. She proposes that the isomeric 7^- level in ^{202}Pt is far more hindered, thus longer lived (280 μs), than the same level (with half-life 14 ns) in ^{200}Pt because in the latter the 5^- level is less than 90 keV below the 7^- level, permitting a fairly fast E2 decay, whereas she proposes that in ^{202}Pt the 5^- state is *above* the 7^- state, forcing an E3 decay to the 4^+ state below it, and that the increased hindrance of the E3 decay explains the longer half-life, cf. Figs. 5.51 and 5.52.

In conclusion, the specific reasons for the observation of a gamma ray at 563 keV from an isomer in ^{203}Au and the absence of a conversion electron in ^{203}Au compared to the

one detected in ^{205}Au remain to be explained more completely in terms of the shell model low-lying levels.

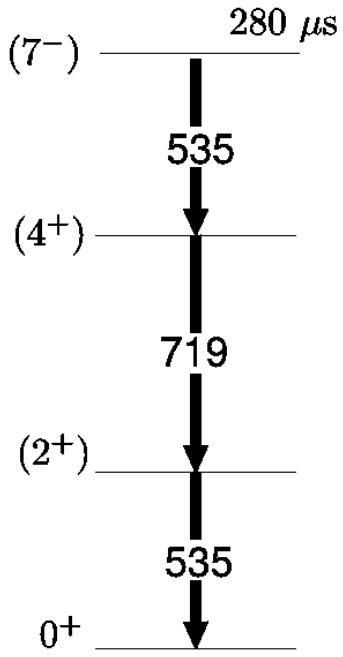

Figure 5.51: Level scheme for ^{202}Pt, taken from Caamaño [76].

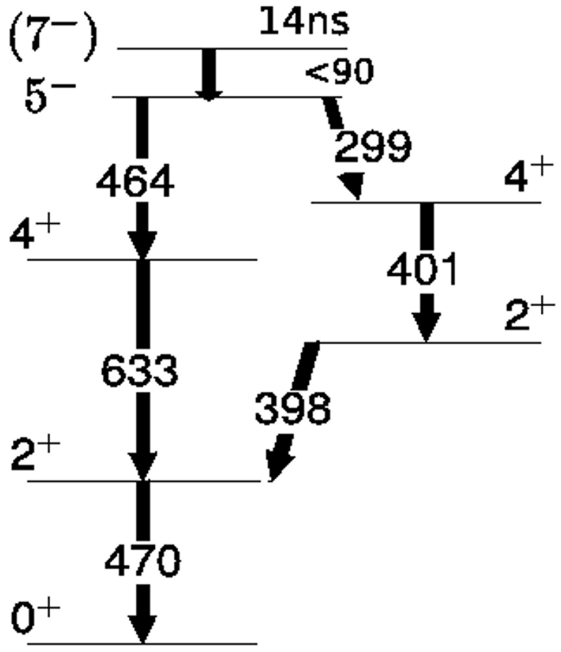

Figure 5.52: Level scheme for ^{200}Pt, taken from Caamaño [76].

Chapter 6

Conclusion

An improved, high-statistics measurement of the isomeric decay of ^{190}W produced in projectile fragmentation was carried out, allowing $\gamma - \gamma$ coincidence measurements to be performed for the first time for this nuclide and a more accurate lifetime to be obtained, compared to an earlier experiment [7]. The data show no evidence for the previously reported 591 keV transition as part of the gamma cascade of a rotational band. The previous (10^-) spin-parity assignment for this isomer [7, 81] is now disregarded in the light of the data described here. Reduced hindrance factors were calculated, blocked BCS calculations were performed, and PES calculations were carried out (by F.Xu), enabling a tentative new decay scheme to be adduced. As part of the investigation into the high intensity X-rays of $\sim 1\,\mu$s half-life, the gamma decay data from a $\sim 1\,\mu$s isomer in ^{191}W, obtained by Steer [79], was confirmed. However, several observations remain to be explained, cf. Section 5.1.4. As noted in the Introduction (see Section 1.1), describing the motivation for its investigation, ^{190}W is very much a 'transitional' nuclide. Indeed, it seems quite possible that there may be several different isomers, of differing lifetimes and types, in this most intriguing of nuclides.

In what may be regarded as a proof of principle regarding the detection of very rare decays in exotic nuclei, a highly converted transition, of probable multipolarity M4, was detected for the first time in ^{205}Au and the lifetime of the isomeric state measured. Beta-delayed gamma decays from this isomeric state, as well as those from the ground state, were observed.

In ^{203}Au, the previous observation of gamma decay with energy 563 keV from an isomer was observed, though with a longer lifetime. OXBASH shell model calculations and Weisskopf half-life estimates have been presented for both Au nuclides investigated here and reasons proffered to explain the fact that no conversion electron was observed in the decay of ^{203}Au.

Bibliography

[1] C.Normand *et al.*, J.Radioanal.Nucl.Chem. **282**, 395 (2009).

[2] *The Euroschool Lectures on Physics with Exotic Beams*, edited by J. Al-Khalili and E. Roeckl (Springer, Berlin Heidelberg, 2004), Vol. 1.

[3] E. M. Burbidge, G. R. Burbidge, W. A. Fowler, and F. Hoyle, Reviews of Modern Physics **29**, 547 (1957).

[4] `http://www.orau.org/ria/whycrucial.htm`, (site visited Oct 2009).

[5] P. Walker, in *Capture gamma-ray spectroscopy and related topics: 12th International Symposium. AIP Conference Proceedings* (American Institute of Physics, U.S.A., 2006), Vol. 819, pp. 16–23.

[6] M. Pfützner *et al.*, Phys. Lett. B **444**, 32 (1998).

[7] Z. Podolyák *et al.*, Phys. Lett. B **491**, 225 (2000).

[8] P. Sarriguren, Phys. Rev. C **77**, (2008).

[9] P. Stevenson *et al.*, Phys. Rev. C **72**, 047303 (2005).

[10] Y. Sun, P. M. Walker, F.-R. Xu, and Y.-X. Liu, Phys. Lett. B **659**, 165 (2008).

[11] L. Robledo, R. Rodríguez-Guzmán, and P. Sarriguren, J. Phys. G. **36**, 115104 (2009).

[12] F.Iachello and A.Arima, *The Interacting Boson Model* (Cambridge University Press, London, 1987).

[13] Z. Podolyák *et al.*, Physics Letters B **672**, 116 (2009).

[14] C. Wennemann *et al.*, Zeitschrift Für Physik A **347**, 185 (1994).

[15] J. Lilley, *Nuclear Physics: Principles and Applications* (J.Wiley and Sons, Chichester, 2001).

[16] J. Blatt and V. Weisskopf, in *Theoretical Nuclear Physics* (J.Wiley & Sons, New York, 1952), p. 119.

[17] K.S.Krane, *Introductory Nuclear Physics* (J.Wiley & Sons, Hoboken, NJ, 1988).

[18] `http://www.astro.rug.nl/~hidding/ao/ao.html`, (site visited Jan 2010).

[19] M.G.Mayer, Phys. Rev. **75**, 1969 (1949).

[20] O. Haxel, J. H. D. Jensen, and H. E. Suess, Phys. Rev. **75**, 1766 (1949).

[21] I.J.Cullen, Private communication.

[22] R.F.Casten, *Nuclear Structure from a Simple Perspective*, 2nd ed. (Oxford Science Publications, Oxford; New York, 2000).

[23] J. Rainwater, Phys. Rev. **79**, 432 (1950).

[24] P.E.Hodgson, *Growth Points in Nuclear Physics* (Pergamon Press, Oxford, 1980), Vol. 1.

[25] D.Halliday, *Introductory Nuclear Physics*, 2nd ed. (J.Wiley and Sons, New York, 1955).

[26] J. Orce, Deformed Nuclei, `http://www.pa.uky.edu//~jnorce/deformation/`, 2003, (site visited Feb 2010).

[27] C. Wheldon, Ph.D. thesis, Dept. of Physics, University of Surrey, 1999.

[28] W.E.Burcham, *Elements of Nuclear Physics* (Longman, London and New York, 1979).

[29] F. Xu, P. Walker, J. Sheikh, and R.Wyss, Phys. Lett. B **435**, 257 (1998).

[30] V. M. Strutinsky, Nuclear Physics A **95**, 420 (1967).

[31] P.Möller and J. R. NIX, Nuclear Physics A **536**, 20 (1992).

[32] F.Xu *et al.*, Phys.Lett.B **435**, 257 (1998).

[33] F.Xu, Private Communication, 2008.

[34] G. Jones, Ph.D. thesis, Dept. of Physics, University of Surrey, 2006.

[35] S.G.Nilsson and C.F.Tsang, Nuclear Physics A **131**, 1 (1969).

[36] R. B. Firestone, in *Table of Isotopes*, 8th ed., edited by S. F. C. Coral M. Baglin (Wiley-Interscience, New York, 1999).

[37] T.Bengtsson and I.Ragnarsson, Nuclear Physics A **436**, 14 (1985).

[38] S. S. Wong, *Introductory Nuclear Physics* (Prentice-Hall, U.S.A., 1990).

[39] P. M. Walker and J. J. Carroll, Nuclear Physics News, Volume 17, Issue 2 April 2007, pages 11-15 .

[40] P. Walker, Acta Physica Polonica B **36**, (2005).

[41] K.E.G.Löbner, Phys. Lett. **26B**, 369 (1968).

[42] K.Narimatsu, Nuclear Physics A **601**, 69 (1996).

[43] J. Orce, K-isomers, `http://www.pa.uky.edu/~jnorce/K-isomers/`, 2003, (site visited Feb 2010).

[44] K. Jain *et al.*, Nuclear Physics A **591**, 61 (1995).

[45] C. Gallagher and S. Moskowski, Phys. Rev. **111**, 1282 (1958).

[46] R. D. Piccard, Notes on Modern Physics and Ionizing Radiation, `http://oak.cats.ohiou.edu/~piccard/radnotes/alphabeta.html`, 2004.

[47] H. Geissel, Nuclear Instruments and Methods in Physics Research B **70**, 286 (1992).

[48] FRS Setup, `http://www-w2k.gsi.de/frs-setup`, (site visited Jun 2009).

[49] R.Serber, Phys. Rev. **72**, 1114 (1947).

[50] T.Kurtukian-Nieto, Ph.D. thesis, Universidade de Santiago de Compostela, Facultad de Fisica, Departamento de Fisica de Particulas, 2007.

[51] L. Audouin, Nuclear Physics A **768**, 1 (2006).

[52] A.Garnsworthy, Ph.D. thesis, University of Surrey, 2007.

[53] A. Garnsworthy, Private communication, 2008.

[54] T.Baumann, Minicourse on Experimental techniques at the NSCL Fragment Separators, 2001.

[55] K-H.Schmidt *et al.*, Nuclear Instruments and Methods in Physics Research A **260**, 287 (1987).

[56] G.F.Knoll, *Radiation Detection and Measurement*, 3rd ed. (John Wiley and Sons, Hoboken, NJ, 2000).

[57] D. Bazin *et al.*, Nuclear Instruments and Methods in Physics Research:A **482**, 307 (2002).

[58] D.J.Morrissey and B.M.Sherrill, Phil.Transactions: Mathematical, Physical and Engineering Sciences **356**, 1985 (1998).

[59] D. B. R. Anne and A. Mueller, Nuclear Instruments and Methods in Physics Research A **257**, 215 (1987).

[60] Seetram, `http://www-wnt.gsi.de/CHARMS/seetraminfo/seetram2.htm`, (site visited Mar 2010).

[61] *BC-480: Blue Wavelength Shifter*, Bicron, Saint-Gobain Ceramics and Plastics, 2005.

[62] M.V.Ricciardi, Ph.D. thesis, Universidad de Santiago de Compostela, 2004.

[63] H. Weick, MWPCs, http://www-linux.gsi.de/~weick/frs/mwpc.html, (site visited Mar 2010).

[64] MUSIC80 Manual, http://www-w2k.gsi.de/frs/technical/FRSsetup/detectors/music80/music80_manual.pdf, (site visited Oct 2009).

[65] S. Pietri *et al.*, Nuclear Instruments and Methods in Physics Research B **261**, 1079 (2007).

[66] S. Pietri *et al.*, Acta Physica Polonica B **38**, 1255 (2007).

[67] S. Pietri *et al.*, Eur. Phys. J. Special Topics **150**, 319 (2007).

[68] R.Kumar *et al.*, Nuclear Instruments and Methods in Physics Research A **598**, 754 (2008).

[69] XIA, http://www.xia.com/DGF-4C.html, (site visited Mar 2010).

[70] *Digital Gamma Finder (DGF) Pixie-4 Manuals*, version 1.10 ed., X-ray Instrumentation Associates, 8450 Central Ave., Newark, CA 94560 USA, 2004.

[71] R.Grzywacz, Nuclear Instruments and Methods in Physics Research B **204**, 649 (2003).

[72] C.Leroy and P-G.Rancoita, in *Principles of radiation interaction in matter and detection* (World Scientific Publishing Co., Singapore, 2004), p. 81.

[73] C.Scheidenberger *et al.*, Nuclear Instruments and Methods in Physics Research B **142**, 441 (1998).

[74] N.Iwasa *et al.*, Nuclear Instruments and Methods in Physics Research B **126**, 284 (1997).

[75] K-H.Schmidt, Some remarks on the identification of fragmentation products of heavy projectiles, www-win.gsi.de/charms/Preprints/Identification/ident2.pdf, (site visited Jul 2009).

[76] M. Caamaño, Eur. Phys. J. A. **23**, 201 (2005).

[77] Australian National University BrIcc v2.2b, 2010, http://physics.anu.edu.au/nuclear/bricc/.

[78] G. Lane and G.D.Dracoulis, private communication, Aug 2008.

[79] S. Steer, Ph.D. thesis, Dept. of Physics, University of Surrey, 2008.

[80] Z. Podolyák *et al.*, Phys. Rev.C **62**, 034303 (2000).

[81] P. Walker and F. Xu, Phys. Lett. B **635**, 286 (2006).

[82] Evaluated Nuclear Structure Data File (ENSDF), http://www.nndc.bnl.gov/ensdf, (site visited Feb 2010).

[83] P.Möller, J. R. Nix, and K.-L. Kratz, Atomic Data and Nuclear Data Tables **66**, 131 (1997).

[84] S. Steer, Int. Journal of Mod. Phys. E. **18**, 1002 (2009).

[85] LBNL Isotopes Project, http://ie.lbl.gov/atomic/x2.pdf, (site visited Mar 2010).

[86] F. Kondev, Nuclear Data Sheets **101**, 521 (2004).

[87] P. Möller, J. R. Nix, W. D. Myers, and W. J. Swiatecki, Atomic data and nuclear data tables **59**, 185 (1995).

[88] B. Brown, A. Etchegoyen, and W. Rae, The computer code OXBASH, MSU-NSCL report number 524, 1988.

[89] L. Rydström *et al.*, Nuclear Physics A **512**, 217 (1990).

[90] G. H. Herling and T.T.S.Kuo, Nuclear Physics A **181**, 113 (1972).

[91] M. D.Eccleshall, Phys. Lett. **19**, 301 (1965).

[92] M. Martin, Nuclear Data Sheets **70**, 315 (1993).

[93] A. Poletti *et al.*, Nuclear Physics A **580**, 64 (1994).

[94] K.-H. Maier *et al.*, Phys. Rev. C **32**, 1416 (1985).

[95] P. Zeyen *et al.*, Z. Phys **325**, 451 (1986).

[96] J.A.Becker *et al.*, Phys. Rev. C **26**, 914 (1982).

[97] B.Fornal *et al.*, PRL **87**, 212501 1 (2001).

Appendix A

FRS settings

Table A.1: **Details of the experimental setup for the ^{192}W setting**

Time on setting	40 hrs
Energy of primary beam	1 GeV/A
Typical spill intensity (pps)	1x10^9
Typical spill length (s)	10
Typical spill period (s)	20
Target thickness	Be 2446 mg/cm2
Stopper thickness (mm)	9
Dipole 1 (B [T])	1.16200
Dipole 1 (ρ [m])	11.2407
Dipole 2 (B [T])	1.16474
Dipole 2 (ρ [m])	11.317
Dipole 3 (B [T])	0.8439
Dipole 3 (ρ [m])	11.2908
Dipole 4 (B [T])	0.8476
Dipole 4 (ρ [m])	11.2441
Nb foil thickness (after target) (mg/cm^2)	221
Nb foil thickness (after S2 degrader) (mg/cm^2)	108
S2 degrader thickness (mg/cm^2)	4900
S2 degrader angle (mrad)	5.537
S4 degrader thickness (mg/cm^2)	3185
S1 Slit acceptance (mm)	-100 $\rightarrow$ +9
S2 Slit acceptance (mm)	-100 $\rightarrow$ +100
S3 Slit acceptance (mm)	-100 $\rightarrow$ +100
S4 Slit acceptance (mm)	-100 $\rightarrow$ +100
Magnification from target to S2	0.73
Dispersion from target to S2 (mm/%)	-6.474
Magnification from target to S4	1.118
Dispersion from target to S4 (mm/%)	7.239
Distances from end of D4(mm)	
MW41	1050
MUSIC41	1390
MUSIC42	1960
MW42	2300
SLITS (S4)	2390
Scintillator41	2950
S4 degrader	3250
Stopper	4407
Scintillator43	4990

Table A.2: **Details of the experimental setup for the ^{203}Au setting**

Time on setting	5 h
Energy of primary beam	1 GeV/A
Typical spill intensity (pps)	1.00 x 10^9
Typical spill length (s)	1
Typical spill period (s)	7
Target thickness	Be 2446 mg/cm2
Stopper thickness (mm)	3 x DSSSDs 1mm thick
Dipole 1 (B [T])	1.1781
Dipole 1 (ρ [m])	11.07085
Dipole 2 (B [T])	1.1651
Dipole 2 (ρ [m])	11.18456
Dipole 3 (B [T])	0.7853
Dipole 3 (ρ [m])	11.31318
Dipole 4 (B [T])	0.8000
Dipole 4 (ρ [m])	11.25072
Nb foil thickness (after target) (mg/cm2)	223
Nb foil thickness (after S2 degrader) (mg/cm2)	108
S2 degrader thickness (mg/cm2)	5050
S2 degrader angle (mrad)	11.90
S4 degrader thickness (mg/cm2)	2181
S1 Slit acceptance (mm)	-10 $\rightarrow$ 0
S2 Slit acceptance (mm)	0 $\rightarrow$ +50
S3 Slit acceptance (mm)	-20 $\rightarrow$ 0
S4 Slit acceptance (mm)	-20 $\rightarrow$ +50
Magnification from target to S2	0.73
Dispersion from target to S2 (mm/%)	-6.474
Magnification from target to S4	1.11523
Dispersion from target to S4 (mm/%)	7.2203
Distances (from end of D4)(mm)	
MW41	1050
MUSIC41	1390
MUSIC42	1960
SLITS (S4)	2200
MW42	2559
Scintillator41	3000
S4 degrader	3250
Stopper	4407
Scintillator43	4990

Table A.3: **Details of the experimental setup for the ^{205}Au setting**

Time on setting	15 h
Energy of primary beam	1 GeV/A
Typical spill intensity (pps)	1.00 x 10^9
Typical spill length (s)	1
Typical spill period (s)	10
Target thickness	Be 2446 mg/cm2
Stopper thickness (mm)	3 x DSSSDs 1mm thick
Dipole 1 (B [T])	1.19080
Dipole 1 (ρ [m])	11.2407
Dipole 2 (B [T])	1.17750
Dipole 2 (ρ [m])	11.317
Dipole 3 (B [T])	0.8086
Dipole 3 (ρ [m])	11.3132
Dipole 4 (B [T])	0.8132
Dipole 4 (ρ [m])	11.2507
Nb foil thickness (after target) (mg/cm2)	223
Nb foil thickness (after S2 degrader) (mg/cm2)	108
S2 degrader thickness (mg/cm2)	5050
S2 degrader angle (mrad)	12.04
S4 degrader thickness (mg/cm2)	2286.000
S1 Slit acceptance (mm)	-20 $\rightarrow$ +20
S2 Slit acceptance (mm)	0 $\rightarrow$ +100
S3 Slit acceptance (mm)	-30 $\rightarrow$ +10
S4 Slit acceptance (mm)	-100 $\rightarrow$ +100
Magnification from target to S2	0.73
Dispersion from target to S2 (mm/%)	-6.474
Magnification from target to S4	1.11523
Dispersion from target to S4 (mm/%)	7.2203
Distances (from end of D4)(mm)	
MW41	1050
MUSIC41	1390
MUSIC42	1960
SLITS (S4)	2200
MW42	2559
Scintillator41	3000
S4 degrader	3250
Stopper	4407
Scintillator43	4990

Appendix B

Published papers